Mixed Mode Fracture in Fibre Reinforced Polymer Composites

by

Mark Conroy

B.E.

A thesis submitted for the degree of Doctor of Philosophy
of the National University of Ireland

School of Mechanical & Materials Engineering
University College Dublin

November 2015

Prof Michael Gilchrist
Head of School

Prof Alojz Ivanković
Dr Neal Murphy
Supervisors

Declaration

I certify that the work presented in this thesis is, to the best of my knowledge and belief, original, except as acknowledged in the text, and that the material has not been submitted, either in whole or in part, for a degree at this or any other university.

Signed: _____

Date: _____

Abstract

It has been widely reported that the delamination toughness of adhesive joints and polymer matrix composites can vary considerably depending on the mode of loading. For this reason, extensive research has been aimed at devising fracture test methods based on beam-like geometries, which enable the testing of these joint systems under variable modes of loading. However, central to the analysis of these mixed mode test methods, is the definition of a consistent parameter for the characterisation of the mode mixity in the fracture process zone for a given geometry and loading arrangement.

This requirement has led to the development of a number of contrasting analytical partitioning theories in the literature which aim to address this problem. The most notable of these are the initial global analysis by Williams and a subsequent local analysis by Hutchinson and Suo. However, significant differences exist between the local and global approaches in the case of fracture in asymmetric geometries, and experimental evidence has been put forward on various occasions supporting each. Other semi-analytical and analytical partitioning theories have also been put forward by Davidson et al. and, more recently, Wang & Harvey. However, much confusion still surrounds the area of mixed mode partitioning in beam-like geometries, and considerable disagreement remains within the fracture mechanics community as to which partitioning theory, if any, should be used in practice.

In this thesis, a new semi-analytical partitioning scheme is proposed based on the findings from a finite element analysis of fracture in beam-like geometries. The fracture process zone is modelled using a cohesive zone model and the energy going into both opening and shearing, and hence the mode mixity, is obtained using a mode decomposed J-integral approach. A parametric study is carried out to examine the effect of various substrate and cohesive properties on the mode mixity. In an initial study, it is found that if no damage is modelled (purely elastic case), the numerical partitioning closely follows the local partitioning of Hutchinson and Suo. Once damage is introduced using the cohesive zone model, it is found that the numerical partition deviates away from the local solution and in all cases tends towards the global solution of Williams.

The parametric study reveals that the numerical mode partition moves towards the global solution when the substrate stiffness (E) or cohesive toughness (G) is increased, or the cohesive strength (t) is decreased. Each of these parameters that affect the mode mixity are linked through the developed cohesive zone length ($l_{cz} = f(EG/t^2)$). For each individual test geometry, it is found that the mode partition is uniquely dependent on the numerical cohesive zone length. At this point, it is hypothesised that the size of the

cohesive zone relative to the size of the K dominant region is the controlling factor in the mode mixity, where the upper and lower bounds of the partitioning solution are given by the local and global analytical solutions respectively (region of K dominance scales with smallest characteristic dimensions). To test this hypothesis, the normalised mode mixity is plotted against the normalised cohesive zone length for all cases over a range of geometries, loadings and cohesive properties. A unique dependency is observed, thus supporting the proposed hypothesis. This hypothesis is further tested using a different cohesive zone formulation and it is still found to hold true. A best fit exponential function is fitted to the observed unique dependency and this forms the basis for the proposed semi-analytical cohesive analysis (SACA).

SACA works on the basis that if the cohesive zone length can be estimated from known cohesive properties, then the mode mixity can be estimated from the unique dependency curve. Analytical expressions exist, which were presented by Suo (mode I) and Cox & Yang (mode II), that can accurately estimate cohesive zone lengths in beam like geometries under mode I and mode II loadings. It is shown in this work that these expressions can also be used to accurately estimate the cohesive zone length under mixed mode loadings by using the maximum of the mode I and mode II cohesive lengths, where the mode I and mode II cohesive zone lengths are obtained by using the energy dissipated in mode I and mode II respectively. As the mode partition is not known initially for each case, the final estimated length, and hence mode mixity, is obtained using an iterative procedure. The final solution is shown to be independent of the initial guess of mode mixity. This procedure is coded into an excel macro and is available for download on the UCD Centre of Adhesion and Adhesives webpage.

Finally, the SACA approach is assessed using an experimental program. In this series of experiments, the true delamination failure locus of a carbon fibre-epoxy composite is obtained using a range of symmetric double cantilever beam specimens loaded with uneven bending moments. A number of asymmetric fracture tests are then carried out and partitioned using a range of analytical partitioning theories including the new SACA approach. It is found that the SACA partitioning of the asymmetric specimens produces the best fit to the symmetrically measured failure locus. This experimental result supports the numerical findings that the true partitioning in the general case is neither local nor global and can only be accurately estimated by accounting for the effect of damage at the crack tip, as in the SACA approach. The SACA partitioning is also applied to previously contrasting experimental data available in the literature, and good agreement is obtained in all cases, suggesting that the proposed semi-analytical cohesive analysis provides an efficient and accurate method for predicting mixed mode partitions.

Dedicated to my parents, Martin and Ita,

and
my Aisling

Acknowledgements

I would like to express my sincere gratitude to my supervisors Prof. Alojz Ivanković and Dr. Neal Murphy for their continuous support and guidance throughout my PhD. I am forever indebted to them.

I am eternally grateful to Prof. Gordon Williams, Prof. Tony Kinloch and Prof. Aleksandar Karač for their invaluable contributions to this project. I would also like to thank the members of ESIS TC4; the knowledge, insights and friends I have gained from my involvement with this group over the past four years has been invaluable.

I would like to thank Prof. Bent F. Sørensen for kindly accommodating me during my research visit to DTU and for many helpful discussions on the project during my stay. I would also like to thank the technical staff at DTU for their help, in particular Jan Sjølin, Christian H. Madsen, Steffen Rasmussen and Malcolm McGugan.

I would like to gratefully acknowledge the financial support of the Irish Research Council and Henkel Ireland Ltd. The materials provided by Bombardier Aerospace are also gratefully acknowledged. The SFI/HEA Irish Centre for High-End Computing (ICHEC) are gratefully acknowledged for the provision of computational facilities and support. I would also like to thank Prof. Michael Thouless for providing the UEL subroutine for the Uncoupled Dugdale CZM.

I wish to thank all of my educators throughout the years from Camross N.S., Colaiste Phobal Ros Cré and University College Dublin. I am very lucky to have had some wonderful teachers that gave me great encouragement along the way.

I would like to thank Ms. Agnieszka Wisniewska, Ms. Martine Kisielewicz and Mr. Oran O'Rua for their help with administrative matters during my time in UCD.

Thanks to all of my colleagues and friends in room 314 for everything from helpful discussions to the occasional mighty session.

I would like to thank the lads for never failing to lighten the day with some banter via Viber or otherwise.

I would especially like to thank my parents, Ita and Martin, and my sisters for all their support and encouragement throughout the years.

Finally, I would like to thank my wonderful Aisling. The impact of your incredible patience, love, support and encouragement throughout the years has been immeasurable.

Contents

List of Figures

List of Tables

Abbreviations

(A)DCB	(Asymmetric) Double Cantilever Beam
(A)FRMM	(Asymmetric) Fixed Ratio Mixed Mode
(A)MMB	(Asymmetric) Mixed Mode Bend
(A)ELS	(Asymmetric) End Loaded Split
ASTM	American Society for Testing and Materials
C-ELS	Calibrated End Loaded Split
CFRP	Carbon Fibre Reinforced Polymer
COH2D4	Two dimensional cohesive element with four nodes
CTE	Crack Tip Element
CTO	Crack Tip Opening
CZM	Cohesive Zone Model
D-NSF	Davidson-Non Singular Field partitioning
DCB-UBM	Double Cantilever Beam loaded with Uneven Bending Moments
DIC	Digital Image Correlation
DTU	Denmark Technical University
ESIS	European Structural Integrity Society
FPZ	Fracture Process Zone
GFRP	Glass Fibre Reinforced Polymer
HS	Hutchinson and Suo local partitioning
IDI	Interaction Domain Integral
ISO	International Organisation for Standardisation
LSE	Least Squares Error
LVDT	Linear Variable Displacement Transducer
MDJ	Mode Decomposed J Integral
NL	Non-Linear

PTFE	Polytetrafluoroethylene
R curve	Resistance curve
RHS	Right Hand Side
SACA	Semi Analytical Cohesive Analysis
SACA(D)	Semi Analytical Cohesive Analysis using Dugdale CZM
SACA(L)	Semi Analytical Cohesive Analysis using Linear softening CZM
SD	Standard Deviation
SSEL	Steady State Element
UCD	University College Dublin
UD	Uni-Directional
VCCT	Virtual Crack Closure Technique
WH/WH-E	Wang and Harvey - Euler beam theory partitioning
WH-T	Wang and Harvey - Timoshenko beam theory partitioning
W	Williams global partitioning

Chapter 1

Introduction

1.1 FRP Composites

1.1.1 Overview

Fibre reinforced polymer-matrix (FRP) composite materials are currently used extensively across a wide range of industry sectors due to their many favourable properties. These properties include high strength to weight ratios, high stiffness to weight ratios, improved fatigue resistance, and improved corrosion resistance when compared to many traditional materials [1]. Composite materials are not a new phenomenon and have been used in various forms since their first inception as a combination of mud and straw (wattle and daub) over 6000 years ago [2]. While the materials combined to make composites have advanced since that time, the principles behind their use remain the same. Effectively, two or more materials are combined to create a new material with desirable properties from each of the constituent materials, and sometimes with properties which arise solely from the combination, e.g. toughness in nano particle/polymer composites [3]. The current work focuses on long fibre reinforced polymer composites. In these materials, high strength and high moduli fibres, which are most commonly made from glass (GFRP) or carbon (CFRP), are embedded within the polymer matrix resin. The main functions of the fibres are to provide strength and stiffness. Fibres are used as they possess strength and stiffness well beyond what is observed in the same bulk material. The reason for this is down to the fact that the fibres are so thin ($\approx 5 - 10\mu m$) that the crystals can be aligned to form an ordered structure, which will contain significantly less defects compared to bulk material [4]. The main functions of the matrix are to hold the fibres together, provide resistance to buckling, and provide impermeability. Matrix

resin can come in many different forms, either thermosetting (e.g. epoxies) or thermoplastics (e.g. PEEK). Fibres can be aligned in a single direction (uni-directional) or can be woven to provide strength in more than one direction (multi-directional). A single layer of fibres is known as a ply or lamina; multiple layers of plies are then combined together to form a laminate structure.

1.1.2 Applications

The use of fibre-reinforced composite material has grown steadily since the 1960s. They now find applications in multiple sectors including space, aerospace, automotive, wind energy, sports equipment, among others. They are particularly sought after in sectors where weight savings are a critical factor. The use of composites initially complemented the traditional structural materials in many areas, and their use was confined to secondary structures. This has changed, however, and they are now being utilised in primary load bearing structures. This is particularly evident in the case of the aerospace sector, where the wing structures and fuselages of the Boeing 787 Dreamliner and Airbus A350 are made primarily from CFRP. Along with the aerospace sector, CFRP is now also used almost exclusively as the main material in high performance cars and bicycles, and in motorsport vehicles. A CFRP monocoque of a Lambroghini Aventador is shown in fig. 1.1.

(a) CFRP monocoque of Lambroghini Aventador. (b) Lambroghini Aventador.

FIGURE 1.1: CFRP monocoque of Lambroghini Aventador on display at ECCM 15, Venice, 2012.

While CFRP is popular in high performance applications, the most commonly used composite material for general applications is the cheaper and lower modulus GFRP, which can be found in wind turbine blades, piping, storage tanks, yachts, concrete reenforcement bars, as well as secondary aircraft structures among many other general applications. The use of composites are not without their drawbacks, however.

1.1.3 Limitations

One of the major drawbacks of laminated composite materials is that they are prone to develop delaminations. These delaminations occur when a crack starts between two plies; these may occur due presence of an unwanted air inclusion after manufacturing, or they may develop due to an impact during service. In either case, the occurrence of delaminations is detrimental to the performance of composites and can result in a loss of stiffness and strength, and can ultimately lead to catastrophic component failures. Delaminations are particularly dangerous as they can occur beneath the surface and go undetected to the naked eye. This uncertainty surrounding the structural integrity of composite materials is a major cause for concern. Recently, the United Stated Government Accountability Office published a report on their oversight of safety of composite airplanes [5]. In this report, they identified four key safety related concerns, which are listed below:

- limited information on the behaviour of airplane composite structures.
- technical issues related to the unique properties of composite materials.
- standardisation of repair materials and techniques.
- training and awareness.

The first two concerns specifically relate to the uncertainty surrounding how these materials will behave in service. The characterisation of composite strength and stiffness has long been well understood; however, it is the characterisation of composite toughness, its resistance to delaminations, that is the real unknown leading to the issues raised in the report cited above. A thorough understanding of what it takes to propagate cracks in composite materials is required for competent structural analyses of composite components. This has long been recognised, and a lot of work has been done to standardise toughness testing of composites [6–10]; however, much work still remains to be done, particularly in relation to mixed mode testing.

1.2 Fracture of Composite Materials

1.2.1 Mixed Mode Fracture

Before discussing the fracture of composite materials, it is important to introduce the idea of mixed mode loading (mode mixity). There are three pure modes in which a

crack can be loaded, corresponding to modes I, II and III; mode I loading results in a state of pure tensile stresses at the crack tip, mode II loading results in a state of pure in-plane shear stress at the crack tip, and mode III loading results in a state of pure out of plane shear stresses at the crack tip. These three modes of loading are represented graphically in fig. 1.2. Mixed mode loading occurs when a mixture of opening and shear loads are applied to a crack tip. Only in-plane mixed mode I/II is considered in this work; therefore, when mixed mode loading is referred to hereafter, it can be inferred to mean mixed mode I/II loading. In order to determine what the relative amounts of one mode to another mode for a given mixed mode loading (mode mixity), a consistent parameter is required. The most commonly used parameter for characterising mode mixity is the relative energy release rate (ERR) in each mode. The mode mixity (G_{II}/G) is specifically defined here as the mode II energy release rate (G_{II}) divided by the total energy release rate (G), where $G = G_I + G_{II}$. Other definitions of mode mixity exist which are based on stress and displacement [11]; however, these definitions are only equivalent to the ERR based definition for a crack in an ideally elastic material.

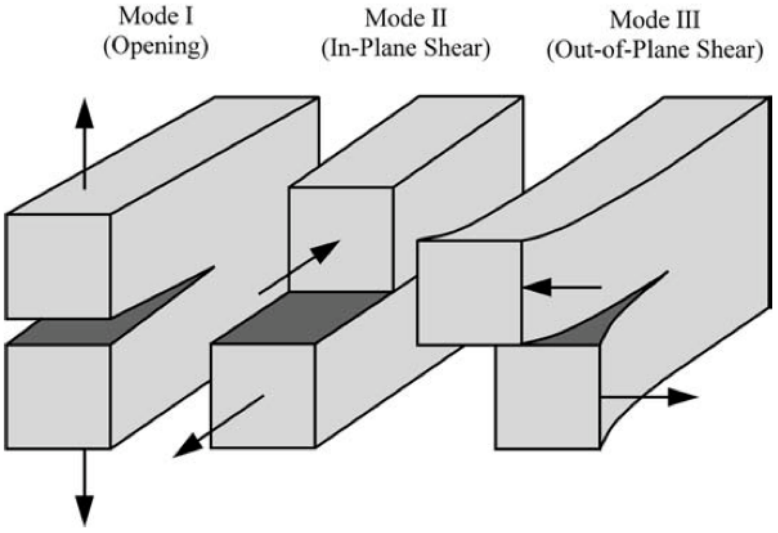

FIGURE 1.2: Pure modes of loading applied to crack [12].

Mixed mode fracture in laminated composite materials presents a unique set of challenges not previously seen in monolithic materials. When a crack in a monolithic material is subjected to a mixed mode loading, it will generally kink to stay locally in a state of pure mode I [13]. This behaviour of mixed mode cracking in monolithic materials is well understood and theoretical predictions are in good agreement with experimental observations [14]. However, when an interlaminar crack in a composite material is subjected to a mixed mode loading, it is forced to grow globally in plane under mixed mode conditions due to the constraint of adjacent plies. The initiation and propagation of

these mixed mode cracks can lead to multiple different damage mechanisms, all of which can interact to contribute to either a higher or, more worryingly, lower initiation toughness than in the pure mode tests. Dillard et al. [14] reported a number of cases where the mixed mode toughness was considerably lower (up to 50% in some cases) than the pure mode I toughness for various adhesive joint systems. This is particularly worrying from a design perspective as the mode I toughness is generally taken as the minimum toughness when designing structures. Therefore, by not characterising the toughness of a composite system in mixed mode, one might be missing out on vital information that could lead to non-conservative designs. By measuring toughness as a function of mode mixity, one can generate what is known as a mixed mode failure criterion, or failure locus. Numerous failure criteria have been proposed in literature based on experimental investigations of toughness of composite materials as a function of mixed mode loading [15–19]. However, each of the proposed failure criteria are essentially best fit curves, which lack any physically consistent predictive capabilities. It is of therefore of critical importance to fully characterise the way in which each individual material will behave in service under a full range of mixed mode loadings; this is essential to help eliminate the risk of non-conservative design, and address the concerns raised in [5]. Unfortunately, the measurement of the mixed mode failure locus is not a straightforward task, and one must currently rely on the accuracy of analytical partitioning, of which there are many differing theories, to determine the correct mode of loading for a given test configuration. A number of the most widely used mixed mode partitioning theories are introduced in the following section.

1.2.2 Mixed Mode Fracture Testing

Central to the analysis of all mixed mode test methods is the accurate decomposition of ERRs as a function of material properties, specimen geometry and loading configuration. Beam-like geometries as seen in fig. 1.3 have formed the cornerstone for the development of fracture tests due to the ease of extracting total energy release rates based on simple beam theory [20]. Using beam theory, the total energy release rate for an increment of crack growth in fig. 1.3 can be shown to be given by:

$$G = \frac{M_1^2(1+\gamma)^3}{16BEI}\Big(\frac{1}{\gamma^3} + k^2 - \frac{(1+k)^2}{(1+\gamma)^3}\Big) \tag{1.1}$$

where E is the beam modulus in the bending direction and B is the out of plane width, k is the applied moment ratio as defined in fig. 1.3, γ is the beam height ratio as defined in fig. 1.3, and I is the second moment of area of half the uncracked specimen, which is

Test Description	γ	k	G_{II}/G
Double Cantilever Beam (DCB) [7, 9]	1	-1	0
End Load Split (ELS) [8]	1	1	1
Fixed Ratio Mixed Mode (FRMM) [6]	1	0	0.4286
Mixed Mode Bend (MMB) [10]	1	-1 – 1	0 – 1
Asymmetric DCB (ADCB)	0 – ∞	-1	?
Asymmetric ELS (AELS)	0 – ∞	1	?
Asymmetric FRMM (AFRMM)	0 – ∞	0	?
Asymmetric MMB (AMMB)	0 – ∞	-1 – 1	?

TABLE 1.1: Common fracture test configurations and resulting mode partitions.

given by:

$$I = \frac{Bh^3}{12}; \quad h = \frac{(h_1 + h_2)}{2} \tag{1.2}$$

By varying the beam height ratio, γ, and the applied moment ratio, k, it is possible to

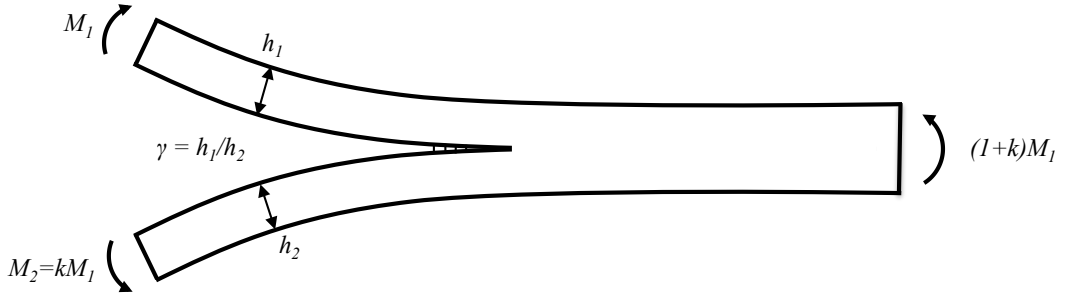

FIGURE 1.3: Beam like geometry subjected to pure bending moments (M_1, M_2).

produce different mode mixities. Common fracture tests with the corresponding γ and k values are outlined in table 1.1.

The first four test methods outlined in table 1.1 use symmetric specimens, i.e. the crack is located centrally ($\gamma = 1$). It turns out that it is straightforward to analytically determine the mode I and mode II energy release rates in symmetric samples subjected to bending moments, without making any assumptions about the crack tip damage zone. The mode I and mode II ERR can be determined analytically using the mode decomposed J integral approach, which is outlined in chapter 2. The global mode partition is dependent only on the applied moment ratio k. The relationship between the applied moment ratio and mode mixity for symmetric specimens is given by eq. 1.3, and plotted in fig. 1.4.

$$\frac{G_{II}}{G} = \frac{1}{1 + \frac{4}{3}\frac{(1-k)^2}{(1+k)^2}} \tag{1.3}$$

Each of the symmetric tests outlined in table 1.1 are standardised in some form. The pure mode fracture tests, DCB [7], ELS [7], are the most commonly used test methods for the characterisation of fracture toughness in composites. The FRMM test, where a load is applied to one arm of a symmetric specimen ($k = 0, \gamma = 1$), is also a commonly used method of obtaining the mixed mode toughness, at $G_{II}/G = 3/7$. This test is currently being prepared as a draft standard by the ESIS TC4 committee [6]. The popularity of these tests (DCB,ELS,FRMM) is partly due to the ease with which the tests can be carried out on standard tensile testing machines. Finally, the last symmetric test is the mixed mode bend test (MMB), which is an ASTM standard [10]. This test method allows for the testing of symmetric specimens where the moment ratio k can be varied. This allows the mode mixity to be varied from pure mode I to pure mode II and can therefore cover the full range of mixed mode loadings. The previous test examples are therefore subsets of the MMB test. However, it is not a trivial task to apply varying moment ratios to test specimens and this requires the use of a specialised test rig; the test rig used in the ASTM standard is the one developed by Reeder and Crews Jr. [21] and later modified by Reeder and Crews Jr. [22], Reeder [23]. Other test rig configurations were proposed by Fernlund and Spelt [24], Sørensen et al. [25]. The test rig used in the current work is the double cantilever beam specimen loaded with uneven bending moments (DCB-UBM); this test rig was developed by Sørensen et al. [25]. In this test method, the moments are applied directly, and are not the result of applied transverse forces, as in each of the previous test cases; this offers a number of distinct advantages over the standard tests, in particular it allows for the direct calculation of the applied energy release rate based on the applied moments from eq. 1.1, as it does not require the crack length estimation or correction factors in order to determine the resultant moment at the crack tip. The DCB-UBM test rig is used for fracture testing in the current project, and is discussed in further detail in chapter 5.

Each of the test methods presented in the first half of table 1.1 have equivalent test procedures but with the cracks located off-centre, or asymmetrically. These are presented in the bottom half of table 1.1. Unfortunately, unlike their symmetric counterparts, the mode partition cannot be determined analytically using the mode decomposed J integral procedure. The reason is that the mode decomposed J integral requires the integration around the beam using an arbitrary path, but which must be symmetric about the crack tip; in the symmetric test case, the horizontal sections of the path are chosen to coincide with the outer surfaces of the beams, which means that the J integral contribution along these sections vanish, and the remaining sections (across the beam thicknesses) are chosen far away from the crack tip where the stress and strain distribution are known directly as a function of the applied moments. This allows the direct calculation

of the decomposed energy release rates, which depend only on the applied moment ratio. However, for asymmetric specimens the analysis is not so straightforward; the free surface can only be chosen on one side (due to the condition of path symmetry), therefore the integration must be performed horizontally within the beam at some point, where the stresses can not be estimated, either analytically or numerically, without accurate details of the fracture process zone. The numerical calculation of the mode decomposed J integral as a function of fracture process zone properties forms the basis of the work presented in this thesis.

Firstly however, there is a number of mixed mode analytical partitioning theories which have been developed in the literature, which aim to predict the mode partition in beam like geometries as a function of both loading and beam height ratio. In each of these cases, assumptions are made about crack tip conditions, which then allow the partitions to be predicted for a given loading and geometry. The mixed mode partitioning theories considered in this work are the initial global analysis developed by Williams [20](W), the local crack tip analysis developed by Suo and Hutchinson [26](HS), the empirical non-singular field approach developed by Davidson et al. [27](D-NSF), and the more recent Euler beam theory analysis developed by Wang and Harvey [28](WH). Other analytical partitioning theories have been proposed in the literature based on various plate and beam theories [29–31]. There is no general agreement between the predicted partitions from any of these partitioning theories for asymmetric fractures, though they all agree for symmetric specimens and correctly predict the relationship given in eq. 1.3. Despite this fact, each of these partitioning theories have been shown, at one point or another, to produce consistent failure loci, when used to partition asymmetric fractures [32–35]. It is therefore not known which, if any, of these partitioning theories should be used to partition mixed mode fractures in the general case. Each of these theories are presented in the following section.

1.2.3 Mixed Mode Partitioning Theories

1.2.3.1 Williams [20]

Williams [20] first proposed a fully analytical approach for decomposing ERRs into mode I and mode II components based on classical beam theory, without considering the details of local stress and strain distributions. The method involves identifying the contributions from the applied moments which cause pure opening (mode I) and pure in-plane shearing (mode II). These decomposed moment contributions are then used to

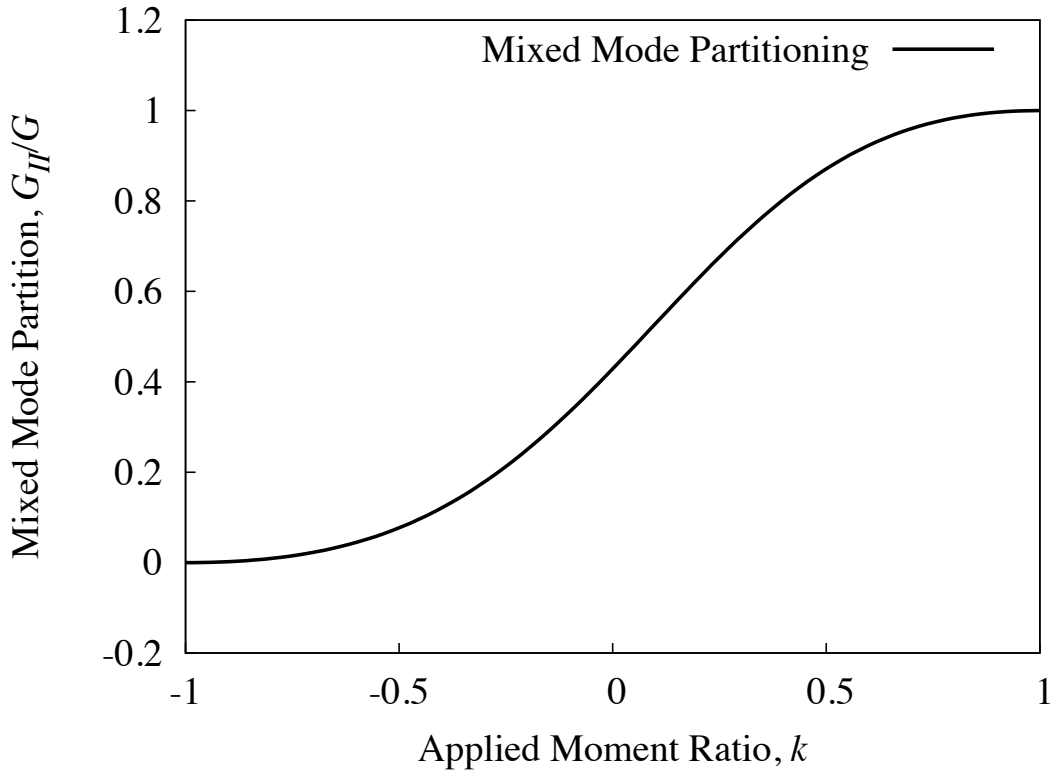

FIGURE 1.4: Relationship between mixed mode partition and applied moment ratio for symmetric specimens (γ =1,k varied)

calculate the individual ERR contributions for the general loading configuration. This approach is often referred to as the global approach.

Williams [20] proposed that the applied moments could be decomposed into components which caused pure mode I (M_I) and pure mode II (M_{II}). By proposing that pure mode I occurs when moments are equal and opposite ($-M_1 = M_2$), and pure mode II occurs when beam curvatures are equal ($M_1/EI_1 = kM_1/EI_2$), it is possible to represent the applied moments as a combination of the decomposed moments as:

$$\begin{aligned} M_1 &= M_{II} - M_I \\ kM_1 &= \psi M_{II} + M_I \end{aligned} \tag{1.4}$$

where $\psi = (h_2/h_1)^3$. The resultant mode I and mode II energy release rates can be found directly by substituting eqs. 1.4 into eq. 1.1 as no cross product term containing $M_I M_{II}$ is produced. The resulting decomposed energy release rates are given by:

$$G_I = \frac{6M_I^2(1+\psi)}{B^2 E h_2^3} \tag{1.5a}$$

$$G_{II} = \frac{18M_{II}^2 h_2(1+\psi)}{B^2 E h_1^2} \tag{1.5b}$$

1.2.3.2 Suo and Hutchinson [26]

Separately, Suo and Hutchinson [26] proposed a solution based on the decomposition of stress intensity factors (SIFs) by considering local conditions at the crack tip. Thus, in contrast to the Williams [20] global partitioning approach, this approach assumes the presence of a K dominant region and involves the numerical solution of integral equations; this partitioning approach is commonly referred to as the local partitioning approach.

In the local approach [26], the partitioning of eq. 1.1 is carried out by obtaining the singular field stress distributions at the crack tip and solving for the decomposed stress intensity factors K_I, K_{II}. Using the relation between energy release rate and stress intensity factors for homogeneous isotropic materials i.e.

$$G = \frac{(K_I^2 + K_{II}^2)}{E} \tag{1.6}$$

the decomposed energy release rates are expressed as:

$$G_I = \frac{1}{E}\Big(\frac{P}{\sqrt{2h_1 U}} cos(\omega) + \frac{M}{\sqrt{2h_1^3 V}} sin(\omega+\phi)\Big)^2 \tag{1.7a}$$

$$G_{II} = \frac{1}{E}\Big(\frac{P}{\sqrt{2h_1 U}} sin(\omega) - \frac{M}{\sqrt{2h_1^3 V}} cos(\omega+\phi)\Big)^2 \tag{1.7b}$$

where M and P are linear combinations of the applied loads. In the particular case of the loading shown in fig. 1.3, these are defined as:

$$\begin{aligned} P = -C_2\frac{(M_1+M_2)}{h_1}, \quad M = M_1 - C_3(M_1+M_2) \\ C_2 = \frac{6/\gamma}{(1/\gamma+1)^3}, \quad C_3 = \frac{1}{(1/\gamma+1)^3} \end{aligned} \tag{1.8}$$

and U, V and ϕ are geometric factors defined by:

$$\begin{aligned} U = \frac{1}{1+4\gamma+6\gamma^2+3\gamma^3}, \quad V = \frac{1}{12(1+\gamma^3)} \\ \phi = sin^{-1}(6\gamma^2(1+\gamma)\sqrt{UV}) \end{aligned} \tag{1.9}$$

ω, which is a function of γ, can not be obtained analytically and is extracted from a rigorous numerical solution of the case in which $\gamma \to 0$, and then linearly approximated over the range $0 \leq \gamma \leq 1$. The value of ω at $\gamma = 1$ is known because the mode partition

is exact in this case. The proposed linear approximation is given by:

$$\omega = 52.1 - 3\gamma \tag{1.10}$$

This solution is valid only for $0 \leq \gamma \leq 1$. Values for $\gamma \geq 1$ can be obtained by using $(1/\gamma)$ in place of γ in eqs. 1.8-1.10, and swapping M_1 and M_2 in eq. 1.8 [36].

1.2.3.3 Davidson et al. [27]

At the same time as Suo and Hutchinson [26] developed their partitioning based on the solution of integral equations derived from 2D elasticity, Schapery and Davidson [37] developed a similar technique based on classical plate theory. In this work, they developed a crack tip element approach where the applied loads were combined to form a concentrated crack tip force (N_c) and moment (M_c), which are defined in eq. 1.11 for the pure moment loading shown in fig. 1.3:

$$\begin{aligned} N_c &= a_{12}(1+k)M_1 \\ M_c &= M_1 + (a_{12}\frac{h_1}{h_2} - a_{22})(1+k)M_1 \end{aligned} \tag{1.11}$$

where a_{12} and a_{22} are functions of the plate elastic moduli and geometry; their exact definitions can be found in [37]. The total energy release rate G was calculated by multiplying the crack tip force and moments by the respective displacements and rotations behind the crack tip. They proposed the energy release rate be given in the form of:

$$G = \frac{1}{2}(c_1 N_c^2 + c_2 M_c^2 + 2c_{12} N_c M_c) \tag{1.12}$$

where c_1, c_{12} and c_2 are again functions of the plate elastic moduli and geometry, and can be found in [37]. Schapery and Davidson [37] reported that there was not enough information available in plate theory to fully decompose the energy release rate into mode I and mode II components, and the remaining information needed to be obtained from the continuum analysis of a specific loading case. The form of the proposed ERR partition is given by:

$$\frac{G_{II}}{G} = \frac{(N_c\sqrt{c_1}cos\Omega + M_c\sqrt{c_1}sin(\Omega+\Gamma))^2}{c_1 N_c^2 + c_2 M_c^2 + 2\sqrt{c_1 c_2}N_c M_c sin\Gamma} \tag{1.13}$$

where $\sin\Gamma = c_{12}/\sqrt{c_1 c_2}$, and Ω is the mode mix parameter. The mode mix parameter Ω is similar to the ω parameter presented in Suo and Hutchinson [26], as it must be determined from a separate continuum analysis of a specific case. Davidson et al. [38] obtain this parameter by solving the mode partition of a specific case using the virtual

crack closure technique in a finite element analysis. As this is a fully elastic analysis, a singular stress field forms at the crack tip; it is therefore called the crack tip element-singular field (CTE-SF) approach, and produces partitioning results very close to those predicted by Suo and Hutchinson [26]. Davidson et al. [27] applied the CTE-SF approach to partition asymmetric fractures in CFRP delaminations and found that it did not accurately predict the failure locus, which was measured using symmetric specimens. To address this issue, a new mixed mode parameter was derived based on the experimental results, and termed this the crack tip element-non singular field (CTE-NSF) approach. The value of Ω found to produce accurate results for CFRP delaminations is given by:

$$\Omega_{NSF} = \begin{cases} -24, & \text{if} \quad (\log_{10}\eta) < -0.468 \\ 60.409(\log_{10}\eta) - 41.738(\log_{10}\eta)^3, & \text{if} \quad -0.468 \leq (\log_{10}\eta) \leq 0.468 \\ 24 & \text{if} \quad (\log_{10}\eta) \geq 0.468 \end{cases} \tag{1.14}$$

where $\eta = h_2/h_1$. Only CTE-NSF is considered further in this work due to the direct similarities between CTE-SF and the HS solution.

1.2.3.4 Wang and Harvey [28]

Wang and Harvey [28] recently developed a set of partitioning theories based on both Euler and Timoshenko beam theory by imposing two sets of orthogonal pure modes in both theories. The method of deriving the pure modes follows the approach taken by Williams [20]; however, the assumptions made are different. Firstly, they assumed, as in Williams [20], that the applied moments could be decomposed into those that cause opening and those that cause shearing. i.e.:

$$\begin{aligned} M_1 &= M_I + M_{II} \\ kM_1 &= \theta M_I + \beta M_{II} \end{aligned} \tag{1.15}$$

The values of θ and β are then found by imposing conditions which are thought to constitute a pure mode. Firstly, the value of θ is found by imposing zero relative shearing displacements directly behind the crack tip, which constitutes a pure mode I. An expression is derived relating the relative shearing displacements to the applied moments and beam height ratios, this expression is equal for both Euler and Timoshenko beam theories; by setting this expression equal to zero, it is possible to directly find the value of θ from eq. 1.15 . Once the value of θ is known, the value of β can be found by imposing the orthogonal condition. i.e. the orthogonal condition requires that the modes

do not interact when substituted back into eq. 1.1 (no $M_I M_{II}$ term is produced). The values of β and θ found from imposing a zero relative shearing displacement are given by:

$$\theta = -\eta^2; \quad \beta = \frac{\eta^2(3+\eta)}{(1+3\eta)} \tag{1.16}$$

where $\eta = h_2/h_1 = 1/\gamma$. A second method of imposing a pure mode is to impose zero relative opening displacement directly behind the crack tip, which results in a pure mode II. Again, an expression in Euler and Timoshenko beam theory is derived for the relative opening displacement directly behind the crack tip; in this case, the expressions are different in Euler and Timoshenko beam theory. When the expression is set to zero, the value of β can be found directly from eq. 1.15. The resulting value of β in Timoshenko beam theory is equivalent to the value obtained from imposing a zero relative shearing displacement; therefore, only one set of pure modes exist in Timoshenko beam theory. The resulting mode I and mode II energy release rates in Timoshenko beam theory are obtained by substituting eq. 1.15 and eq. 1.18 back into eq. 1.1, which results in:

$$\begin{aligned} G_I &= \frac{24\eta}{B^2 h_1^3 E(1+\eta)} M_I^2 \\ G_{II} &= \frac{6(1+\beta^2/\eta^3 - (1+\beta)^2/(1+\eta)^3)}{B^2 h_1 E} M_{II}^2 \end{aligned} \tag{1.17}$$

When the expression for zero crack tip opening is set to zero in Euler beam theory, the resulting value of β is different from the one obtained from imposing a zero relative shearing displacement. The value of β obtained, and the corresponding orthogonal value of θ, are given by:

$$\theta^{'} = -1; \quad \beta^{'} = \eta^3 \tag{1.18}$$

This set of pure modes is equal to the pair derived by Williams [20], whom arrived at this point by simply assuming that equal curvatures produced mode II and equal and opposite moments produced mode I. However, by imposing two sets of conditions at the crack tip of an ideal Euler beam, Wang and Harvey [28] found that two sets of pure modes I and II occur. i.e. pure mode I is predicted to occur at two different loading ratios, and pure mode II is predicted to occur at two different loading ratios for a given geometry. It must be noted at this point that it is the opinion of the author that elementary beam theories cannot be used with any great confidence in the vicinity of a crack tip for the purpose of determining accurate displacements and forces, and it is believed that any attempts to do so will lead to results which are far removed from the physical reality. What is predicted to happen in between these pure modes is a clear indication of the un-physical nature of the results obtained; negative forces are predicted to act on positive displacements, thus generating rather than dissipating

energy. This is termed by the authors as 'stealthy interactions' and is accounted for in the expressions for mode I and mode II ERR by subtracting the energy created so that the overall energy remains the same; this results in negative ERRs between the observed pure modes, which is not physically consistent. The resulting mode I and mode II ERRs for the Wang-Harvey Euler beam theory are given by:

$$\begin{aligned} G_I &= \frac{24\eta}{B^2 h_1^3 E(1+\eta)} M_I^2 + \frac{72\eta(\eta-1)(1+3\eta)}{B^2 h_1^3 E(1+\eta)} M_I M_{II} \\ G_{II} &= \frac{6(1+\beta^2/\eta^3-(1+\beta)^2/(1+\eta)^3)}{B^2 h_1 E} M_{II}^2 - \frac{72\eta(\eta-1)(1+3\eta)}{B^2 h_1^3 E(1+\eta)} M_I M_{II} \end{aligned} \tag{1.19}$$

1.2.4 Assessment of the accuracy of analytical partitioning theories

Firstly, each of the partitioning theories presented in the previous section are plotted in fig. 1.5 for each of the asymmetric test methods outlined in table 1.1. It is evident that there is considerable disagreement between each of the partitioning theories based on the various assumptions which have been made in their formulations.

Numerous experimental studies have investigated the accuracy of each of these partitioning theories at different stages. Hashemi et al. [32] carried out asymmetric tests on carbon epoxy composite and applied both local (HS) and global (W) partitioning. It was found that the global approach produced a more physical failure locus and it was proposed that this was likely due the fracture process zone being larger than the relatively small K dominant region (often $\leq 1\%$ of smallest beam thickness [39]). For such cases it was argued that the global approach provided the most accurate partitioning. Ducept et al. [33] carried out a similar study on glass reinforced epoxy composite and found that the local (HS) partitioning accurately predicted the symmetrically measured failure locus, and the global (W) partitioning performed poorly. Davidson et al. [27] also carried out asymmetric tests on carbon epoxy composite and compared the resulting failure loci, obtained via local (HS) and global (W) partitioning, to the already measured *true* failure locus obtained using symmetric specimens. It was found that neither HS or W partitioning approach predicted the mode partition adequately. It was from this data that the D-NSF partitioning theory was obtained. The D-NSF partitioning has been also been shown to produce accurate partitions in other configurations of CFRP composites [34]. Wang and Harvey [28] repartitioned the CFRP experiments presented in Hashemi et al. [32] using both the Euler (WH-E) and Timoshenko (WH-T) partitioning theories, and compared the partitions to an assumed linear failure locus along with the original partitions of W and HS. They found that the WH-E partitioning theory produced the best fit to the assumed failure locus, and claimed that this theory offered

the 'best and most simple explanation for all of the experimental observations'. They also found that the Timoshenko beam theory partition (WH-T) performed by far the poorest of all the partitioning theories. The WH-T partitioning theory is therefore not considered further in this work and the Euler beam partition is referred to simply as WH partitioning theory. Overall, the experimental studies to date have failed to shine any further light on which partitioning theory, if any, should be used in the general case to partition asymmetric fractures. Each theory can be argued to work for a single case but there is no consistency across all composite materials. It is believed that the state of damage at the crack tip plays an important role in determining the correct mode mixity, something which is not considered by any of the mixed mode partitioning theories.

Parmigiani and Thouless [40] and Sills and Thouless [41] carried out a numerical assessment of the accuracy of the local (HS) partitioning theory; in this study, cohesive zone models were used to study the effect of damage zone size on mode mixity in beam like geometries. Parmigiani and Thouless [40] showed that local partitioning is reproduced if the cohesive length scale is sufficiently small, and more surprisingly, that local partitioning is accurate at and beyond cohesive length scales where there is no K dominant stress field present. Based on these findings, it was proposed that local partitioning would be accurate for most practical situations.

1.3 Aims of Thesis

It is evident that considerable uncertainty still surrounds the area of mixed mode partitioning when it comes to partitioning the ERR for asymmetric fracture tests in composites and adhesive joints. There is a critical need to establish accurate mixed mode partitions in asymmetric geometries. One might argue that these are not needed due to the fact that symmetric specimens can be used to obtain the full mixed mode failure locus. However, accurate partitioning of asymmetric specimens may lead to the standardisation of more straightforward mixed mode test methods, such as the AFRMM test. This will lead to mixed mode testing becoming more accessible, particularly in industry, where it is currently overlooked despite it's critical importance. Apart from this, not all structures in real life will be symmetric so it is also of critical importance to analyse these asymmetric structures and determine how they will behave in-service. The goals of the current thesis are to:

- Establish a consistent method of numerically determining mixed mode partitions in beam like geometries.

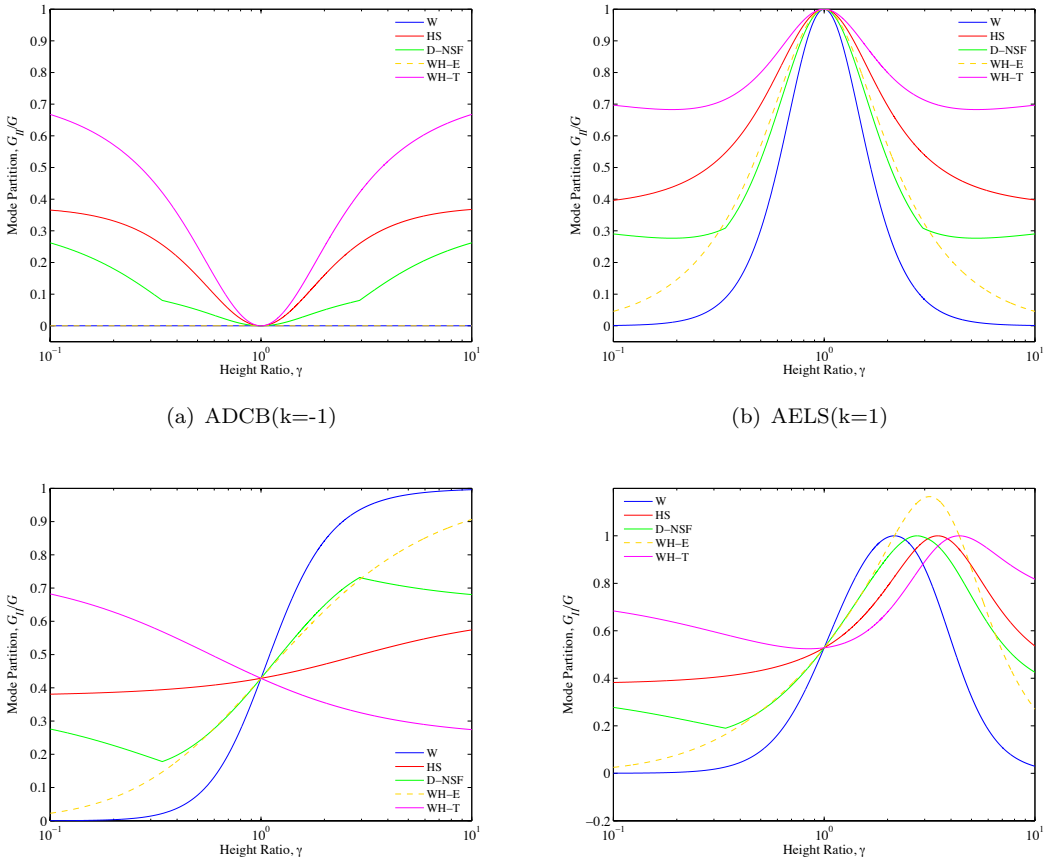

(a) ADCB(k=-1)

(b) AELS(k=1)

(c) AFRMM(k=1)

(d) AMMB(k=0.1)

FIGURE 1.5: Predicted mode partitions for asymmetric fracture tests as a function of beam height ratio. Predicted partitions are from Williams [20](W), Suo and Hutchinson [26](HS), Davidson et al. [27] (D-NSF) and Wang and Harvey [28] (WH-E(Euler)), (WH-T(Timoshenko)).

- Use this numerical technique to investigate the effect of fracture process zone size on the mixed mode partition.
- Critically assess the accuracy of each of the current analytical partitioning theories based on the numerical results.
- Establish a consistent method of partitioning fractures in asymmetric specimens, that can be used to describe all of the supposed conflicting experimental evidence in the literature.
- Critically assess the performance of the newly proposed partitioning scheme by carrying out a series of mixed mode delamination experiments.

1.4 Thesis Outline

The following is a brief outline of the contents of each chapter in this thesis

- Chapter 2 presents a literature review of current numerical methods for obtaining mixed mode partitions. Linear elastic partitioning results are presented using the virtual crack closure technique, interaction domain integral, and the mode decomposed J integral approach.
- Chapter 3 introduces damage into the simulations with the use of cohesive zone models. The global mode partition is studied as a function of cohesive properties and the results are compared to the predictions of current analytical partitioning theories.
- Chapter 4 outlines the development of a new semi analytical cohesive analysis based on the numerical findings in the previous chapter. This new approach is applied to partition experimental data presented in the literature and it's performance is critically assessed.
- Chapter 5 outlines an experimental investigation of current analytical partitioning theories and the newly developed SACA partitioning using the DCB-UBM test rig. The true mixed mode delamination failure locus of UD/CFRP is measured using symmetric specimens, and is then used as a benchmark to assess the performance of each of the partitioning methods.
- Chapter 6 summarises the findings made in this thesis and recommendations for future work in the area are outlined.

Chapter 2

Numerical Partitioning: Linear Elastic Cases

2.1 Introduction

In this chapter, the numerical mixed mode partitioning of elastic beam-like geometries is considered. All simulations are carried out using Abaqus [42], a broadly used commercial finite element analysis software. The asymmetric fixed ratio mixed mode (AFRMM) test method is used in this study as it highlights the significant differences that exist between the various partitioning theories. As such, it serves as a good test to evaluate the performance of each of the analytical partitioning theories. The analytical predictions, which are discussed in chapter 1, are presented in fig. 2.1 for the AFRMM ($k = 0$) test for height ratios ranging from 0.1 to 10. For each geometry and loading arrangement, the numerical results are compared to each of the analytical predictions. In this purely elastic case, no crack tip yielding or damage is considered.

The numerical mode partition is calculated using three different numerical techniques.

- The first technique, which was initially developed for use with the finite element method, is the virtual crack closure technique (VCCT) [43]. In this method, the nodal forces at the crack tip are multiplied by the displacements directly behind the crack tip.
- The second method, known as the interaction domain integral (IDI) [44], is a more complex approach that involves the interaction of known singular fields with the numerical stress and strain fields in order to decompose the loading into individual mode I and mode II stress intensity factors.

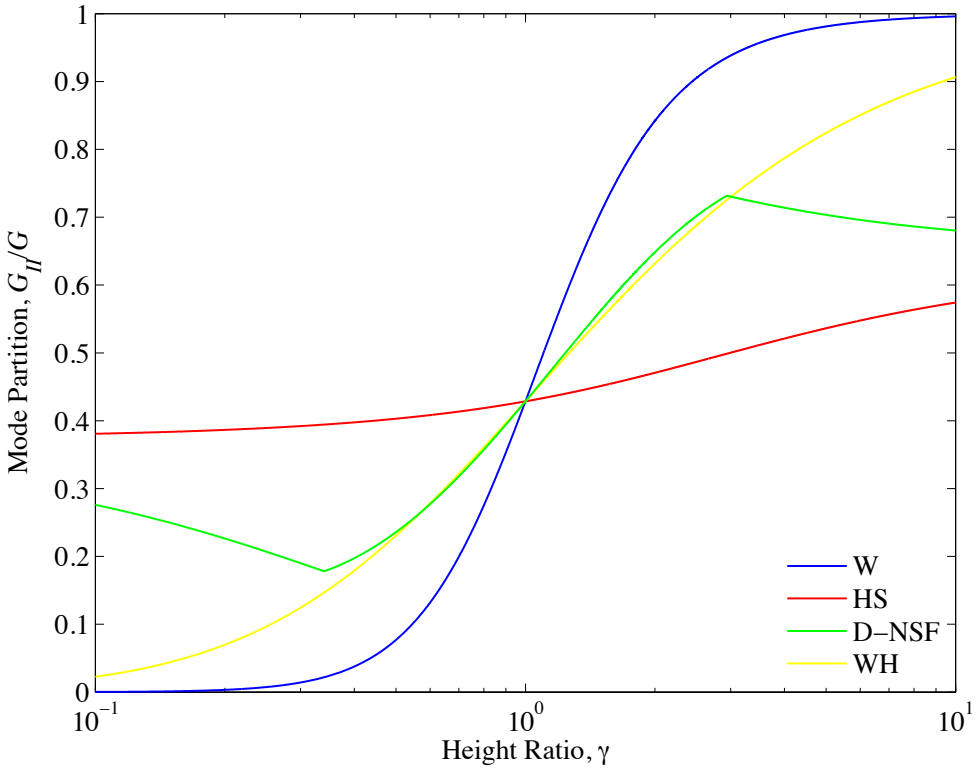

FIGURE 2.1: Analytical partitioning theories

- The third method is the mode decomposed J integral approach proposed by Ishikawa et al. [45]. In this method, the J integral is calculated over a symmetric path surrounding the crack tip where the stresses, strains and displacements are decomposed into symmetric and anti-symmetric components in order to obtain the mode I and mode II ERR contributions respectively.

The theory and application of each partitioning technique is discussed in further detail in section 2.2.

The convergence of the mode partition using each numerical method is studied as the mesh size is reduced. In the initial test cases, only isotropic material properties are considered. It has been shown [46, 47] that the local partitioning solution depends very weakly on material orthotropy, and it is suggested by Suo et al. [47] that the isotropic solution offers sufficient accuracy for partitioning orthotropic composite laminates. Also, the 2D analytical partitioning theories of Williams [20], Wang and Harvey [28] and Davidson et al. [27] do not account for the out of plane material properties and hence do not predict any change in mode partitioning for varying material orthotropy. The

effect of material orthoptropy on mode mixity is numerically assessed in section 2.6 by repeating each AFRMM test case with orthotropic material properties.

In the absence of any crack tip damage in these purely elastic cases, a singularity dominated region (K dominant region) is allowed to develop close to the crack tip. In the final part of this chapter, the extent of the region of K dominancy is studied in each case. This has previously been reported to be in the order of 1% of the beam thickness for a double cantilever beam specimen loaded in bending [16, 48]. The size of the region is reported to scale with the beam thickness for these symmetric specimens, and not with the crack length as is the case for a crack in an infinite plate [49]. Here, it is of interest to study how the size of the K dominant region scales with the relevant beam thicknesses for asymmetric specimens. This study is of particular importance because it indicates the level of damage which would be tolerated for the local partitioning to remain theoretically valid.

2.2 Numerical Partitioning

2.2.1 Overview

This section deals with numerical techniques for evaluating mixed mode partitions in beam like geometries. In all cases, it is required to evaluate the individual mode I and mode II energy release rates G_I, G_{II} or stress intensity factors K_I, K_{II} in order to obtain the mode mixity G_{II}/G. In this chapter, three different techniques are compared. These are:

- Virtual Crack Closure Technique (VCCT).
- Interaction Domain Integral (IDI).
- Mode Decomposed J Integral (MDJ).

2.2.2 Virtual Crack Closure Technique

One of the most widely used methods for numerically calculating energy release rates is the virtual crack closure technique (VCCT), which is the numerical implementation of the crack closure integral suggested by Irwin [50]. Irwin proposed that the energy released when a crack propagated by a distance Δa was equal to the energy required to close the crack over the same distance. As Δa approaches zero, the energy required

to close the crack faces divided by the area closed can be equated to the energy release rate G. The mathematical representation of the crack closure integral is given by [50]:

$$\begin{aligned} G = &\lim_{\Delta a \to 0} \frac{1}{2\Delta a} \int_0^{\Delta a} \sigma_{yy}(\Delta a - x)\Delta v(-x)dx \\ &+ \lim_{\Delta a \to 0} \frac{1}{2\Delta a} \int_0^{\Delta a} \sigma_{xy}(\Delta a - x)\Delta u(-x)dx \end{aligned} \tag{2.1}$$

as applied to an arbitrary crack tip as seen in fig. 2.2. σ_{yy} and σ_{xy} are the normal and

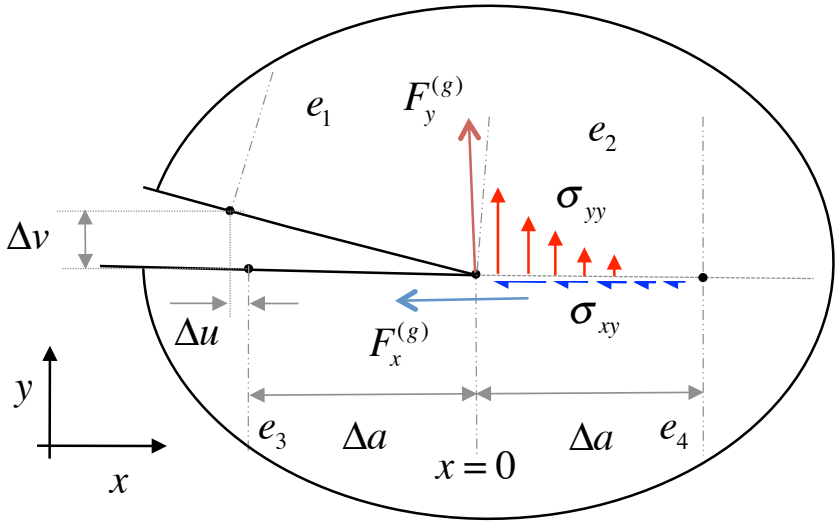

FIGURE 2.2: Arbitrary crack tip under mixed mode loading. The crack tip is located at $x = 0$ and is propagating in the $+x$ direction. The crack tip is meshed with regular quadrilateral linear elements

shear stresses respectively acting ahead of the crack tip, and Δv and Δu are the relative opening and shearing displacements behind the crack tip respectively. Eq. 2.1 can be decomposed into mode I and mode II components by separating the first and second integrals [43].

$$\begin{aligned} G_I &= \lim_{\Delta a \to 0} \frac{1}{2\Delta a} \int_0^{\Delta a} \sigma_{yy}(\Delta a - x)\Delta v(-x)dx \\ G_{II} &= \lim_{\Delta a \to 0} \frac{1}{2\Delta a} \int_0^{\Delta a} \sigma_{xy}(\Delta a - x)\Delta u(-x)dx \end{aligned} \tag{2.2}$$

Rybicki and Kanninen [43] were the first to calculate the crack closure integral numerically, making use of linear finite elements. By inserting stiff springs at the connecting nodes at the crack tip in the opening and shearing directions, Rybicki and Kanninen [43]

could equate the integrals of stresses over Δa to the forces in the springs at the crack tip, where Δa is equal to the distance between nodes in the regular quadrilateral mesh as seen in fig. 2.2. By replacing the integral of stresses in eq. 2.2 with the resultant global forces at the crack tip in the opening and shearing directions ($F_y^{(g)}$, $F_x^{(g)}$), eq. 2.2 reduces to:

$$\begin{aligned} G_I &= \frac{1}{2B\Delta a}(F_y^{(g)}\Delta v) \\ G_{II} &= \frac{1}{2B\Delta a}(F_x^{(g)}\Delta u) \end{aligned} \tag{2.3}$$

where Δu and Δv are evaluated at a distance Δa behind the crack tip. While Rybicki and Kanninen [43] inserted stiff springs in order to obtain the overall forces acting on the plane ahead of the crack tip, this is not specifically required in a finite element analysis in order to obtain the correct global forces. In any finite element analysis, there is a calculation of the element forces at each node $F^{(e_i)}$; this is the force acting on this node due to the deformation of the particular element(e_i). Therefore, the crack tip node seen in fig. 2.2 will have four element forces acting on it, and each element force can be decomposed into an opening $F_y^{(e_i)}$ and shearing force $F_x^{(e_i)}$. In order to obtain the correct global force acting across the crack plane at the crack tip node in fig. 2.2, one must sum the element forces on one side of the crack plane. i.e.

$$\begin{aligned} F_x^{(g)} &= F_x^{(e_1)} + F_x^{(e_2)} = -(F_x^{(e_3)} + F_x^{(e_4)}) \\ F_y^{(g)} &= F_y^{(e_1)} + F_y^{(e_2)} = -(F_y^{(e_3)} + F_y^{(e_4)}) \end{aligned} \tag{2.4}$$

As the forces and displacements are readily available in any finite element calculation, this form of the crack closure integral presented in eq. 2.3 provides a very simple and efficient technique for numerically estimating energy release rates and mode partitions. It is important to note that equation 2.3 is only valid for linear elements that are regular in size in the vicinity of the crack tip. The use of the VCCT was extended to higher order elements and singular elements by Ramamurthy et al. [51], Raju [52]. Nairn [53] extended the analysis to arbitrarily placed side nodes and corrected for crack face pressures, which were shown to be incorrectly accounted for in [52].

The simulations carried out in this study use 8 node quadratic CPE8 elements, with a regular quadrilateral mesh. The VCCT equations that apply to a regular quadratic finite element mesh with mid side nodes are given by [52–54] and are outlined below:

$$\begin{aligned} G_I &= \frac{1}{2B\Delta a}(\Delta v_1 F_{y,1'}^{(g)} + \Delta v_2 F_{y,2'}^{(g)}) \\ G_{II} &= \frac{1}{2B\Delta a}(\Delta u_1 F_{x,1'}^{(g)} + \Delta u_2 F_{x,2'}^{(g)}) \end{aligned} \tag{2.5}$$

where $F^{(g)}$ and $\Delta u, \Delta v$ are the global nodal forces and relative crack opening displacements respectively as defined in eq. 2.3. The locations at which each of the values are calculated are detailed in fig. 2.3. The values subscripted as $1', 1$ are evaluated at the crack tip node and the equivalent adjacent nodes behind the crack tip respectively, and the values subscripted as $2', 2$ are evaluated at the mid-side nodes directly ahead of and behind the crack tip respectively.

This approach was implemented as an automated post processing technique using Python scripting and Matlab. A Python script was developed to extract the relevant element forces and nodal displacements from the simulations to a series of text files. A Matlab script was then developed to read in this data and calculate G_I and G_{II} from eq. 2.5, and hence the mode partition G_{II}/G. The results for each of test case are presented in section 2.4.

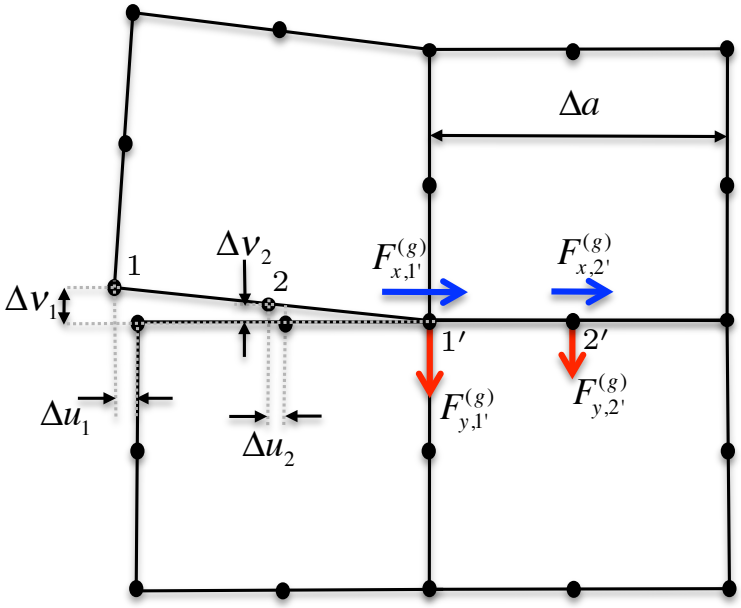

FIGURE 2.3: Application of the VCCT to a 2D 8 node quadratic element.

2.2.3 Interaction Domain Integral

Another common method for partitioning energy release rates at the crack tip is the interaction domain integral (IDI). This approach is based on the J integral and requires the superposition of stress, strain and displacement fields from known stress intensity factor solutions in order to decompose the numerical field into the individual mode I

and mode II stress intensity factors. This method was first proposed by Yau et al. [44]. The J integral proposed by Rice [55] for a crack propagating in the x direction is given as:

$$J = \int_{\Gamma} \left(W dy - \sigma_{ij} n_j \frac{\partial u_i}{\partial x} ds \right) \tag{2.6}$$

where Γ is an arbitrary path surrounding the crack tip which starts on the lower cracked face and ends on the upper crack face, σ_{ij} are the components of the stress tensor, u_i the displacement vector, n_j the outwards normal to Γ, s the distance along the path Γ and W the strain energy density defined as:

$$W = \int_0^{\epsilon} \sigma_{ij} d\epsilon_{ij} \tag{2.7}$$

where ϵ_{ij} are the components of the strain tensor. It was shown by Rice [55] that this integral was equivalent to the energy release rate analysis of Griffith and Irwin for a crack in an isotropic linear elastic medium under infinitesimal strains. Therefore under 2D in plane loading, J can be expressed as:

$$J = G = \frac{1}{E'}(K_I^2 + K_{II}^2) \tag{2.8}$$

where $E' = E$ for plane stress and $E = E/(1-\nu^2)$ for plane strain. E is the Young's modulus and ν is the Poisson's ratio. The evaluation of eq. 2.6 around a contour Γ surrounding the crack tip will yield the overall energy release rate G, but this approach does not yield sufficient information to obtain the individual energy release rates G_I and G_{II}. To achieve this, Yau et al. [44] proposed interacting known singular field solutions as a method of decomposing the ERRs in the following technique. Take the known singular field solutions presented by Irwin:

$$\left.\begin{aligned}
\sigma_{xx} &= \frac{K_I}{\sqrt{2\pi r}} \cos\left(\frac{\theta}{2}\right)\left[1 - \sin\left(\frac{\theta}{2}\right)\sin\left(\frac{3\theta}{2}\right)\right] \\
\sigma_{yy} &= \frac{K_I}{\sqrt{2\pi r}} \cos\left(\frac{\theta}{2}\right)\left[1 + \sin\left(\frac{\theta}{2}\right)\sin\left(\frac{3\theta}{2}\right)\right] \\
\sigma_{xy} &= \frac{K_I}{\sqrt{2\pi r}} \cos\left(\frac{\theta}{2}\right)\sin\left(\frac{\theta}{2}\right)\cos\left(\frac{3\theta}{2}\right) \\
u_x &= \frac{K_I}{2\mu}\sqrt{\frac{r}{2\pi}} \cos\left(\frac{\theta}{2}\right)\left[\kappa - 1 + 2\sin^2\left(\frac{\theta}{2}\right)\right] \\
u_y &= \frac{K_I}{2\mu}\sqrt{\frac{r}{2\pi}} \sin\left(\frac{\theta}{2}\right)\left[\kappa + 1 - 2\cos^2\left(\frac{\theta}{2}\right)\right]
\end{aligned}\right\} \text{mode I} \tag{2.9}$$

$$\left.\begin{aligned}
\sigma_{xx} &= \frac{-K_{II}}{\sqrt{2\pi r}}\sin\left(\frac{\theta}{2}\right)\left[2+\cos\left(\frac{\theta}{2}\right)\cos\left(\frac{3\theta}{2}\right)\right] \\
\sigma_{yy} &= \frac{K_{II}}{\sqrt{2\pi r}}\sin\left(\frac{\theta}{2}\right)\cos\left(\frac{\theta}{2}\right)\cos\left(\frac{3\theta}{2}\right) \\
\sigma_{xy} &= \frac{K_{II}}{\sqrt{2\pi r}}\cos\left(\frac{\theta}{2}\right)\left[1-\sin\left(\frac{\theta}{2}\right)\sin\left(\frac{3\theta}{2}\right)\right] \\
u_x &= \frac{K_{II}}{2\mu}\sqrt{\frac{r}{2\pi}}\sin\left(\frac{\theta}{2}\right)\left[\kappa+1+2\cos^2\left(\frac{\theta}{2}\right)\right] \\
u_y &= \frac{-K_{II}}{2\mu}\sqrt{\frac{r}{2\pi}}\cos\left(\frac{\theta}{2}\right)\left[\kappa-1-2\sin^2\left(\frac{\theta}{2}\right)\right]
\end{aligned}\right\} \text{mode II} \tag{2.10}$$

where μ is the shear modulus, r, θ are the polar co-ordinates, with the origin at the crack tip for a crack extending in the direction of $\theta = 0$, $\kappa = (3-\nu)/(1+\nu)$ for plane stress, and $\kappa = 3-4\nu$ for plane strain. By imposing this known singular field solution, also termed auxiliary field, (denoted by subscript 2) on top of the deformed field for which we require the mode decomposition (denoted by subscript 1), it is possible to obtain a new combined field (denoted by subscript 0). i.e.:

$$\begin{aligned}
\sigma_{ij}^{(0)} &= \sigma_{ij}^{(1)} + \sigma_{ij}^{(2)} \\
\epsilon_{ij}^{(0)} &= \epsilon_{ij}^{(1)} + \epsilon_{ij}^{(2)} \\
u_i^{(0)} &= u_i^{(1)} + u_i^{(2)}
\end{aligned} \tag{2.11}$$

The J integral of the combined field (subscript 0) is given by:

$$J^{(0)} = \int_\Gamma \Big(\int_0^\epsilon (\sigma_{ij}^{(1)} + \sigma_{ij}^{(2)}) d(\epsilon_{ij}^{(1)} + \epsilon_{ij}^{(2)}) dy - (\sigma_{ij}^{(1)} + \sigma_{ij}^{(2)}) n_j \frac{\partial (u_i^{(1)} + u_i^{(2)})}{\partial x} ds \Big) \tag{2.12}$$

which, upon expansion, reduces to:

$$J^{(0)} = J^{(1)} + J^{(2)} + M^{(1,2)} \tag{2.13}$$

where $M^{(I,II)}$ is termed the interaction integral and can be evaluated from:

$$M^{(1,2)} = \int_\Gamma \Big(W^{(1,2)} dy - \Big[\sigma_{ij}^{(1)} n_j \frac{\partial u_i^{(2)}}{\partial x} + \sigma_{ij}^{(2)} n_j \frac{\partial u_i^{(2)}}{\partial x} \Big] ds \Big) \tag{2.14}$$

$W^{(1,2)}$ is the mutual energy density and can be obtained from:

$$W^{(1,2)} = \int_0^\epsilon \sigma_{ij}^{(1)} d\epsilon_{ij}^{(2)} = \int_0^\epsilon \sigma_{ij}^{(2)} d\epsilon_{ij}^{(1)} \tag{2.15}$$

Due to superposition properties of linear elasticity, it is also possible to combine the mode I and mode II SIFs from the auxiliary fields $(K_I^{(2)}, K_{II}^{(2)})$ to the current unknown field SIFs $(K_I^{(1)}, K_{II}^{(1)})$ to produce the combined field SIFs given by $((K_I^{(1)}+K_I^{(2)}), (K_{II}^{(1)}+K_{II}^{(2)}))$. Substituting the combined field SIFs into eq. 2.8 and expanding results in the

following expression for $J^{(0)}$ for the combined field:

$$J^{(0)} = \frac{1}{E'}({K_I^{(1)}}^2 + {K_{II}^{(1)}}^2) + \frac{1}{E'}({K_I^{(2)}}^2 + {K_{II}^{(2)}}^2) + \frac{2}{E'}(K_I^{(1)}K_I^{(2)} + K_{II}^{(1)}K_{II}^{(2)}) \quad (2.16)$$

which is equivalent to:

$$J^{(0)} = J^{(1)} + J^{(2)} + \frac{2}{E'}(K_I^{(1)}K_I^{(2)} + K_{II}^{(1)}K_{II}^{(2)}) \quad (2.17)$$

Now by direct comparison between eq. 2.13 and eq. 2.17, it is evident that:

$$M^{(1,2)} = \frac{2}{E'}(K_I^{(1)}K_I^{(2)} + K_{II}^{(1)}K_{II}^{(2)}) \quad (2.18)$$

As it is possible to evaluate $M^{(1,2)}$ directly from the known quantities of the numerical and auxiliary fields along the chosen contour, it turns out that if the auxiliary fields are chosen in the following way, it is possible to deduce the required SIFs $K_I^{(1)}$ and $K_{II}^{(1)}$.

Firstly, if the auxiliary field is chosen to be pure mode I (i.e. $K_{II}^{(2)} = 0$) with an intensity of 1 (i.e. $K_I^{(2)} = 1$), eq. 2.18 reduces to:

$$M^{(1,2)} = \frac{2}{E'}(K_I^{(1)}) \quad (2.19)$$

and conversely, if the auxiliary field is chosen to be pure mode II (i.e. $K_I^{(2)} = 0$) with an intensity of 1 (i.e. $K_{II}^{(2)} = 1$), eq. 2.18 then reduces to:

$$M^{(1,2)} = \frac{2}{E'}(K_{II}^{(1)}) \quad (2.20)$$

Using this approach it is possible to determine the mixed mode SIFs for the general loading of a crack in a 2D homogenous isotropic solid. The implementation of this approach into the finite element method is outlined by Yau et al. [44]. Shih and Asaro [56] extended this method for use with general anisotropic materials by utilising the anisotropic singular field solutions outlined by Barnett and Asaro [57]. As mentioned previously, this method is already coded into Abaqus as a post processing technique. In Abaqus, the interaction integral of eq. 2.14 is transformed into an area integral using Gauss' divergence theorem. The resulting integral takes the form:

$$M^{(1,2)} = \sum_A \sum_{p=1}^{N} \Big\{ \big[-W^{(1,2)}\delta_{1i} + \sigma_{ij}^{(1)}\frac{\partial u_i^{(2)}}{\partial x_1} + \sigma_{ij}^{(2)}\frac{\partial u_i^{(1)}}{\partial x_1} \big] \frac{\partial q_1}{\partial x_i} \det[\boldsymbol{J}] \Big\}_p w_p \quad (2.21)$$

where N is the number of Gaussian points in each element, A is the domain over which the integral is carried out, and q_1 is an arbitrary continuous function which goes from a value of one at the crack tip to a value of zero at the domain boundaries. x_1, x_2 are

the global coordinates and ξ, η are the local parametric coordinates, which are detailed in fig. 2.4 for a quadratic element. w_p are the Gaussian weights associated with each integration point and $[\mathbf{J}]$ is the jacobian of the element, which is given by:

$$[\boldsymbol{J}] = \begin{bmatrix} \frac{\partial x_1}{\partial \xi} & \frac{\partial x_2}{\partial \xi} \\ \frac{\partial x_1}{\partial \eta} & \frac{\partial \eta}{\partial xi} \end{bmatrix} \tag{2.22}$$

It is shown by Shih et al. [58] that the domain integral solution is independent of the choice of function for q_1, provided it is a continuous function which is equal to zero at the domain boundary and equal to one at the crack tip. While the line integral and the domain integral are theoretically equivalent, the transformation of the line integral into a domain integral has a number of distinct advantages for numerical calculation. Firstly, the values of stress and strain are available directly at integration points and do not need to be extrapolated to nodes, therefore increasing accuracy over a line integral. Secondly, the accuracy of the domain integral does not rely solely on the accuracy of the field solution along a single remote contour, and therefore accurate solutions can be obtained with a coarser mesh.

In order to obtain results from an Abaqus simulation, it is required to specify the crack tip and the domain for which the integral is calculated. This procedure is applied to all cases in line with the VCCT technique. Results from these cases are presented in section 2.4

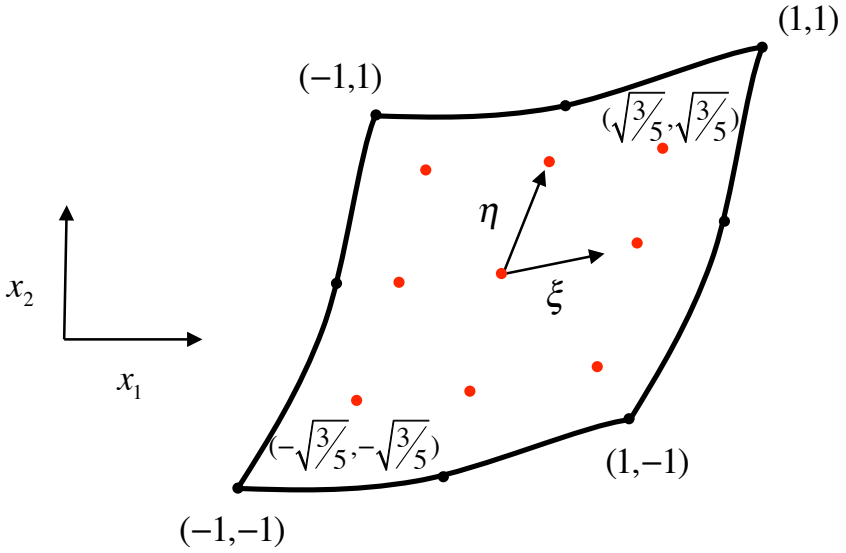

FIGURE 2.4: Quadratic finite element with global (x_1, x_2) and parametric (ξ, η) coordinates. Integration (Gaussian) point locations are shown with red dots, along with the associated Gaussian weights.

2.2.4 Mode Decomposed J integral Approach

It was shown in the previous section that the J integral calculation of eq. 2.6 does not provide enough information to decompose the ERR into the individual mode I and mode II ERRs, and hence can not be used in this form to obtain mixed mode partitions. We have seen that Yau et al. [44] proposed an elaborate method for decomposing the ERRs based on interacting singular fields in the IDI technique. About the same time, Ishikawa et al. [45] proposed a different technique for decomposing the J integral into mode I and mode II components. This is achieved by directly decomposing the stress, strain and displacement fields into symmetric (causing mode I) and antisymmetric (causing mode II) components along a symmetric integration path about the crack plane. i.e. paths containing P and P' in fig. 2.5. The decomposed stress, strain and displacement fields are then given as:

$$\begin{aligned}
\sigma_{ij} &= \sigma^I_{ij} + \sigma^{II}_{ij} = \frac{1}{2}\begin{bmatrix} \sigma_{11}+\sigma'_{11} & \sigma_{12}-\sigma'_{12} \\ \sigma_{12}-\sigma'_{12} & \sigma_{22}+\sigma'_{22} \end{bmatrix} + \frac{1}{2}\begin{bmatrix} \sigma_{11}-\sigma'_{11} & \sigma_{12}+\sigma'_{12} \\ \sigma_{12}+\sigma'_{12} & \sigma_{22}-\sigma'_{22} \end{bmatrix} \\
\epsilon_{ij} &= \epsilon^I_{ij} + \epsilon^{II}_{ij} = \frac{1}{2}\begin{bmatrix} \epsilon_{11}+\epsilon'_{11} & \epsilon_{12}-\epsilon'_{12} \\ \epsilon_{12}-\epsilon'_{12} & \epsilon_{22}+\epsilon'_{22} \end{bmatrix} + \frac{1}{2}\begin{bmatrix} \epsilon_{11}-\epsilon'_{11} & \epsilon_{12}+\epsilon'_{12} \\ \epsilon_{12}+\epsilon'_{12} & \epsilon_{22}-\epsilon'_{22} \end{bmatrix} \\
u_i &= u^I_i + u^{II}_i = \frac{1}{2}\begin{bmatrix} u_1+u'_1 \\ u_2-u'_2 \end{bmatrix} + \frac{1}{2}\begin{bmatrix} u_1-u'_1 \\ u_2+u'_2 \end{bmatrix}
\end{aligned} \tag{2.23}$$

It is important to note that the decomposed stresses (i.e. $\sigma^I_{ij}, \sigma^{II}_{ij}$) satisfy the conservation laws of linear and angular momentum in the absence of body forces, i.e.:

$$\begin{aligned}
\frac{\partial \sigma^M_{ij}}{\partial x_i} &= 0 \\
\sigma^M_{ij} &= \sigma^M_{ji}
\end{aligned} \tag{2.24}$$

where $(M = 1, 2)$. The decomposed stress, strain and displacement values, i.e. $(\sigma^I_{ij} + \sigma^{II}_{ij}), (\epsilon^I_{ij} + \epsilon^{II}_{ij}), (u^I_i + u^{II}_i)$, are then substituted directly into eq. 2.6 to obtain:

$$J = \int_\Gamma \Big(\int_0^\epsilon (\sigma^{(I)}_{ij} + \sigma^{(II)}_{ij}) d(\epsilon^{(I)}_{ij} + \epsilon^{(II)}_{ij}) dy - (\sigma^{(I)}_{ij} + \sigma^{(II)}_{ij}) n_j \frac{\partial (u^{(I)}_i + u^{(II)}_i)}{\partial x} ds \Big) \tag{2.25}$$

and upon expanding:

$$J = J_I + J_{II} + \text{terms involving } I.II \tag{2.26}$$

where:

$$J_I = \int_\Gamma \Big(\int_0^\epsilon \sigma_{ij}^{(I)} d\epsilon_{ij}^{(I)} dy - \sigma_{ij}^{(I)} n_j \frac{\partial u_i^{(I)}}{\partial x} ds \Big)$$
$$J_{II} = \int_\Gamma \Big(\int_0^\epsilon \sigma_{ij}^{(II)} d\epsilon_{ij}^{(II)} dy - \sigma_{ij}^{(II)} n_j \frac{\partial u_i^{(II)}}{\partial x} ds \Big) \tag{2.27}$$

It turns out that there is no interaction between the orthogonal fields I, II and hence the terms involving the product of $I.II$ can be shown to reduce to zero [45]. Therefore J_I and J_{II} in eq. 2.27 equate to the mode I and mode II ERRs G_I and G_{II} when the integrals are applied along a remote contour surrounding a crack in an elastic body under infinitesmal strains as seen in fig. 2.5. Ishikawa et al. [45] also showed the decomposed integrals (eq. 2.27) to be path independent, provided the path started on the lower crack face and ended on the upper crack face. This method provides a direct

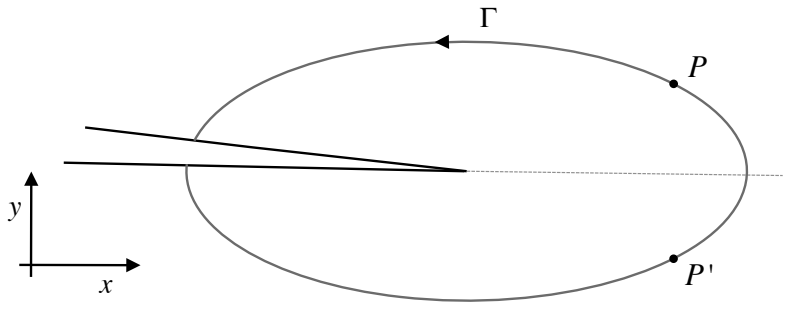

FIGURE 2.5: Symmetric path surrounding the crack tip containing points P and P'.

approach for estimating mixed mode partitions by decomposition of the stress strain and displacement fields. The main advantage of this approach over the previous VCCT and IDI is not evident in the current analysis where only elastic material properties are considered. However, the mode decomposed J integral can be easily applied to cases where non linear deformations are occurring at the crack tip, as is the case in cohesive zone modelling. Indeed one of the reasons for applying it in conjuction with both the VCCT and IDI techniques to the purely elastic cases is to verify the procedure is working. To calculate the integrals of eq. 2.27 in practice, the symmetric paths are selected as node sets in Abaqus and the values are again extracted using a python script and the integrals are then calculated with a Matlab script. The integral is approximated numerically using the trapezoidal rule.

2.3 Case Setup

The AFRMM test geometry and loading is outlined in fig. 2.6. The beams are modelled as 2D plane strain, linear elastic and isotropic with a Young's modulus of 75 GPa and a Poisson's ratio of 0.38. These values are chosen as they are typical of FRP composite elastic properties in the aligned-fibre(x) direction. In any case, the partitioning is independent of the substrate elastic properties (isotropic) so the numerical solution remains general. For these elastic test cases, small strain theory is used.

The beam is fully built in at the un-cracked end, while a pure moment is applied to the top beam of the cracked end. Using the Euler beam analysis outlined in [20], the ERR, G, for an increment of crack growth in the AFRMM test case is given by:

$$G = \frac{6M_1^2}{B^2E}\Big(\frac{1}{h_1^3} - \frac{1}{(h_1+h_2)^3}\Big) \tag{2.28}$$

where M_1 is the moment applied to the top beam, B is the substrate thickness, E is the Young's modulus and h_1 and h_2 are the upper and lower beam heights respectively. For all 2D simulations, a nominal thickness, B, of 1 m is assigned in the out of plane direction. All simulations use a structured orthogonal mesh with quadratic elements in plane strain, unless stated otherwise. Quadratic elements are chosen for this study as they offer a number of advantages over linear elements in bending, despite the increased computational cost. A significant advantage of quadratic elements is that they circumvent the problem of shear locking, which is commonly encountered in linear elements where they are subjected to bending. Shear locking is the inability of the element to deform to the required shape, which can result in an overestimate of the stiffness of a beam in bending. While this issue can be addressed by using reduced integration within the element, this must be accompanied by hourglass control to ensure the stiffness of the element is not underestimated. The placement of the mid-side nodes in quadratic elements means they can accurately deform to the required shape in bending and hence they are not prone to the problem of shear locking. Secondly, a study by Nairn [53] on the VCCT technique using various element formulations found that the quadratic element with mid-side nodes produced the fastest rate of convergence. Each of the cases are meshed and run in Abaqus and the VCCT, IDI, and mode decomposed J integral techniques are then applied as a post processing tool to calculate the mixed mode partition.

The mode mixity, $\frac{G_{II}}{G}$, is calculated over a range of γ ratios ranging from 0.1 to 10. To achieve varying γ ratios, h_1 is kept constant at $3mm$ while h_2 is varied between $30, 15, 6, 3, 1.5, 0.6$ & 0.3 mm.

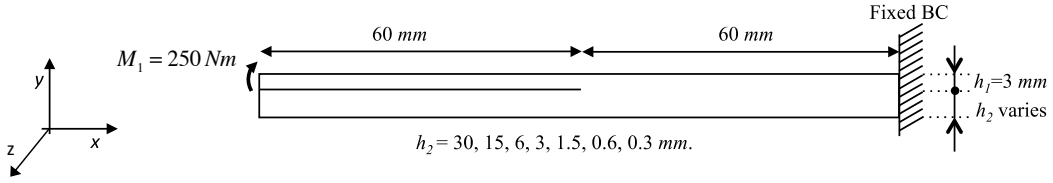

FIGURE 2.6: AFRMM test case geometry and loading.

2.4 Results

2.4.1 Converged Results

The converged VCCT, IDI, and mode decomposed J integral (MDJ) partitions of the AFRMM linear elastic test cases are plotted in fig. 2.7 along with the aforementioned analytical solutions. The numerical values, along with the associated total energy release rates, G, are outlined in table 2.1. The converged values are obtained by extrapolating to zero element size in each case. The details of the convergence patterns for each method are discussed in section 2.4.2. In table 2.1, the applied energy release rate for each case, G, is calculated using eq. 2.28, and compared to the numerical energy release rate obtained using each partitioning method. Each of the partitioning methods yield a value for the mode I and mode II energy release rates, G_I, G_{II}, which are then summed to obtain the numerical energy release rate G (i.e. $G = G_I + G_{II}$). The ability of each partitioning method to accurately predict the correct total ERR is paramount and serves as an important check that the numerical procedures are implemented correctly. The ERR values presented in table 2.1 are converted to $\%G$ error values in table 2.2 using:

$$\%G_N \text{ error} = \frac{G_{ANA} - G_N}{G_{ANA}} * 100, \quad (N = VCCT,\ IDI,\ MDJ) \tag{2.29}$$

where G_{ANA} is the analytical energy release rate calculated using eq. 2.28, and $G_N, (N = VCCT,\ IDI,\ MDJ)$ are the total energy release rates calculated using the VCCT (eq. 2.5), IDI (eqs. 2.19-2.21), and MDJ (eq. 2.27) numerical techniques respectively.

2.4.1.1 Discussion

First and foremost, it is evident from table 2.2 that all of the numerical methods are accurate in predicting the total energy release rate G to within $\approx .05\%$ of the exact analytical value when the results are extrapolated to zero element size. The VCCT and IDI are the most accurate, with maximum errors of $\approx .01\%$. The MDJ technique is the

	G (J/m^2)				G_{II}/G		
γ	ANA (eq. 2.28)	VCCT	IDI	MDJ	VCCT	IDI	MDJ
0.1	158.32540	158.32539	158.33253	158.38399	0.37845	0.37825	0.37835
0.2	157.71091	157.71089	157.70603	157.77226	0.38112	0.38098	0.38103
0.5	152.57613	152.57578	152.56384	152.66042	0.39716	0.39700	0.39713
1	138.63889	138.64048	138.64082	138.71942	0.42857	0.42850	0.42876
2	111.49794	111.50164	111.50767	111.49025	0.47601	0.47610	0.47606
5	66.75206	66.74936	66.75171	66.73579	0.54001	0.54024	0.54001
10	39.40279	39.40633	39.40258	39.39319	0.57479	0.57486	0.57494

TABLE 2.1: Converged values of G and G_{II}/G for the AFRMM test geometry and loadings outlined in fig. 2.6 using VCCT, IDI, and MDJ partitioning techniques.

	$\%G$ error		
γ	VCCT	IDI	MDJ
0.1	-0.00001	0.00450	0.03700
0.2	-0.00001	-0.00309	0.03890
0.5	-0.00023	-0.00806	0.05524
1	0.00115	0.00139	0.05808
2	0.00332	0.00873	-0.00690
5	-0.00404	-0.00052	-0.02437
10	0.00899	-0.00052	-0.02437

TABLE 2.2: $\%G$ error values for the VCCT, IDI, and MDJ partitioning techniques for a range of γ values in the AFRMM test.

least accurate with a maximum error of $\approx .05\%$. The reason for this is likely due to the fact that the mode decomposed J integral is calculated as a line integral and not an area integral as in the IDI technique. However, this level of accuracy is deemed sufficient for the current study of mixed mode partitions. The numerical mixed mode partitions using VCCT, IDI and MDJ, which are plotted in fig. 2.7, all converge to the same value, which is very close to the analytical predictions of Suo and Hutchinson [26]. This result is not surprising given that in this purely elastic analysis, a K dominant region is allowed to develop at the crack tip upon loading. This singularity dominant region matches the stress, strain and displacement field assumptions of Suo and Hutchinson [26], when they used numerical equations to extract mixed mode stress intensity factors for the infinite lower beam case ($\gamma = 0$) and then linearly averaged between $\gamma = 0$ and $\gamma = 1$ using eq. 1.10. The $\%\frac{G_{II}}{G}$ differences from the analytical prediction of Suo and Hutchinson [26], $\frac{G_{II}}{G}_{HS}$, are given in table 2.3 and are calculated using:

$$\%\frac{G_{II}}{G}_{N}\text{difference} = \frac{\frac{G_{II}}{G}_{N} - \frac{G_{II}}{G}_{HS}}{\frac{G_{II}}{G}_{HS}} * 100, \quad (N = VCCT,\ IDI,\ MDJ) \tag{2.30}$$

From table 2.3, it is clear that each of the numerical solutions predict the same mode partition to a high degree of accuracy and they predict slight deviations from the local

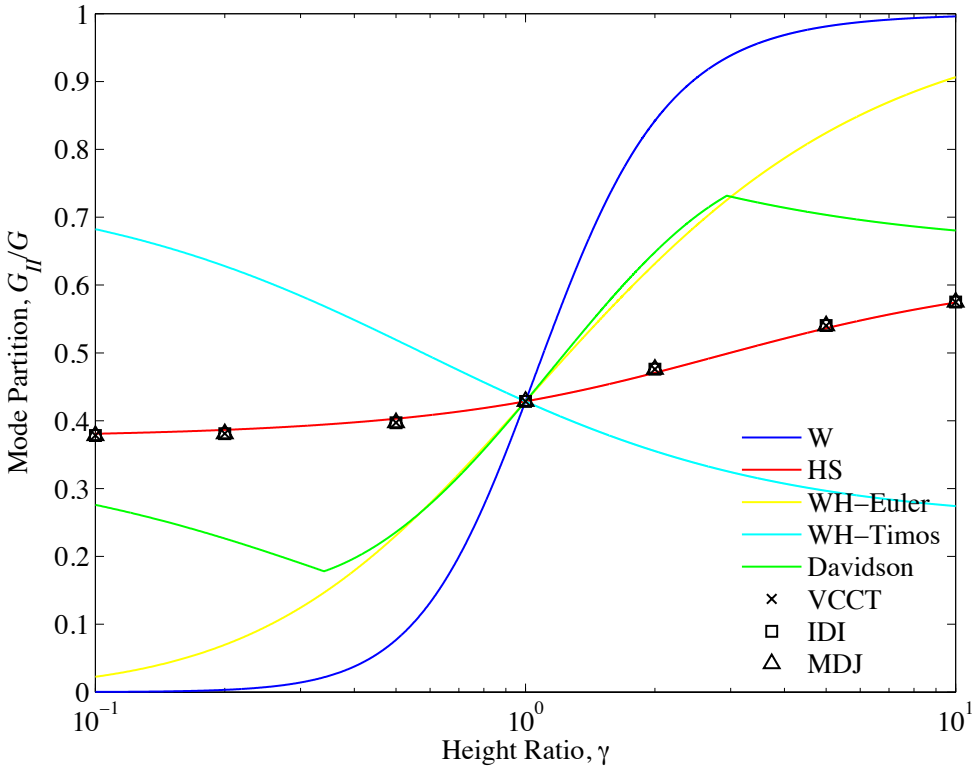

FIGURE 2.7: Converged values of G_{II}/G for the AFRMM test geometry and loadings outlined in fig. 2.6 using VCCT, IDI, and MDJ partitioning techniques.

	$\%G_{II}/G$ diff. from $(G_{II}/G)_{HS}$		
γ	VCCT	IDI	MDJ
0.1	-1.0395	-1.0921	-1.0665
0.2	-1.6519	-1.6898	-1.6769
0.5	-1.4211	-1.4593	-1.4280
1	0.0260	0.0091	0.0712
2	1.2450	1.2652	1.2553
5	1.2383	1.2805	1.2386
10	0.7051	0.7172	0.7316

TABLE 2.3: $\%G_{II}/G$ difference from $(G_{II}/G)_{HS}$ for the VCCT, IDI, and MDJ partitioning techniques for a range of γ values in the AFRMM test.

numerical solution of Suo and Hutchinson [26]. The numerical solutions are closest to the local analytical predictions near the limits ($\gamma = 0.1, 10$), for which a numerical solution was obtained using integral equations, and at $\gamma = 1$, for which an exact solution exists. In the intermediate regions ($\gamma = 0.2, 0.5, 2, 5$) the differences are up to $\approx 1.5\%$. These differences are not due to numerical errors but in fact due to the approximation in the analytical solution, and it is noted by Suo and Hutchinson [26] that the linear approximation given in eq. 1.10 can lead to errors of the order of 1%. It is therefore taken that the numerical solutions are accurate and are deemed to be *correct* in this

case. These numerical results further verify that the linear approximation in the local analytical partitioning can be used to obtain accurate mixed mode partitions in cases where a singular dominant region exists. Conversely, it is clear from fig. 2.7 that the partitioning theories of Williams [20],Wang and Harvey [28] and Davidson et al. [27](CTE-NSF) cannot be used to accurately partition where a K dominant region exists at the crack tip.

2.4.2 Convergence Study

A summary of the converged values of mode partition (G_{II}/G) and energy release rate (G) were presented in the previous section for VCCT, IDI and MDJ partitioning of the AFRMM test case. In this section, all of results from the convergence study are presented and discussed. For each AFRMM height ratio, six simulations are carried out with the element size (l_{el}) varied with respect to the smallest beam height, h_c, ($h_c = \min(h_1, h_2)$). A regular grid of square elements is used in all simulations and so the element length l_{el} corresponds to the length of each side of the element. Values of $\frac{l_{el}}{h_c}$ used in each case are $\frac{1}{1}, \frac{1}{2}, \frac{1}{3}, \frac{1}{10}, \frac{1}{20}$ and $\frac{1}{30}$. Therefore, the coarsest mesh only has one element across the smallest beam height and the finest mesh has 30 elements across the smallest beam height.

2.4.2.1 Convergence of total energy release rate G

The total energy release rate from each method is normalised with respect to the analytical energy release rate (G_{ANA}) and the results are plotted against the normalised element length ($\frac{l_{el}}{h_c}$) in figs. 2.8-2.10 for the VCCT, IDI and MDJ techniques respectively. The corresponding $\%G$ errors are presented in tables 2.4-2.6 for the VCCT, IDI and MDJ techniques respectively.

Figure 2.8 and table 2.4 show the errors associated with total ERR calculation using the VCCT partitioning. Interestingly, the VCCT approach is accurate to within $\approx .01\%$ for all elements sizes and does not exhibit any clear convergence pattern. The $\%G$ error tends to increase as the beam height ratio γ is increased, which may be due to the smaller applied energy release rate in the higher γ cases, which acts as the denominator in the $\%G$ error calculation. The applied energy release rates resulting from an applied moment of 250 N/m are outlined in table 2.1 for each case. Overall, the errors are negligible and the converged G values reported in section 2.4.1 are taken from the finest mesh simulated in each case (i.e. $l_{el}/h_c = 30$).

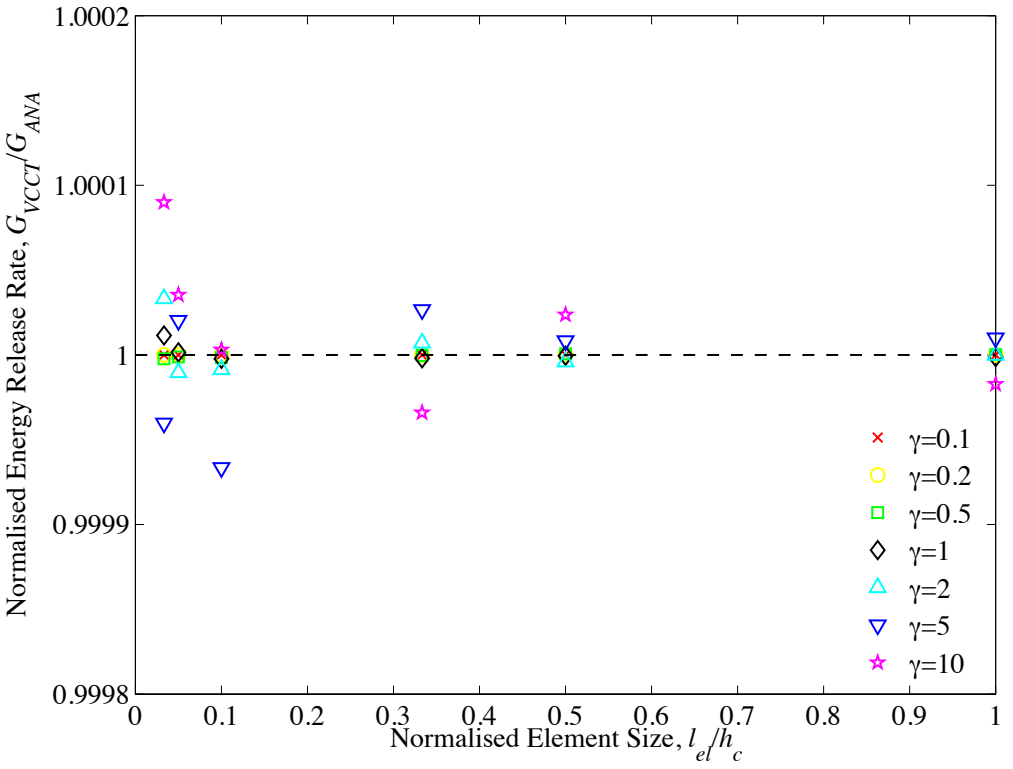

FIGURE 2.8: Values of G for the AFRMM test geometry and loadings outlined in fig. 2.6 obtained using VCCT partitioning normalised w.r.t analytical G value and plotted as a function of the normalised element size.

	$\%G_{VCCT}$ error for each γ ratio						
l_{el}/h_c	$\gamma = 0.1$	$\gamma = 0.2$	$\gamma = 0.5$	$\gamma = 1$	$\gamma = 2$	$\gamma = 5$	$\gamma = 10$
1/30	-0.000008	-0.000010	-0.000230	0.001148	0.003316	-0.004035	0.008991
1/20	-0.000002	-0.000016	-0.000126	0.000152	-0.001043	0.002027	0.003532
1/10	-0.000002	-0.000003	-0.000158	-0.000230	-0.000863	-0.006655	0.000296
1/3	-0.000002	-0.000003	-0.000034	-0.000201	0.000706	0.002660	-0.003404
1/2	-0.000002	0.000003	0.000064	-0.000057	-0.000406	0.000820	0.002367
1/1	-0.000002	-0.000003	0.000019	-0.000136	-0.000011	0.000991	-0.001731

TABLE 2.4: $\%G$ error values obtained using VCCT partitioning as a function of element size for a range of γ values in the AFRMM test.

The errors associated with the total ERR calculation using the IDI partitioning are outlined in figure 2.9 and table 2.5. Most noticeably, the errors are significant (up to 30%) for larger element sizes. Unlike the VCCT approach, this method requires accurate stress distributions in the vicinity of the crack tip. At least 30 elements are required across the smallest beam height in order to ensure errors in G are of the order of 1%. Despite this, if the results from the coarsest mesh (l_{el}/h_c) are discarded, there is a clear convergence pattern that is almost linear as the element size is reduced. In order to obtain a converged result, a second order polynomial is fitted to the remaining five data

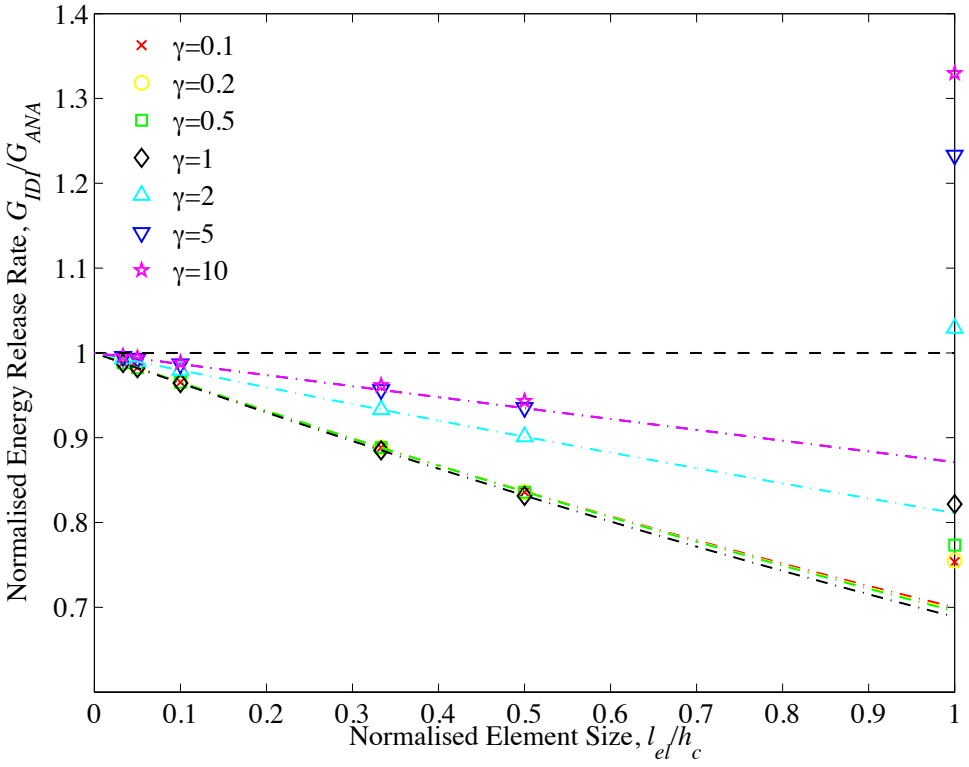

FIGURE 2.9: Values of G for the AFRMM test geometry and loadings outlined in fig. 2.6 obtained using IDI partitioning normalised w.r.t analytical G value and plotted as a function of the normalised element size.

	$\%G_{IDI}$ error for each γ ratio						
l_{el}/h_c	$\gamma = 0.1$	$\gamma = 0.2$	$\gamma = 0.5$	$\gamma = 1$	$\gamma = 2$	$\gamma = 5$	$\gamma = 10$
1/30	-1.1656	-1.1673	-1.1706	-1.1966	-0.6798	-0.4390	-0.3852
1/20	-1.7467	-1.7443	-1.7474	-1.7952	-1.0206	-0.6577	-0.5756
1/10	-3.4710	-3.4626	-3.4646	-3.5624	-2.0430	-1.3139	-1.1517
1/3	-11.1703	-11.1602	-11.1722	-11.4895	-6.6889	-4.3565	-3.8317
1/2	-16.4190	-16.4103	-16.4286	-16.8632	-9.8817	-6.4643	-5.6894
1/1	-24.6552	-24.4567	-22.6681	-17.8441	2.9077	23.3011	32.9779

TABLE 2.5: $\%G$ error values obtained using IDI partitioning as a function of element size for a range of γ values in the AFRMM test.

points and each curve is extrapolated to zero element size. The extrapolated values of G are reported in tables 2.1 and 2.2; the $\%G$ errors associated with the extrapolated values are less than .01% in all cases. Despite accurate results being obtained with extrapolation, it is inconvenient that there are errors of $1-2\%$ when the finest mesh is used. One possible solution to this, without further increasing the computational cost, is to use singular elements, as recommended in the Abaqus manual [42]. Singular elements drop the mid side nodes of the elements at the crack tip to the quarter point and can more accurately capture the square root singular stress field ahead of the crack

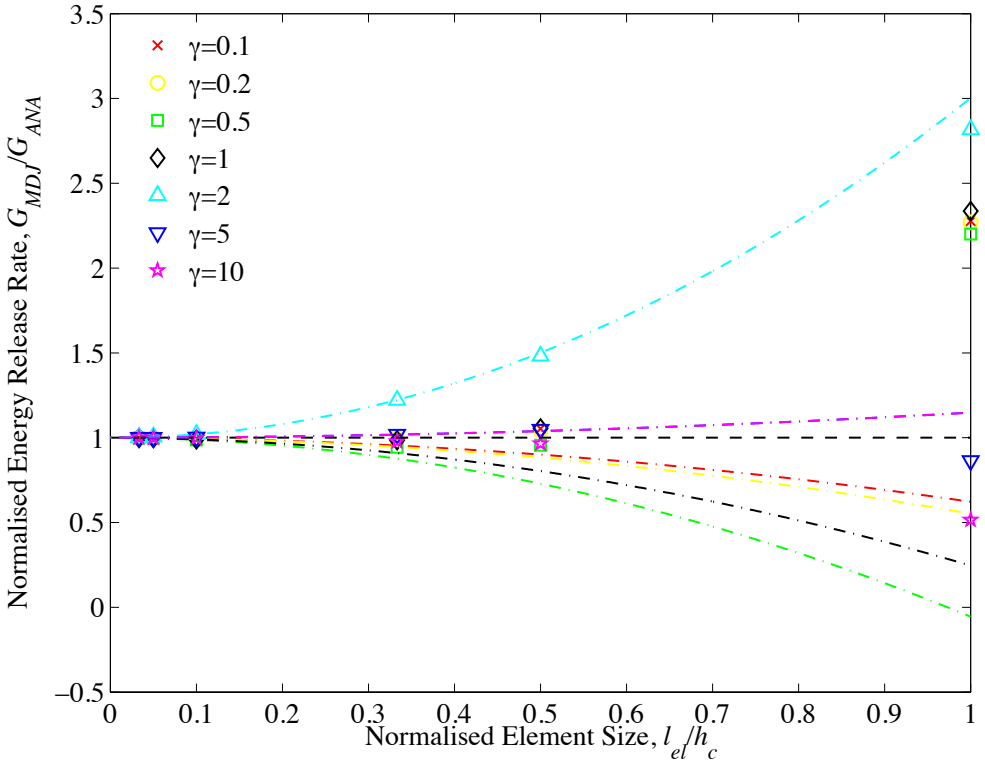

FIGURE 2.10: Values of G for the AFRMM test geometry and loadings outlined in fig. 2.6 obtained using MDJ partitioning normalised w.r.t analytical G value and plotted as a function of the normalised element size.

	$\%G_{MDJ}$ error for each γ ratio						
l_{el}/h_c	$\gamma = 0.1$	$\gamma = 0.2$	$\gamma = 0.5$	$\gamma = 1$	$\gamma = 2$	$\gamma = 5$	$\gamma = 10$
1/30	-0.0762	-0.0856	-0.1681	-0.1410	0.2250	0.0202	-0.0207
1/20	-0.1625	-0.1833	-0.3649	-0.3004	0.5076	0.0541	-0.0404
1/10	-0.5402	-0.6179	-1.2964	-1.0182	2.0219	0.2022	-0.1789
1/3	0.1436	-0.4466	-5.6123	-1.5122	22.1990	1.8318	-2.2560
1/2	5.2741	4.2846	-4.4215	5.4536	48.1963	4.7755	-3.4588
1/1	127.6395	126.9566	120.0513	133.5780	181.6722	-13.5833	-48.4858

TABLE 2.6: $\%G$ error values obtained using MDJ partitioning as a function of element size for a range of γ values in the AFRMM test.

tip. The effect of using singular elements at the crack tip on the convergence pattern of each partitioning method is studied in section 2.4.2.3.

The errors associated with the total ERR calculation using the MDJ partitioning are outlined in figure 2.10 and table 2.6. As in the IDI case, unrealistic values are obtained when the coarsest mesh is used. The MDJ integral calculation is carried out over a remote contour using the trapezoidal rule so it requires a considerable number of nodal points to be able to accurately calculate the integral. It is therefore no surprise that the coarse meshes do not provide accurate results. Based on the results, at least 10

elements are required across the smallest beam thickness in order to reduce the errors to the order of $1-2\%$. It is believed that more accurate results could be obtained with a coarser mesh using this method if a more advanced numerical integration procedure was implemented. The error for the finest mesh is considerably better than obtained with IDI method, with a maximum error of .23% compared to the 1.2% obtained with the IDI technique. A convergence pattern is also noticeable in the cases where the number of elements across the smallest beam thickness are greater or equal to ten. This constitutes three points and so again a second order polynomial is fitted to the data and the curves are extrapolated to zero element size to obtain converged G values. The extrapolated values of G are reported in tables 2.1 and 2.2; the $\%G$ errors associated with the extrapolated values are less than .05% in all cases.

2.4.2.2 Convergence of mixed mode partition G_{II}/G

For each of the seven beam height ratios that are carried out ($\gamma = 0.1, 0.2, 0.5, 1, 2, 5, 10$), the convergence of the mixed mode partitions obtained using VCCT, IDI and MDJ partitioning are plotted for each γ ratio in figures 2.11-2.17. The corresponding numerical values are presented alongside in tables 2.7-2.13. Looking at each of the figures, it is clear that each of the partitioning methods converge to the same mode partition value when extrapolated to zero element size, and the converged values differ slightly from the local solution of Suo and Hutchinson [26]. The only exception is the $\gamma = 1$ case in fig. 2.14. In this case, all of the methods converge to the known analytical solution, which is predicted by all partitioning theories for symmetric cases. The converged values are reported alongside the zero element size row in each of the tables 2.7-2.13. These extrapolated values were also reported and discussed in section 2.4.1.

The VCCT partitioning exhibits non-monotonic convergence behaviour in each of the asymmetric tests (figs. 2.11,2.12,2.13,2.15,2.16,2.17). In the symmetric case ($\gamma = 1$), VCCT predicts the correct mode partition regardless of element size (fig. 2.14). In cases where $\gamma < 1$, G_{II}/G is predicted to increase initially as the element size is reduced and then decrease as the element size approaches zero. Conversely, in cases where $\gamma > 1$, G_{II}/G is predicted to decrease initially as the element size is reduced and then increase as the element size approaches zero. This non-monotonic convergence behaviour was first reported by Nairn [59]. In each case, a 2^{nd} order polynomial was found to accurately fit the convergence pattern and this quadratic function was then extrapolated to zero element size to obtain a converged value of the mixed mode partition from the VCCT method. Surprisingly, despite the VCCT method resulting in accurate ERR values for coarse meshes, inaccurate mode partitions are obtained with the same coarse meshes

for asymmetric specimens. These results show the importance of using a sufficiently small mesh, and/or fitting an extrapolating function, in order to obtain accurate mode partitions using the VCCT method.

As was seen in the previous section with the convergence of the total ERR from the IDI technique, the convergence of the mode partition using IDI also follows an almost linear convergence pattern when the coarsest mesh is disregarded. However, as the predicted G values are inaccurate when the number of elements across the smallest beam height are less than ten, only the three finest meshes are considered when fitting the quadratic extrapolating function i.e. in the range $0 \leq l_{el}/h_c \leq 0.1$. In all cases the value of the mode partition G_{II}/G decreases as the element size decreases and converges to the same value as predicted by extrapolating the VCCT method. Unlike the VCCT method, errors in the mode partition are predicted in the symmetric case for all mesh sizes and only an accurate value is obtained by extrapolation to zero element size. Overall, if accurate results are to be obtained using the IDI method with a regular orthogonal mesh, then the mesh must be sufficiently refined (> 30 elements across smallest beam height) or it is recommended that an extrapolation to zero element size is performed if high levels of accuracy ($< 1\%$error) are required. The effect of using singular elements on the convergence of the mode partition in the IDI method is studied in the following section.

As with the IDI partitioning, only cases where there are at least ten elements across the smallest beam thickness are considered accurate for MDJ partitioning based on the results from the convergence of the total energy release rate G; therefore, only values in the range of $0 \leq l_{el}/h_c \leq 0.1$ are used to fit the quadratic extrapolation function. Disregarding these cases, it can be seen that the MDJ partition converges in a monotonic manner for all cases in this range. There is no particular pattern as to when the value of G_{II}/G increases or decreases as the element size is reduced. As in the IDI case, a quadratic function is fitted to the data points for the three finest mesh simulations and the function is extrapolated to zero element size to obtain a converged value of mode mixity. As seen in section 2.4.1, the converged values from the MDJ partitioning lie very close to the converged values from both the VCCT and IDI methods. As with the VCCT and IDI methods, fine meshes and/or extrapolation to zero element size is required if accurate mixed mode partitions are to be obtained using the MDJ partitioning technique.

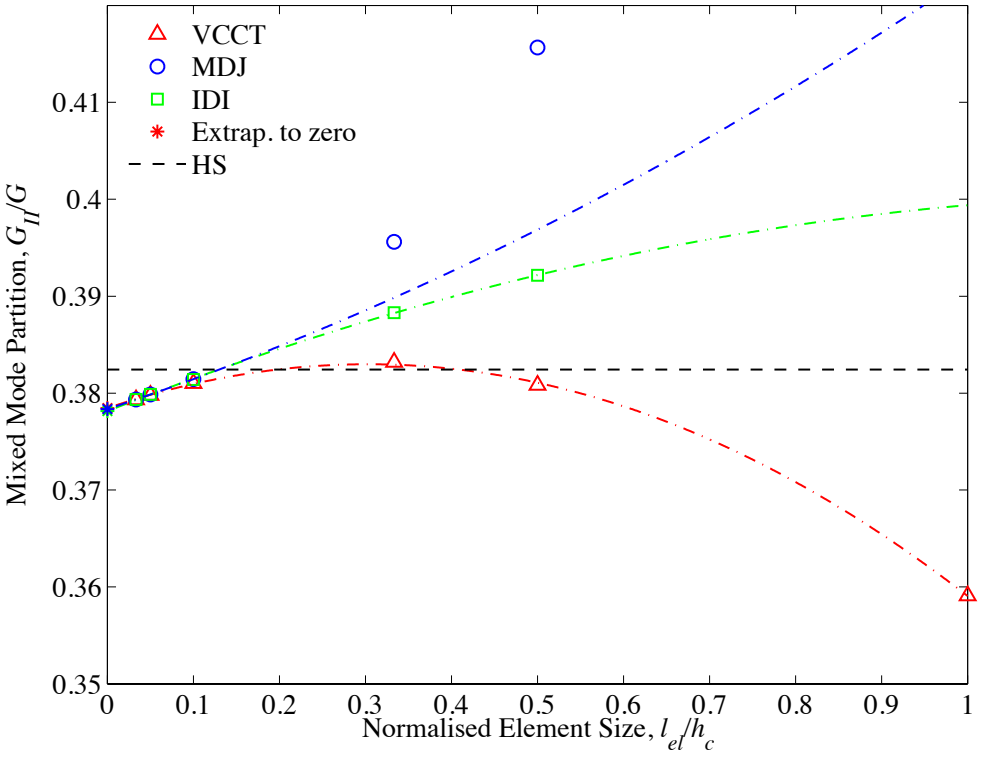

FIGURE 2.11: Values of G_{II}/G for the AFRMM test geometry ($\gamma = 0.1$) obtained using VCCT, IDI and MDJ partitioning plotted as a function of the normalised element size. For both MDJ and IDI, only values in the range of $0 \leq l_{el}/h_c \leq 0.1$ are used to fit the quadratic extrapolation function.

	G_{II}/G		
l_{el}/h_c	VCCT	IDI	MDJ
0*	0.37845	0.37825	0.37835
1/30	0.37932	0.37934	0.37935
1/20	0.37978	0.37987	0.37986
1/10	0.38101	0.38141	0.38144
1/3	0.38320	0.38830	0.39560
1/2	0.38083	0.39216	0.41565
1/1	0.35910	0.42380	0.49520

TABLE 2.7: Values of G_{II}/G for the AFRMM test geometry ($\gamma = 0.1$) obtained using VCCT, IDI and MDJ partitioning as a function of the normalised element size. * Values of zero element size obtained by extrapolating 2^{nd} order polynomial to zero.

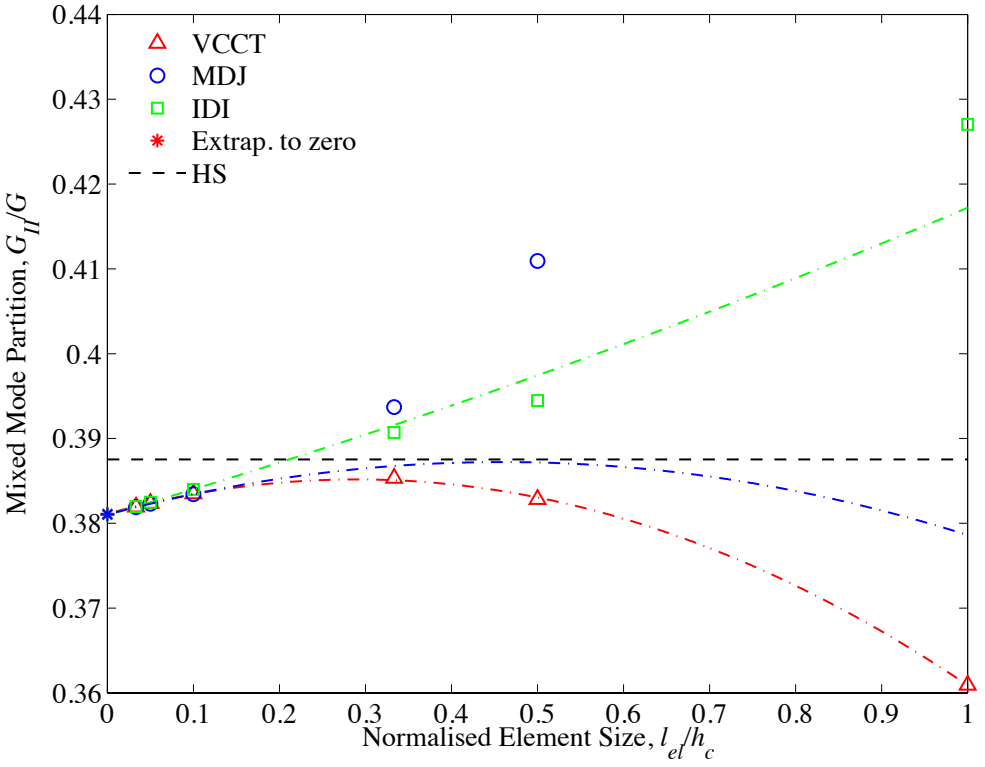

FIGURE 2.12: Values of G_{II}/G for the AFRMM test geometry ($\gamma = 0.2$) obtained using VCCT, IDI and MDJ partitioning plotted as a function of the normalised element size. For both MDJ and IDI, only values in the range of $0 \leq l_{el}/h_c \leq 0.1$ are used to fit the quadratic extrapolation function.

	G_{II}/G		
l_{el}/h_c	VCCT	IDI	MDJ
0*	0.38112	0.38098	0.38103
1/30	0.38192	0.38197	0.38189
1/20	0.38236	0.38247	0.38230
1/10	0.38350	0.38401	0.38343
1/3	0.38532	0.39070	0.39371
1/2	0.38283	0.39448	0.41093
1/1	0.36093	0.42705	0.49161

TABLE 2.8: Values of G_{II}/G for the AFRMM test geometry ($\gamma = 0.2$) obtained using VCCT, IDI and MDJ partitioning as a function of the normalised element size. * Values of zero element size obtained by extrapolating 2^{nd} order polynomial to zero.

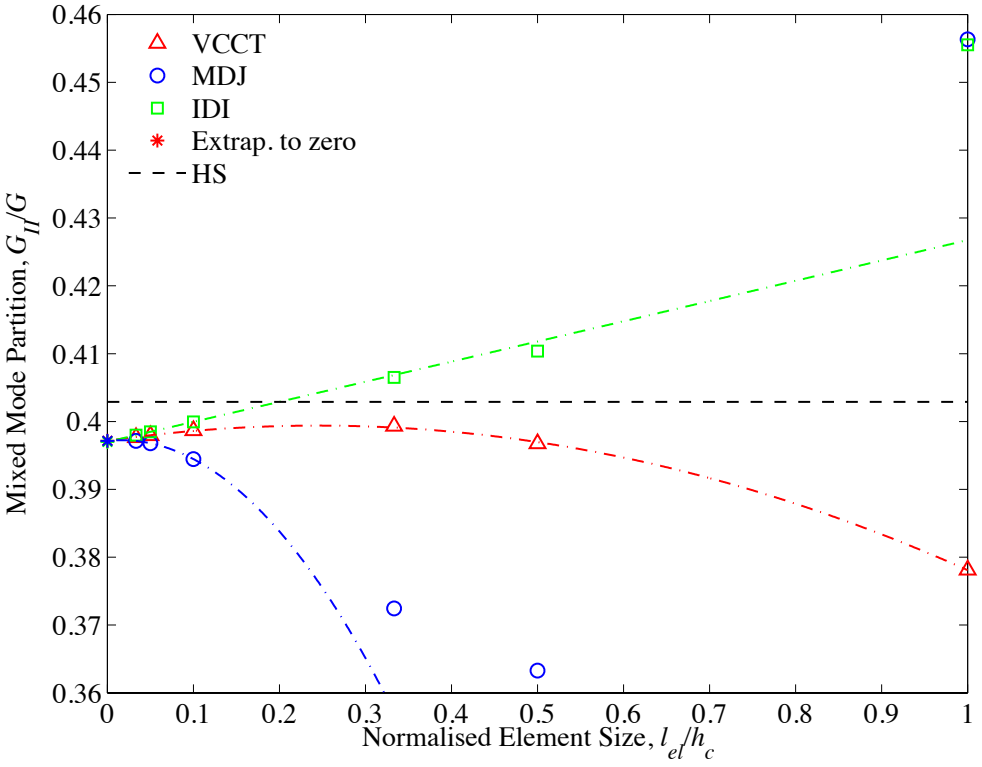

FIGURE 2.13: Values of G_{II}/G for the AFRMM test geometry ($\gamma = 0.5$) obtained using VCCT, IDI and MDJ partitioning plotted as a function of the normalised element size. For both MDJ and IDI, only values in the range of $0 \leq l_{el}/h_c \leq 0.1$ are used to fit the quadratic extrapolation function.

	G_{II}/G		
l_{el}/h_c	VCCT	IDI	MDJ
0*	0.39716	0.39700	0.39713
1/30	0.39765	0.39799	0.39713
1/20	0.39794	0.39848	0.39680
1/10	0.39868	0.39995	0.39447
1/3	0.39933	0.40650	0.37243
1/2	0.39676	0.41037	0.36329
1/1	0.37812	0.45552	0.45633

TABLE 2.9: Values of G_{II}/G for the AFRMM test geometry ($\gamma = 0.5$) obtained using VCCT, IDI and MDJ partitioning as a function of the normalised element size. * Values of zero element size obtained by extrapolating 2^{nd} order polynomial to zero.

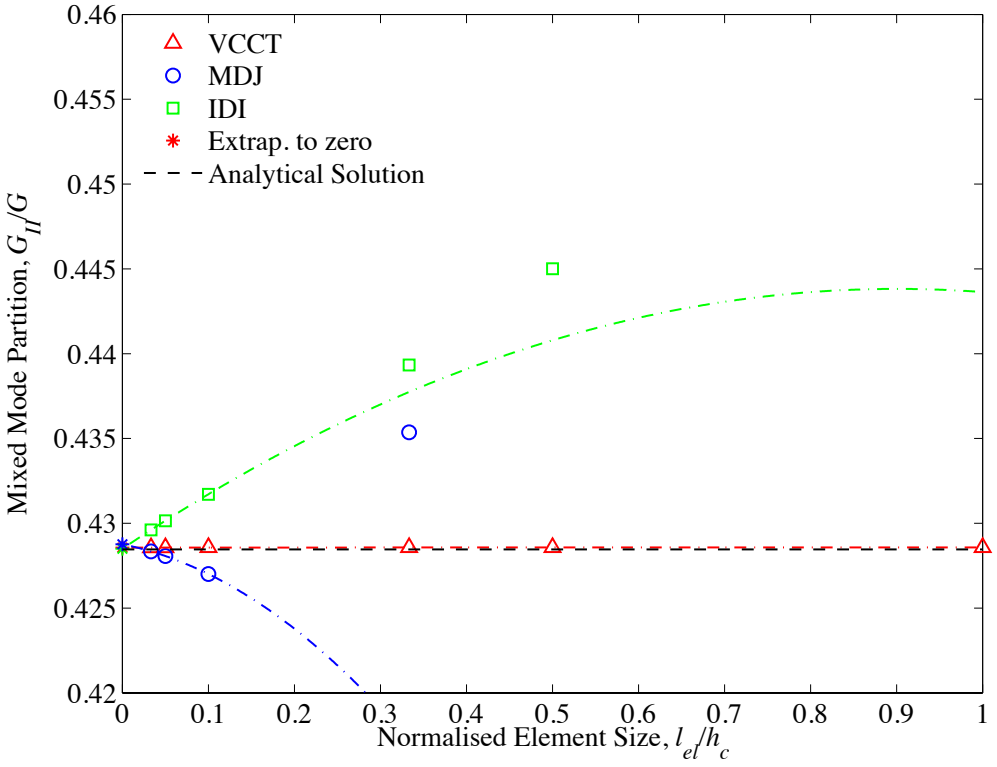

FIGURE 2.14: Values of G_{II}/G for the FRMM test geometry ($\gamma = 1$) obtained using VCCT, IDI and MDJ partitioning plotted as a function of the normalised element size. For both MDJ and IDI, only values in the range of $0 \leq l_{el}/h_c \leq 0.1$ are used to fit the quadratic extrapolation function.

	G_{II}/G		
l_{el}/h_c	VCCT	IDI	MDJ
0*	0.42857	0.42850	0.42876
1/30	0.42857	0.42961	0.42834
1/20	0.42857	0.43015	0.42807
1/10	0.42857	0.43171	0.42701
1/3	0.42857	0.43934	0.43537
1/2	0.42857	0.44500	0.46203
1/1	0.42857	0.52953	0.47764

TABLE 2.10: Values of G_{II}/G for the AFRMM test geometry ($\gamma = 1$) obtained using VCCT, IDI and MDJ partitioning as a function of the normalised element size. * Values of zero element size obtained by extrapolating 2^{nd} order polynomial to zero.

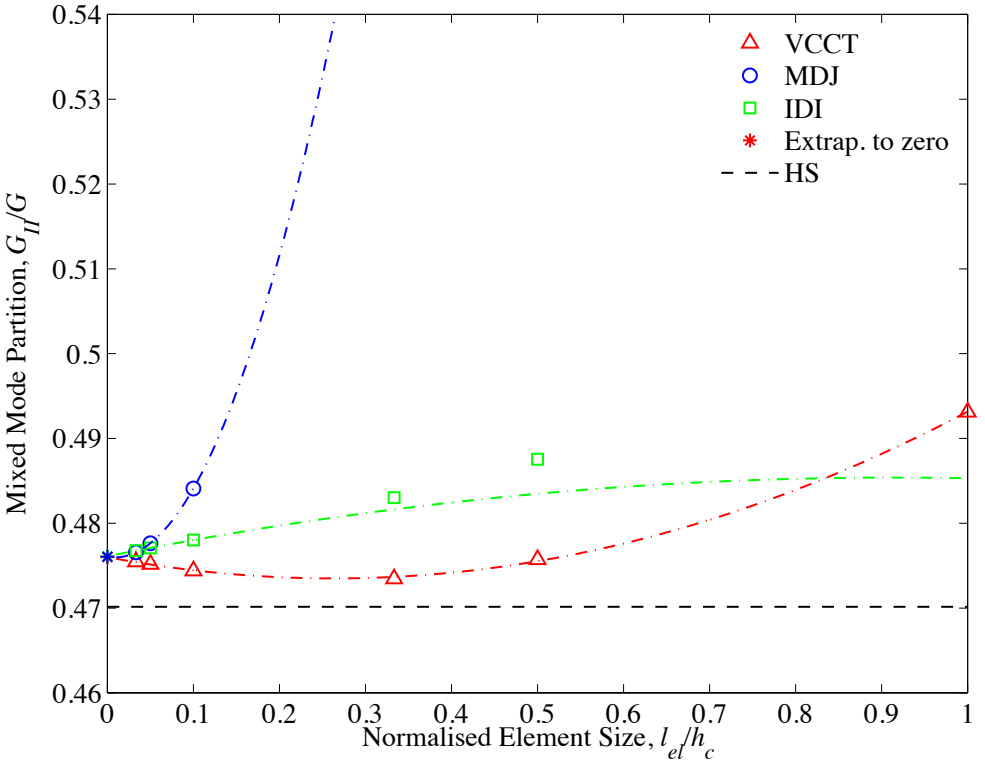

FIGURE 2.15: Values of G_{II}/G for the AFRMM test geometry ($\gamma = 2$) obtained using VCCT, IDI and MDJ partitioning plotted as a function of the normalised element size. For both MDJ and IDI, only values in the range of $0 \leq l_{el}/h_c \leq 0.1$ are used to fit the quadratic extrapolation function.

	G_{II}/G		
l_{el}/h_c	VCCT	IDI	MDJ
0*	0.47601	0.47610	0.47606
1/30	0.47547	0.47677	0.47658
1/20	0.47519	0.47709	0.47765
1/10	0.47441	0.47802	0.48410
1/3	0.47346	0.48303	0.55975
1/2	0.47573	0.48754	0.63294
1/1	0.49313	0.60088	0.68521

TABLE 2.11: Values of G_{II}/G for the AFRMM test geometry ($\gamma = 2$) obtained using VCCT, IDI and MDJ partitioning as a function of the normalised element size. * Values of zero element size obtained by extrapolating 2^{nd} order polynomial to zero.

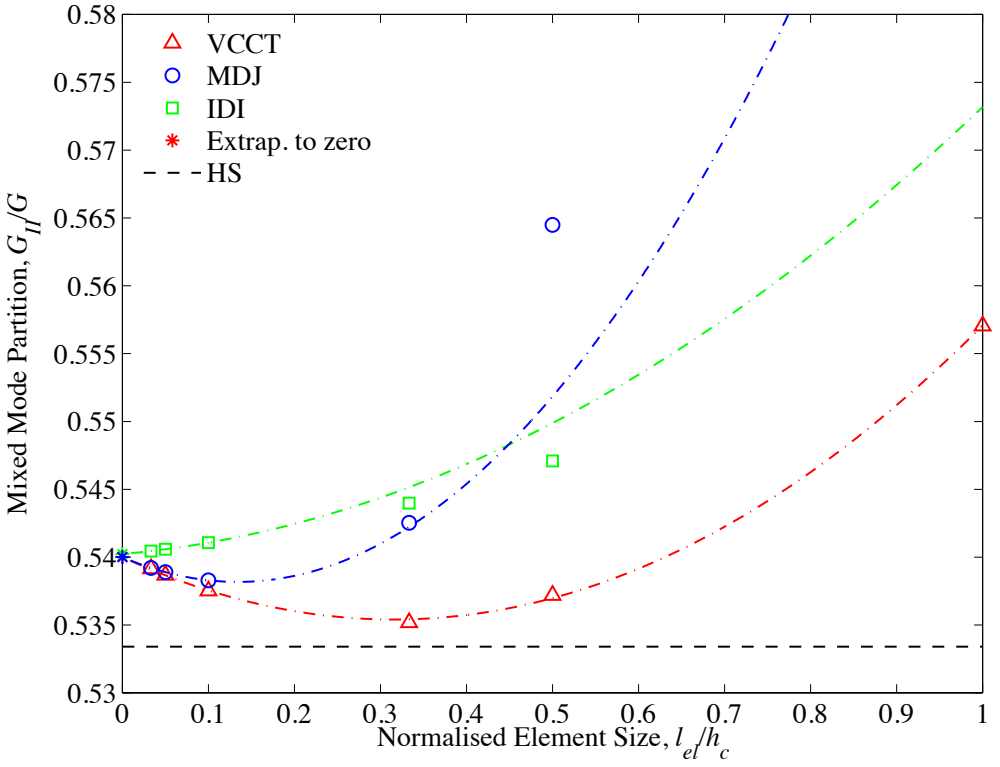

FIGURE 2.16: Values of G_{II}/G for the AFRMM test geometry ($\gamma = 5$) obtained using VCCT, IDI and MDJ partitioning plotted as a function of the normalised element size. For both MDJ and IDI, only values in the range of $0 \leq l_{el}/h_c \leq 0.1$ are used to fit the quadratic extrapolation function.

	G_{II}/G		
l_{el}/h_c	VCCT	IDI	MDJ
0*	0.54001	0.54024	0.54001
1/30	0.53916	0.54045	0.53921
1/20	0.53868	0.54059	0.53890
1/10	0.53753	0.54107	0.53830
1/3	0.53519	0.54399	0.54254
1/2	0.53719	0.54710	0.56449
1/1	0.55705	0.68209	0.33759

TABLE 2.12: Values of G_{II}/G for the AFRMM test geometry ($\gamma = 5$) obtained using VCCT, IDI and MDJ partitioning as a function of the normalised element size. * Values of zero element size obtained by extrapolating 2^{nd} order polynomial to zero.

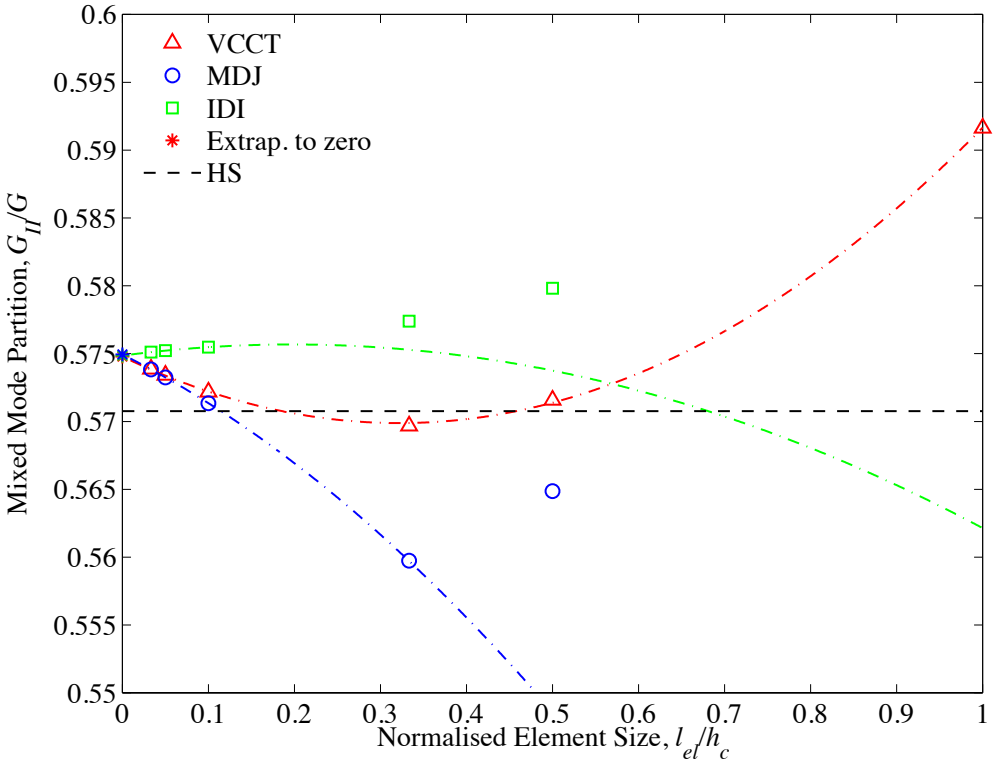

FIGURE 2.17: Values of G_{II}/G for the AFRMM test geometry ($\gamma = 10$) obtained using VCCT, IDI and MDJ partitioning plotted as a function of the normalised element size. For both MDJ and IDI, only values in the range of $0 \leq l_{el}/h_c \leq 0.1$ are used to fit the quadratic extrapolation function.

	G_{II}/G		
l_{el}/h_c	VCCT	IDI	MDJ
0*	0.57479	0.57486	0.57494
1/30	0.57387	0.57511	0.57384
1/20	0.57342	0.57522	0.57325
1/10	0.57218	0.57548	0.57136
1/3	0.56968	0.57740	0.55975
1/2	0.57158	0.57982	0.56487
1/1	0.59163	0.72110	0.01515

TABLE 2.13: Values of G_{II}/G for the AFRMM test geometry ($\gamma = 10$) obtained using VCCT, IDI and MDJ partitioning as a function of the normalised element size. * Values of zero element size obtained by extrapolating 2^{nd} order polynomial to zero.

2.4.2.3 The effect of using singular elements

It has been observed in the previous sections that the rate of convergence of the total ERR is slow when using the IDI partitioning technique. In this section, the case of $\gamma = 0.1$ is repeated with singular elements placed at the crack tip. This requires only a very minimal change to the mesh as only the mid-side nodes of the elements at the crack tip need to be moved to the quarter point, as illustrated in figure 2.18. The application

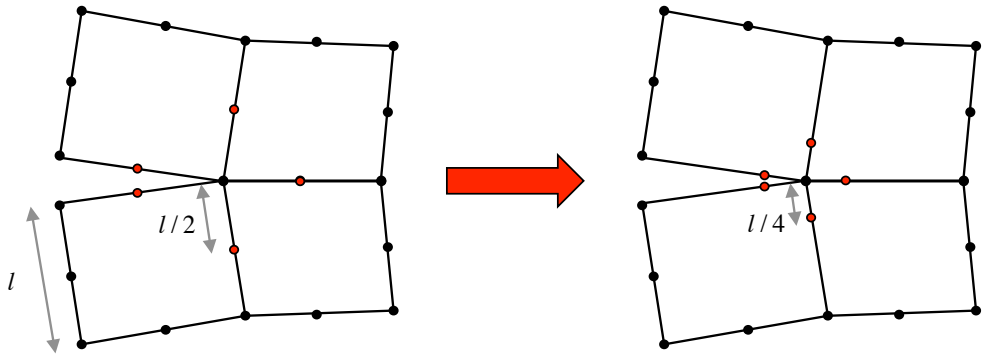

FIGURE 2.18: Moving the midside nodes at the crack tip to the quarter point to more accurately capture the square root singularity.

of the IDI and MDJ techniques to partitioning these cases where there are singular elements is exactly the same as if there are regular quadratic elements. However, the application of the VCCT partitioning needs to be altered to deal with the quarter point elements. The details of this modified technique can be found in [53].

The normalised values of the total ERR obtained from each partitioning method using both singular and regular elements are presented in fig. 2.19 and the corresponding $\%G$ error values are shown in table 2.14. From the graph it is evident that the VCCT partitioning of the singular element does not converge to the correct ERR, and it can be seen from the table that a $\%G$ error of 0.58% is obtained for the finest mesh size compared to an error of $8e{-}6\%$ for the same simulation using regular quadratic elements. The reason for this change in behaviour in the VCCT method is not known but it is not surprising given the complexity of the modified VCCT approach when dealing with singular elements. This result is in contrast to results reported by Nairn [53], where it was found that the singular elements converged to the same ERR value as regular quadratic elements when using VCCT. As expected, the G values obtained from the IDI method converge at a much faster rate towards the correct ERR value when singular elements are used at the crack tip. The $\%G$ error for the third finest mesh reduces from

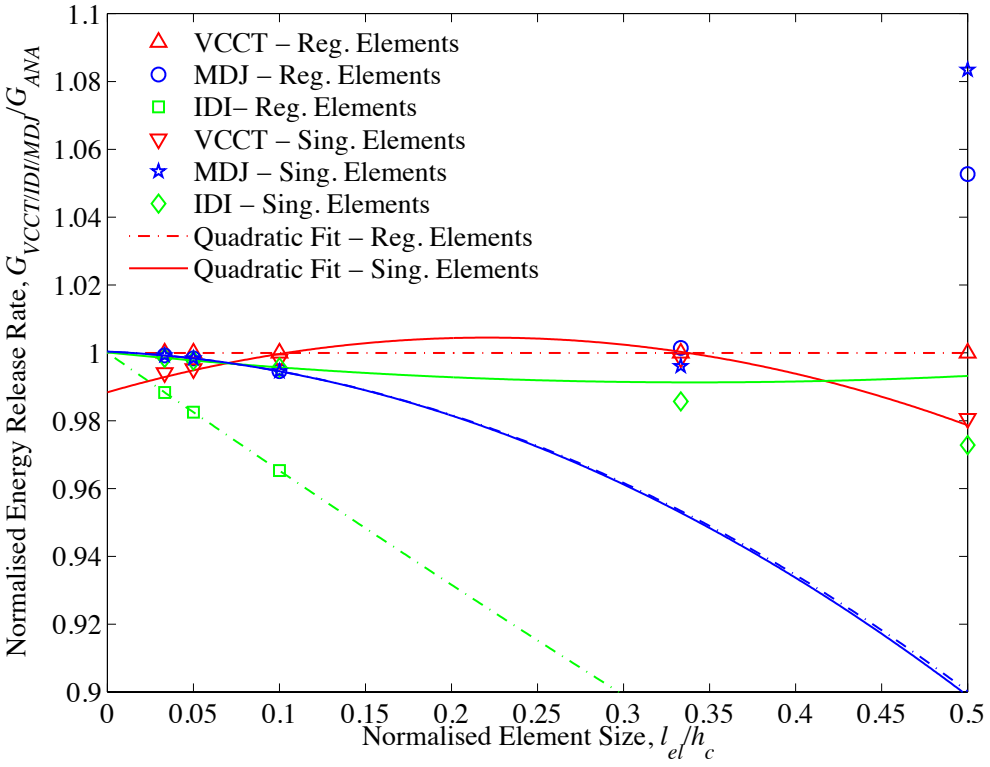

FIGURE 2.19: Normalised values of G for the AFRMM ($\gamma = 0.1$) test geometry obtained using VCCT, IDI and MDJ partitioning using both regular and singular elements plotted as a function of the normalised element size.

	%G error					
	VCCT		IDI		MDJ	
l_{el}/h_c	Regular	Singular	Regular	Singular	Regular	Singular
1/30	-0.000008	-0.588056	-1.1656	-0.1487	-0.0762	-0.0763
1/20	-0.000002	-0.470122	-1.7467	-0.2245	-0.1625	-0.1628
1/10	-0.000002	-0.183232	-3.4710	-0.4266	-0.5402	-0.5431
1/3	-0.000002	-0.154993	-11.1703	-1.4309	0.1436	-0.3910
1/2	-0.000002	-1.938067	-16.4190	-2.7193	5.2741	8.3433
1/1	-0.000002	-19.686773	-24.6552	-15.9074	127.6395	-332.3959

TABLE 2.14: %G error values obtained using VCCT, IDI and MDJ partitioning with regular and singular elements as a function of element size for $\gamma = 0.1$ in the AFRMM test.

-3.47% when using regular elements down to -0.42% when using singular elements and a similar trend can be seen at all mesh densities. The increase in accuracy of the stress, strain and displacement fields in the vicinity of the crack tip when using the singular elements has a clear positive effect on the accuracy of the IDI technique when estimating the total ERR G. Interestingly, the use of singular elements has very little effect on the total ERR when the MDJ partitioning is used. There is an increase in the error when very coarse meshes are used but these cases are inaccurate in any case. As the integral

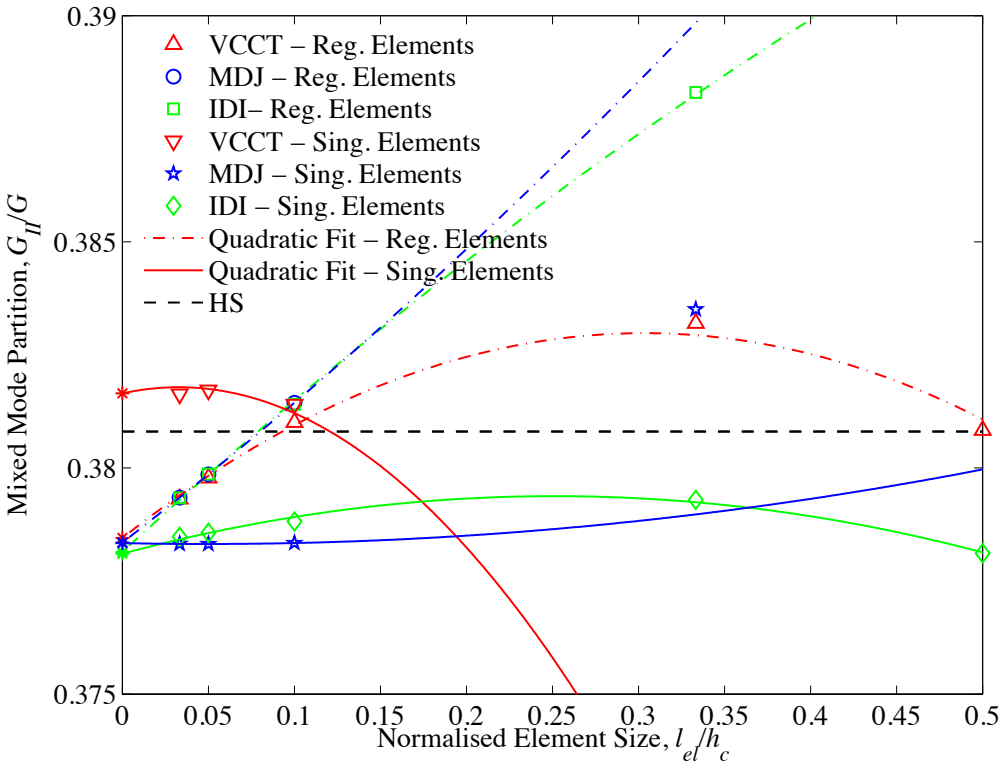

FIGURE 2.20: Values of G_{II}/G for the AFRMM ($\gamma = 0.1$) test geometry obtained using VCCT, IDI and MDJ partitioning using both regular and singular elements plotted as a function of the normalised element size. For MDJ, only values in the range of $0 \leq l_{el}/h_c \leq 0.1$ are used to fit the quadratic extrapolation function.

	$\%G_{II}/G$ difference from regular converged value					
	VCCT		IDI		MDJ	
l_{el}/h_c	Regular	Singular	Regular	Singular	Regular	Singular
1/30	0.255273	0.866608	0.2603	0.0341	0.2629	-0.0082
1/20	0.378174	0.890395	0.4004	0.0565	0.3980	-0.0088
1/10	0.702211	0.807140	0.8077	0.1223	0.8167	-0.0032
1/3	1.281301	-2.091747	2.6293	0.2489	4.5587	1.3627
1/2	0.655693	-6.437962	3.6492	-0.0632	9.8588	6.7046
1/1	-5.088426	-30.413244	12.0120	-13.6852	30.8834	52.1234

TABLE 2.15: $\%G_{II}/G$ difference from regular converged value obtained using VCCT, IDI and MDJ partitioning with regular and singular elements as a function of element size for $\gamma = 0.1$ in the AFRMM test.

is calculated remotely, it is likely that the increase in accuracy at the crack tip has no significant effect on the field values where the integral is calculated.

The mode partition values G_{II}/G obtained from each partitioning method using both singular and regular elements are presented in fig. 2.20 and the corresponding $\%G_{II}/G$ differences from the regular converged value (taken as the average of the VCCT, IDI

and MDJ extrapolated values in table 2.7) are shown in table 2.15. As before, only the three smallest mesh sizes are used to fit the MDJ extrapolation curve; however, five points are used to fit the IDI extrapolation curve in this case due to the increased accuracy of G when using singular elements. These $\%G_{II}/G$ differences from the regular converged value give a clear indication of the rate of convergence of the mode partition towards the *correct* value. As is the case with the total ERR, the VCCT mode partition does not converge to the same value when singular elements are used. The $\%G_{II}/G$ difference from the correct value for the finest mesh is 0.87% when singular elements are used compared to 0.26% when regular elements are used. The convergence rate of the mode partitions using both the IDI and MDJ techniques are improved considerably when singular elements are used. The $\%G_{II}/G$ difference using the IDI method is .03% when using singular elements compared to 0.26% when using regular elements for the finest mesh. Similarly, the $\%G_{II}/G$ difference using the MDJ method is $-.00082\%$ when using singular elements compared to 0.26% when using regular elements for the finest mesh. It is interesting that when using the MDJ technique, the rate of convergence of the total ERR is not greatly affected when singular elements are used but the rate of convergence of the mode partition increases significantly when singular elements are introduced. As the energy predictions for the mode decomposed J integral are reasonably good for regular elements where $l_{el}/h_c \leq 1/3$, there is not significant room for improvement in the total G prediction by introducing singular elements. However, the accuracy of singular stresses at the crack tip clearly lead to more accurate stress decompositions away from the crack tip, and hence the rate of convergence towards the correct mode partition is improved with the use of singular elements.

In summary it has been shown that more accurate mode partitions can be obtained by using singular elements at the crack tip when IDI and MDJ partitioning techniques are used. However, the use of singular elements result in increased inaccuracy when using VCCT partitioning. When using regular elements, the IDI technique is the least accurate technique at predicting the total energy release rate G, and this error can be reduced significantly by using singular elements. The use of singular elements has little effect on the predicted ERR when using the MDJ technique, and they have a negative effect on the predicted ERR when VCCT partitioning is used. In conclusion it is recommended that singular elements are only used where IDI or MDJ partitioning techniques are employed.

2.5 Region of K dominancy

In this section the extent of the region of K dominancy is investigated for each γ ratio outlined in fig. 2.6 in the AFRMM test. Using the full field solutions of Inglis [49] and Westergaard [60], Irwin [50] noticed that the stress very close to any crack tip in an elastic medium scaled inversely with the square root of the distance from the crack tip. i.e.:

$$\sigma \propto \frac{1}{\sqrt{r}} \tag{2.31}$$

Irwin argued that it was the stress close to the crack tip which determined whether a crack would propagate. Irwin introduced a scaling factor, K, into equation 2.31, which was termed the stress intensity factor. i.e.

$$\sigma = \frac{K}{\sqrt{2\pi r}} \tag{2.32}$$

This result meant that regardless of specimen size or geometry, the stresses close to the crack tip would be equivalent in two specimens of the same elastic material if the applied stress intensity factors were equivalent. This then allowed one to measure the stress intensity factor required to propagate a crack in a given material, termed the critical stress intensity factor K_c, and then use this value to determine when a crack would propagate in a different geometry of the same material. This analysis formed the basis of linear elastic fracture mechanics (LEFM). Numerous handbooks were drawn up with stress intensity factor solutions for common geometries which allowed engineers to apply LEFM principles in design. Irwin [50] showed the stress approach to fracture, using K, and the energy approach, using G, were equivalent in an elastic material and related through:

$$G = \frac{1}{E'}K^2 \tag{2.33}$$

However, real materials are not perfectly elastic and the infinite stresses predicted at the tip of an elastic crack clearly do not represent the physical reality. Most common engineering materials will exhibit some form of yielding when the stresses reach a certain magnitude; therefore in a propagating crack there will be a small yield or plastic zone present directly at the crack tip. This zone is illustrated in figure 2.21. The singularity dominated region, or K dominant region, is defined as the region over which the stresses are accurately described by a square root dependence in an elastic material. Therefore if the plastic zone grows larger than the K dominant region, then the stresses at the crack tip no longer exhibit an inverse square root dependence and the assumptions of LEFM break down. In the fracture of composite laminates and adhesive joints, it is common that the plastic zone will grow larger than the size of the K dominant region. However,

because this damage is constrained in plane (i.e. between substrates in the case of an adhesive failure, or between plies as in the case of a composite delamination), the loaded beams remain elastic and so it is possible to obtain accurate values of energy release rate directly from beam theory without assuming the presence of a K dominant region. The mixed mode stress intensity factor solutions presented by Suo and Hutchinson [26] assume the presence of a singular stress field at the crack tip so it is of interest here to examine the extent of the singular field for the current AFRMM test specimens.

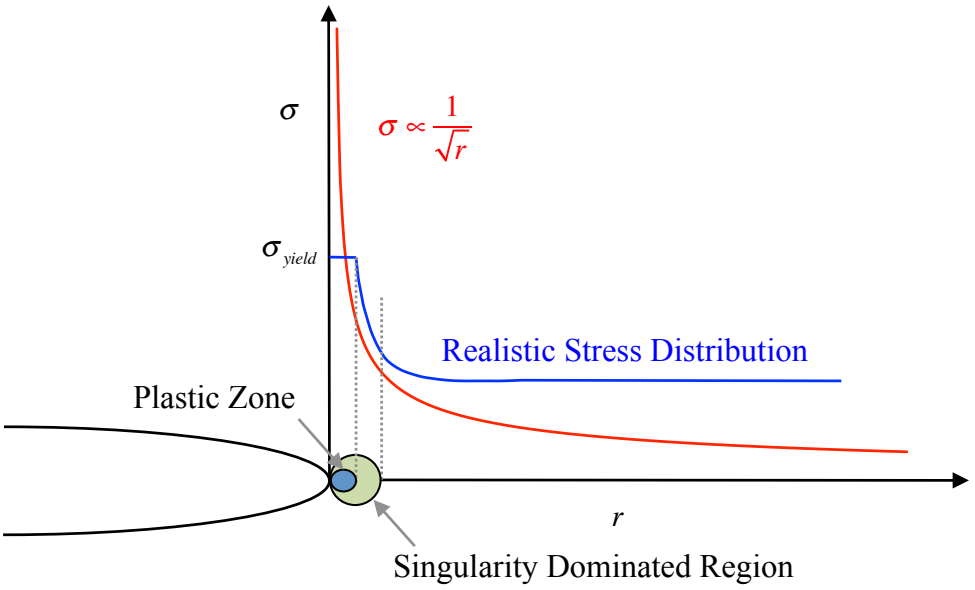

FIGURE 2.21: Singular stress distribution vs. realistic stress distribution at a loaded crack tip.

The size of the K dominant region in beam-like geometries has previously been studied by Wilson [48] and Charalambides et al. [16] for double cantilever beam specimens loaded in mode I and is reported to be of the order of 1% of the substrate height. The size of the region is reported to scale with the substrate height and not the crack length, as in infinite geometries.

2.5.1 Case Setup

The AFRMM test case outlined in fig. 2.6 is repeated here but with a refined mesh in the vicinity of the crack tip. The refined mesh is required to accurately capture high stress gradients close to the crack tip. The refined mesh pattern at the crack tip is shown in figure 2.22. Quadratic elements were used as before but here the elements at the crack tip were collapsed to form triangular elements, with the mid side nodes moved to the

quarter point to more accurately capture the stress singularity. The regular element size away from the crack tip in all cases was $5 \times 10^{-5} m$, with the elements reducing gradually to $2 \times 10^{-6} m$ at the crack tip. The stress intensity factors are obtained using the IDI technique and are reported in table 2.16. To check the accuracy of the IDI technique using this refined mesh, the $\%G$ error is also reported and the mode partition G_{II}/G is compared to the extrapolated IDI values (G_{II}/G (Ext.)) reported in section 2.4.1. It is evident that the refined mesh produces very accurate results with the maximum error in .00054% in the prediction of the total ERR G. The refined mesh is also capable of producing the extrapolated value of the mixed mode partition to a high degree of accuracy.

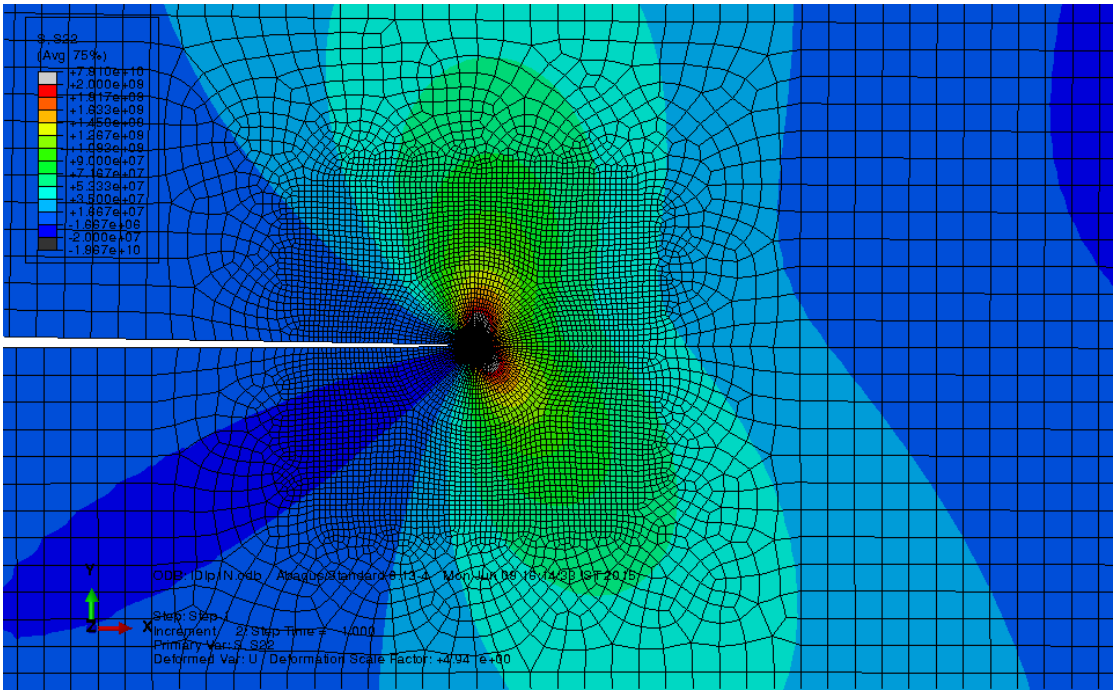

FIGURE 2.22: Mesh refinement close to the crack tip to pick up high stress gradients.

γ	K_I $Pa\sqrt{m}$	K_{II} $Pa\sqrt{m}$	$\%G$ error	G_{II}/G	G_{II}/G (Ext.)
0.1	2937368	-2291343	0.00012	0.3783	0.3783
0.2	2925368	-2294939	0.00012	0.3810	0.3810
0.5	2839846	-2304278	0.00011	0.3970	0.3970
1	2635230	-2282174	0.00015	0.4286	0.4285
2	2262737	-2157229	0.00014	0.4761	0.4761
5	1640396	-1777749	0.00021	0.5401	0.5402
10	1211635	-1409205	0.00054	0.5750	0.5749

TABLE 2.16: Values of K_I, K_{II} , G_{II}/G and $\%G$ errors obtained using IDI partitioning for the AFRMM test geometry and loadings outlined in fig. 2.6 and using the mesh refinement shown in fig. 2.22. The G_{II}/G values are compared to the converged IDI values reported in section 2.4.1.

2.5.2 Results

The normal and shear stresses ahead of the crack tip ($\theta = 0$) are plotted as a function of the normalised distance ahead of the crack tip in figs. 2.23 and figs. 2.24 respectively for the $\gamma = 0.1$ case. The distance ahead of the crack tip, r, is normalised with h_c, where h_c is the smallest beam height as before. Also plotted in each case is the square root singular stresses σ_K, which are obtained from equation 2.32 for mode I and mode II by using the corresponding numerical values of the stress intensity factor, K_I, K_{II} obtained from IDI and outlined in table 2.16. In both cases it can be seen graphically

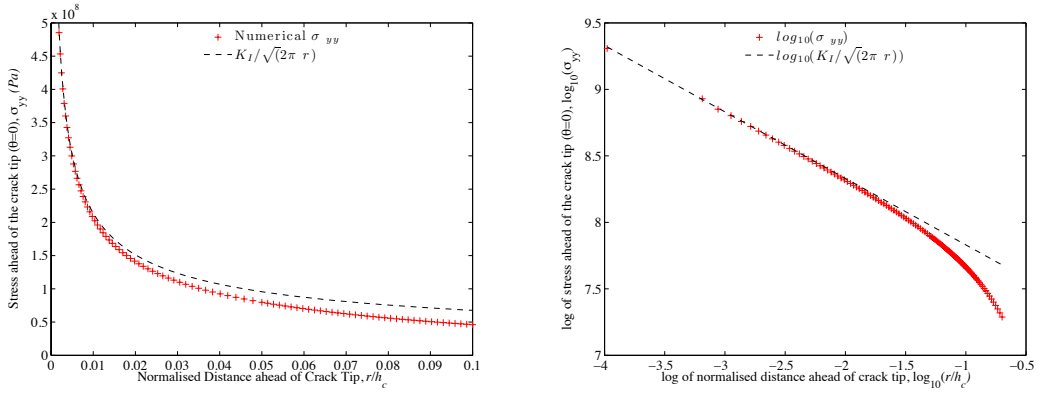

(a) Normal plot (b) log-log plot

FIGURE 2.23: Normal stress plotted as a function of normalised distance ahead of the crack tip and compared with square root singular field.

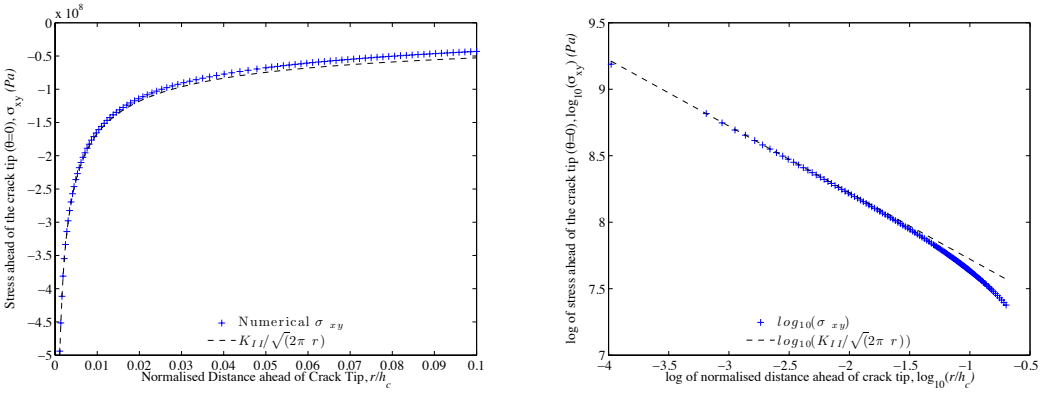

(a) Normal plot (b) log-log plot

FIGURE 2.24: Shear stress plotted as a function of normalised distance ahead of the crack tip and compared with square root singular field.

that the numerical stresses follow the predicted square root singular field very closely up to about a normalised distance of $1-2\%$ and then starts to deviate away. The shear

stresses remain much closer to the singular solution at larger distances than the normal stresses. Each of the other γ ratios follow a similar trend; as a way of obtaining a more comparative estimate of the range of the singular field in each case, the % deviation away from the singular solution is calculated as a function of the distance ahead of the crack tip for each case. The % deviation from the singular solution is given by:

$$\%\ \text{deviation}^{I} = 100 * \frac{(\sigma_K - \sigma_{yy})}{\sigma_{yy}}; \quad \sigma_K = \frac{K_I}{\sqrt{2\pi r}} \tag{2.34}$$

for mode I and

$$\%\ \text{deviation}^{II} = 100 * \frac{(\sigma_K - \sigma_{xy})}{\sigma_{xy}}; \quad \sigma_K = \frac{K_{II}}{\sqrt{2\pi r}} \tag{2.35}$$

for mode II. The % deviations of the opening stresses from the singular solution are plotted in fig. 2.25; the % deviations of the shear stresses from the singular solution are plotted in fig. 2.26. As an indicative measure of the size of the K dominant region in each case, the r/h_c values at 10% deviation from the singular solution are obtained from the graphs and outlined in table 2.17. The approach of using a 10% deviation to study the range of K dominance is adopted from Charalambides et al. [16].

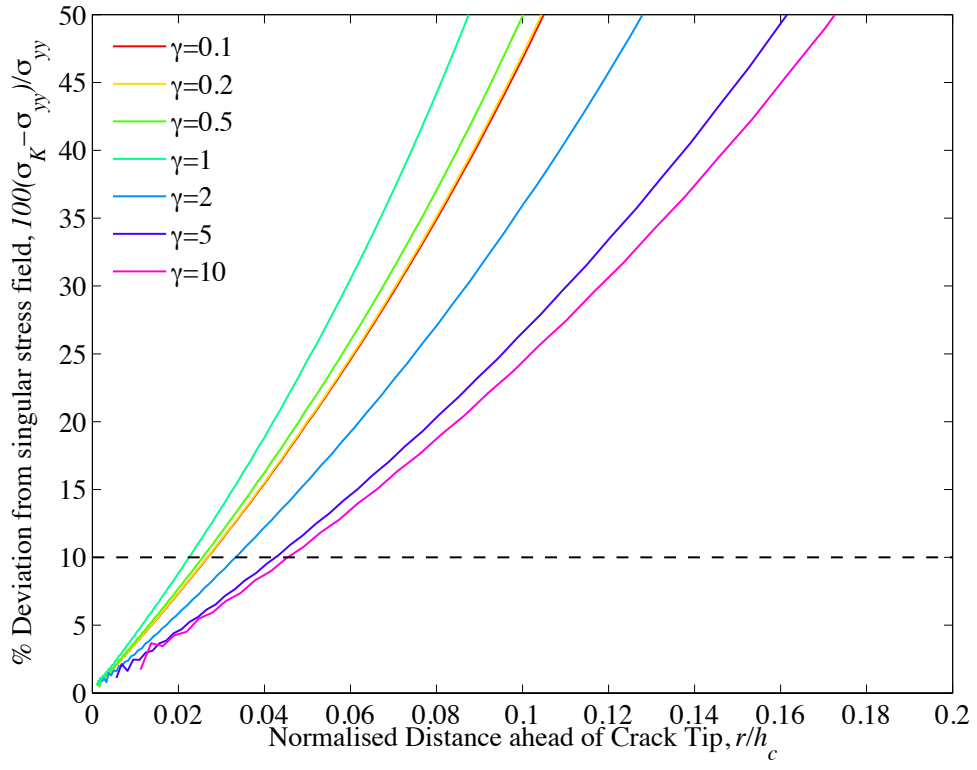

FIGURE 2.25: % deviations of the opening stresses from the singular solution for the AFRMM test for various γ ratios.

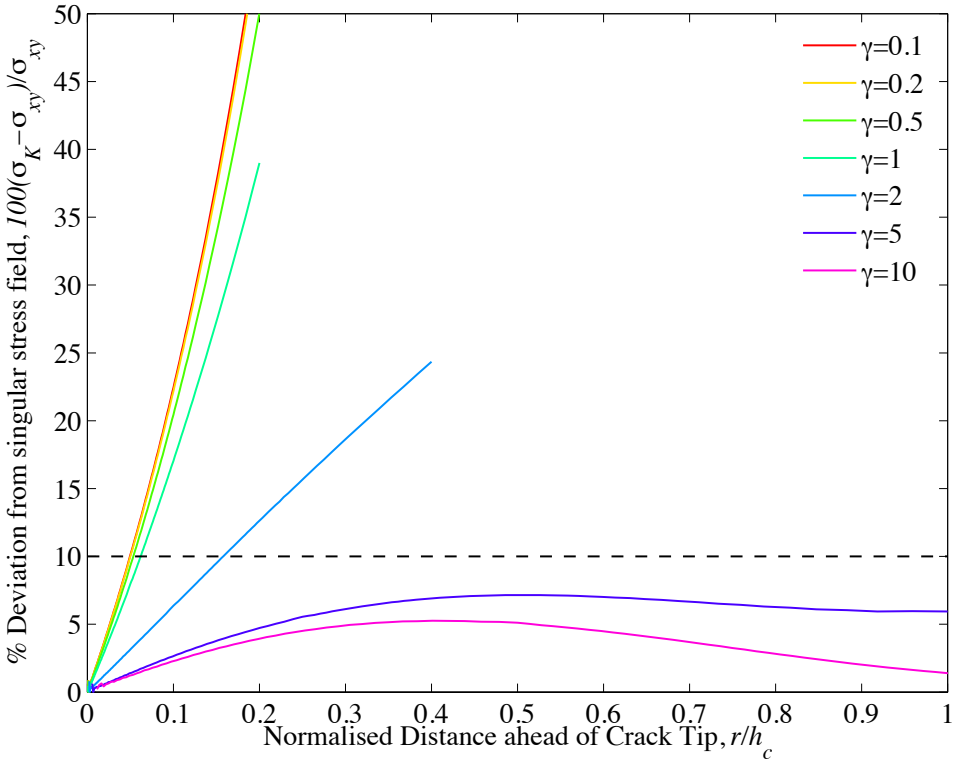

FIGURE 2.26: % deviations of the shearing stresses from the singular solution for the AFRMM for various γ ratios.

γ	r/h_c value at 10% dev. mode I	mode II
0.1	0.027	0.050
0.2	0.027	0.050
0.5	0.025	0.054
1	0.023	0.063
2	0.034	0.158
5	0.043	-
10	0.045	-

TABLE 2.17: Values of r/h_c at 10 % deviation of the opening and shearing stresses from the respective singular solutions.

2.5.3 Discussion

Focusing on the deviation of the opening stresses in fig. 2.25, it is clear that each γ ratio produces a similar divergence pattern from the singular field. The range of the singular field is similar in each case which confirms that it does scale reasonably well with the smallest characteristic dimension of the problem (i.e. h_c). The r/h_c values at 10% deviation are presented in table 2.17 and these range from 2.5−4.5% of the smallest beam height. This is quite limiting if one considers that common beam heights in standard

fracture mechanics tests are of the range of $2-5$ mm. This would mean a damage zone size of the order of $50-200$ μm would be large enough to obliterate the singular dominant region completely. Taking the strip-yield model proposed by Dugdale [61] and Barenblatt [62] with typical composite properties ($G_{IC} = 200J/m^2; \sigma = 45MPa; E = 75GPa$):

$$r_y = \frac{\pi}{8}\frac{EG}{\sigma^2} = 2.9mm \tag{2.36}$$

where r_y is the predicted size of the damage zone, it is clear that the presence of a K dominant region is unlikely in the fracture of composites and adhesive joints in beam-like geometries. The deviation of the mode II stresses from the singular fields are plotted in fig. 2.26. The extent of the mode II singular field does not seem to scale very well with the smallest characteristic dimension. For $\gamma = 5, 10$, the numerical field never deviates more than 10% from the singular field over the measured range. The r/h_c 10% deviation from the singular fields of the remaining cases are outlined in table 2.17 and they range from $5-15.8\%$ of the smallest beam height. These are of similar order to the mode I singular fields though it is not surprising that they are larger due to the nature of shear loading. However, despite the fact that the mode II loading produces larger K dominant regions in perfectly elastic materials, mode II loading is not in general more prone to experience a K dominant region in practice as it will be seen in the following sections that this mode II loading tends to produce significantly larger damage regions compared to mode I loading in the same material.

2.6 Orthotropic Material Properties

The final study in this chapter is to examine the effect of material orthotropy on the mixed mode partition. Up to now it has been assumed that the isotropic partitioning solutions offer a reasonable prediction for the mode mixity in composite laminates. The partitioning solutions of Williams [20] (W), Wang and Harvey [28] (WH) and Davidson et al. [27] (D-NSF) are based on Euler beam theory (W, WH) and classical plate theory (D-NSF) respectively and do not predict any dependence on material orthotropy. Suo et al. [47] obtained numerical solutions for the orthotropic cases by solving integral equations and found only a very weak dependence on material orthotropy. This is assessed here numerically by repeating the AFRMM test cases with orthotropic material properties.

2.6.1 Analytical Solution

Hooke's law for an elastic orthotropic material is outlined in eq. 2.37

$$\begin{Bmatrix} \epsilon_{11} \\ \epsilon_{22} \\ \epsilon_{33} \\ \epsilon_{23} \\ \epsilon_{31} \\ \epsilon_{12} \end{Bmatrix} = \begin{bmatrix} b_{11} & b_{12} & b_{13} & 0 & 0 & 0 \\ b_{21} & b_{22} & b_{23} & 0 & 0 & 0 \\ b_{31} & b_{32} & b_{33} & 0 & 0 & 0 \\ 0 & 0 & 0 & b_{44} & 0 & 0 \\ 0 & 0 & 0 & 0 & b_{55} & 0 \\ 0 & 0 & 0 & 0 & 0 & b_{66} \end{bmatrix} \begin{Bmatrix} \sigma_{11} \\ \sigma_{22} \\ \sigma_{33} \\ \sigma_{23} \\ \sigma_{31} \\ \sigma_{12} \end{Bmatrix} \tag{2.37}$$

where the $1, 2$ and 3 directions correspond to the principal axes of the material (x, y, z) as outlined in fig. 2.6. ϵ_{ij}, σ_{ij} and b_{ij} are the components of strain, stress and compliance respectively. The components of compliance are given by:

$$\begin{aligned} b_{11} &= \frac{1}{E_{11}}; \quad b_{12} = \frac{-\nu_{12}}{E_{11}}; \quad b_{13} = \frac{-\nu_{13}}{E_{11}}; \quad b_{44} = \frac{1}{\mu_{23}} \\ b_{21} &= \frac{-\nu_{21}}{E_{22}}; \quad b_{22} = \frac{1}{E_{22}}; \quad b_{23} = \frac{-\nu_{23}}{E_{22}}; \quad b_{55} = \frac{1}{\mu_{31}} \\ b_{31} &= \frac{-\nu_{31}}{E_{33}}; \quad b_{32} = \frac{-\nu_{32}}{E_{33}}; \quad b_{33} = \frac{1}{E_{33}}; \quad b_{66} = \frac{1}{\mu_{12}} \end{aligned} \tag{2.38}$$

for plane stress, where E_{ij} are the components of Young's modulus, ν_{ij} are the components of Poisson's ratio and μ_{ij} are the components of shear modulus. For plane strain, these compliance values are replaced by [63]:

$$b_{ij} \rightarrow b_{ij} - \frac{b_{i3}b_{j3}}{b_{33}} \tag{2.39}$$

It was stated by Suo et al. [47] that the stresses in an orthotropic medium should only depend on two non-dimensional elastic parameters (λ, ρ), which are given by:

$$\lambda = \frac{b_{11}}{b_{22}}; \quad \rho = \frac{2b_{12} + b_{66}}{2\sqrt{b_{11}b_{22}}} \tag{2.40}$$

The stress intensity factors are then given by:

$$\begin{aligned} K_I &= \frac{\lambda^{3/8}}{\sqrt{2n}}\Big(\frac{P}{\sqrt{h_1 U}}cos(\omega) + \frac{M}{\sqrt{h_1^3 V}}sin(\omega + \phi)\Big) \\ K_{II} &= \frac{\lambda^{1/8}}{\sqrt{2n}}\Big(\frac{P}{\sqrt{h_1 U}}sin(\omega) - \frac{M}{\sqrt{h_1^3 V}}cos(\omega + \phi)\Big) \end{aligned} \tag{2.41}$$

where M, P, U, V and ϕ are geometric factors and are as defined in chapter 1. n is a function of ρ and is given by:

$$n = \sqrt{\frac{1+\rho}{2}} \tag{2.42}$$

As with the isotropic solution, each value required in eq. 2.41 can be found explicitly except for ω. It is shown by Suo [46] that ω is a function of only ρ and γ. Suo [46] obtained values of ω for a range of values of ρ and γ by solving integral equations and the results are outlined in table 2.18. It is evident from table 2.18 that ω is only very

γ \ ρ	-0.5	0	1	2	3	4
0	51.0	51.7	52.1	52.2	52.2	52.3
0.5	50.4	50.4	50.9	51.1	51.1	51.7
1	49.1	49.1	49.1	49.1	49.1	49.1

TABLE 2.18: Values of ω in degrees as a function of γ and ρ [46].

weakly dependent on ρ and the isotropic approximation given in equation 1.10 offers an excellent approximation across a wide range of orthotropic material properties. Sih et al. [64] provided expressions for the relationship between SIFs and ERRs for an orthotropic material as:

$$\begin{aligned} G_I &= \Big(b_{11}b_{22}\frac{1+\rho}{2}\Big)\lambda^{-1/4}K_I^2 \\ G_{II} &= \Big(b_{11}b_{22}\frac{1+\rho}{2}\Big)\lambda^{1/4}K_{II}^2 \end{aligned} \tag{2.43}$$

By substituting the expressions for K_I, K_{II} given in eq. 2.41 into eq. 2.43, the mode partition G_{II}/G can be expressed as:

$$\frac{G_{II}}{G} = \left(\frac{\Big(\frac{P}{\sqrt{h_1 U}}cos(\omega) + \frac{M}{\sqrt{h_1^3 V}}sin(\omega+\phi)\Big)^2}{\Big(\frac{P}{\sqrt{h_1 U}}sin(\omega) - \frac{M}{\sqrt{h_1^3 V}}cos(\omega+\phi)\Big)^2} + 1\right)^{-1} \tag{2.44}$$

It is clear from equation 2.44 that the ERR partition will not be dependent on λ and will only be affected by material orthotropy in as much as ω is influenced by ρ. This influence has been shown to be very weak so it is expected that the overall effects of material orthotropy on the mixed mode partition will be negligible.

2.6.2 Case Setup

In the numerical test case carried out in this section, typical UD CFRP elastic properties are used, which are approximated as transversely isotropic. This means only five independent elastic properties are required instead of the usual nine for a general orthotropic material. These elastic properties are given in table 2.19. The AFRMM cases which are carried out are as outlined in figure 2.6. One simulation is carried out for each γ ratio using the refined mesh outlined in section 2.5 and figure 2.22 using plane strain

E_{11}	115 GPa
E_{22}	10 GPa
ν_{12}	0.3
ν_{23}	0.38
μ_{12}	4.6 GPa

TABLE 2.19: Values of elastic properties used.

quadratic CPE8 elements. The mixed mode partition is obtained numerically using the IDI technique. It is also possible to obtain an improved analytical estimation from the approximations presented in table 2.18. Using the elastic properties outlined in table 2.19, the value of ρ is 3.87 under plane strain conditions. Therefore, taking the solution for ω at $\rho = 4$ from table 2.18, the improved linear approximation of ω is given as:

$$\omega = 52.3 - 3.2\gamma \tag{2.45}$$

which is valid for $\gamma \leqslant 1$. Values for $\gamma \geq 1$ can be obtained by using $(1/\gamma)$ in place of γ in eqs. 1.8, 1.9 and 2.45, and swapping M_1 and M_2 in eq. 1.8 [36].

2.6.3 Results

The SIFs (K_I, K_{II}) and ERR (G) values obtained from IDI partitioning of the orthotropic specimens are outlined in table 2.27. The $\%G$ error is also calculated for each simulation. These errors are calcuted w.r.t. the analytical ERR (G), which is calculated from eq. 2.28 by replacing E with $(1/b_{11})$; for plane strain, E is therefore given by:

$$E = \frac{E_{11}}{1 - \nu_{13}\nu_{31}} \tag{2.46}$$

The mixed mode partitions, which are obtained from IDI partitioning, are presented in table 2.28. For comparison, the mode partitions obtained in section 2.5 from the isotropic simulations, which were also obtained using IDI partitioning, are also presented. Also presented in table 2.28 are both the isotropic and orthotropic analytical solutions (eq. 2.44) using the respective approximations for ω, which are given in eq. 1.10 and 2.45 for isotropic and orthotropic $\rho = 3.87$ materials respectively. These analytical solutions are plotted in figure 2.29 along with the numerical data.

2.6.4 Discussion

It is evident from table 2.27 that sufficiently accurate values of G are obtained from the IDI partitioning of orthotropic material properties ($< .015\%$ error). The numerical and

γ	$K_I\ Pa\sqrt{m}$	$K_{II}\ Pa\sqrt{m}$	$G\ (J/m^2)$	$\%G$ error
0.1	997544.3	-1370523	119.74	-0.01431
0.2	994024.8	-1371711	119.27	-0.00160
0.5	964108.7	-1379703	115.39	0.00009
1	892465.5	-1371567	104.85	0.00010
2	764111.1	-1300565	84.32	0.00019
5	552955.8	-1072637	50.48	0.00001
10	408425.5	-849827.4	29.80	0.00003

FIGURE 2.27: Values of K_I, K_{II}, G and $\%G$ errors obtained using IDI partitioning for the AFRMM test geometry and loadings outlined in fig. 2.6 for orthotropic material properties ($\rho = 3.87, \lambda = 0.1$).

	G_{II}/G - Numerical		G_{II}/G - Analytical	
γ	IDI ($\rho = 3.87$)	IDI ($\rho = 1$)	HS ($\rho = 3.87$)	HS ($\rho = 1$)
0.1	0.3748	0.3783	0.3794	0.3824
0.2	0.3768	0.3810	0.3848	0.3875
0.5	0.3941	0.3970	0.4012	0.4029
1	0.4286	0.4286	0.4285	0.4285
2	0.4792	0.4761	0.4719	0.4702
5	0.5444	0.5401	0.5362	0.5334
10	0.5789	0.5750	0.5739	0.5708

FIGURE 2.28: A comparison of G_{II}/G for orthotropic ($\rho = 3.87$) and isotropic ($\rho = 1$) material properties using both numerical(IDI) and analytical(HS) [46] techniques.

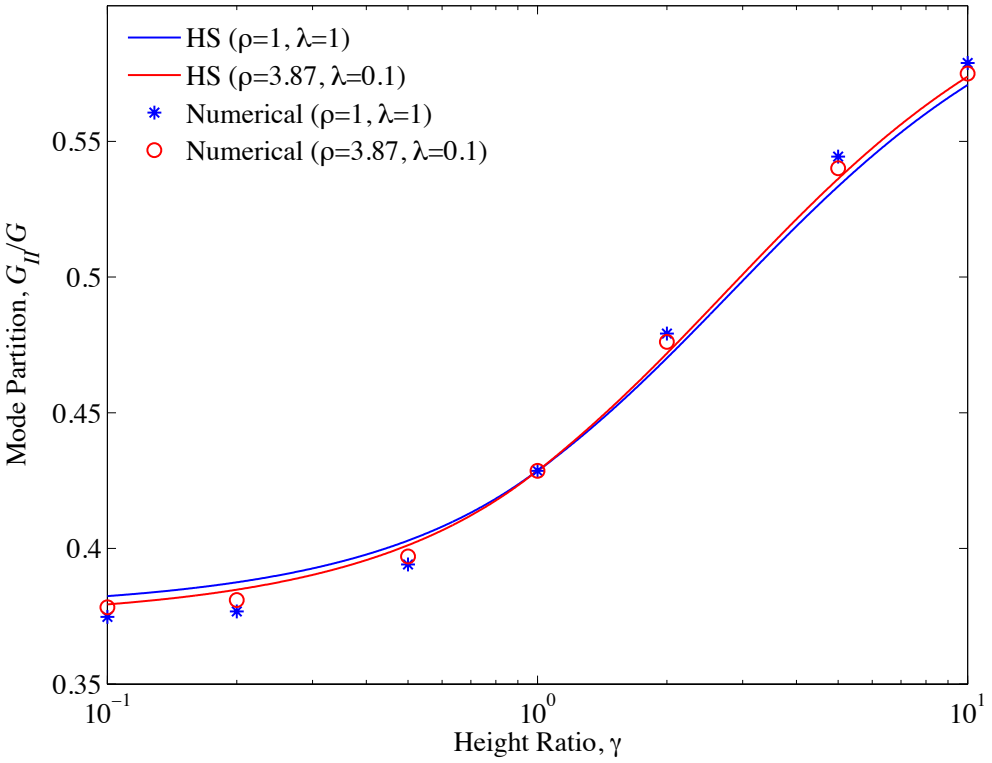

FIGURE 2.29: A comparison of G_{II}/G for orthotropic ($\rho = 3.87$) and isotropic ($\rho = 1$) material properties using both numerical(IDI) and analytical(HS) [46] techniques.

analytical mode partitions for isotropic ($\rho = 1$), and orthotropic ($\rho = 3.87$) materials are outlined in table 2.28 and figure 2.29. It is immediately noticeable from fig. 2.29 that the differences between the isotropic and orthotropic ($\rho = 3.87$) analytical predictions are almost negligible. Again, this is due to the very weak dependence of ω on ρ which was observed in table 2.18. This weak dependence is verified numerically as the differences between the isotropic and orthotropic solutions are also very small. Both the orthotropic and isotropic numerical solutions are close to the orthotropic analytical solution, which suggests that the differences between the solutions is small enough to lie within the range of error of the linear approximation. It is therefore concluded, in agreement with Suo [46], that the isotropic solution offers an excellent approximation for mixed mode partitions in elastic orthotropic composite laminates. As both the singular (HS) and global partitioning solutions (W) do not predict any effect of material orthotropy on the mode partition, the study on the effect of damage in chapter 3 can therefore be simplified to deal with isotropic substrates only.

2.7 Chapter Conclusions

In this chapter, the mixed mode partitioning of the asymmetric fixed ratio mixed mode (AFRMM) test is investigated as a function of beam height ratio and compared to the analytical solutions of Williams [20], Suo and Hutchinson [26], Wang and Harvey [28] and Davidson et al. [27]. Elastic properties are used in all cases and no crack propagation or damage is modelled. The virtual crack closure technique (VCCT), interaction domain integral (IDI) and mode decomposed J (MDJ) integral are all used to obtain numerical partitions. The background theory and application of each of these partitioning methods are presented and discussed.

In all initial cases, regular quadratic elements are used and converged values of the total ERR(G) and mode partition(G_{II}/G) are obtained by extrapolating to zero element size. It is found that each of the partitioning techniques (VCCT, IDI, MDJ) predict the correct ERR to a high degree of accuracy ($< .06\%$ error). Each numerical partitioning technique also predicts the same mixed mode partition up to the third significant digit. Most interestingly, this predicted partition is very close to the analytical prediction of Suo and Hutchinson [26], and it is evident that the other analytical solutions of Williams [20], Wang and Harvey [28] and Davidson et al. [27](CTE-NSF) should not be used to predict mode partitions in ideally elastic beam-like geometries. It is no surprise that the local solution of Suo and Hutchinson [26] performs so well in predicting the elastic mixed mode partitions as the assumptions made in the analytical analysis are matched in the numerical simulations. The main assumption is the presence of singular stress

fields at the crack tip, which is allowed to develop in the numerical simulations in the absence of any damage or cohesive zone.

The convergence pattern of the total ERR and mixed mode partition is also studied in detail for each of the numerical partitioning techniques. For regular quadratic elements, it is found that the total ERR is accurately predicted by the VCCT method for all mesh sizes ($< .01\%$ error), but the mode partition follows a non monotonic convergence pattern as the mesh size is reduced. A quadratic function was found to fit this convergence pattern. The total ERR obtained from the IDI technique was found to converge slowly towards the correct value in an almost linear manner as the mesh size was reduced, though errors of the order of $1-2\%$ were still present for the finest mesh simulation. It was found that at least ten elements were required across the minimum beam height to obtain ERR errors of less than 5%. The mixed mode partition exhibited a similar linear convergence pattern when using IDI partitioning. The MDJ partitioning technique was also found to require at least 10 elements across the smallest beam height to obtain accurate ERR values. This result was expected given the numerical integration procedure (trapezoidal rule). However, unlike the IDI techhnique, accurate values were obtained with the finest mesh simulation ($< 0.23\%$ error). The mode partition followed a fairly linear convergence pattern for the three finest mesh sizes in each case. In conclusion, it is seen that each method can produce accurate ERR and mode partition values using regular quadratic elements if the mesh size is reduced sufficiently and/or the results are extrapolated to zero element size. An extra simulation was carried out at $\gamma = 1$ to examine the effect of using singular elements at the crack tip. It was found that singular elements greatly increased the convergence rate of the IDI technique for both total ERR and mode partition. This was expected given the dependence of the IDI technique on the accuracy of crack tip singular stress fields. It was found that singular elements also increased the convergence rate of the mode partition using the MDJ partitioning, though the rate of ERR convergence remained unaffected. A modified VCCT approach is required to deal with singular elements and it was found that this technique did not converge to the correct ERR value (-0.6% error) and the mode partition converged to a different value compared to each of the other techniques. While the associated errors are small, it is recommended that singular elements are not used in conjunction with VCCT partitioning.

Also studied in this chapter is the extent of the region of K dominancy in each case. It is found that the mode I K dominant field scales with the smallest beam height and is the order of $2.5-4.5\%$ of the smallest beam height. With the use of a typical example, this range is shown to be very limiting and it is concluded that it is likely that there will be no mode I K dominant region present in the fracture of common composites

and adhesive joints. It will be shown in the following chapter that this will have very important implications for the estimation of the true mode mixity in common fracture tests. The extent of the mode II K field does not scale as well with the smallest beam height when $\gamma < 1$ and the region of K dominancy is larger than in mode I ($5 - 15.8\%$ of smallest beam height). However, it is noted that the damage region that develops under mode II loading is often considerably larger than in mode I so it is more likely that the K dominant region will be non-existent under mode II loading.

Finally, this chapter examines the effect of orthotropic material properties on the numerical mixed mode partition. It had been assumed up to this point that isotropic solution offers adequate accuracy for the prediction of mixed mode partitions in orthotropic composite laminates, as suggested by Suo [46]. It is seen that the analytical solution only changes slightly with the introduction of orthotropic material properties and this is validated here with numerical simulations. It is found that the change in mode partition due to material orthotropy is negligible and that the isotropic analytical solution offers an excellent approximation for mixed mode partitions in elastic orthotropic materials. As both the singular (HS) and global partitioning solutions (W) do not predict any effect of material orthotropy on the mode partition, it is reasonable to assume that material orthotropy will not effect the mode partition significantly when damage is introduced at the crack tip; the study on the effect of damage in chapter 3 is therefore simplified to examine isotropic substrates only.

Chapter 3

Numerical Partitioning: Cohesive Zones

3.1 Introduction

It has been seen in the previous chapter that the mode partitioning of linear elastic cases is accurately predicted by the local partitioning approach of Suo and Hutchinson [26]. However, it is also seen that the size of the K dominant region is only of the order of a few percent of the size of the substrate thickness. This is shown to be very restrictive in the fracture of current composite materials and structural adhesives where tough resins are commonly used. The toughening of resins, with the addition of particles or otherwise, often leads to the growth of significant damage regions [3, 65]. In the absence of a K dominant region, it is unclear how well the local partitioning solution will perform, given that this analytical solution assumes the presence of a singular field. In this chapter, damage is introduced at the crack tip using a cohesive zone model, and the effect of varying levels of damage on the mixed mode partition is studied in detail.

3.1.1 Chapter Layout

In the first part of this chapter, the use of cohesive zone models are reviewed and discussed. Based on this research, suitable cohesive zone models are chosen for use in this study and their formulations are outlined.

Secondly, the mode partitioning of cohesive zones is assessed using the MDJ technique, as before. This is implemented in two different forms; first by integration along an external path fully surrounding the cohesive zone ($J_{\Gamma_{ext}}$), and second by integrating over the

cohesive surfaces directly ($J_{\Gamma_{coh}}$). These are shown to be mathematically equivalent when the cohesive zone is propagating in a self similar manner in the absence of a crack tip singularity. Also, the integration of the energy going into the crack tip element (CTE) and the virtual crack closure technique (VCCT) is studied and compared to the previous partitioning techniques. This study avails of the fixed ratio mixed mode test (fig. 1.3 - $\gamma = 1, k = 0$), a case in which all partitioning theories agree. As the mode partition is known in advance, this allows the various partitioning techniques to be critically assessed.

Once an accurate partitioning technique is established, a parametric study is carried out to investigate the effect of various cohesive properties on the global mixed mode partition in asymmetric specimens. Both the asymmetric fixed ratio mixed mode(AFRMM) and asymmetric double cantilever (ADCB) test geometries are used in this study.

Finally, the effect of using a different cohesive zone formulation is studied. Up to this point, a coupled linear-softening cohesive zone formulation proposed by Camanho et al. [66] is used. An uncoupled Dugdale formulation developed by Yang et al. [67] is used in a number test cases to examine the effect of cohesive shape and formulation on the resulting mixed mode partition.

3.2 Cohesive Zone Models

3.2.1 Background

Cohesive zones have been used extensively to simulate fracture since the concept was first introduced by Dugdale [61] and Barenblatt [62]. Dugdale originally used this concept to study yielding behaviour in steel sheets due to the presence of a crack. It was assumed by Dugdale that all of the yielding took place in a thin strip ahead of the crack tip and could therefore be accurately represented by yielding along a line. The bounding stress was set to the yield stress of the material and it was assumed that the stress remained constant once the yield stress was reached. Barenblatt [62] used a similar approach to model atomic bonds and coupled this idea with equilibrium in an elastic body. Hillerborg et al. [68], using the same approach as Barenblatt [62], used this method at the macro scale to study the propagation of cracks in concrete, where the bounding stress was again equated to the tensile strength of the material. In contrast to linear elastic fracture mechanics, where the stress becomes singular at the crack tip, cohesive zones limit the stress which develops at the crack tip by introducing a predefined stress-displacement relationship, or cohesive law. This effectively creates an extended crack tip where the

surfaces are bounded by these cohesive stresses. Work must be done to separate these surfaces completely, according to the stress-displacement relationship, and this work can be equated to the fracture toughness of the material. This cohesive zone approach has been shown to be extremely useful in predicting failure in a wide range of materials such as concrete [68]; epoxies [65, 69]; polyethylene [70]; PMMA [71]; composites [72]; ceramics [73]; bone [74]; among others [75].

In almost all cases cases, the cohesive zone is phenomenological in nature in that it does not actually represent the true fracture mechanisms in a given material but instead smears all of the fracture processes into one line, or plane, and represents this entire process by a traction-displacement curve. This has contributed to the robustness of the cohesive zone approach as they can be used across many different scales to represent many different things. For example, they can be used at the nano scale to simulate the actual separation of atomic bonds, or they can be used at the macro scale to simulate the separation of adhesive joints [76, 77]. When the traction-displacement law is used on a macro scale to simulate failure of adhesive joints or composite laminates, it can represent a combination of many different processes, such as void formation and coalescence, crazing, shear banding, micro-cracking, fibre bridging or other local mechanisms which may occur depending on the structure of the adhesive or composite. It is therefore challenging to derive an exact cohesive law from physical considerations alone, and is not surprising that many different types of cohesive laws exist in the literature.

Two main families of cohesive zone laws exist in literature; those which are derivable from a potential function, and those which are not. Potential based mixed cohesive zones were first used by Needleman [78] to study particle debonding in an elastic-viscoplastic matrix. This model was further developed in Xu and Needleman [79] to allow for exponential softening curves in mode I and mode II. Tvergaard and Hutchinson [80] and Camacho and Ortiz [81] used a similar potential cohesive zone based on an effective displacement, though these were not formulated to simulate mode dependent fracture (i.e. where toughness is dependent on the mode of loading). Sørensen and Kirkegaard [82] proposed a method for directly measuring a general mixed potential function in composite laminates using a J integral approach. Starting with the potential, one can derive specific opening and shear traction-displacement relations by partially differentiating the potential function with respect to opening and shearing displacements respectively. However, there have been many concerns regarding the use of potential based cohesive zones, and these have been well documented [83–85]. In particular, they are known to produce non-physical negative energy dissipation under certain mixed mode loadings [84]. Another problem for the current work is that potential based cohesive zones are

not in general consistent with the definition of a failure locus outlined in chapter 1. i.e.:

$$G \neq f(\frac{G_{II}}{G}) \tag{3.1}$$

To illustrate these limitations of potential functions, a number of test cases are carried out using an example potential based cohesive zone in appendix A.

Other cohesive zones formulations that are not derivable from a potential are path dependent. That is, a different overall ERR may be achieved for each different opening path, even if the same final displacement is reached. That is not necessarily un-physical as many damage mechanisms such as plasticity and frictional sliding exhibit path dependence [86]. The most commonly used path dependent cohesive zone models are those developed by Camanho et al. [66], Turon et al. [87] and Alfano and Crisfield [88]. The Camanho et al. [66] formulation is implemented into finite element software Abaqus and the Alfano and Crisfield [88] formulation is implemented in to F.E. software Ansys. These cohesive zone formulations are similar in that the traction vector follows the displacement vector, also called truss-like [86], and the damage is introduced using a damage variable, which is incremented from zero to one as a function of the opening displacements. Each of these cohesive zone models follow a failure locus and therefore are consistent with the definitions of chapter 1. These models have been used to successfully predict mode dependent delamination in composite laminates [66, 88, 89].

The cohesive zone model developed by Camanho et al. [66] is used as the basis for the current study. In all cases, the cohesive zone is set up to linearly soften the effective stress as a function of the effective displacement and is referred to hereafter as the coupled linear-softening CZM. An uncoupled cohesive zone, developed by Yang et al. [67], which has been used extensively to accurately model failure in adhesive joints, is also used in the final part of this chapter to examine the effect of varying cohesive zone formulation and shape on the results. This is uncoupled in that the mode I and mode II cohesive shapes are fixed and these will be followed in each mode up until the point that a failure criterion is satisfied. There is therefore a weak coupling between both modes, but only to determine the point of failure and not to determine cohesive stresses. Due to the uncoupled nature of this cohesive zone, it is actually derivable from a potential function [86]. However, due to the explicit enforcement of a failure locus, it does not suffer from the same problems seen by general potential based cohesive zones (i.e. eq. 3.1). This cohesive zone is set up to follow the constant stress (Dugdale) shape and is referred to hereafter as the uncoupled Dugdale CZM. This cohesive zone is implemented as a user subroutine in Abaqus. The exact formulations of the two cohesive zones are outlined in the following sections.

3.2.2 Coupled Linear-Softening CZM [66]

Two different cohesive zone formulations are used in this study. The first cohesive zone, which is inbuilt into Abaqus, is used to model both the AFRMM and the ADCB test cases. The cohesive zone is based on the formulation proposed by Camanho et al. [66]. The formulation is shown graphically in fig. 3.1, and is set up to initiate under a quadratic stress criterion. i.e. when

$$\left(\frac{\langle t_N \rangle}{t_{NC}}\right)^2 + \left(\frac{t_S}{t_{SC}}\right)^2 = 1 \tag{3.2}$$

where t_N and t_S are the normal and shear stresses respectively in the cohesive zone and t_{NC} and t_{SC} are the chosen pure mode cohesive strengths in opening and shearing respectively. The quadratic stress criterion (eq. 3.2) has been used previously to accurately predict delamination onset in composite laminates [89, 90]. The Macauley bracket $\langle\rangle$ indicates that compressive normal stresses do not contribute to the criterion. i.e.:

$$\langle t_N \rangle = \begin{cases} 0, & t_N < 0 \\ t_N, & t_N \geq 0 \end{cases} \tag{3.3}$$

Up to the point of initiation, the response of the cohesive zone is uncoupled in opening and shear and governed by

$$\begin{bmatrix} t_N \\ t_S \end{bmatrix} = \begin{bmatrix} k_{yy} & 0 \\ 0 & k_{xx} \end{bmatrix} \begin{bmatrix} \delta_N \\ \delta_S \end{bmatrix} \tag{3.4}$$

where k_{xx} and k_{yy} are the initial penalty stiffnesses in the shearing and normal directions respectively, which are both set at 1e15 Pa/m in the current work. These penalty stiffnesses are required as the cohesive zone model is implicit in the finite element analysis, i.e. they form part of the global stiffness matrix. Recently some explicit cohesive zones have been developed for use in finite element analysis [83], and they have been used extensively in finite volume simulations [70, 71, 73]. Implicit cohesive zones are known to present problems for arbitrary crack simulations as the insertion of many layers of effective 'springs' can reduce the stiffness of the global structure. However, they do not present such problems for use as a single layer along a predefined crack path as in the current simulations. As stated in Turon et al. [91], these penalty stiffnesses lack physical meaning and are largely a numerical artefact for undamaged material points. They should be set high enough to provide reasonable stiffness but not too high to cause numerical difficulties [87, 92]. In other words, these stiffnesses should be set as high as

possible without causing numerical difficulties. A stiffness of 1e15 Pa/m was found to work well for the current simulations. In this current formulation, it is also required to set the stiffnesses equal in mode I and mode II directions to avoid unphysical behaviour under changing mode mix. This issue is addressed further in Appendix B.

After damage initiation, a linear softening law is effected using an overall damage variable D, which is incremented from zero to one as a function of the overall effective displacement, δ_{eff}, where $\delta_{eff} = \sqrt{\delta_N^2 + \delta_S^2}$, as:

$$D = \frac{\delta_{eff}^f(\delta_{eff}^{\max} - \delta_{eff}^0)}{\delta_{eff}^{\max}(\delta_{eff}^f - \delta_{eff}^0)} \tag{3.5}$$

where δ_{eff}^f is the effective displacement at final failure, δ_{eff}^0 is the effective displacement at damage initiation, and $\delta_{eff}^{\max}$ is the maximum effective displacement that has occurred up to that point in time. The cohesive tractions in the softening regime, which are coupled through D, are then computed from

$$\begin{aligned} t_N &= \begin{cases} (1-D)\bar{t}_N, & \text{if } \bar{t}_N \geq 0 \\ \bar{t}_N, & \text{if } \bar{t}_N < 0 \end{cases} \\ t_S &= (1-D)\bar{t}_S \end{aligned} \tag{3.6}$$

where $\bar{t}_N$ and $\bar{t}_S$ are the tractions predicted by the pre-damage stiffness matrix (eq. 3.4) at the current displacements. Along with pure mode cohesive strengths and penalty stiffnesses, it is also required to specify the mixed mode failure locus. The following linear criterion is used

$$\left(\frac{G_I}{G_{IC}}\right) + \left(\frac{G_{II}}{G_{IIC}}\right) = 1 \tag{3.7}$$

where G_I and G_{II} are the energies dissipated in mode I and mode II respectively up to that point in time, and G_{IC} and G_{IIC} are the prescribed pure mode cohesive toughnesses. The linear failure criterion has been used extensively to describe mixed mode failure loci [15, 93] in composites. While it has been shown to be more successful in describing failure loci in thermoplastic epoxy composites [15], it is required here to ensure mode independent fracture due to limitations of the cohesive zone formulation. Under certain conditions, this cohesive zone formulation has been reported to be thermodynamically inconsistent under variable mixed mode loading, which can result in incorrect energy dissipation [87, 94]. This is investigated and shown to be the case in appendix B. In order to avoid this situation, the linear failure criterion is used with the pure mode cohesive strengths and toughnesses set to be equal in all test cases. Though the overall

toughness ($G_I + G_{II}$) will not change as a function of mode mixity in these cases, it is still of interest to study the partition of energies as a function of cohesive properties.

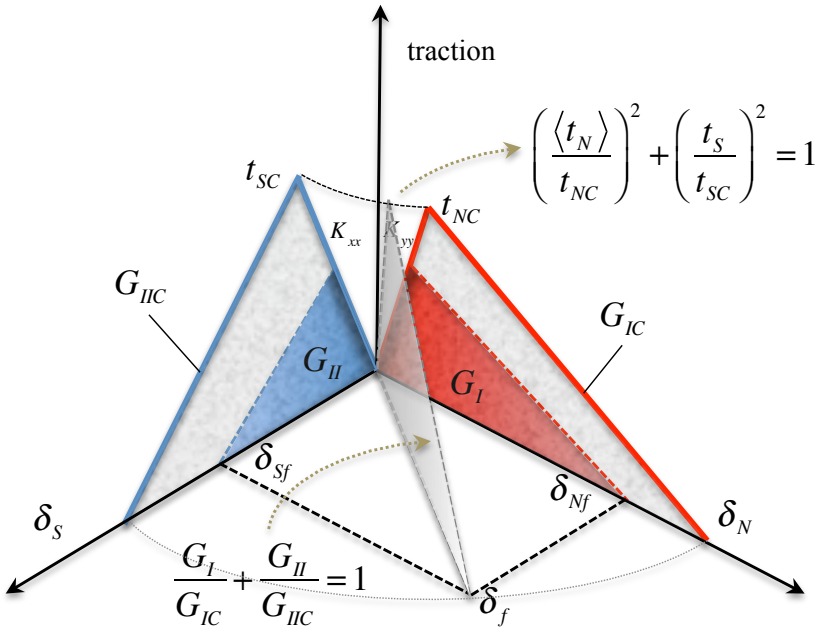

FIGURE 3.1: Coupled Linear-Softening Cohesive Zone Model

3.2.3 Uncoupled Dugdale (constant traction) CZM [67]

A second cohesive zone model is used to repeat the AFRMM test case in the final part of this chapter; this is an uncoupled formulation developed by Yang et al. [67], and is implemented as a user element (UEL) subroutine in Abaqus. This cohesive zone has been used previously by Parmigiani and Thouless [40] and Sills and Thouless [41] to study the effect of cohesive properties on mode mixity, and is used here for comparative purposes. The cohesive zone model is shown in fig. 3.2. Prior to damage initiation, the response of the element is equivalent to the coupled linear softening cohesive zone (i.e. eq. 3.4), and the penalty stiffnesses are also both set to 1e15 Pa/m. In this formulation, the stresses remain uncoupled and constant as they follow the prescribed pure mode Dugdale type laws exactly until the failure criterion is satisfied, at which point the stress is dropped suddenly to zero in both modes. The linear failure criterion (eq. 3.7) is also used in this formulation.

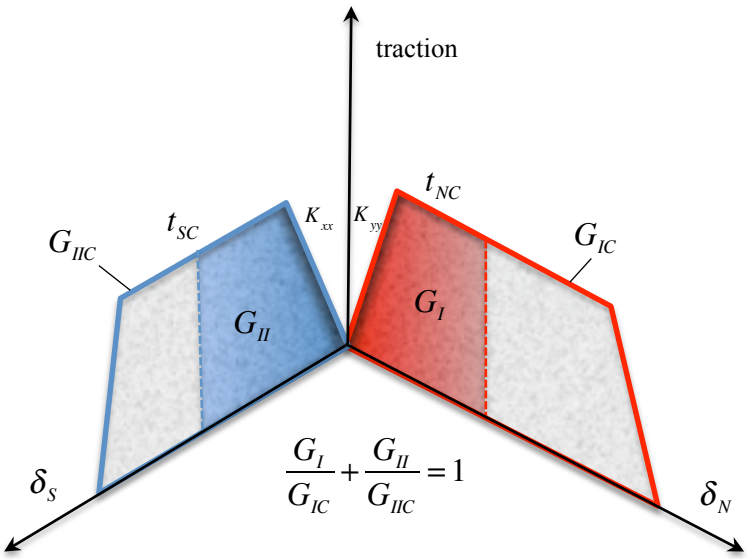

FIGURE 3.2: Uncoupled Dugdale Cohesive Zone Model

3.3 Partitioning techniques for Cohesive Zones

3.3.1 Introduction

In this section, a number of partitioning techniques are examined in order to determine an accurate method for partitioning fractures in the presence of cohesive zones. The FRMM test case is used as a benchmark test as the correct mode partition is known in advance. Firstly, the mode decomposed J integral (MDJ) proposed by Ishikawa et al. [45] is implemented in two separate forms. The first form is the same as that applied in chapter 2 where the integral is applied externally ($J_{\Gamma_{ext}}$); in this case the external path fully surrounds the cohesive zone. The second form is when the integral is applied over the cohesive surfaces ($J_{\Gamma_{coh}}$). It is shown in the following section that these two methods are equivalent when the damage zone is propagating in a self-similar manner in the absence of a singularity. These two methods are global in that they calculate the energy being released in mode I and mode II over the whole model. The third method is a local method and involves measuring the energy going directly into the crack tip cohesive element and is called the crack tip element (CTE) approach. The final method is the virtual crack closure technique, which has been applied to partition fractures in the previous chapter.

3.3.2 Partitioning Techniques

The following section outlines four methods used for partitioning a typical fracture process zone, as shown in fig. 3.3. The fracture process zone consists of a crack tip

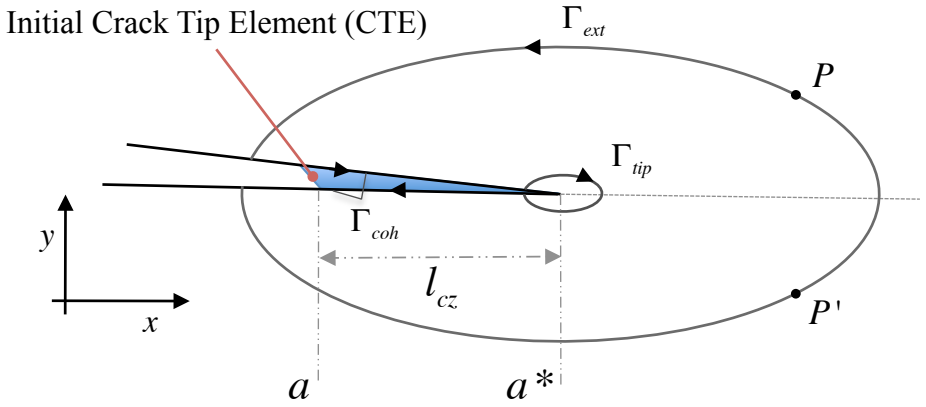

FIGURE 3.3: Fracture Process Zone.

located at a, where cohesive stresses drop to zero, and a damage zone tip located at a^*, where the quadratic initiation criterion (eq. 3.2) is satisfied. The distance between a and a^* is the cohesive zone length (l_{cz}). The following partitioning techniques are applied in this section:

3.3.2.1 MDJ integral applied externally ($J_{\Gamma_{ext}}$)

When the damage region is propagating in a self similar manner under monotonic loading between linear elastic beams, the concept of energy release rate G can be related to the path independent J integral proposed by Rice [55]. It was shown by Rice [55] that the J integral computed over any arbitrary closed contour in an elastic body is zero. For the fracture process zone shown in fig. 3.3, this can be described as:

$$J_{\Gamma_{ext}} + J_{\Gamma_{coh}} + J_{\Gamma_{tip}} = 0 \tag{3.8}$$

where Γ_{ext} is a path going continuously from a point on the lower fully cracked face to the upper fully cracked face around the crack tip, Γ_{coh} corresponds to a path along the upper and lower surfaces of the active cohesive zone and Γ_{tip} corresponds to an infinitely small path surrounding the crack tip. The J integral is computed from eq. 2.6. By applying the J integral externally along Γ_{ext}, it is possible to account for energy contributions from the cohesive surfaces ($J_{\Gamma_{coh}}$) and crack tip singularity ($J_{\Gamma_{tip}}$). A method

for decomposing the J integral into mode I and mode II components was presented in chapter 2. This method, proposed by Ishikawa et al. [45], is also directly applicable to partitioning fractures where cohesive zones are present. As before, the mode decomposition is achieved by considering symmetric integration paths about the crack plane. i.e. paths containing P and P' in fig. 3.3. The stress, strain and displacement fields are decomposed into symmetric (causing mode I) and antisymmetric (causing mode II) components according to eq. 2.23. The respective decomposed stress, strain and displacement values, i.e. $(\sigma_{ij}^I, \epsilon_{ij}^I, u_i^I)$, $(\sigma_{ij}^{II}, \epsilon_{ij}^{II}, u_i^{II})$, are then substituted directly into eq. 2.6 to calculate the decomposed J integral components (J_I, J_{II}). These are given by:

$$\begin{aligned} J_{I_{\Gamma_{ext}}} &= \int_\Gamma \Big(\int_0^\epsilon \sigma_{ij}^{(I)} d\epsilon_{ij}^{(I)} dy - \sigma_{ij}^{(I)} n_j \frac{\partial u_i^{(I)}}{\partial x} ds \Big) \\ J_{II_{\Gamma_{ext}}} &= \int_\Gamma \Big(\int_0^\epsilon \sigma_{ij}^{(II)} d\epsilon_{ij}^{(II)} dy - \sigma_{ij}^{(II)} n_j \frac{\partial u_i^{(II)}}{\partial x} ds \Big) \end{aligned} \tag{3.9}$$

3.3.2.2 MDJ integral applied along cohesive surfaces ($J_{\Gamma_{coh}}$)

In cases where the crack tip singularity is suppressed by the cohesive zone (i.e. $J_{tip} = 0$), the J integral applied externally is equal to the J integral applied over the cohesive surfaces. i.e.

$$J_{\Gamma_{ext}} = -J_{\Gamma_{coh}} \tag{3.10}$$

In cases where eq. 3.10 is satisfied and the fracture process zone is propagating in a self similar manner, the mode decomposed ERR components can be found directly by integrating over the cohesive surfaces, as the mode decomposed J integral reduces to

$$\begin{aligned} J_{I_{\Gamma_{coh}}} &= \int_{\Gamma_{coh}^+} t_N \frac{\partial \delta_N}{\partial x} ds \\ J_{II_{\Gamma_{coh}}} &= \int_{\Gamma_{coh}^+} t_S \frac{\partial \delta_S}{\partial x} ds \end{aligned} \tag{3.11}$$

where t_N, t_S, δ_N and δ_S are the normal and shear cohesive tractions and opening displacements respectively. Γ_{coh}^+ indicates that the integration only needs to be performed over one surface, which arises due to the symmetry of stresses on the upper and lower cohesive surfaces.

3.3.2.3 Local crack tip element approach (CTE)

This local approach monitors the energy which goes into the initial crack tip element over time as it fails. The energies are calculated by integrating the area under the

respective normal and shear traction separation curves of the first cohesive element, as indicated by the red and blue shaded regions in fig. 3.1 respectively. These integrals are given by:

$$G_{I_{CTE}} = \int_0^{\delta_{Nf}} t_N d\delta_N$$
$$G_{II_{CTE}} = \int_0^{\delta_{Sf}} t_S d\delta_S \tag{3.12}$$

where δ_{Nf} and δ_{Sf} are the normal and shear displacements at final failure, as indicated in fig. 3.1.

3.3.2.4 Virtual Crack Closure Technique (VCCT)

As a method of comparison, VCCT is applied to monitor the energy release rate and mode partition at the crack tip. The VCCT approach is outlined in chapter 2 and is calculated using eq. 2.5. The nodal forces are obtained from the continuum elements directly above and below the first cohesive element at the crack tip, and the opening displacements are obtained directly behind the crack tip as before (2.3). It is not believed that this method will produce accurate results once damage initiates at the crack tip as it can not account for dissipated energy.

3.3.3 Case Setup

The beam in fig.D.1(b) is set up and meshed in ABAQUS using plane strain quadratic elements (CPE8). A structured orthogonal mesh is used with an element size of 0.1 mm.

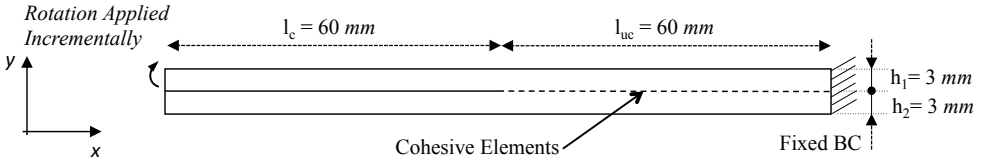

FIGURE 3.4: Fixed Ratio Mixed Mode (FRMM).

This ensures 30 elements across the beam thickness, which is more than sufficient to accurately model stress gradients due to bending. Zero thickness linear-softening cohesive elements (COH2D4), as described in section 3.2.2, are placed in the un-cracked region. The length of the cohesive elements were also 0.1 mm, which ensured exact nodal ties between the substrates and the cohesive zone. This element size was chosen to ensure at least 10 elements spanned the active cohesive zone [95]. The constitutive thickness, B, is

set at the default of 1 m. The substrate stiffness is assumed linear elastic and isotropic, with a Young's modulus E of 50 GPa, the mode I and mode II toughnesses (G_{IC}, G_{IIC}) are both set to $200J/m^2$, and the opening and shear strengths (t_{NC}, t_{SC}) are both set to 45 MPa. The quadratic initiation criterion (eq. 3.2) and the linear failure locus (eq. 3.7) are used. The beam is built in at the un-cracked end and a pure rotation is applied to the top beam of the cracked end. The pure rotation is effected through a rigid surface, which is tied to the end of the loaded beam. The rotation required to cause crack propagation(Θ_c) is worked out from elementary beam theory. The rotation required to initiate fracture is given by:

$$\Theta_c = \frac{M_c}{E}\Big(\frac{l_c + x}{I_1} + \frac{(l_{uc} - x)(1 + k)}{I_1 + I_2}\Big) \tag{3.13}$$

where M_c is the moment required to apply an ERR equal to the cohesive toughness; M_c can be obtained by substituting $G = 200J/m^2$ in eq. 2.28; l_c and l_{uc} are the initial cracked length and uncracked lengths of the specimen, x is a measure of the crack growth length (initially at 0), and I_1 and I_2 are the second moment of area for the upper and lower beams in fig. D.1(b). i.e.:

$$I_1 = \frac{Bh_1^3}{12}; \quad I_2 = \frac{Bh_2^3}{12} \tag{3.14}$$

A rotation of $1.5 \times \Theta_c$ is applied to make sure steady state fracture occurs.

There are two distinct stages throughout the loading that can be explained by referring to eq. 3.13; Initially as Θ is increased, the applied moment M increases proportionally until M_c is reached. At this point, the cohesive surfaces cannot sustain any further increase in M and so the applied moment remains constant at M_c. However, as Θ is increased beyond Θ_c, something else must give. Looking at eq. 3.13, in order to increase the RHS, x must increase (as I_1 is the smallest denominator). Therefore, after the critical moment is reached, the crack length grows proportionally with the applied rotation, which results in a steady state crack growth. This is shown graphically in fig. 3.5 and very good agreement is obtained between the analytical predictions of eq. 3.13 and the numerical measurement of moment and crack length for the current simulation. There is a slight offset in the prediction of the crack growth, and this can be attributed to the fact that the analytical solution does not account for the presence of a cohesive region ahead ahead of the crack tip.

Once steady state fracture occurs $(\Theta/\Theta_c > 1)$, each individual cohesive zone element ahead of the crack tip will go through the same loading history. Therefore, if the local approach is applied to an element which experiences the fully developed FPZ passing by,

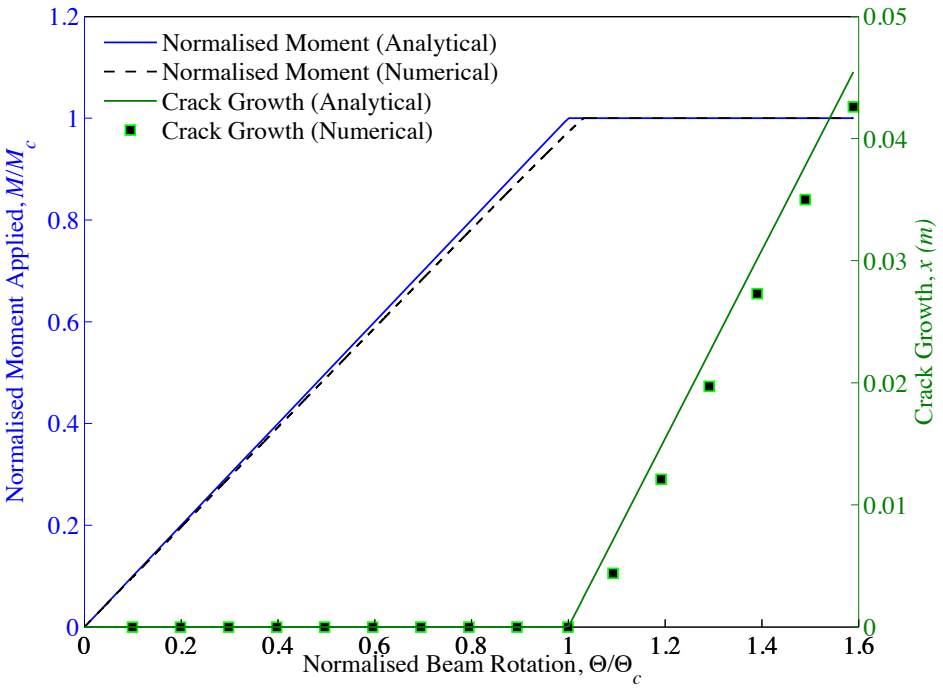

FIGURE 3.5: Normalised moment (M/M_c) and crack growth length (x) plotted as a function of normalised beam rotation Θ/Θ_c (Analytical and Numerical) for the FRMM test outlined in fig. D.1(b).

theoretically it must give the same mode partition as an instantaneous global approach. However, the initial crack tip element does not experience a steady state FPZ passing by as it will have already started to damage before the steady state damage region has fully formed; it is therefore of interest to study the partition of energies going into this element up to $\Theta/\Theta_c = 1$ (when it fails) to see how it compares to the global partition and analytical approaches.

Each of the three partitioning techniques outlined in the previous section are therefore applied to analyse the mixed mode partition during damage development at the crack tip ($0 < \Theta/\Theta_c \leq 1$). These are then compared to the analytical solution for mode mixity and energy release rate. The analytical ERR can be obtained from beam theory and is given by eq. 2.28. The mode mixity for this symmetric case is also known to be exact and each of the partitioning theories predicts this. Interestingly, it is possible to obtained a closed form solution for the mode mixity in the symmetric specimens with pure moments applied, which equals the solutions predicted in fig. 1.4, by theoretically applying the mode decomposed J integral around an external boundary.

3.3.4 Results

The mode partitioning results of each method are plotted in fig. 3.6. The mode partitions are plotted throughout the damage development and compared to the analytical mode partition, which has a value of $G_{II}/G = 3/7 = 0.4286$ for this FRMM case[20, 26]. At $\Theta/\Theta_c = 1$, the damage region is fully developed and begins to propagate in a self similar manner, and therefore results from $J_{\Gamma_{ext}}$ and $J_{\Gamma_{coh}}$ approaches do not change after this. As the CTE approach monitors the energy going into the first cohesive element, this element fails completely at $\Theta/\Theta_c = 1$ as the crack begins to propagate. The energy accounted for by each method ($G = G_I + G_{II}$) is plotted in fig. 3.7. This energy is normalised w.r.t. the applied energy release rate G_{app}. The applied ERR G_{app} is calculated at each time point using 2.28, where the instantaneous applied moment (M_1) is obtained directly from the numerical results by integrating the stress distribution in the loaded beam.

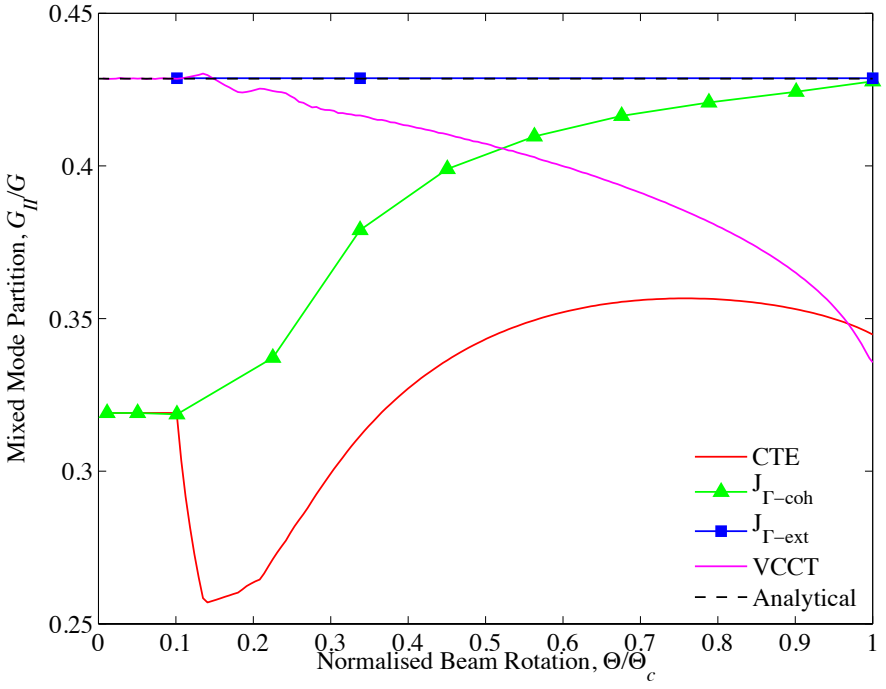

FIGURE 3.6: Mixed mode partition obtained from various partitioning techniques during FPZ development in the Fixed Ratio Mixed Mode (FRMM) test.

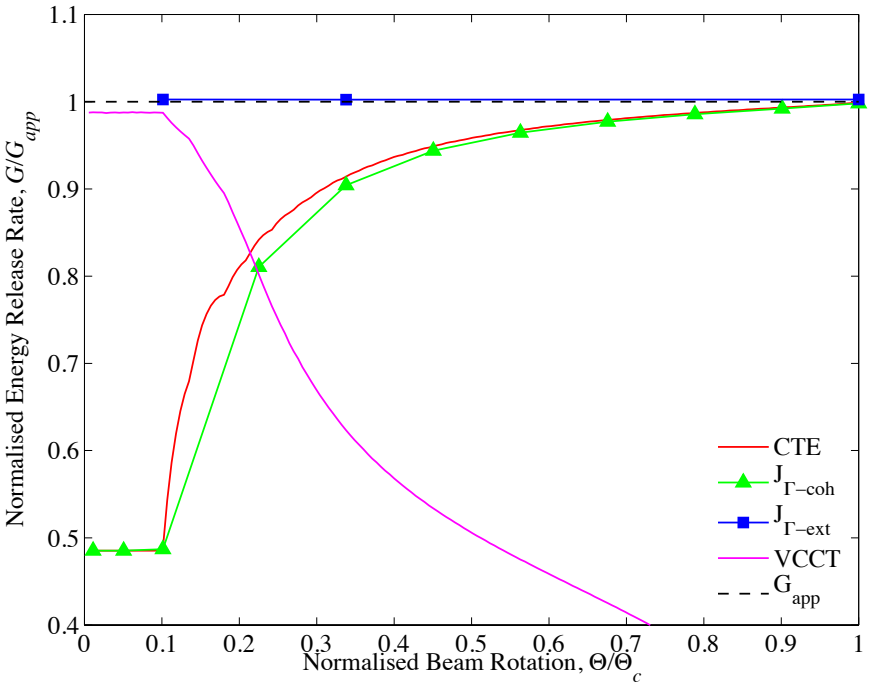

FIGURE 3.7: Total ERR obtained from various partitioning techniques during FPZ development in the Fixed Ratio Mixed Mode (FRMM) test.

3.3.5 Discussion

Throughout the entire development of the fracture process zone (FPZ), the local CTE approach does not predict the analytical partition of energies. At final failure of this element ($\Theta/\Theta_c = 1$), the overall mode partition of energies G_{II}/G over time is equal to 0.34, significantly different from the analytical mode partition of 0.4286. One might be inclined to think that this failure to reproduce the analytical solution is an error associated with the cohesive zone element. However, this is not the case. The difference between the CTE partition at crack initiation (Θ/Θ_c) = 1 and the analytical partition may be explained by the fact that each element in the developing FPZ experiences different loading conditions (e.g. initial crack tip has only traction free surfaces behind when it is loaded, whereas an element further ahead has an active cohesive zone behind when it is first loaded). The displacement ratios (normal vs. shear) are plotted for the initial cohesive element (CTEL) and an element which experiences steady state fracture (SSEL) (located 10 mm ahead of the original crack tip) in fig. 3.8. It is evident from this plot that the elements undergo different loading histories. The initial crack tip element (CTEL) opens at almost a constant displacement ratio, whereas the element experiencing steady state (SSEL) initially experiences more shear displacement. The corresponding normal and shear stress-displacement curves for both the CTEL and SSEL are shown in

fig. 3.9. It is clear that the different loading history leads to different stress-displacement relationships in both normal and shear, which is the reason a different mode mix is predicted locally during damage development. Therefore, monitoring a single element locally in time will not produce an accurate global mode partition when the fracture process is not in steady state. Initially, integration over the cohesive surfaces ($J_{\Gamma_{coh}}$)

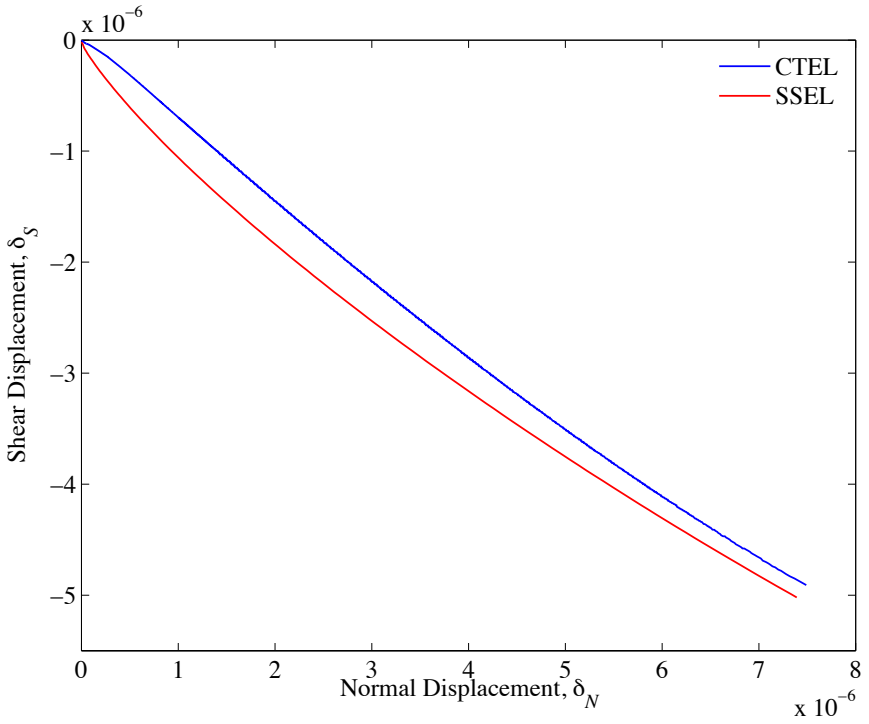

FIGURE 3.8: Displacement ratio for the crack tip element (CTEL) and element 10 mm ahead of the crack tip that experiences steady state fracture (SSEL).

does not predict the correct mode partition of energies either. However, as the damage zone develops, the mode partition moves towards the analytical solution and predicts the correct partition at crack initiation. This is explained by considering the energy contributions from each method. As the damage region develops, it is seen in fig. 3.7 that the total ERRs predicted by both the $J_{\Gamma_{coh}}$ and CTE approaches make up only a fraction of the applied energy (some of which is stored in the changing elastic fields surrounding the crack tip). Therefore, partitioning using these methods will not give the correct global partition of energies during damage development. Once the damage region is fully developed, no more energy goes into changing elastic fields surrounding the crack tip and all of the energy is absorbed only by the cohesive surfaces. Therefore, integrating along the cohesive surfaces yields the correct ERR and mixed mode partition at $\Theta/\Theta_c = 1$.

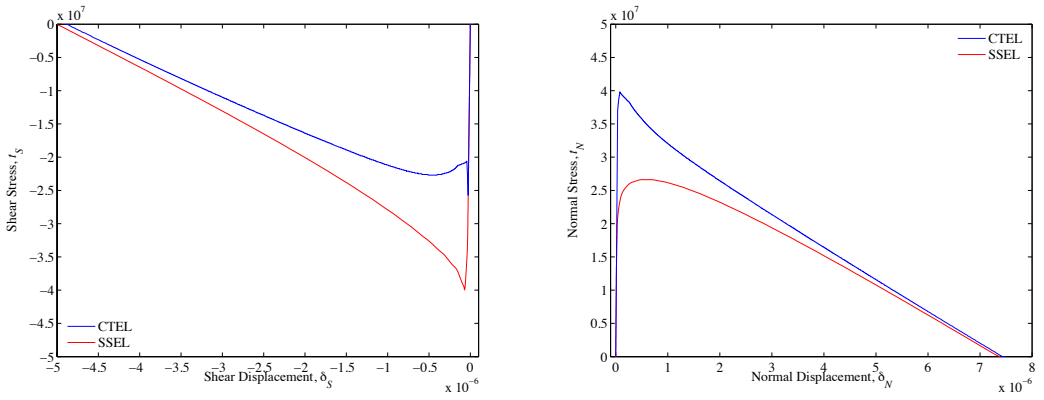

(a) Shear traction vs. shear displacement.

(b) Normal traction vs. normal displacement.

FIGURE 3.9: Normal and shear traction-displacement curves for crack tip element (CTEL) and element 10 mm ahead of the crack tip that experiences steady state fracture (SSEL).

By applying the J integral externally, it is possible to account for the energy stored in the elastic singular fields surrounding the crack tip, and the energy stored in the cohesive surfaces, according to eq. 3.10. As expected it can be seen in fig. 3.6 and fig. 3.7 that the external J integral accurately predicts the mixed mode partition and applied energy release rate throughout all stages of loading.

As expected, the VCCT method initially produces accurate mode partitions; however, once damage initiates (i.e. when stresses in the initial cohesive element first begin to soften; this occurs at $\Theta/\Theta_C \approx 0.1$ - fig. 3.6), the VCCT partitioning suddenly becomes inaccurate. This can be explained by studying the energy that VCCT accounts for during damage development (fig. 3.7); up to damage initiation, VCCT accurately accounts for the applied ERR; however, after damage initiation it no longer accounts for the total applied ERR, and hence the mode partition will not be valid. It is therefore clear that VCCT can not be used to partition the current cases, where the effect of damage on the resulting mode partition is required.

3.3.6 Conclusion

In conclusion, a number of common numerical partitioning approaches were tested for accuracy and/or appropriateness against the benchmark of the FRMM test. The CTE approach was found to produce a different partition than the known analytical partition. This was attributed to the fact that all of the elements in a developing damage region undergo a different loading history, and while globally the mode partition is correct, there is no requirement that locally this has to be the case. Integration along the cohesive

surfaces ($J_{\Gamma_{coh}}$) was initially found to give an incorrect mixed mode partition during damage development, but this could be explained by the fact that it does not account for all of the applied energy. At the point of crack initiation, it was found to give the same partition as the mode decomposed J integral ($J_{\Gamma_{ext}}$).

The external mode decomposed integral ($J_{\Gamma_{ext}}$) always captures the correct total ERR and mode partition regardless of crack tip condition, i.e. developing damage region or steady state. However, as it is numerically cumbersome to apply the external J integral in all cases in order to obtain the correct mixed mode partition, integration along the cohesive surfaces ($J_{\Gamma_{coh}}$) is deemed to be the most straightforward approach to numerically partition cohesive zones. There is just one limitation with this approach and that is that it must only be applied when the crack has initiated and is propagating in a steady steady state manner (i.e. $\Theta/\Theta_c > 1$). This condition is satisfied in all of the following test cases before the mixed mode partition is calculated.

Finally, it was found that the VCCT partitioning did not produce accurate partitions once damage started to develop at the crack tip. Though it initially captured the applied ERR and correct mode partition before damage initiation, it is clear that this method should not be used to obtain total ERR and mode partitions in the presence of cohesive zones.

3.4 Mixed Mode Partitioning of Asymmetric Geometries

3.4.1 Introduction

As a suitable mode partitioning method is now established, the current section deals with mode partitioning in asymmetric geometries as a function of cohesive properties. As discussed previously, a number of analytical solutions exist for this problem but there is considerable disagreement between the predicted mode partitions for asymmetric specimens [20, 26–28]. The predicted mode partitions from various analytical solutions for the AFRMM and ADCB tests are outlined in fig. 3.10. The partitioning theories shown are from Williams [20](W), Suo and Hutchinson [26](HS), Davidson et al. [27](D-NSF) and Wang and Harvey [28](WH). It was seen in the previous chapter that the local partitioning solution of Suo and Hutchinson [26] was the most appropriate for partitioning fractures in the absence of any crack tip damage. The aim of this current study is to determine which, if any, of these partitioning theories is the most appropriate to partition fractures in the presence of damage development at the crack tip.

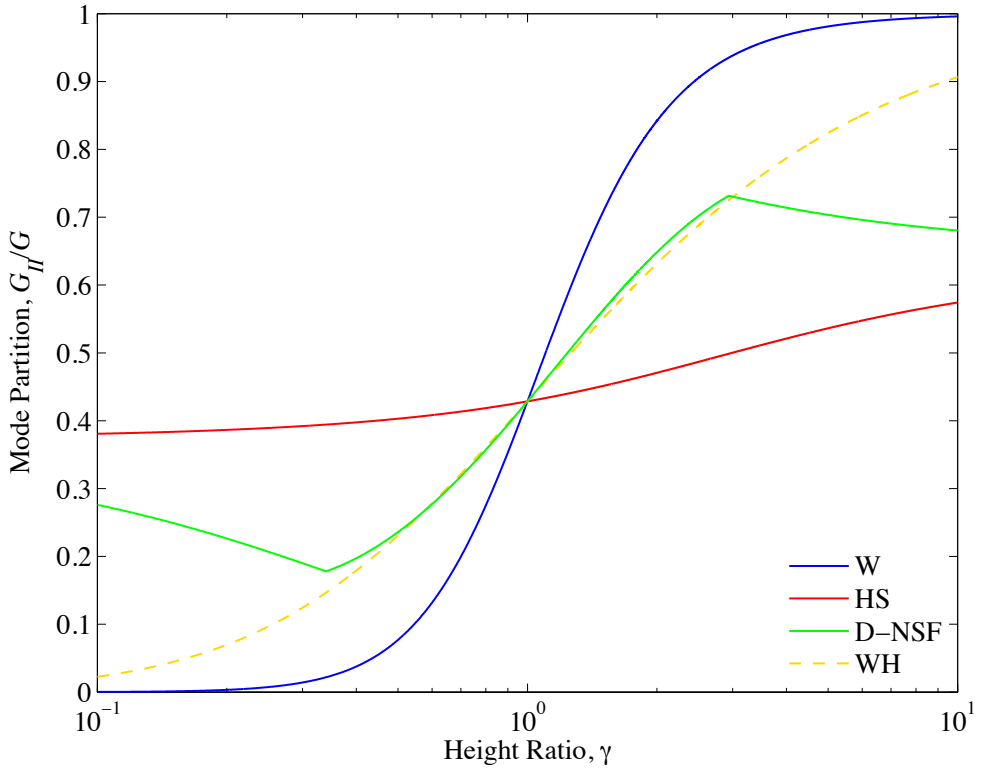

(a) Asymmetric Fixed Ratio Mixed Mode (AFRMM)($k = 0$).

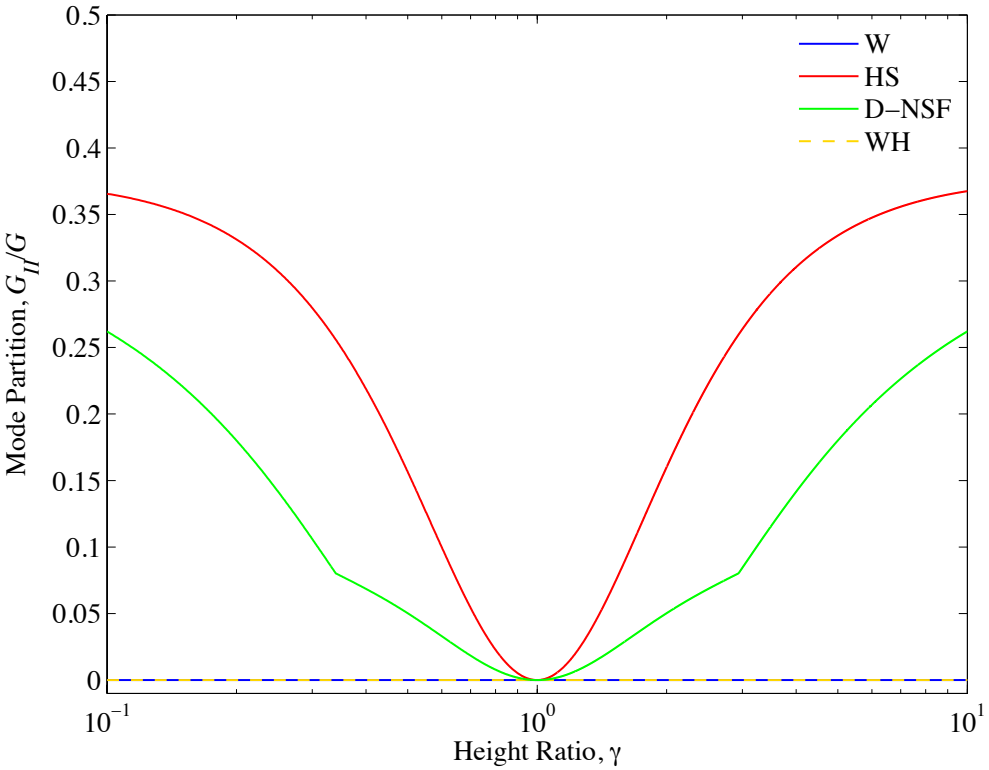

(b) Asymmetric Double Cantilever Beam (ADCB) ($k = -1$).

FIGURE 3.10: Mixed Mode Partitioning Theories.

3.4.2 Test Case Setup

Both the asymmetric fixed ratio mixed mode (AFRMM) (fig. 3.11(a)) and the asymmetric double cantilever (ADCB) (fig. 3.11(b)) test geometries are used in this work. In each test case, the beam geometry is meshed with a regular grid of 2D plane strain,

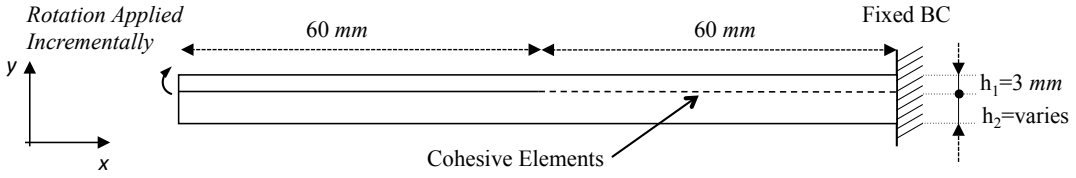

(a) Asymmetric Fixed Ratio Mixed Mode (AFRMM).

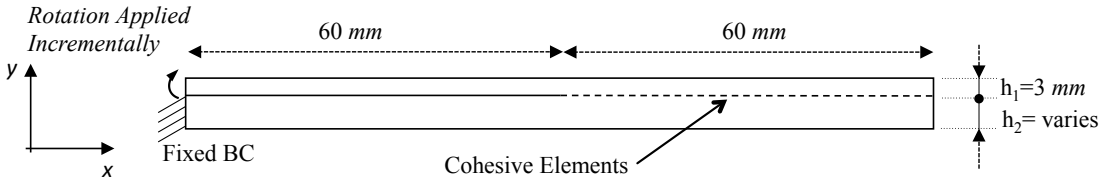

(b) Asymmetric Double Cantilever Beam (ADCB).

FIGURE 3.11: Beam Geometries and Loading Conditions.

8 node quadratic elements in Abaqus. As in the previous section, the beam material is assumed linear elastic and isotropic, with a Young's modulus of 50 GPa and a Poisson's ratio of 0.38. Loading is achieved through a fixed rotation, which is applied to a rigid surface that is tied to the end of the loaded beam. A rotation boundary condition is preferred as it induces a pure bending moment and also allows the crack to propagate in a numerically stable manner when the damage region is fully developed. This boundary condition also mimics the pure moment loading that is assumed in the analytical partitioning theories. Cohesive elements are inserted along the crack plane in the undamaged region as indicated in fig. 3.11. As in the previous section, a rotation, Θ, is incrementally applied to the top beam from $\Theta = 0$ to up to $\Theta = 1.5 \times \Theta_c$ in each case to ensure steady state fracture is achieved. In the initial test cases, only the coupled linear-softening formulation proposed by Camanho et al. [66] is considered. However, a comparative study is carried out at the end of this section on the AFRMM test with the uncoupled Dugdale CZM formulation. The particular test case properties for both the AFRMM and ADCB test cases are as follows:

3.4.2.1 AFRMM

The geometry, loading and boundary conditions used in the AFRMM test case can be seen in fig. 3.11(a). The loading and boundary conditions are the same as those in the previous section, with only the geometries and cohesive properties changing. Seven different γ ($\gamma = h_1/h_2$) ratios are simulated corresponding to $0.1, 0.2, 0.5, 1, 2, 5$ and 10. In each of the test cases, the mode I and mode II cohesive toughnesses (G_{IC}, G_{IIC}) are set equal (i.e. $G_C = G_{IC} = G_{IIC}$), as are the normal and shear cohesive strengths (i.e. $t_C = t_{NC} = t_{SC}$). Therefore, along with the beam height ratio, the only properties which are varied in this study are the cohesive strength t_C and cohesive toughness G_C. For each γ ratio, the cohesive toughness is set to values of 200 and 3000 J/m^2, and for each of these toughness values, three different cohesive strengths are simulated, corresponding to 20 MPa, 45 MPa and 95 MPa. This results in a total of 42 cases.

3.4.2.2 ADCB

The geometry, loading and boundary conditions used in the ADCB test case can be seen in fig. 3.11(b). In this case, one cracked arm is fixed and the other cracked arm is rotated as before using a rigid surface. The un-cracked end is left unconstrained. This boundary condition ensures that equal and opposite moments are induced in the substrate arms. Four different γ ratios are simulated, corresponding to $0.2, 0.5, 2$ and 5. As in the AFRMM test case, two toughness values of 200 and 3000 J/m^2 are simulated using the coupled linear softening CZM at each γ ratio, and for each of these toughness values, three different cohesive strengths are simulated, corresponding to 20 MPa, 45 MPa and 95 MPa. This results in a total of 24 cases.

3.4.3 Post Processing

For each case, the simulation is stopped at $\Theta/\Theta_c = 1.5$. At this point, a path is created along the cohesive surface and the opening and shear stress and strain components are printed from each node. A check is performed to ensure that the cohesive zone has initiated and is propagating, but has not yet reached the end of the beam. As the constitutive thickness of the cohesive zone is set to 1 m, the strain output is equal to the relative normal and shear displacements (δ_N, δ_S). The constitutive thickness can differs from the actual thickness, which is set to zero, and is required to have a finite value for numerical reasons (strain calculation); the value of the constitutive thickness does not effect the response of the element. A typical output of stresses and relative

displacements from the cohesive path is shown in fig. 3.12. It can be seen that up until the point of damage initiation (at a^*), the displacements are effectively zero (due to penalty stiffnesses of $1e15Pa/m$). At the point of cohesive failure (at a), the cohesive stresses simultaneously drop to zero and the element is deleted from the simulation. The mode I and mode II ERR components are obtained by integrating over this path using eq. 3.11. The cohesive zone length ($l_{cz} = a^* - a$) is also recorded in each case.

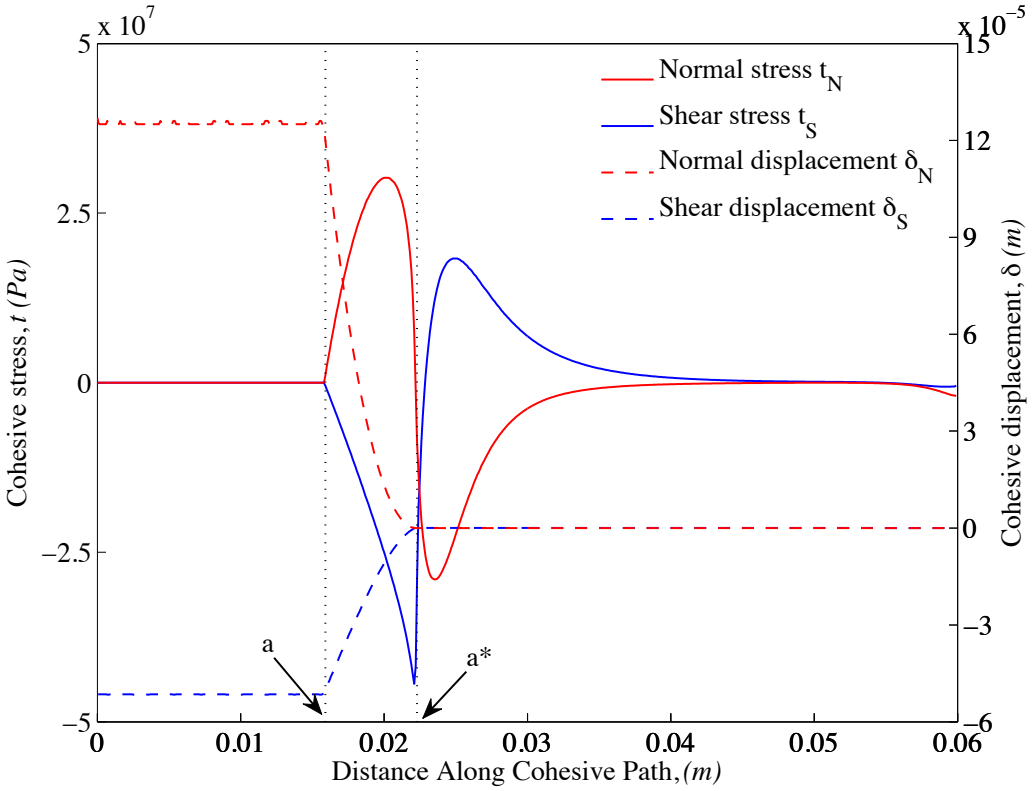

FIGURE 3.12: Typical stress and displacement profile along the cohesive zone during steady state propagation during AFRMM test ($\gamma = 0.1, t_c = 45MPa, G_c = 3000J/m^2$).

3.4.4 Results and Discussion

3.4.4.1 AFRMM

The numerical partitioning of the AFRMM test case, modelled with the coupled linear-softening CZM, is presented in fig. 3.13, and compared to the analytical partitioning theories. For $\gamma = 1$, each of the analytical partitioning theories agree and the cohesive zone solutions accurately predict this partition for all cohesive properties. When $\gamma \neq 1$, it is evident that the mixed mode partition is dependent on the cohesive properties and in all cases the solution lies between the local solution of Suo and Hutchinson [26] and the

global solution of Williams [20]. For high strengths and low toughnesses, the predicted mode partition lies close to the local partitioning solution of Suo and Hutchinson [26] and as the toughness is increased and/or the strength is decreased, the mode partition moves towards the global solution of Williams [20]. In general the numerical solution cannot be accurately predicted by any of the analytical partitioning theories.

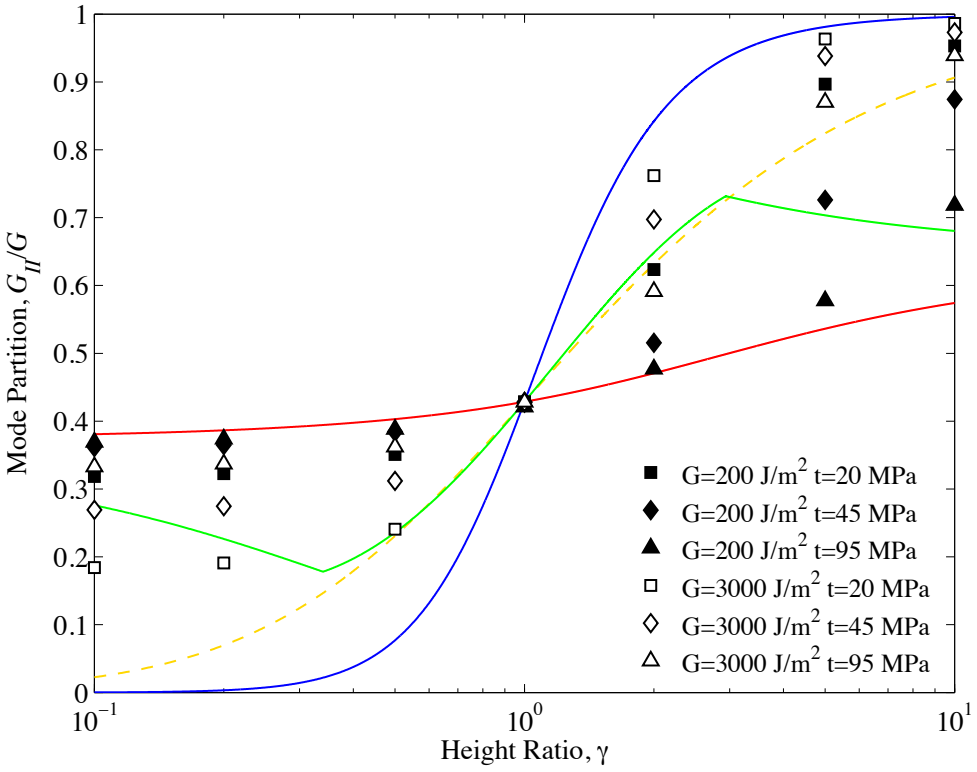

FIGURE 3.13: Numerical mode partitions from cohesive zone analysis of the Asymmetric Fixed Ratio Mixed Mode (Coupled Linear-Softening Cohesive Zone). Analytical solutions can be identified by referring to fig. 3.10(a).

The stress profiles in the steady state cohesive zones are plotted in fig. 3.14 and fig. 3.15 for $\gamma = 0.5$ and $\gamma = 2$ respectively. These are representative of all cases where $\gamma < 1$ and $\gamma > 1$ respectively. It is clear that in all cases the resulting cohesive zone length is strongly dependent on the cohesive properties. For a given toughness value, a reduction in the cohesive strength results in an increase in the cohesive zone length. Also, an increase in the cohesive toughness for a given cohesive strength results in an increase in the cohesive zone length. From fig. 3.13, it is noticeable that the mode partitions are closer to the solution of Williams [20] for $\gamma > 1$ compared to $\gamma < 1$ for equivalent cohesive properties. This pattern is also mirrored in the cohesive zone length data seen in fig. 3.14(b) and fig. 3.15(b). For $\gamma > 1$, the loading becomes mode II dominant and this results in larger cohesive zone lengths for equivalent properties compared to

mode I dominated loadings. The fact that the shift towards the global solution observed in fig. 3.13 for $\gamma > 1$ is accompanied with a significant increase in the cohesive zone length is a clear indication that the cohesive zone length may play an important role in defining the mode mixity. To further study the effect of the cohesive zone length on the mixed mode partition, the numerical mode partitions (G_{II}/G) are plotted against the corresponding cohesive zone lengths (l_{cz}) for each case in fig. 3.16. It is evident

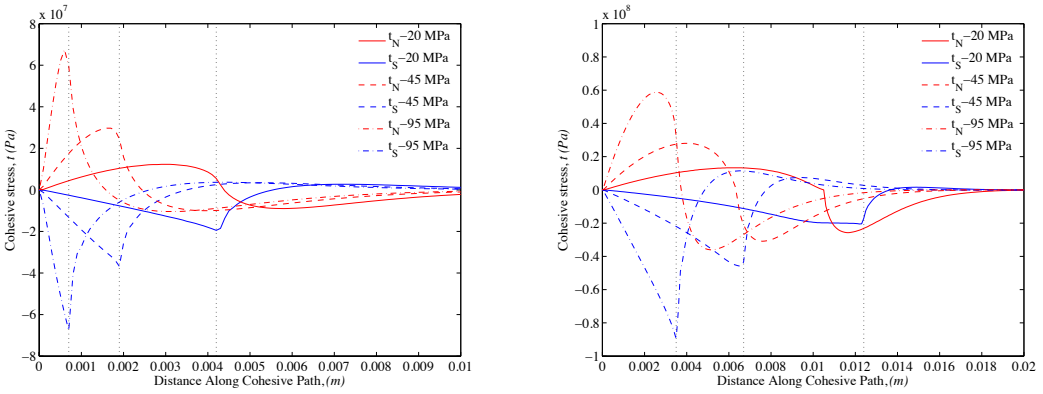

(a) Normal and shear stress distribution in the cohesive zone ($G = 200J/m^2$)

(b) Normal and shear stress distribution in the cohesive zone ($G = 3000J/m^2$).

FIGURE 3.14: Stress profile ahead of the crack tip during steady state fracture in the AFRMM test ($\gamma = 0.5$).

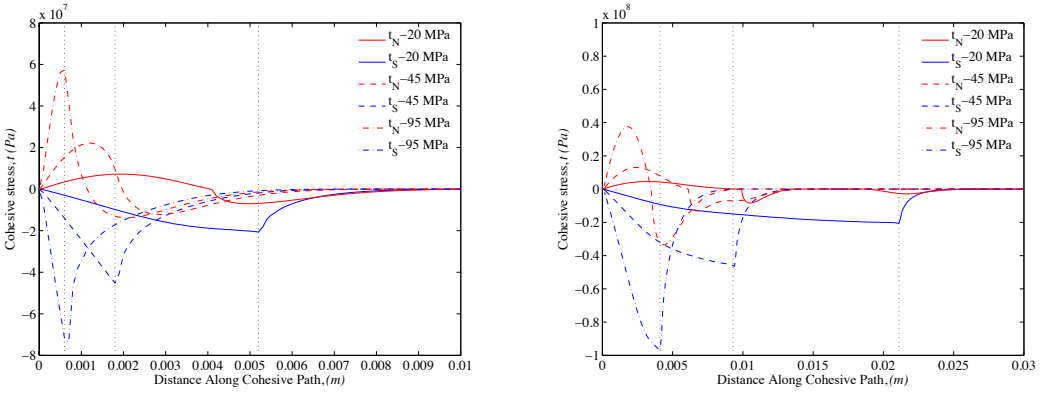

(a) Normal and shear stress distribution in the cohesive zone ($G = 200J/m^2$)

(b) Normal and shear stress distribution in the cohesive zone ($G = 3000J/m^2$)

FIGURE 3.15: Stress profile ahead of the crack tip during steady state fracture in the AFRMM test ($\gamma = 2$).

from fig. 3.16 that for small cohesive zone lengths, the mode partition is close to the local solution and as the cohesive zone length increases, the mode partition deviates away from the local solution and approaches the global solution of Williams [20]. It is particularly evident from figs. 3.16(e) 3.16(f) that the global solution forms the upper

bound. It was seen in chapter 2 that for zero cohesive zone length (infinite cohesive strength), the local solution of Suo and Hutchinson [26] provided an accurate estimate of the mixed mode partition. The analytical mode partitions of Suo and Hutchinson [26] and Williams [20] therefore provide the lower and upper bounds for the cohesive zone solution respectively. For the sake of consistency, the Suo and Hutchinson [26] solution is referred to hereafter as the lower bound and the Williams [20] solution is referred to as the upper bound, despite the fact that the absolute values of the solutions of Suo and Hutchinson [26] and Williams [20] can be lower or higher than each other depending on the γ and k ratio. For each height ratio, a unique function describes the dependence of the mode partition on the cohesive zone length. It is straightforward to comprehend why the local solution of Suo and Hutchinson [26] forms the lower bound for small cohesive zone lengths. This lower bound was the main focus of the previous chapter where the purely elastic solutions correspond to an infinite cohesive strength and zero cohesive zone length. It was found then that the local solution produced a very accurate estimate of the mixed mode partition so it is no surprise that it performs equally well here for small cohesive zone lengths. However, as the cohesive zone length increases and the K dominant region is eclipsed, the assumptions of the local partitioning are no longer valid and they no longer predict the correct mode partition. The reasons why the mode partition approach the global solution of Williams [20] for increasing damage lengths are somewhat more speculative. It is believed that as the damage region grows, there is no longer a stress concentration and beam theory can more accurately describe the deformations in the cohesive region. Therefore, as the damage region grows, the global solution will form the upper bound solution where there is no stress concentration and the displacements of the cohesive region are predicted exactly by beam theory. In reality however the mode partition will most likely fall somewhere between these upper and lower bounds and neither will be able to accurately predict the mode partition. Based on this reasoning, it is believed that the length of the cohesive zone relative to the size of the K dominant region will be critical factor for determining where the actual mode partition lies between these upper and lower bounds.

For all cases in which $\gamma < 1$, the rate at which the mode partition approaches the global solution is almost constant. However, for $\gamma > 1$, the rate at which the global solution is approached increases significantly with increasing γ. i.e. for similar cohesive zone lengths in cases where $\gamma < 1$ and cases where $\gamma > 1$, the mixed mode partition is much closer to the global solution in the $\gamma > 1$ case. The reason for this may be explained by referring back to chapter 2. In chapter 2 it was seen that the extent of the mode I singular field scaled with the smallest characteristic dimension (fig. 2.25). Therefore, it follows that the impact of cohesive zone length on a given geometry should scale

with the smallest characteristic dimension of that geometry. In all cases the smallest characteristic dimension corresponds to the smallest beam thickness. i.e.:

$$h_c = \min[h_1, h_2] \tag{3.15}$$

Scaling the cohesive zone length with the smallest characteristic dimension results in a new quantity termed the normalised cohesive zone length, or normalised damage length, given by:

$$l_{nd} = l_{cz}/h_c \tag{3.16}$$

As h_1 is kept constant and h_2 varied according to fig. 3.11(a), the smallest characteristic dimension remains constant for all cases where $\gamma \leq 1$ but is indirectly proportional to γ when $\gamma > 1$. Therefore, the increased rate at which the mode partition approaches the global solution may be attributed to the decreasing characteristic dimension. However, as the mode mixity also changes towards mode II dominant when $\gamma > 1$, this increased rate at which the mode partition approaches the global solution could also be attributed to the increased damage lengths due to mode II being the dominant mode. It is possible to eliminate this factor in the ADCB case as the mode mix is predicted to be mode I dominant for both $\gamma < 1$ and $\gamma > 1$ (fig. 3.10(b)).

3.4.4.2 ADCB

The results of the ADCB test case, modelled with the coupled linear softening cohesive zone, are presented in fig. 3.17. For the ADCB case, the analytical partitioning solutions of Williams [20] and Wang and Harvey [28] predict that the loading is always pure mode I, regardless of the beam height ratio, and the partitioning solutions of Suo and Hutchinson [26] and Davidson et al. [27] predict a considerable variation in the mode partition as a function of the beam height ratio. The cohesive zone solution again predicts that partitioning lies in between the local ([26]) and the global solution ([20]), and shows a similar trend going from local to global for increasing toughness and decreasing strength. The solutions are again shifted towards the global solution for $\gamma > 1$. The mode mixity is plotted against the cohesive zone length for each case in fig. 3.18. Again, the mode mix is close to the local solution when the cohesive zone length is small, and it moves towards the global solution as the cohesive zone length increases. In this ADCB test case, the mode partition does not reach the upper bound solution of Williams [20] for the given substrate and cohesive properties as the loading is predominantly mode I, which does not produce large fracture process zones compared to mode II loading. From fig. 3.18, it is evident that the rate at which the global solution is approached remains relatively constant when $\gamma < 1$ but seems to increase with γ when $\gamma > 1$. As the

loading is predominantly mode I in all cases, the only varying factor is the smallest characteristic dimension, which changes only when $\gamma > 1$ according to fig. 3.11(b). In the following section, the cohesive zone length is normalised w.r.t. the smallest characteristic dimension for all cases.

3.4.4.3 Mode Mixity vs. Cohesive Zone Length

Based on the numerical findings presented in the previous sections 3.4.4.1 and 3.4.4.2, it is evident that the cohesive zone length (l_{cz}) plays an important role in determining the mode mixity for both the AFRMM and ADCB test cases. In all cases tested, the mode partition went from the local solution of Suo and Hutchinson [26] towards the global solution of Williams [20] as a function of increasing cohesive zone length. It was also observed that the rate at which the global solution was approached with increasing cohesive zone length was also dependent on the smallest characteristic dimension of the geometry. This observation is in line with the findings from chapter 2 where the extent of the mode I K dominant region was found to scale reasonably with the smallest characteristic dimension in the AFRMM test. The cohesive length data from all cases in figs 3.16 and 3.18 are therefore normalised w.r.t. the smallest characteristic dimension according to eq. 3.16. As the lower and upper bounds of the mode partition are given by Suo and Hutchinson [26] and Williams [20], the mode mixity is normalised with respect to these solutions in all cases by introducing a normalised mode mix parameter, f, where f is given by:

$$f = \frac{\frac{G_{II}}{G} - \frac{G_{II}}{G}_{W}}{\frac{G_{II}}{G}_{HS} - \frac{G_{II}}{G}_{W}} \tag{3.17}$$

where $(\frac{G_{II}}{G})_{HS}$ and $(\frac{G_{II}}{G})_{W}$ are the partitions predicted by the local (eq. 1.7) and global (eq. 1.5) analytical approaches respectively. For an f value equal to one, the mode partition is equal to the local solution of Suo and Hutchinson [26] and for an f value equal to zero, the mode partition is equal to the global solution of Williams [20]. For an intermediate mode partitioning value, the normalised mode mixity f indicates how 'local' or how 'global' the mode partition is according to eq. 3.17. The normalised cohesive zone length (l_{nd}) and normalised mode mixity (f) are calculated for each simulation from the AFRMM and ADCB test cases and are plotted against each other in fig. 3.19 Based on the results in fig. 3.19, it is evident that all of the cases approach the global solution at the same rate as a function of increasing normalised cohesive zone length, notwithstanding some small scatter. Overall, the rate at which the global solution is approached follows an exponential trend. At small normalised damage lengths the mode partition is close to the local solution and then approaches the global solution exponentially as a function of increasing normalised damage length. This is an important result

as it indicates that the mode mixity in asymmetric specimens is uniquely dependent on the normalised length of the cohesive zone which develops during fracture, regardless of applied moment ratio k and beam height ratio γ. However, this has only been tested on the coupled linear softening cohesive zone up to now. In the following section, the AFRMM test is repeated using the uncoupled Dugdale CZM to examine the effect of varying the cohesive zone formulation and shape.

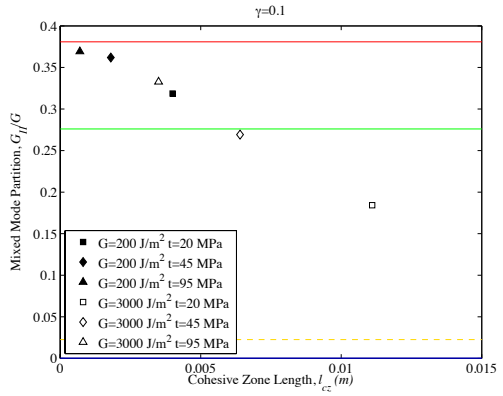

(a) Mode partition vs. cohesive zone length ($\gamma = 0.1$)

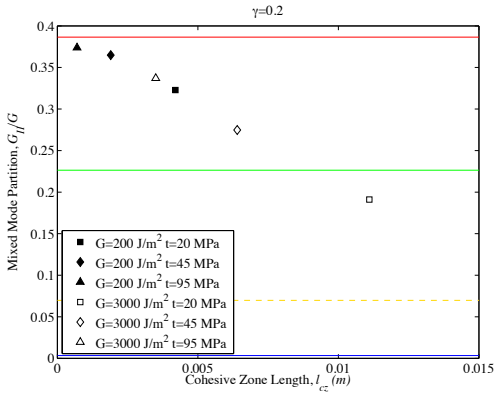

(b) Mode partition vs. cohesive zone length ($\gamma = 0.2$)

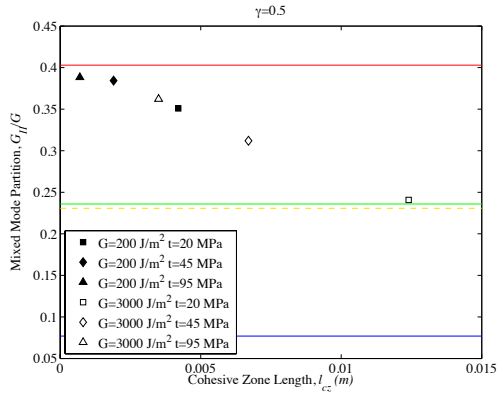

(c) Mode partition vs. cohesive zone length ($\gamma = 0.5$)

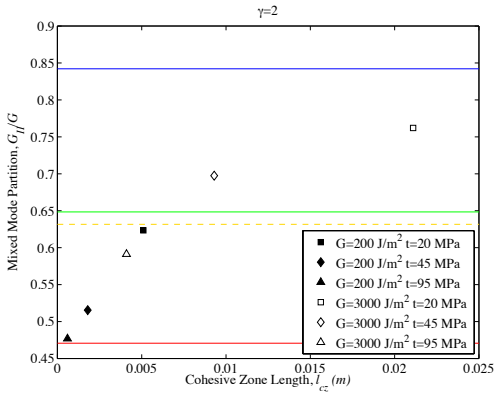

(d) Mode partition vs. cohesive zone length ($\gamma = 2$)

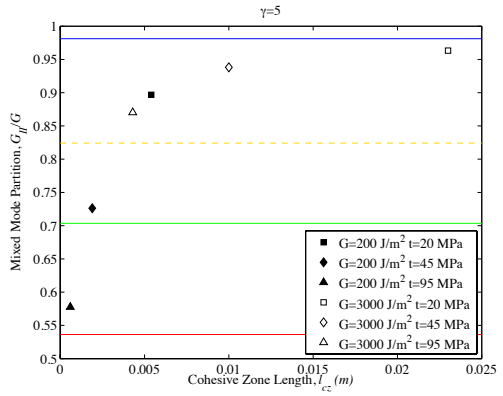

(e) Mode partition vs. cohesive zone length ($\gamma = 5$)

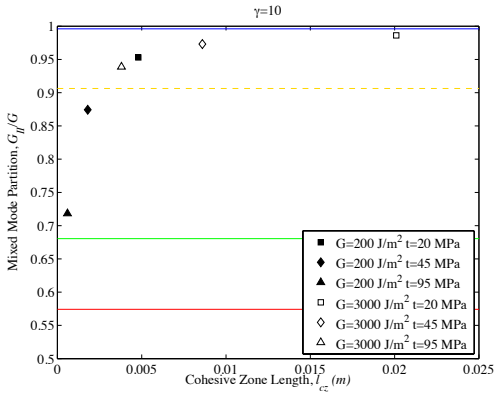

(f) Mode partition vs. cohesive zone length ($\gamma = 10$)

FIGURE 3.16: Numerical mode partition plotted against numerical cohesive zone length for different beam height ratios in the AFRMM test. Analytical solutions are also plotted for each case - W (blue), HS (red), D-NSF (green) and WH (yellow).

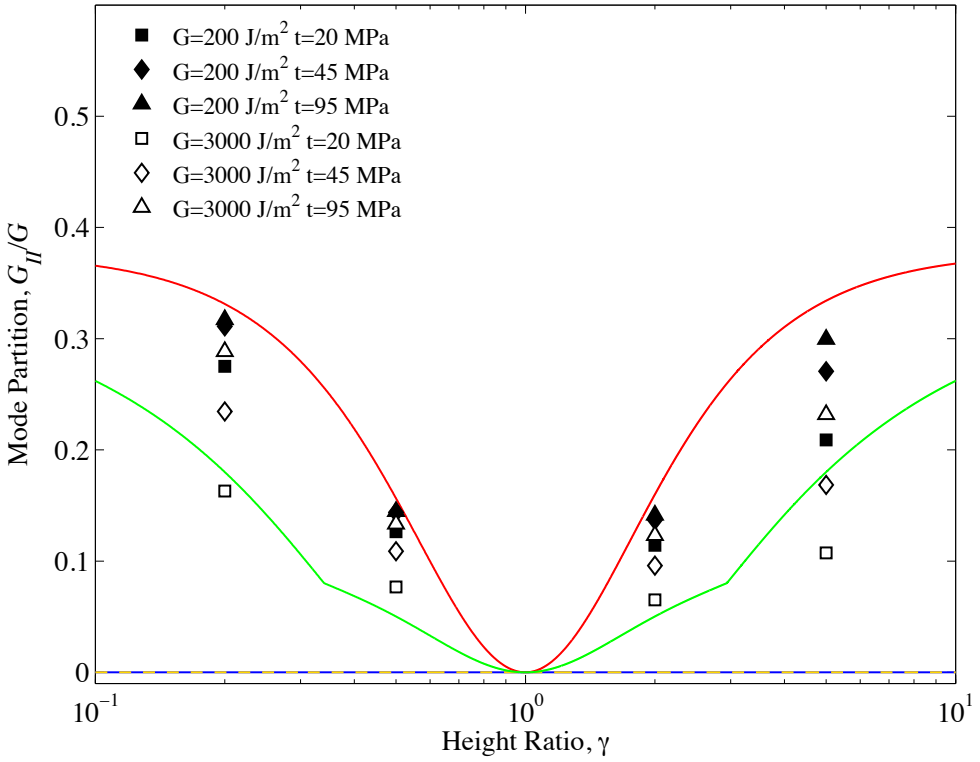

FIGURE 3.17: Numerical mode partitions from cohesive zone analysis for the Asymmetric Double Cantilever Beam (Coupled Linear Softening Cohesive Zone). Analytical solutions are also plotted for each case - W (blue), HS (red), D-NSF (green) and WH (yellow).

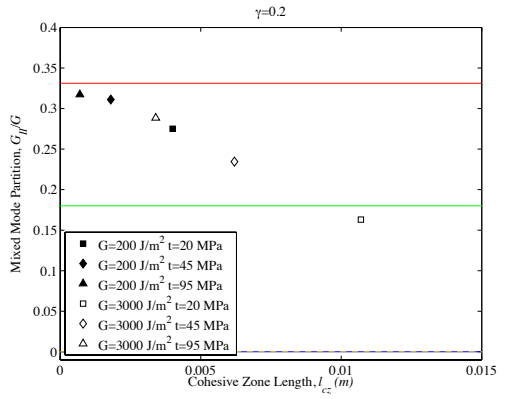

(a) Mode partition vs. cohesive zone length ($\gamma = 0.2$)

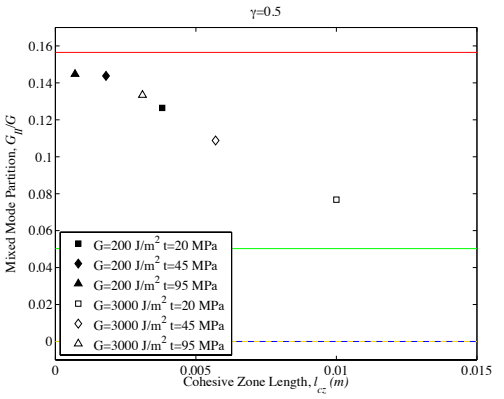

(b) Mode partition vs. cohesive zone length ($\gamma = 0.5$)

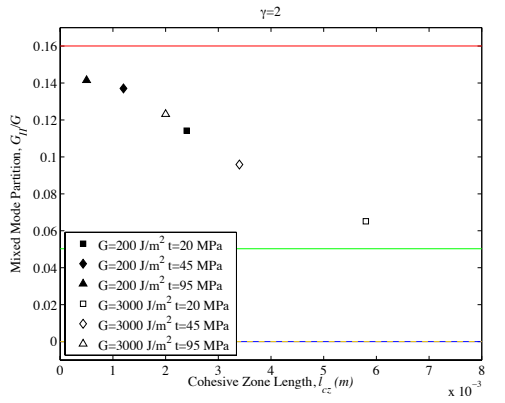

(c) Mode partition vs. cohesive zone length ($\gamma = 2$)

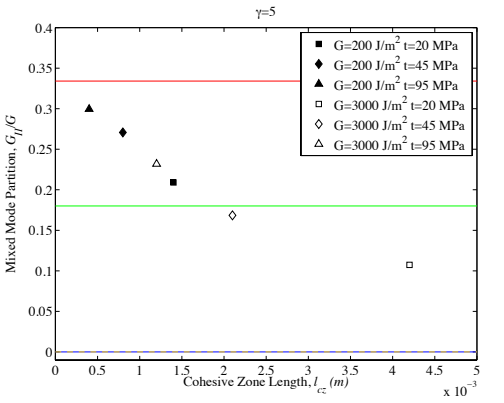

(d) Mode partition vs. cohesive zone length ($\gamma = 5$)

FIGURE 3.18: Numerical mode partition plotted against numerical cohesive zone length for different beam height ratios in the ADCB test. Analytical solutions are also plotted for each case - W (blue), HS (red), D-NSF (green) and WH (yellow).

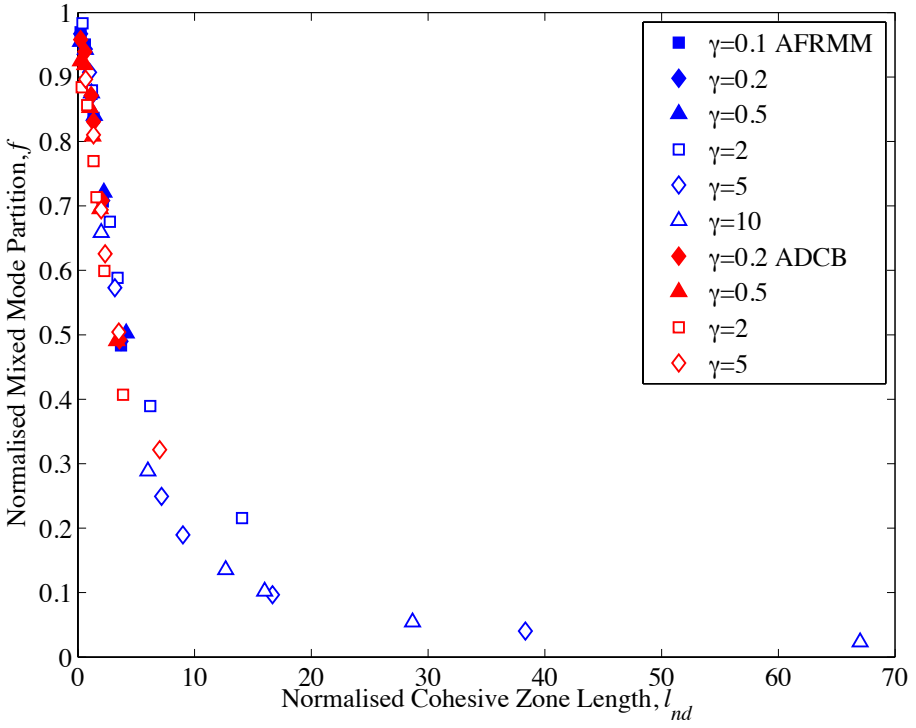

(a)

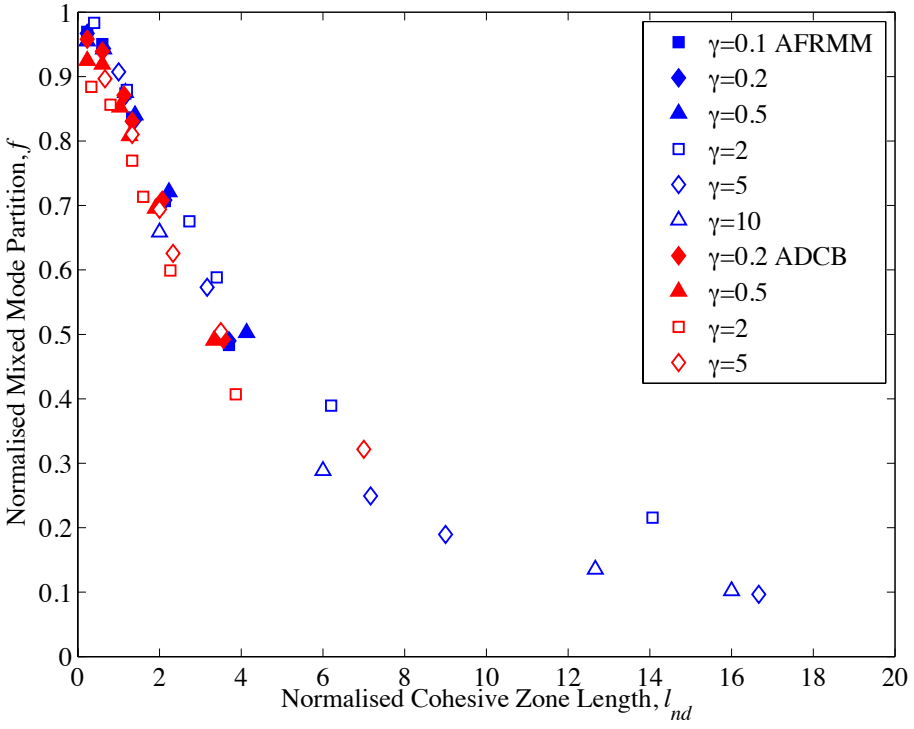

(b)

FIGURE 3.19: Normalised mode mixity vs. normalised cohesive zone length for AFRMM (blue) and ADCB (red) test cases for (a) entire data set, and (b) zoomed in at l_{nd} close to zero.

3.5 Mode Partitioning of Uncoupled Dugdale CZM

3.5.1 Case Setup

In this section the AFRMM test (fig. 3.11(a)) is repeated but with the uncoupled Dugdale CZM inserted in place of the coupled linear softening CZM for two beam height ratios ($\gamma = 0.1, \gamma = 10$). The same combinations of cohesive properties as used in the previous section are also used here. The cohesive properties correspond to two toughness values of $200J/m^2$ and $3000J/m^2$ and for each toughness value, three cohesive strengths are tested corresponding to $20MPa$, $45MPa$ and $95MPa$. In three cases convergence was not obtained; these cases occurred at each cohesive strength when $G_C = 3000J/m^2$ at $\gamma = 10$. Additional cases are carried out to investigate the effect on the mode partition when $G_{IC} \neq G_{IIC}$. As stated previously, this study was only possible with the uncoupled Dugdale cohesive zone model as the coupled linear-softening cohesive zone suffers from thermodynamic inconsistencies under variable mixed mode loading when pure mode toughnesses are unequal. The additional cases at $\gamma = 0.1$ correspond to:

- $G_{IC} = 500J/m^2, G_{IIC} = 3000J/m^2, t_C = 45MPa$
- $G_{IC} = 3000J/m^2, G_{IIC} = 500J/m^2, t_C = 45MPa$

and additional cases at $\gamma = 10$ correspond to:

- $G_{IC} = 200J/m^2, G_{IIC} = 800J/m^2, t_C = 95MPa$
- $G_{IC} = 800J/m^2, G_{IIC} = 200J/m^2, t_C = 95MPa$

The mode partitions are calculated as before by integrating over the cohesive surfaces when the fracture process zone is propagating in steady state. As the cohesive zone is uncoupled, the mode I and mode II laws generally reach the cohesive strength at different points. Therefore, there are generally two distinct cohesive zone lengths corresponding to mode I and mode II, which can easily be separated by individually plotting the mode I and mode II components of stress along the cohesive zone. When this is the case, the largest of the two cohesive zone lengths is recorded as the cohesive zone length (l_{cz}) for the purpose of this study.

3.5.2 Results and Discussion

The mode partitions are plotted as a function of the cohesive zone length in fig. 3.20 for $\gamma = 1$ and $\gamma = 10$. In both cases a similar trend to the linear-softening cohesive

zone is observed. When the cohesive zone length is small, the mode partition is close to the local solution and as the cohesive zone length increases, the mode partition moves towards the global solution. Comparing fig. 3.20(a) and fig. 3.16(a), it is evident that there is an overall shift towards the local partitioning for the Dugdale CZM solution compared to the linear softening CZM solution. This may be explained by the fact that the developed cohesive zone length will be shorter for a Dugdale shape cohesive zone compared to a linear softening cohesive zone for the same toughness and strength properties, again suggesting that the cohesive zone length is the critical parameter. In the cases where $G_{IC} \neq G_{IIC}$, the predicted partitions also lie between the local and the global solution and follow the same trend as cases where $G_{IC} = G_{IIC}$ going from local to global for increasing damage lengths. The mode partitions and cohesive zone lengths are normalised according to eq. 3.17 and eq. 3.16 respectively as before. These are plotted over the normalised data from the previous section in fig. 3.21.

The normalised data from the uncoupled Dugdale CZM reasonably follow the trend predicted by the linear softening CZM in fig 3.21. This is another important result as it suggests that the dependency of the mode partition on the cohesive zone length is independent of cohesive zone shape and formulation. Therefore, there is scope to use this numerically observed dependency for estimating mixed mode partitions based on analytically predicted cohesive zone lengths. This idea forms the basis of the semi-analytical cohesive analysis (SACA), which is presented in the next chapter.

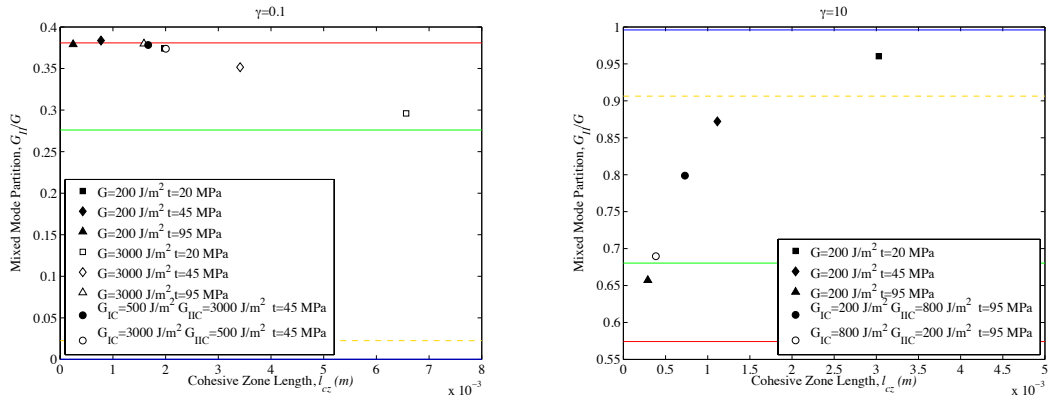

(a) Mode partition vs. cohesive zone length ($\gamma = 0.1$) (b) Mode partition vs. cohesive zone length ($\gamma = 10$)

FIGURE 3.20: Numerical mode partition plotted against numerical cohesive zone length for different beam height ratios in the AFRMM test (Uncoupled Dugdale CZM). Analytical solutions can be identified by referring to fig. 3.10(a).

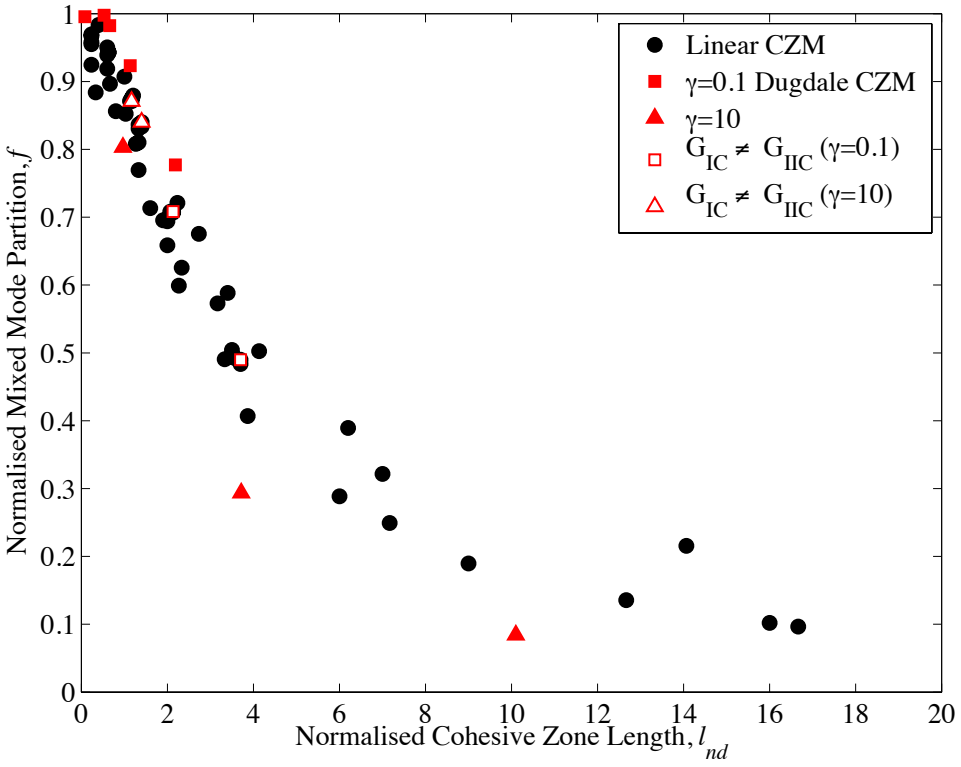

FIGURE 3.21: Normalised mode mixity vs. normalised cohesive zone length for uncoupled Dugdale CZM (red) plotted on top of previous results from linear softening CZM (black) for all test cases

3.6 Chapter Conclusions

In the first part of this chapter, the use of cohesive zone models were reviewed. In particular, the limitations of potential based cohesive zones were discussed and an example problem was presented in Appendix A to highlight these limitations. The main limitation for the current work was that such cohesive zones are not consistent with the definition of the failure locus outlined in chapter 1. i.e. $G_c \neq f(G_{II}/G)$. The two cohesive zones which were chosen for use in this study were the coupled linear softening CZM developed by Camanho et al. [66] and the uncoupled Dugdale CZM developed by Yang and Thouless [69].

In the second section of this chapter, a number of common numerical partitioning approaches were tested for accuracy and/or appropriateness against the benchmark of the fixed ratio mixed mode (FRMM) test. The various techniques were the mode decomposed J integral applied over an external path ($J_{\Gamma_{ext}}$), the mode decomposed J integral applied over the cohesive surfaces ($J_{\Gamma_{coh}}$), and the monitoring of energy going directly into the initial crack tip element (CTE). The CTE approach was found not to reproduce

the correct analytical mode partition, as it is unable to provide all of information about the overall mode partition in the developing fracture process zone. The external mode decomposed integral ($J_{\Gamma_{ext}}$) was found to always capture the correct mode partition regardless of crack tip condition, i.e. singular or non-singular. Finally, integration along the cohesive surfaces ($J_{\Gamma_{coh}}$) was found to give the same partition as the mode decomposed J integral ($J_{\Gamma_{ext}}$) in the absence of any crack tip singularities when the cohesive zone is propagating in a self similar manner. As the external J integral ($J_{\Gamma_{ext}}$) is cumbersome to implement for asymmetric cases, it is recommended that that integration over the cohesive surfaces ($J_{\Gamma_{coh}}$) be implemented during steady state crack propagation in the remainder of the study.

Once an accurate partitioning technique is established, a parametric study is carried out to investigate the effect of various cohesive properties on the global mixed mode partition in asymmetric specimens. Both the asymmetric fixed ratio mixed mode(AFRMM) and asymmetric double cantilever (ADCB) test geometries are used in this study. The mode partition is studied as a function of varying cohesive properties. In the initial part of this study only the coupled linear softening cohesive zone is tested. A number of conclusions are drawn from this study:

- When the fracture process zone is small, the local partitioning solution is also recovered from the cohesive zone solution.
- As the cohesive zone size grows, the partition deviates away from the local solution of Suo and Hutchinson [26], and in all cases moves towards the global solution of Williams [20], which seems to form the upper bound.
- The cohesive zone properties are chosen to represent values which would typically be expected in composites and adhesive joints, and it is found that in most cases the numerical partition lies between the local and global solutions, suggesting limited applicability of both the local and global approaches in their current form.

It is observed that the rate at which the mode partition approaches the global solution with increasing cohesive zone length is dependent on the smallest characteristic length scale of the geometry. For decreasing size of the smallest characteristic dimension, the rate at which the global solution is approached is increased. This is consistent with the idea that the cohesive zone length relative to the size of the K dominant region is the controlling factor in determining the mode mixity between local and global solutions as it was observed in chapter 2 that the mode I K dominant region scales with the smallest characteristic dimension in asymmetric beam-like geometries. All cohesive zone lengths are therefore normalised with respect to the smallest characteristic dimension of the

geometry. The mode partition is also normalised with respect to the upper and lower bound solutions. When the normalised cohesive length is plotted against the normalised mixed mode mix for all cases, it is observed that all cases approach the global solution by following a unique curve (fig. 3.19).

Finally, the effect of using a different cohesive zone formulation is studied. An uncoupled Dugdale formulation developed by Yang et al. [67] is used in a number of AFRMM test cases to examine the effect of cohesive shape and formulation on the resulting mixed mode partition. A number of extra cases are also carried out to examine the effect when $G_{IC} \neq G_{IIC}$. It is found that in all cases a similar trend is produced as with the linear softening cohesive zone. For small cohesive zone lengths, the mixed mode partition is close to the singular solution of Suo and Hutchinson [26] and as the cohesive zone length increases, the mode partition deviates towards the global solution of Williams [20]. Cases where $G_{IC} \neq G_{IIC}$ also follow this trend closely. When the cohesive zone lengths and mode partitions are normalised as before, it is found that they closely follow the trend predicted by the linear softening cohesive zone data. This is an important result as it suggests that a simple curve can be used to predict the normalised mode partition if the normalised cohesive zone length is known, regardless of cohesive zone shape and formulation, loading and geometry. This presents a very powerful tool for estimating mode partitions in asymmetric specimens if the cohesive zone lengths can be estimated analytically or otherwise, which does not require each case to be modelled numerically. This forms the basis for the development of the semi-analytical cohesive analysis (SACA), which is presented in the next chapter.

Chapter 4

Semi Analytical Cohesive Analysis

4.1 Introduction

In the previous chapter, the numerical mode mixity was studied as a function of cohesive properties in common asymmetric fracture test geometries and it was found that the mode mixity is dependent on the cohesive zone properties. As all of the analytical partitioning theories are dependent only on loading and geometry, they cannot be used to accurately predict the mode partition from the numerical cohesive zone analysis. It is found that a unique trend defines the normalised mode mixity as a function of the normalised cohesive zone length, where the upper and lower bounds of the cohesive zone solution are given by the local solution of Suo and Hutchinson [26] and the global solution of Williams [20]. In this section, a semi-analytical approach (SACA) is proposed which makes use of this observed unique dependency by analytically estimating cohesive zone lengths. This greatly reduces the time required to analyse mixed mode fractures and eliminates the need to carry out a numerical analysis for each individual case. The underlying idea is that if the cohesive zone length can be estimated analytically from the assumed substrate and cohesive properties, then the mode mixity can be obtained directly from the empirically measured curve.

4.1.1 Chapter Layout

The layout of the chapter is as follows:

- In the initial part of the chapter, a unique curve is fitted to the numerical data obtained in the previous chapter (i.e. from fig. 3.21).
- Secondly, a method for analytically estimating the cohesive zone length in slender beam-like geometries is presented. The required shape factors for both the linear softening and Dugdale cohesive zones are obtained by fitting the numerical data from the previous chapter.
- As the estimated cohesive zone length is dependent on the mode mixity, an iterative procedure must be developed in order to find the mode mixity. This approach is called the semi-analytical cohesive analysis (SACA) and is implemented as an excel macro which is freely available for download. The development and workings of this macro is presented in this section.
- The accuracy of the new SACA partitioning approach is tested by carrying out a number of numerical verification test cases. The cohesive zone lengths and mode mixities are recorded directly from the numerical simulations and then compared to the independently estimated values from the SACA approach.
- Finally, the SACA approach is tested in its ability to partition experimental data. In this section, the SACA partitioning is applied to two conflicting experimental case studies taken from literature. In the original papers, asymmetric fracture tests are carried out on CFRP (Hashemi et al. [32]) and GFRP (Ducept et al. [33]) and the predicted failure loci from both the local (Suo and Hutchinson [26]) and global (Williams [20]) partitioning were assessed. These two cases are of particular interest here as they are conflicting in their conclusions. The study by Hashemi et al. [32] concludes that global partitioning is the most appropriate partitioning method, while the study by Ducept et al. [33] predicts that the local partitioning is the most appropriate. In this section, these test cases are repartitioned using the SACA method along with the analytical methods of Wang and Harvey [28] and Davidson et al. [27] and the accuracy of each method is assessed.

4.2 Unique Damage Dependency

In this section, a unique function is fitted to the data presented in fig. 3.21. It is clear that the curve follows an exponential form so the data is fitted initially using an exponential with two fitting parameters. i.e.:

$$f = ae^{b.l_{nd}} \tag{4.1}$$

and then using four fitting parameters parameters. i.e.:

$$f = ae^{b.l_{nd}} + ce^{d.l_{nd}} \tag{4.2}$$

The coefficients of each are optimised using matlab curve fitting tool `cftool`, which works to minimise the least squares error between the function and the data. The optimised coefficients are given in table 4.1 along with the corresponding R^2 values, where R^2 is defined as:

$$R^2 = 1 - \frac{\sum_1^N (f_{data} - f_{fit})^2}{\sum_1^N (f_{data} - \bar{f}_{data})^2} \tag{4.3}$$

where f_{data} is the normalised mode mix value of each data point and f_{fit} is the corresponding normalised mode mix value predicted by the fitted function, $\bar{f}_{data}$ is the mean mode partition obtained from the data values and N is the number of data points.

No. fitting parameters	a	b	c	d	R^2 value
2	1.043	-1.963	-	-	0.958
4	0.9585	-0.2326	0.0985	-0.018	0.963

TABLE 4.1: Coefficients of exponential fit using two (eq. 4.1) and four (4.2) fitting parameters.

The fitted functions using both two and four fitting parameters are presented in fig. 4.1. It is evident from table 4.1 that there is not a significant increase in the R^2 value when four parameters are used compared to two. However, when the fitted functions are plotted alongside the data in fig. 4.1, it is clear that the two parameter function does not accurately follow the data at high l_{nd} values. As this is a once off fit, it is decided to proceed with the more accurate fit, which corresponds to eq. 4.2. Functions with a higher number of fitting parameters were not tested as it was deemed that four fitting parameters provided sufficient accuracy.

As the normalised mode partition must have a limiting value of one at zero cohesive zone length (local partitioning is correct for zero damage (chapter 2)) , the fitting function can be expressed as:

$$f = \begin{cases} 1, & \text{if } l_{nd} \leq 0.26 \\ 0.9585e^{-0.2326l_{nd}} + 0.0985e^{-0.018l_{nd}}, & \text{otherwise} \end{cases} \tag{4.4}$$

Based on this fit, the local partitioning is accurate for cohesive zone lengths up to 26% of the smallest characteristic dimension. The value of $l_{nd} = 0.26$ is the point at which

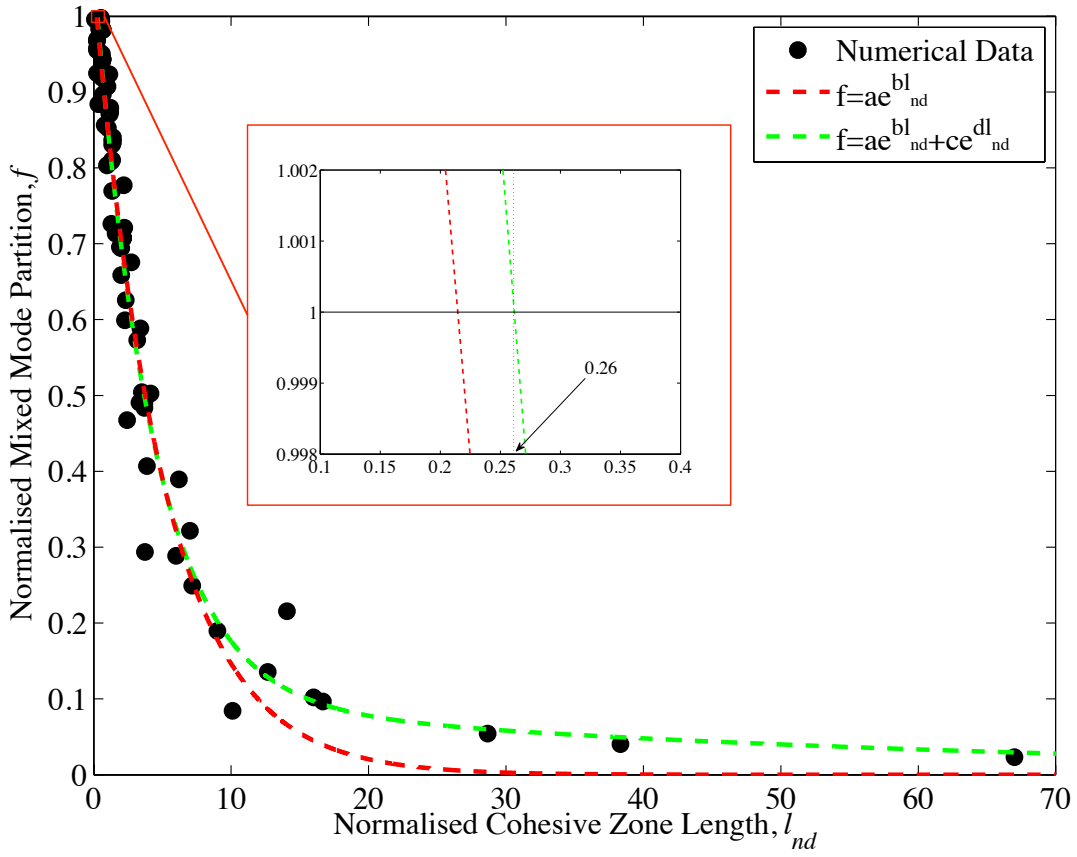

FIGURE 4.1: Exponential fitting (eqs.4.1, 4.2) of numerical data obtained in chapter 3.

$f = 1$, as illustrated from the zoomed portion of fig. 4.1. This length is considerably larger than the size of the K dominant region, which is seen in chapter 2 to be the order of $\approx$ 2-5 % of the smallest beam thickness in asymmetric specimens. Becker et al. [39] and Charalambides et al. [16] also reported that the extent of the K dominant region to be of the order of 1% of the beam thickness in beam-like geometries subjected to bending. Parmigiani and Thouless [40] found that the local solution of Suo and Hutchinson [26] was accurate for cohesive zone lengths which eclipsed the K dominant region, so the results observed here are in agreement with this finding. However, most cohesive zone lengths in the current data, which are based on realistic cohesive and substrate properties, fall well outside of this 30% bracket; this suggests that the local partitioning will, in general, not be accurate for partitioning fractures in composites and adhesive joints. The global partitioning of Williams [20] does not, in general, provide accurate partitioning either, and in most general cases the actual partition lies between the local and global solutions. In general, the mixed mode partition is dependent on multiple cohesive zone and substrate properties, all of which are linked through the normalised cohesive zone length. Taking the unique dependency observed in fig. 4.1, it

is proposed that if a reasonable estimate of the numerical cohesive zone length can be obtained analytically from known substrate and cohesive properties, then an accurate estimate of the mode mixity can be obtained directly from the empirical curve given by eq. 4.4, therefore avoiding the need to carry out numerical mixed mode cohesive zone simulations. The analytical estimation of cohesive zone lengths in slender laminates is considered in the next section.

4.3 Analytical estimation of cohesive zone length

Yang and Cox [96] presented analytical expressions for pure mode I (l_{I_cz}) and pure mode II (l_{II_cz}) cohesive zone lengths in symmetric slender laminates as:

$$l_{I\_cz} = M\Big(E_I^{'}\frac{G_{IC}}{(t_{NC})^2}\Big)^{\frac{1}{4}}h^{\frac{3}{4}} \tag{4.5a}$$

$$l_{II\_cz} = M\sqrt{\Big(E_{II}^{'}\frac{G_{IIC}}{(t_{SC})^2}h\Big)} \tag{4.5b}$$

where M is a scaling factor, which is included here to account for cohesive zone shape, as in [97]; h is half the specimen height and $E_I^{'}$ and $E_{II}^{'}$ are elastic constants, which are given in [74] for slender orthotropic specimens as:

$$\begin{aligned}\frac{1}{E_I^{'}} &= \sqrt{\frac{1}{2E_{11}E_{22}}\left(\Big(\frac{E_{11}}{E_{22}}\Big)^{\frac{1}{2}} + \frac{2(\frac{-v_{21}}{E_{22}}) + \frac{1}{G_{12}}}{2(\frac{1}{E_{11}})}\right)} \\ \frac{1}{E_{II}^{'}} &= \frac{(1 - v_{12}v_{21})}{E_{11}}\end{aligned} \tag{4.6}$$

where E_{11} and E_{22} are the Young's moduli in the x and y directions respectively for the loading configurations presented in fig. 3.11, G_{12} is the in plane shear modulus, and v_{12}, v_{21} are the in-plane Poisson's ratios. For plane strain conditions, these values are replaced by:

$$\begin{aligned}E_{11} &= \frac{E_{11}}{1 - \nu_{13}\nu_{31}} \\ E_{22} &= \frac{E_{22}}{1 - \nu_{23}\nu_{32}} \\ \nu_{12} &= \frac{\nu_{12} + \nu_{13}\nu_{32}}{1 - \nu_{13}\nu_{31}} \\ \nu_{21} &= \frac{\nu_{21} + \nu_{23}\nu_{31}}{1 - \nu_{23}\nu_{32}}\end{aligned} \tag{4.7}$$

The accuracy of eq. 4.5a and 4.5b is studied in detail in Harper and Hallett [97] for mid-plane delaminations under pure mode I and II loadings: it is found that they provide reasonable accuracy for a coupled bilinear cohesive zone when $M = 0.5$. To the best of the present author's knowledge, the accuracy of the expressions have not yet been tested for asymmetric geometries, or in their ability to predict cohesive lengths under general mixed mode conditions. Firstly, to deal with the potential asymmetry of geometry and loading, it is proposed that the h term in eq. 4.5 be defined as:

$$h = \frac{h_1 + |k|h_2}{1 + \frac{\max[h_1,h_2]}{\min[h_1,h_2]}|k|} \tag{4.8}$$

where k is the applied moment ratio as defined in fig. 1.3 for $-1 \leq k \leq 1$. This proposed definition of h is based on the observation that the estimated cohesive zone length is dependent only on the thickness of the loaded arm in the AFRMM test case ($k = 0$), and is dependent on the minimum arm thickness in the ADCB test case ($k = -1$). The mode I and mode II cohesive zone lengths under mixed mode conditions (l'_{I_cz}, l'_{II_cz}) can be estimated by replacing G_{IC} with G_I in eq. 4.5a and G_{IIC} with G_{II} in eq. 4.5b, where G_I and G_{II} are the energies dissipated in mode I and mode II respectively. This results in a mode I and a mode II cohesive zone length defined by:

$$l'_{I\_cz} = M\Big(E'_I \frac{G_I}{(t_{NC})^2}\Big)^{\frac{1}{4}} h^{\frac{3}{4}} \tag{4.9a}$$

$$l'_{II\_cz} = M\sqrt{\Big(E'_{II} \frac{G_{II}}{(t_{SC})^2} h\Big)} \tag{4.9b}$$

The largest of these predicted values is then taken to be the cohesive zone length. i.e.:

$$l_{cz} = \max[l'_{I\_cz}, l'_{II\_cz}] \tag{4.10}$$

In order to obtain values of M for the linear softening and Dugdale cohesive zones, the measured cohesive zone lengths from the numerical test cases carried out in chapter 3 are plotted against the predicted cohesive zone lengths obtained from eq. 4.10: for each case, M is found by forcing the slope of the least squares linear fit between the measured vs. predicted data to be equal to one. This condition results in the following expression for M:

$$M = \frac{\sum_{i=1}^{n} l_{cz_i}^2}{\sum_{i=1}^{n} l_{cz_i} l_{cz\_num_i}} \tag{4.11}$$

where l_{cz} is the predicted cohesive zone length, l_{cz_num} is the measured cohesive zone length from numerical simulations and n is the number of data points. The measured

vs. predicted cohesive zone lengths for the linear softening cohesive zone are plotted in fig. 4.2(a); $M = 0.66$ was found to give the optimum prediction. The measured vs. predicted cohesive zone lengths for the Dugdale cohesive zone are plotted in fig. 4.2(b); in this case, $M = 0.33$ was found to give the best prediction. Interestingly, Planas and Elices [98] previously reported scaling factors of 0.731 for the linear softening cohesive zone and $\pi/8$ for the Dugdale cohesive zone, based on an analytical study of cohesive zone lengths in infinite bodies. These values are in line with the current predictions for the scaling factors in slender specimens. Overall, the proposed equations are shown to give reasonable estimates for both the linear softening (using $M = 0.66$) and Dugdale (using $M = 0.33$) cohesive zones, over a range of cohesive properties, beam height ratios and moment ratios.

4.4 Implementation of SACA procedure

Once a reasonable estimate of the cohesive zone length is obtained analytically, the normalised mode mixity, f, can be estimated directly from the unique dependency curve (eq. 4.4). The value of f can then be substituted directly into eq. 3.17 to obtain an estimate of the mode mixity ($\frac{G_{II}}{G}$). In order to obtain the mixed mode cohesive zone lengths from eq. 4.9, G_I and G_{II} must first be estimated. In the estimation of the cohesive zone lengths shown in figs. 4.2(a) and 4.2(b), the values of G_I and G_{II} were obtained directly from the numerical results; however, as the mode mixity will not generally be known prior to the analysis of experimental data, the values of G_I and G_{II} must be found iteratively. To do this, an initial guess of f is made, which gives a mode mixity value from eq. 3.17. This value of mode mixity is used to partition G_c to obtain G_I and G_{II}. The value of G_c is either known directly from experiments, or can be estimated from a failure locus, if known. The estimated cohesive zone length is then used to obtain an improved estimate of f from eq. 4.4, and the process is iterated until a converged value of cohesive zone length, and hence mode mixity, is obtained (a tolerance value (tol) of $1e-5$ is used in the current work). This process is outlined in fig. 4.3. This procedure is implemented as an excel macro and is available to download from the link below, with instructions included:

- `http://adhesion.ucd.ie/caa/CAA_MixedMode.html`

The excel macro code is given in appendix C and the user interface is shown in fig. 4.4. The information required are the substrate elastic properties, geometry and loading conditions, and cohesive properties. Only isotropic or transversely isotropic material

can be input into the program. This is not deemed to be a significant limitation as most composite materials can be accurately described by transversely isotropic material properties. For transversely isotropic material properties, there are only five independent elastic properties. The five independent properties required by the macro are the Young's moduli in the bending and transverse directions (E_{11}, E_{22}), the in-plane shear modulus (G_{12}), and the in-plane and out of plane poisson's ratios (ν_{12}, ν_{23}). As it is assumed that the material is isotropic in the 2-3 plane, the remaining properties can be deduced from the following relations. i.e.

$$\begin{aligned} E_{33} &= E_{22} \\ \nu_{32} &= \nu_{23} \\ \nu_{13} &= \nu_{12} \\ G_{23} &= \frac{E_{22}}{2(1+\nu_{23})} \end{aligned} \tag{4.12}$$

and also from the following elastic relation:

$$\nu_{ji} = \nu_{ij}\frac{E_j}{E_i} \tag{4.13}$$

These remaining values are calcualted within the macro code before the cohesive zone lengths are calculated from eq. 4.9. It can be specified in the macro whether plane stress or plane strain conditions prevail. If plane strain is selected, eq. 4.7 is used to calculate the elastic properties for use in the estimation of the cohesive zone length (eq. 4.9).

The required geometry and loading properties are the beam heights h_1 and h_2 and applied moment ratio k, according to fig. 1.4. The cohesive properties required are the cohesive strength t_C, cohesive toughness G_c, and shape parameter M (Linear softening or Dugdale). It is recommended that the cohesive strength be set to the interlaminar tensile strength in the case of partitioning composite delamination and the tensile strength of the adhesive in the case of partitioning fracture in an adhesive joint; these are the closest measurable physical properties to the cohesive strength in numerical modelling. The macro program only facilitates the input of one cohesive strength value as this value is assumed equal in normal and shear ($t_C = t_{NC} = t_{SC}$). This decision is made on the basis that there is some recent evidence to suggest that the mode II cohesive strength is very close to the mode I cohesive strength in CFRP delamination [99]. This also reduces the number of variables required and makes the use of this program more straightforward. There are a number of options for inputting the cohesive toughness G_c. If the program is being used to partition fracture tests which have already been performed, the overall toughness G_c will be known directly from the experiments and

this should be entered into the macro. However, if the mode mixity is required for a given loading of a structure for which no fracture test will be performed, an estimate of the failure locus can be input into the macro. The toughness G_c is then calculated from the failure locus based on the estimated mode mixity. Either a linear failure locus corresponding to eq. 3.7 or the BK failure locus [17] can be chosen. The BK failure locus is given by:

$$G_c = G_{IC} + (G_{IIC} - G_{IC})\Big(\frac{G_{II}}{G}\Big)^m \tag{4.14}$$

The critical mode I (G_{IC}) and mode II (G_{IIC}) toughnesses must be specified if either the linear or BK failure locus is chosen. The fitting power m must also be specified if the BK option is chosen. A cohesive law shape must also be chosen. Based on the numerical data presented in chapter 3, only the linear softening ($M = 0.66$) and Dugdale ($M = 0.33$) shapes are available. If the exact shape is unknown, it is believed that these shape factors will provide an upper and lower bound for the SACA solution for a general trapezoidal shape.

Once the geometry and loading conditions, substrate properties, and cohesive properties are inserted into the macro seen in fig. 4.4, the partition button is pressed to run the macro. Multiple cases can be solved simultaneously by entering the data of each individual case in consecutive rows, as seen in fig. 4.4. When the procedure is finished, the macro prints the estimated values of mode partition (G_{II}/G) and cohesive zone length (l_{cz}) for all cases. Also printed are the values of the normalised mode mix (f), the analytical mode partitions predicted by the local $(G_{II}/G)_{HS}$ and global $(G_{II}/G)_W$ partitioning theories, and the number of iterations (i) it took to obtain convergence. The ability of the SACA method to accurately predict cohesive zone lengths and mixed mode partitions is tested in the following section by carrying out a number of verification test cases.

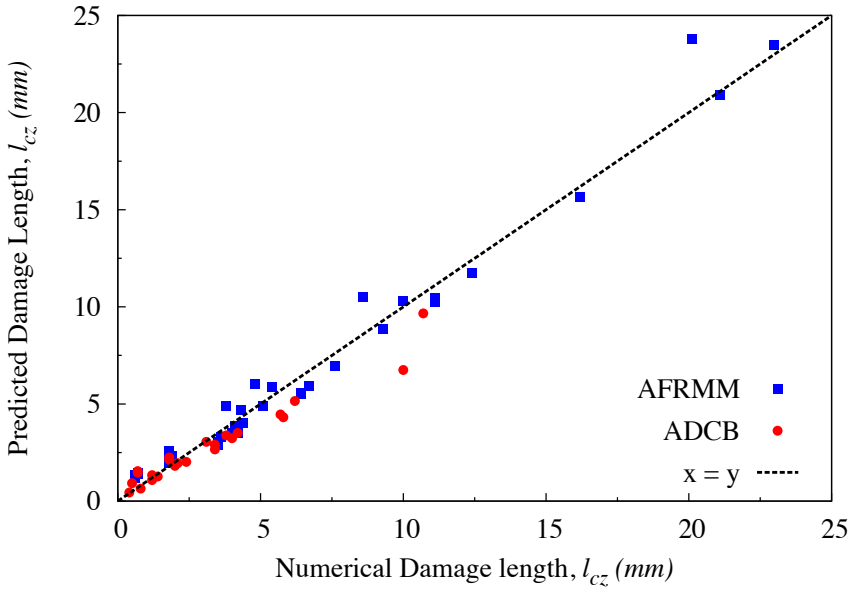

(a) Coupled Linear Softening Cohesive Zone

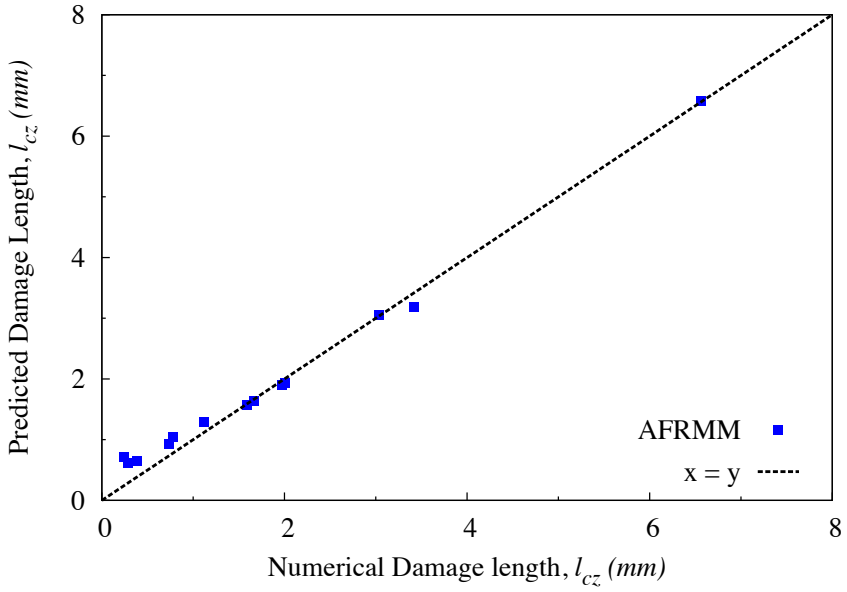

(b) Uncoupled Dugdale Cohesive Zone.

FIGURE 4.2: Numerically obtained damage length plotted against analytically predicted damage length for (a) Coupled Linear-Softening Cohesive Zone ($M = 0.66$) and (b) Uncoupled Dugdale Cohesive Zone ($M = 0.33$).

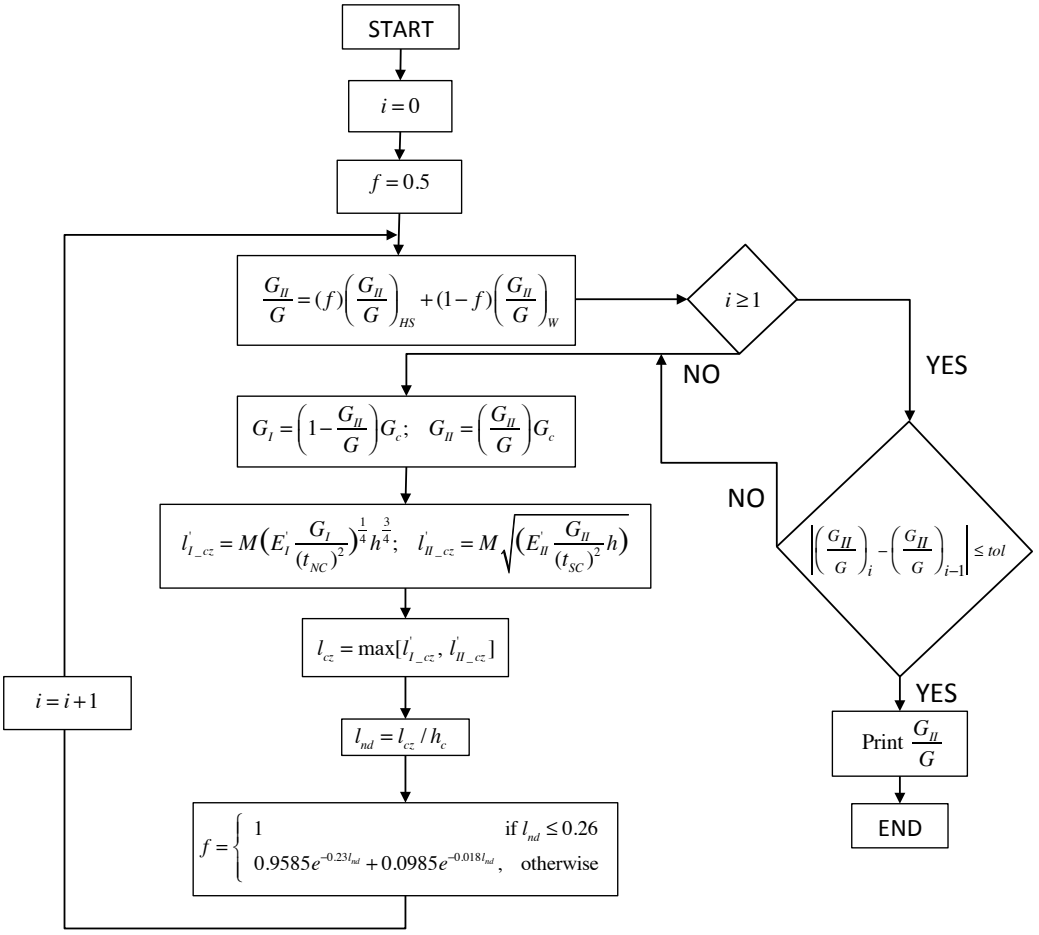

FIGURE 4.3: Program flowchart for the proposed semi-analytical cohesive analysis (SACA).

UCD Mixed Mode Partition

Cohesive Shape: Linear Softening

If experimental G_c data is inserted, this will be used in the calculation. If not, a failure locus must be specified with values of G_{Ic} and G_{IIc}

Partition

Geometry and Loading			Substrate Elastic Properties (Plane Strain)					Cohesive Strength	Failure Locus (optional) Linear, m (BK Law) 1.5		Experiment (optional)	Results					
h_1 mm	h_2 mm	k	E_{11} GPa	E_{22} GPa	G_{12} GPa	ν_{12}	ν_{23}	σ MPa	G_{IC} J/m²	G_{IIC} J/m²	G_C J/m²	G_{II}/G	l_{ss} mm	f	G_{II}/G (W) f = 0	G_{II}/G (HS) f = 1	No. of Loops i
0.73333	3.6667	0	125	10	3.4	0.3	0.38	44			289.132022	0.2828	1.3033	0.7294	0.0033	0.3865	8
0.91827	3.4817	0	125	10	3.4	0.3	0.38	44			319.52113	0.2916	1.5569	0.7417	0.0090	0.3901	8
1.2355	3.1645	0	125	10	3.4	0.3	0.38	44			333.725452	0.3119	1.9088	0.7650	0.0348	0.3971	7
1.1877	3.2123	0	125	10	3.4	0.3	0.38	44			342.995129	0.3074	1.8834	0.7586	0.0290	0.3959	7
1.2847	3.1153	0	125	10	3.4	0.3	0.38	44			363.538714	0.3124	2.0329	0.7591	0.0417	0.3983	7
1.4692	2.9308	0	125	10	3.4	0.3	0.38	44			302.729323	0.3343	2.0522	0.7887	0.0775	0.4031	7
1.4614	2.9386	0	125	10	3.4	0.3	0.38	44			318.519845	0.3319	2.0919	0.7830	0.0757	0.4028	7
1.7075	2.6925	0	125	10	3.4	0.3	0.38	44			312.287059	0.3574	2.3236	0.7946	0.1538	0.4101	6
1.7148	2.6852	0	125	10	3.4	0.3	0.38	44			326.341477	0.3571	2.3793	0.7902	0.1567	0.4103	6
1.7118	2.6882	0	125	10	3.4	0.3	0.38	44			346.328567	0.3551	2.4422	0.7838	0.1555	0.4102	6
1.8677	2.5323	0	125	10	3.4	0.3	0.38	44			334.904447	0.3761	2.5815	0.7910	0.2272	0.4154	6
1.8506	2.5494	0	125	10	3.4	0.3	0.38	44			350.134229	0.3728	2.6159	0.7859	0.2185	0.4148	6
1.9561	2.4439	0	125	10	3.4	0.3	0.38	44			359.551534	0.3878	2.7796	0.7847	0.2753	0.4186	5
2.1907	2.2093	0	125	10	3.4	0.3	0.38	44			355.528738	0.4269	3.0692	0.7880	0.4224	0.4282	3
2.2019	2.1981	0	125	10	3.4	0.3	0.38	44			378.415547	0.4289	3.1819	0.7805	0.4298	0.4287	3
2.1747	2.2253	0	125	10	3.4	0.3	0.38	44			400.071139	0.4239	3.2323	0.7742	0.4117	0.4275	4
2.3828	2.0172	0	125	10	3.4	0.3	0.38	44			362.431869	0.4663	3.3774	0.7449	0.5511	0.4372	5
2.5844	1.8156	0	125	10	3.4	0.3	0.38	44			369.13671	0.5195	3.7471	0.6880	0.6771	0.4481	6

FIGURE 4.4: Excel macro layout.

4.5 Numerical Verification

The proposed SACA approach outlined in fig. 4.3 is tested here for its ability to predict the numerical damage length and mode partition for general numerical cases using the coupled linear softening cohesive zone. The AFRMM (fig. 3.11(a)) test case is used as before but with a number of changes to the substrate and cohesive properties. The substrate Young's modulus is set to 75 GPa and the tests are carried out at $\gamma = 0.1$, 0.2, 0.5, 2, 5, 10. For each γ ratio, five different cohesive toughnesses are tested corresponding to 250, 500, 1000, 2000 and 3000 J/m^2. A linear failure locus is again assumed, with $G_{IC} = G_{IIC}$. In each case the cohesive strength is set to $t_{NC} = t_{SC} = 45MPa$. This results in a total of 30 simulations. The test cases are simulated in Abaqus as before and the mode partition is calculated by applying the mode decomposed J integral (eq. 3.11) along the cohesive surfaces when the simulations reach steady state. The cohesive lengths are also recorded. Before analysing the prediction of mode partition and cohesive zone lengths from the SACA approach, it is possible to use the numerical results to check the validity of the unique empirical curve proposed in eq. 4.4 using the new numerical data. To do this, the normalised mode mixity is plotted against the normalised cohesive zone length for each of the new simulations in fig. 4.5. It can be seen that the proposed empirical curve accurately describes the normalised mode mixity as a function of the normalised cohesive zone length for the new numerical data, and hence adds further weight to the argument that the observed dependence between normalised mode mixity and normalised cohesive zone length is unique.

Once the cohesive zone lengths and mode partitions are recorded from the numerical solution, the required parameters are independently entered into the SACA analysis in order to estimate the cohesive zone lengths and mode partitions. The required parameters are: geometry and loading conditions (h_1, h_2, k); substrate elastic properties $(E_{11}, E_{22}, G_{12}, v_{12}, v_{23})$; cohesive strength (t_C) and cohesive zone shape (M). In the SACA partitioning of this numerical case, G_c is found from the assumed failure locus at a given mode mixity. The SACA predicted damage lengths are plotted against the numerically obtained damage lengths in fig. 4.6(a), and the SACA predicted mode partitions are plotted against the numerically obtained mode partitions in fig. 4.6(b). There is some small scatter in the prediction of the damage length in fig. 4.6(a), though the general trend is accurately predicted. This suggests there may be scope for improvement of the analytical cohesive zone length estimation. However, the predicted mode partitions in fig. 4.6(b) are in very good agreement with the numerically obtained mode partition. This suggests that the mode partition is not overly sensitive to small scatter in the cohesive length estimation, and that the semi-analytical model is sufficient to

give a good estimate of the mode partition in the general case. This SACA approach therefore eliminates the need to numerically model each case individually and makes it feasible to estimate the mode mix efficiently based on substrate and cohesive properties. In the following section, this semi-analytical cohesive analysis is applied to a number of experimental case studies taken from literature.

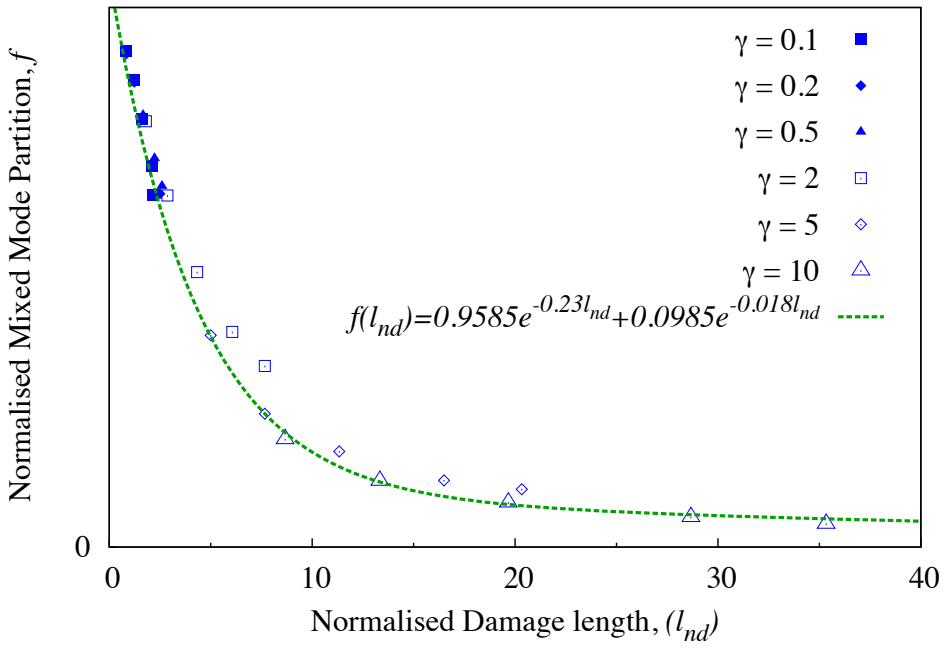

FIGURE 4.5: Numerically obtained damage length scale plotted against the normalised mode mixity, f, for the AFRMM verification test cases using the linear softening cohesive zone.

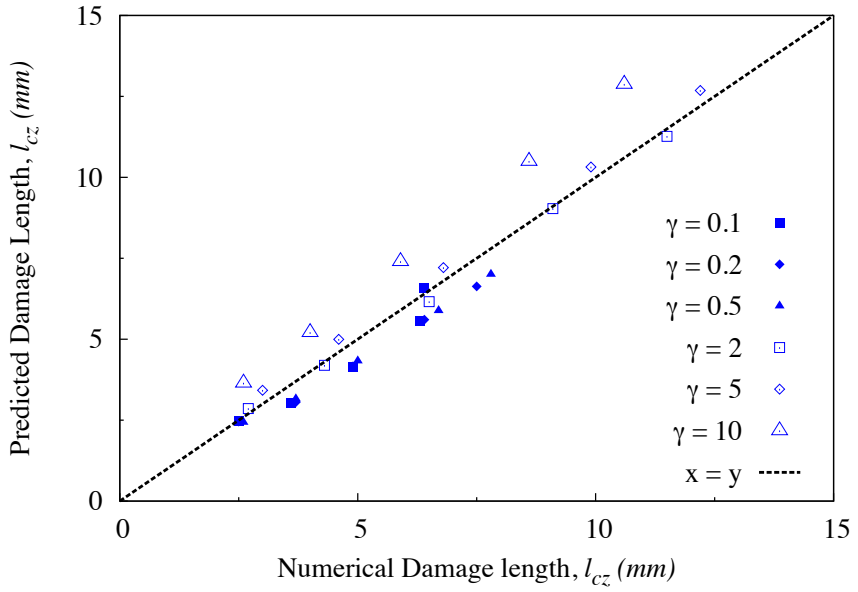

(a) Cohesive Zone Length

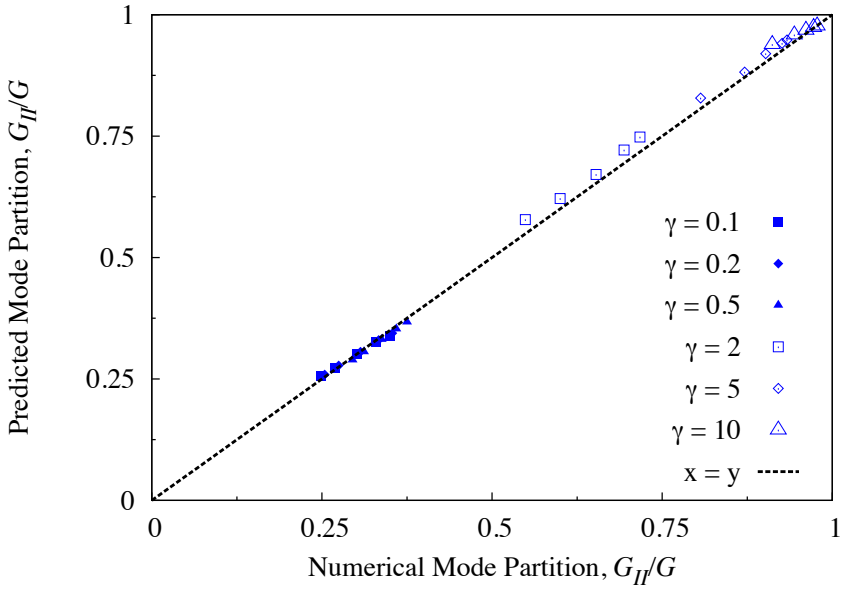

(b) Mixed Mode Partition

FIGURE 4.6: Numerically obtained (a) cohesive zone length, and (b) mode mixity, plotted against SACA predicted damage length and mixed mode partition, respectively, for the AFRMM verification test cases using the linear softening cohesive zone.

4.6 Experimental Case Studies

4.6.1 Introduction

Two case studies from the literature are analysed in this section using the new SACA procedure. In each case, the required properties and loading conditions are obtained from the respective papers and the SACA partitioning is performed using the newly developed excel macro. The predicted failure locus from SACA partitioning is compared to the failure loci predicted by each of the analytical partitioning theories ([20],[26],[27],[28]) and conclusions are drawn about the applicability of each method for partitioning fractures in composites. These two experimental case studies are of particular interest as it is believed they will give a lower and upper bound to the SACA solution. In both original papers, both the partitioning theories of Suo and Hutchinson [26] and Williams [20] are assessed.

In the case of Hashemi et al. [32] where asymmetric fracture tests were carried out on CFRP, the global partitioning of Williams [20] was found to produce a failure locus very close to the expected linear pattern (eq. 3.7), whereas the local partitioning of Suo and Hutchinson [26] did not perform well in predicting a physical failure locus. It was argued in this paper that the damage zone likely exceeded the K dominant region and hence this explained the poor performance of the local solution. It was argued that in such cases that the global solution of Williams [20] should be used to partition. However, it has been seen in the previous chapter that once the damage region grows beyond the K dominant region, the mode partition is not instantly predicted by the global solution of Williams [20], but instead there is a gradual deviation towards the global solution which is found to be uniquely controlled by the normalised cohesive zone length. As this dependency has been measured numerically, it is of interest to see how 'local' or 'global' the predicted mode partitions will be, and whether the predicted SACA partitioning can accurately predict a physical failure locus. A recent study by Harvey and Wang [35] carried out a similar study on this particular data set. In this study, the cases were repartitioned using their newly developed Euler and Timoshenko partitioning theories. It was concluded that the Euler beam theory partitioning of Wang and Harvey [28](WH) best described the failure in this composite system. This conclusion was made on the basis that the linear failure locus was indeed correct. The non-singular field partitioning theory of Davidson et al. [27](D-NSF) was developed by fitting data from CFRP asymmetric fracture tests so it is expected to perform well in partitioning this data set also.

In the second case study, Ducept et al. [33] found that the local partitioning of GFRP delamination accurately predicted the measured failure locus. In this study, the failure locus was measured using symmetric mixed mode bend specimens (fig. 1.4) so it was known to be correct. Ducept et al. [33] found that the global partitioning did not reproduce the measured failure locus and therefore it was deemed to be an inaccurate method of partitioning. It is of interest to see if the SACA partitioning can reproduce the measured failure locus based on the substrate and cohesive properties. It is also of interest to see how the partitioning theories of Wang and Harvey [28] and Davidson et al. [27] will perform in partitioning fractures in GFRP composites. Overall, this study provides an experimental assessment of the general performance and usefulness of each of the partitioning theories, with a particular focus on the new damage dependent SACA partitioning approach.

4.6.2 Hashemi et al.

The first case study is on the AFRMM delamination tests carried out by Hashemi et al. [32] on uni-directional carbon fibre epoxy composite. In this original work, it was found that global partitioning produced the most physical failure locus when applied to partition the asymmetric test data. It was therefore suggested that global partitioning should be used to partition fractures in such material systems. Using the data presented in this paper, it was possible to obtain the beam height ratios and dimensions, and re-partition the data according to the SACA approach, Wang and Harvey [28] Euler (WH) and Davidson et al. [27] non singular field (D-NSF) partitioning theories. Typical uni-directional carbon fibre epoxy elastic properties were assumed as they were not presented in the paper. The values used were $E_{11} = 120\ GPa$, $E_{22} = 10\ GPa$, $G_{12} = 4.6\ GPa$, $v_{12} = 0.3$, $v_{23} = 0.38$. The values of G_c at each height ratio are taken directly from the experimental measurements presented in the paper. The transverse tensile strength of the composite system was used as the cohesive strength, and this was assumed equal in normal and shear. The transverse tensile strength for this composite is 44 MPa [100]. Finally, a value of the shape parameter M must be chosen; Svensson et al. [99] recently measured mode I and mode II cohesive zone laws in carbon fibre reinforced composite and found that a trapezoidal law accurately described the stress as a function of opening displacement. Therefore, both the linear softening ($M = 0.66$) and Dugdale ($M = 0.33$) cases are used here in the SACA analysis as they give an upper and lower bound for the trapezoidal shape. The predicted partitions according to the SACA approach are presented in fig. 4.7 for both the linear softening (L) and Dugdale (D) cohesive zones; these are plotted alongside each of the analytical partitioning theories.

In all cases, the SACA partitioning predicts that the partition lies between the local and the global partitioning. For $\gamma < 1$, the partitioning is closer to the local solution of Suo and Hutchinson [26], and as γ becomes large and mode II becomes dominant, the partitioning approaches the global solution of Williams [20]. In this region of $\gamma > 1$, the SACA partitioning is closest to the analytical solutions of Wang and Harvey [28] and Davidson et al. [27]. As expected, the linear softening cohesive zone partitioning lies closer to the global partitioning compared to the Dugdale partitioning; this is due to the larger cohesive zone length prediction in the linear softening case. The predicted failure loci based on the linear softening and Dugdale partitioning are presented in fig. 4.8, along with the predicted failure loci from the Wang and Harvey [28] (WH) and Davidson et al. [27] (D-NSF) analytical partitioning theories. These are also compared to the local(HS) and global(W) partitioning of the data, which were presented in the original paper. It is immediately evident that each of the partitioning theories are compatible with the data except for HS partitioning. In order to obtain a quantitative assessment of the accuracy of each of the methods, a linear failure locus is assumed to be correct and the least square errors (LSE) are calculated for each partitioning method, where LSE is defined as:

$$\text{LSE} = 100 * \sqrt{\frac{\sum_{1}^{N} \left(\frac{G_{curve} - G_{data}}{G_{data}}\right)^2}{N}} \tag{4.15}$$

where N is the number of data points. For the linear failure locus, the reported mode I and mode II toughness values are used ($G_{IC} = 270 J/m^2$, $G_{IIC} = 630 J/m^2$). The LSE values are presented in table 4.9; it is evident that the SACA(L) partitioning produces the best fit to the assumed linear failure locus. As previously reported, it is also evident from the LSE values that the local partitioning does not produce overall accurate partitioning for this material system. Interestingly, fig. 4.7 indicates that the local partitioning is reasonably accurate for $\gamma < 1$ based on the SACA analysis, but not for $\gamma > 1$. While SACA(L) partitioning produces the best fit, SACA(D) partitioning is also compatible with the experimental results, and also produces a lower LSE than global partitioning. Both the WH and D-NSF partitioning produce a very similar failure locus with similar LSE values and are certainly compatible with the results.

It must be stressed that the failure locus is only assumed and therefore the LSE values are only indicative of the performance of each of the partitioning theories and are in no way absolute. The W partitioning also has a relatively high LSE value in this analysis. However, it is argued in Hashemi et al. [32] failure locus produced by W partitioning is closer to the expected shape. As the failure locus is not known explicitly in this case, the only concrete conclusions that can be made at this point is that the SACA, W, D-NSF, and WH partitioning all produce a physical failure locus, whereas the HS partitioning

does not. However, the ability of the SACA approach to predict a physical failure locus is promising and provides direct experimental evidence that demonstrates that an analytically estimated cohesive zone length can be used to predict partitioning based on the numerically observed unique dependency between local and global partitioning solutions. In the following chapter, the shortcomings of this particular case study are addressed by explicitly measuring the failure locus using symmetric specimens.

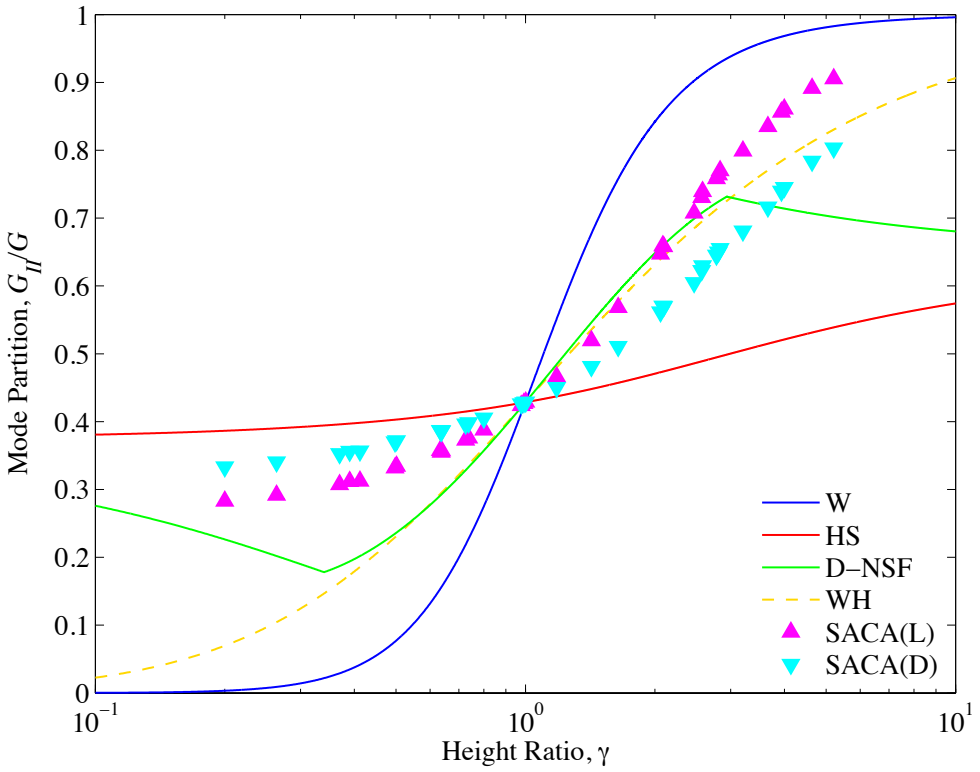

FIGURE 4.7: SACA partitioning (L-linear softening, D-Dugdale) of the AFRMM data obtained in Hashemi et al. [32]

4.6.3 Ducept et al.

The second case study is based on experimental data of Ducept et al. [33]. In this paper, ADCB and asymmetric mixed mode bend (AMMB) test cases were carried out on glass fibre reinforced epoxy composite for a number of different height ratios and moment ratios respectively. AMMB cases are those in which unequal moments are applied to asymmetric substrate arms. The asymmetric tests were then partitioned according to the global and local approaches, and, unlike the previous case study, the resulting failure loci were compared to the true failure locus, which was measured using symmetric specimens. It was found that local partitioning accurately predicted the symmetrically measured failure locus, while the global partitioning did not produce

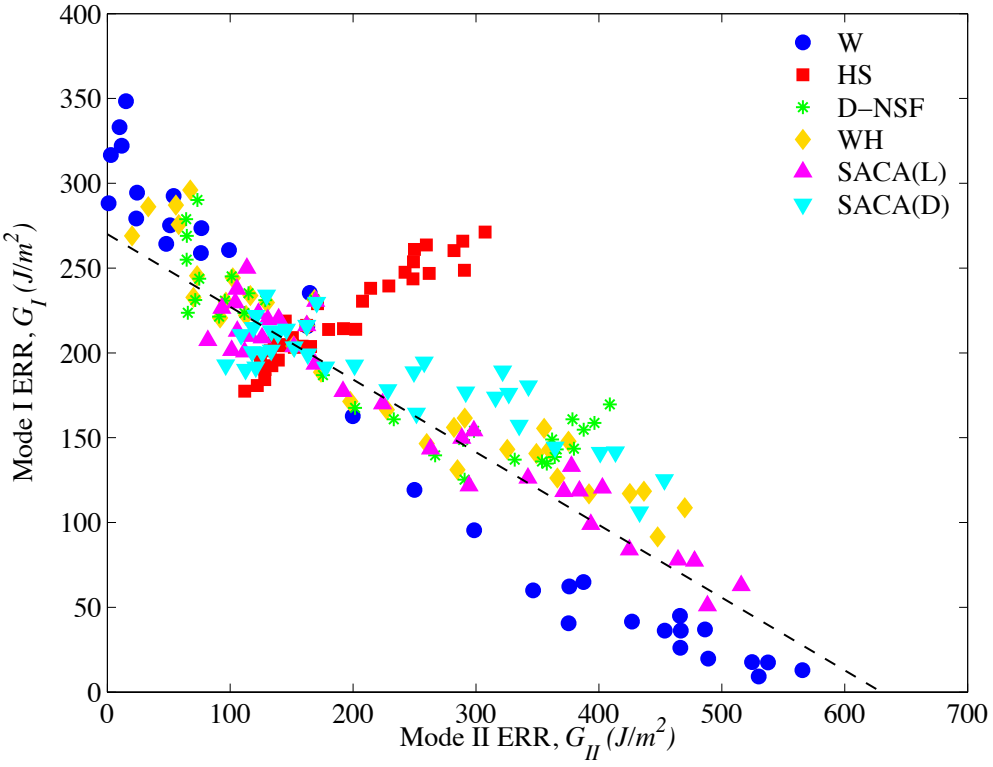

FIGURE 4.8: Predicted failure loci resulting from partitioning of the AFRMM data obtained in Hashemi et al. [32] compared to assumed linear failure locus.

Partitioning Method	Least Squares Error (LSE)
W	15.7%
HS	17.1%
D-NSF	9.2%
WH	7.7%
SACA(L)	5.5%
SACA(D)	9.6%

FIGURE 4.9: Least square errors associated with partitioning of Hashemi et al. [32].

physically consistent results. It was therefore deemed that local partitioning should be used to partition for this material system. The ADCB and AMMB data of Ducept et al. [33] are re-partitioned here using the SACA approach. The glass fibre reinforced epoxy composite elastic properties are given as $E_{11} = 25.7\ GPa$, $E_{22} = 6.5\ GPa$, $G_{12} = 2.5\ GPa$, $v_{12} = 0.32$ and $v_{23} = 0.38$. The values of G_c for each test case are reported in the paper. Again, the transverse tensile strength was used as the cohesive strength, which was again assumed equal in normal and shear; the transverse tensile strength for this composite was not directly available, so a value of 48 MPa, which is typical for GFRP composite, is assumed. As before, both the linear softening ($M = 0.66$) and Dugdale ($M = 0.33$) cohesive zone shapes are used, as they give upper and lower bound results for various trapezoidal cohesive zone shapes. The predicted SACA partitioning, for both

linear softening and Dugdale cohesive zones, are presented in fig. 4.10(a) for the ADCB test cases, and in fig. 4.10(b) for the AMMB test.

It is evident that the SACA partitioning for both the ADCB and AFRMM, for linear softening and Dugdale cohesive zones, is very close to the local partitioning for this material system. The predicted failure loci based on these partitioning results are presented in fig. 4.11. Also presented in fig. 4.11 are the predicted failure loci according to the W, HS, D-NSF and WH partitioning theories, and the symmetrically measured failure locus. The symmetrically measured failure locus is approximated using the BK failure criterion and is given in Ducept et al. [33] as:

$$G_c = 246 + (1680 - 246)\Big(\frac{G_{II}}{G}\Big)^{1.5} \tag{4.16}$$

The LSE errors between the predicted failure loci and the measured failure locus are presented in table 4.2. As outlined in Ducept et al. [33], HS partitioning produces a failure locus close to the symmetrically measured locus, while it is evident that the W partitioning is not compatible with the results. Both the W and WH partitioning predict that the ADCB test remains in pure mode I for all beam height ratios (fig. 3.17). However, the total toughness of the joint is considerably dependent on the beam height ratio in the ADCB test and so it is evident that it does not remain a pure mode I test. Therefore, the partitioning theories of W and WH do not produce physically consistent results and it is evident from the LSE values in table 4.2 that these should not be used to partition this material. While D-NSF partitioning performs slightly better than both W and WH in predicting the measured failure locus, it is still not compatible with the experimental results (LSE=33.2%). The SACA partitioning, using both the linear softening and Dugdale cohesive zones, are both compatible with the experimental results. The local partitioning and SACA(D) perform best when comparing the least squares error (LSE) (eq. 4.15). However, there are only relatively small differences between the resulting failure loci between SACA(D) and SACA(L) partitioning in this case. It is believed that due to the relatively low substrate modulus in this case (25.7 GPa) and the fact that the specimens are loaded in predominantly mode I in all cases, the resulting cohesive zone lengths are small and hence the predicted SACA partitioning is in good agreement with local partitioning. This prediction, which again is in agreement with the experimental results, further demonstrates that the SACA approach can be used to accurately predict mode partitioning.

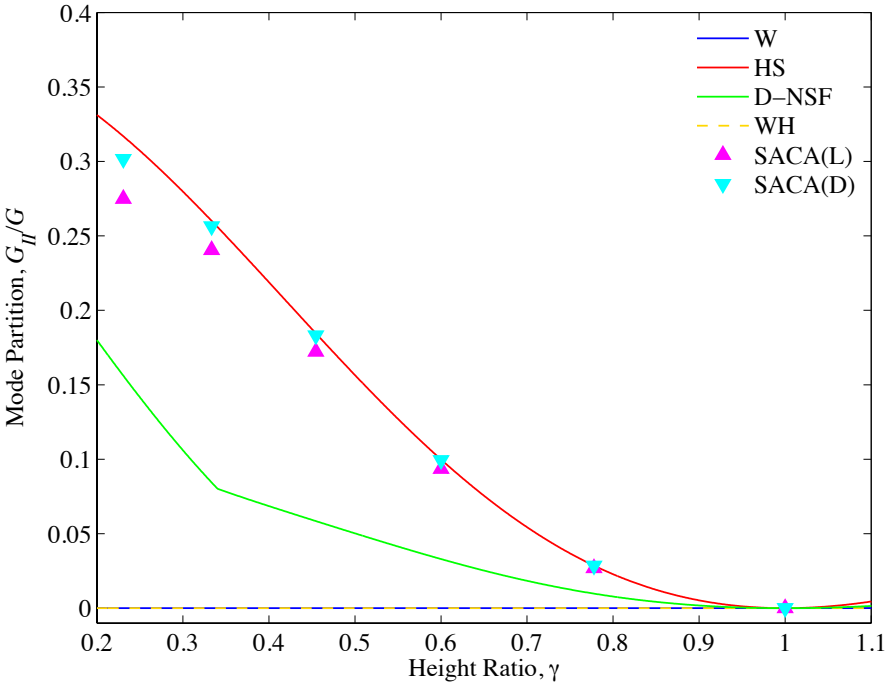

(a) ADCB Partitioning

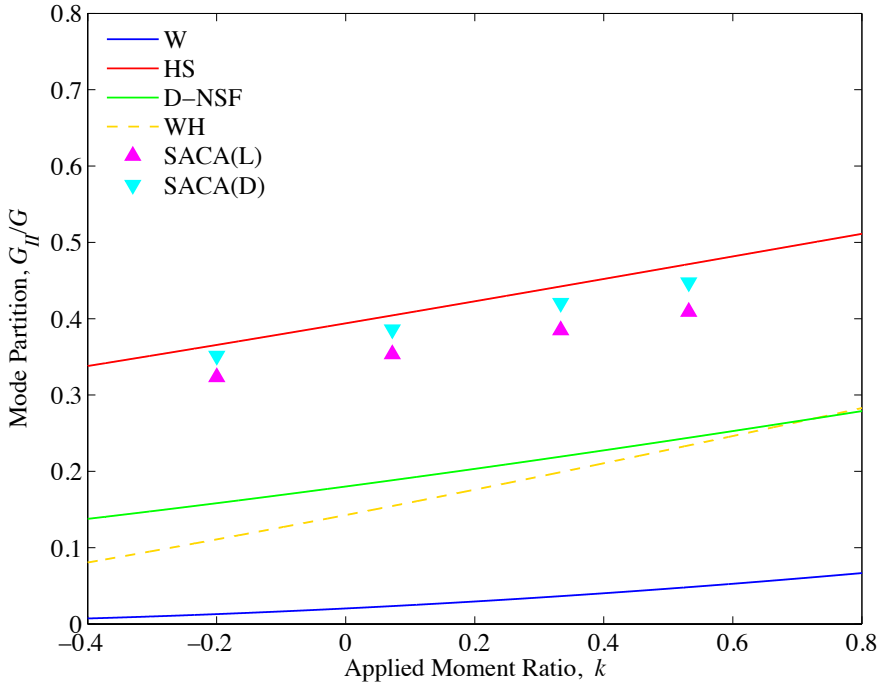

(b) AMMB Partitioning

FIGURE 4.10: SACA (L-linear softening, D-Dugdale) partitioning for (a) ADCB test data and (b) AMMB test data obtained from Ducept et al. [33].

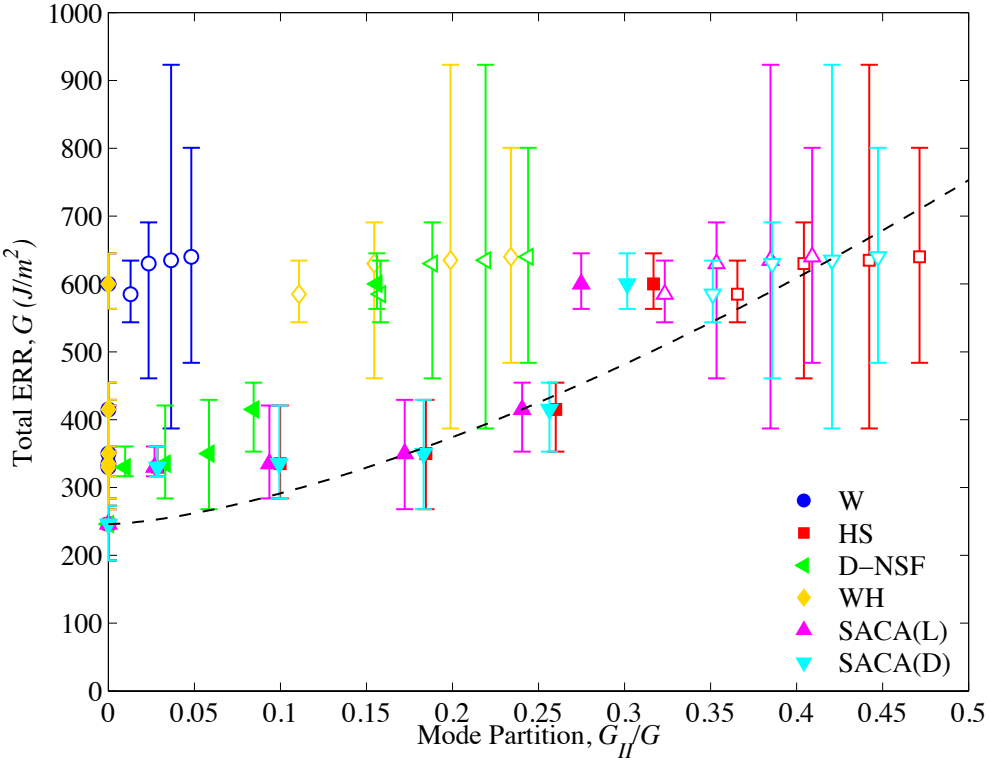

FIGURE 4.11: Predicted failure loci resulting from local, global and SACA (L-linear softening, D-Dugdale) partitioning of the ADCB (filled markers) and AMMB (unfilled markers) data obtained in Ducept et al. [33]. The predicted failure loci are compared to the symmetrically measured failure locus.

Partitioning Method	Least Squares Error (LSE)
W	46.2%
HS	10.9%
D-NSF	33.2%
WH	38.7%
SACA(L)	13.3%
SACA(D)	11.1%

TABLE 4.2: Least square errors (LSE) associated with partitioning of Ducept et al. [33].

4.6.4 Discussion

From two experimental case studies, only the SACA partitioning was consistent with both sets of experimental data. In the partitioning of CFRP data taken from Hashemi et al. [32], each of the partitioning theories except the local partitioning of Suo and Hutchinson [26] could be used to obtain a physical failure locus. As the exact failure locus was not measured explicitly, no further conclusions could be made about the performance of the remaining partitioning theories, though SACA(L) performed best in predicting an assumed linear failure locus, followed by the WH partitioning. In the second case study, the only partitioning methods which were consistent with the results were the local partitioning of Suo and Hutchinson [26] and SACA. As the failure locus was measured explicitly in this case, it is possible to accurately assess the performance of each of the partitioning approaches. The fact that none of the traditional partitioning theories (HS, W, D-NSF, WH) can be used to accurately partition both experimental case studies is in agreement with the findings of chapter 3 where it was observed that the actual partitioning was dependent on the level of damage which developed at the crack tip. In the experiments carried out by Ducept et al. [33], the loading was predominantly mode I which produces smaller cohesive zone lengths. At mode I loading, the toughness was also relatively low and when this is coupled with the fact that the substrates are relatively flexible, the predicted cohesive zone lengths are small enough so the SACA approach predicts that the actual partitioning is close to the local solution, which is in agreement with the experimental findings. On the other hand, in the asymmetric CFRP tests carried out by Hashemi et al. [32], the cohesive zone lengths are predicted to grow when the loading becomes mode II dominant ($\gamma > 1$), which moves the partitioning solution away from the local solution towards the global solution in this region. When these predicted partitions are applied to partition the data, they produce the best fit (SACA(L)) to an assumed linear failure locus.

Combining the results from the two experimental case studies, it can be concluded that the size of the damage zone clearly has an effect on the correct mode partition. For small damage zones, the correct partitioning solution is close to the local solution of Suo and Hutchinson [26] and as the damage zone grows in size, the partition of energies moves away from the local solution of Suo and Hutchinson [26] and towards the global solution of Williams [20]. These findings are in agreement with the numerical findings outlined in chapter 3. Secondly it can be concluded that, based on the success of the SACA approach in predicting the assumed and measured failure loci respectively, the unique dependence between the mode partition and cohesive zone length observed numerically

is also reproduced experimentally, and therefore the SACA approach can be used to accurately predict mixed mode partitions in asymmetric fracture tests.

4.7 Chapter Conclusions

Based on the observed unique dependency between the normalised mode mixity and normalised cohesive zone length in chapter 3, a semi-analytical cohesive analysis (SACA) is proposed for calculating mixed mode partition. This method utilises the analytical estimations of cohesive zone length [96] to determine the mode mixity from the unique dependency curve. Equations are proposed for calculating cohesive zone lengths in asymmetric geometries under general mixed mode conditions; these are found to give reasonable estimates when a shape factor, M, of 0.66 is used for the linear softening cohesive zone, and a shape factor of 0.33 is used for the Dugdale cohesive zone. The required parameters in the SACA analysis are; substrate elastic properties; beam geometry and loading; cohesive strength and shape factor M. A value of G_c is also required for the analysis; this can be obtained directly from experiments, or in the absence of this data, can be estimated directly from an assumed failure locus. The method is found to work well in predicting mixed mode partitions when compared directly to numerically measured values in a verification test case using the coupled linear softening cohesive zone. The proposed unique dependency curve is also found to hold true for this verification test case. The SACA procedure, which is the first partitioning theory to take the damage state at the crack tip into account, is implemented as an excel macro which is made available to download for general use.

Finally, the proposed SACA method is used to re-partition AFRMM and ADCB/AMMB test data from previously conflicting studies in the literature [32, 33], along with the analytical partitioning solutions presented in chapter 1 (i.e. W,HS,D-NSF,WH). Both linear softening and Dugdale cohesive zone shape factors are used in the SACA partitioning as they give an upper and lower bound to the trapezoidal law. It was found that the SACA partitioning (Linear softening and Dugdale) produced results compatible with both case studies, something which all other analytical partitioning theories (W, HS, D-NSF, WH) failed to do. The main conclusions drawn from this study are:

- The mixed mode partition is dependent on the level of damage which develops in experimental tests. Therefore, analytical partitioning theories, none of which account for damage, cannot be used to partition in the general case.

- The unique dependency curve observed in chapter 3 captures the experimentally observed shift from the local(HS) towards the global(W) partitioning as the size of the damage zone increases.
- The proposed semi-analytical cohesive analysis proves an efficient and accurate method for predicting mixed mode partitions.

While the general accuracy of the SACA procedure was assessed in the final section of this chapter, there was one obvious downfall in the analysis of the CFRP data obtained from Hashemi et al. [32] and that was that the predicted failure loci were only compared to an assumed failure locus for each method. This only allowed the very un-physical partitioning of HS to be discarded and meant that one could not make concrete conclusions about the most appropriate partitioning approach from the remaining approaches. In the following chapter, the failure locus of CFRP composite is measured using symmetric specimens loaded with uneven bending moments. This failure locus is then used as a benchmark to assess the performance of the various partitioning theories including SACA to determine which is the most appropriate for partitioning asymmetric fractures in CFRP composite.

Chapter 5

Experimental Analysis

5.1 Introduction

In this chapter, the accuracy of each of the analytical partitioning theories (W [20], HS [26], D-NSF [27], WH [28]), along with the newly developed SACA procedure, are assessed by carrying out symmetric and asymmetric tests on AS4/8552 (carbon/epoxy) composite. This assessment is based on the same principle that is used in the previous chapter when analysing experimental tests taken from the literature. In the case of the experiments carried out by Ducept et al. [33], the correct failure locus was determined by testing symmetric specimens in the mixed mode bend test rig. Therefore, when the asymmetric specimens were tested, they could be compared to the symmetrically measured failure locus and concrete conclusions could be made about the validity of each of the partitioning techniques; in this case it was found that only SACA and the local partitioning of Suo and Hutchinson [26] produced mode partitions that were consistent with the experimental results. However, in the test cases of Hashemi et al. [32], the true failure locus was not known explicitly, and it was assumed to follow a linear criterion (eq. 3.7). Based on this assumed linear criterion, it was found that the partitioning predicted by each of SACA, W [20], D-NSF [27] and WH [28] produced results which could be compatible with the experimental results, and only the local HS [26] partitioning produced results which did not follow a vaguely linear pattern. As SACA was the only partitioning approach to be compatible with both sets of experimental results, this was concluded to be the most accurate partitioning procedure.

However, while the evidence in the previous chapter suggests that the SACA procedure is the only one able to predict accurate partitioning in the general case, this needs further verification. Specifically, due the unknown nature of the true mixed mode failure locus

in the tests carried out by Hashemi et al. [32], it was not possible to make concrete conclusions about the accuracy or applicability of each of the mixed mode partitioning theories in this case, and attempts to do so were based on an assumed failure locus. This shortfall is addressed in the current chapter by measuring the true failure locus of CFRP using symmetric specimens. As in the previous chapter, the symmetrically measured failure locus is assumed to be a material property that is unaffected by geometry or loading history.

This chapter presents an experimental study which utilises the symmetric DCB specimen loaded with uneven bending moments (DCB-UBM) [25]. The symmetric DCB specimens are loaded at different moment ratios in order to achieve different mode mixities. It has been seen that the relationship between the mode mixity and moment ratio for symmetric specimens is independent of details of the crack tip damage zone that develops during fracture, and this relationship is given correctly by each of the analytical partitioning theories (fig. 1.4). This result enables the mode mixity to be varied knowingly from pure mode I to pure mode II and therefore allows for the measurement of the true delamination failure locus. The initiation toughness, G_c, is recorded at each mode mixity and a best fit failure locus is fitted to the data. Asymmetric fixed ratio mixed mode fracture(AFRMM) tests are then carried out at different height ratios and the total initiation toughness, G_c, is measured in each case. The asymmetric tests are then partitioned according to the various analytical partitioning theories including the newly developed SACA procedure and the predicted failure loci are compared to the symmetrically measured failure locus. This allows the performance of each of the partitioning methods to be accurately assessed.

5.1.1 Chapter Layout

The layout of the chapter is as follows:

- A description of the DCB-UBM test rig and testing procedure is outlined, and the background theory is presented. The tests were carried out during a three month research visit to the Technical University of Denmark (DTU). The test rig used was developed and built by Sørensen et al. [25] at the Department of Wind Energy at DTU.
- The testing program is then outlined, accompanied by details of material and specimen preparations.
- The results of the symmetric tests are presented. This data is fitted with a number of empirical failure loci from the literature.

- The results from the asymmetric fracture tests are presented. This data is then partitioned according the the analytical partitioning theories and the new SACA procedure.
- Each of the partitioning methods are assessed by comparing the resulting failure loci to the true failure locus and relevant conclusions are drawn about the most appropriate partitioning technique.

5.2 DCB-UBM Testing

The experimental study consists of two distinct phases. Firstly, the delamination failure locus is obtained using symmetric specimens loaded with uneven bending moments on the DCB-UBM test rig. In the second part of the study, the DCB-UBM test rig is used to carry out AFRMM tests on geometries with varying γ ratios, where $\gamma = h_1/h_2$ as before.

5.2.1 A description of DCB-UBM test rig.

The DCB-UBM test setup is shown in fig. 5.1; a schematic of the DCB-UBM test rig is shown in fig. 5.2[101]. In this test setup, specimens are loaded by a combination of pure bending moments; the bending moments are induced into the substrate arms via transverse arms which are attached to the specimen and loaded through a wire and pulley system. The DCB specimen is inserted into a vertical support, which is fitted with roller bearings to enable the test specimen to move freely in vertical direction. This ensures that no net force can be induced in the sample in the vertical direction. The load blocks, which are attached to the DCB specimen during the manufacturing stage, are designed to fit exactly into the end fixtures of the transverse loading arms. This precision fit, which can be seen close up in fig. 5.3, enables the transfer of the applied moment from the transverse arms to the specimen arms, and also facilitates a quick and efficient setup and changeover of specimens. Springs are attached from the top beam to the transverse arms to negate the downward force due to the weight of the transverse arms during testing as shown in fig. 5.1. A single closed loop of wire goes around the front and back of the specimen to ensure the specimen is loaded in plane. The wire is attached to load cells at the top of the test rig and to a travelling fixture (lower beam) at the bottom of the test rig. The lower beam is attached to a screw driven motor which acts to lower the beam to increase the tension in the wire. As the wire is continuous and the pulleys are mounted on low friction bearings, the forces developed in the wire

will be constant throughout. This force is measured by the two load cells as indicated in fig. 5.2 and an average of the two readings is taken. In theory, only one load cell is required; however, monitoring the load at both sides serves as a check that the machine is operating correctly. Due to the way the wire is wrapped around the pulleys on the transverse arms, two equal and opposite parallel forces act on the transverse arms, which results in pure moments being applied. The applied moments M_1, M_2 are given by

$$\begin{aligned} M_1 &= Pl_1 \\ M_2 &= Pl_2 \end{aligned} \tag{5.1}$$

where l_1 and l_2 are the distances between the pulleys on the transverse arms as indicated in fig. 5.2. The distance between the pulleys on the transverse arms can then be changed to achieve different moment ratios and hence mode mixities according to each of the analytical partitioning theories. As the applied moments are known directly, and assuming that the substrates remain elastic throughout the test, the calculation of the applied energy release rate, G, from this test setup can be calculated from the closed form analytical solution given in chapter 1(eq. 1.1). This is rewritten here as:

$$G = \frac{6(Pl_1)^2}{B^2 E_{11}}\Big(\frac{1}{h_1^3} + \frac{k}{h_2^3} - \frac{(1+k)^2}{(h_1+h_2)^3}\Big) \tag{5.2}$$

where k is the applied moment ratio as before ($k = M_2/M_1 = l_2/l_1$), B is the substrate width, E_{11} is the Young's modulus in the bending (x_1) direction, and h_1, h_2 are the heights of the substrates that the moments M_1, M_2 are applied to respectively. Each of the values in eq. 5.2 are known prior to the test except for the load P. Unlike in standard fracture mechanics test methods where direct loads are applied (e.g. DCB, FRMM, ELS), the toughness calculation in the DCB-UBM test does not require the crack length to be known or estimated. This eliminates the need to measure the crack length during the test and is one of the distinct advantages of the DCB-UBM test method over other standard fracture test methods.

There are a number of assumptions in this test method and these are investigated in detail in Sørensen et al. [25]. Firstly, it is assumed in the calculation of ERR in eq. 5.2 that the forces act perpendicular to the transverse arms throughout the test. However, it is evident that this is not the case due to the rotation of the arms. The error created by this assumption is minimised by starting with the transverse arms 10° off horizontal position in the direction opposite to the rotation. The test then rotates the arm through the horizontal position and the test is stopped after a rotation of 20° (i.e. when the transverse arm reaches 10° off horizontal in the direction of rotation). Sørensen et al. [25] calculated the error associated with this assumption and found that it was always

less that 6% when the rotation was kept to a maximum of 20°. The 10° offset of the transverse arms at the beginning of the test is evident from figs. 5.1 and 5.3. As a maximum rotation of 20° is allowed during the test, this places considerable size requirements on the specimens to ensure that complete fracture is achieved within this rotation. It is for this reason that the samples used in this study are considerably thicker ($\approx 6-10mm$) than what is commonly used in standard fracture tests ($\approx 3-5mm$). Eq. 3.13, which was presented in chapter 3, can be used to estimate the required thickness for a given material based on an expected toughness value. Due to the rotation of the arms, there is also slight deflections of the transverse arms in the horizontal direction. However, any effects of this are effectively negated by having a very large distance between the upper and lower beams, as seen in fig. 5.1. Another assumption is that there is no friction in the pulleys or between the pulleys and the wires, which will not be the case in reality. Sørensen et al. [25] measured the friction by pulling the wire along it's direction when it was under different loads during a test. They found that the frictional load increased proportionally with the applied load but reported that the increase in moment due to friction was $< 3\%$ of the applied moment and so it was also deemed negligible. Finally, in order to apply eq. 5.2 to calculate the fracture toughness, it is paramount that the substrates remain elastic throughout the test. This is checked on an individual basis by unloading the beams and making sure they return to their original position with no visible permanent deformation. Due to the high strength of CFRP, it is not believed that yielding will occur during these tests.

5.2.2 DCB-UBM Test Procedure

For each test, the distance between the pulleys is first set depending on the mode mixity that is required. The relationship between the mode mixity (G_{II}/G) and the pulley distances (l_2/l_1) is given by eq. 5.3 for symmetric specimens:

$$\frac{G_{II}}{G} = \frac{1}{1 + \frac{4}{3}\frac{(1-l_2/l_1)^2}{(1+l_2/l_1)^2}} \tag{5.3}$$

The specimen is inserted between the roller supports so that the angles between the horizontal surface of the support and each side of the specimen are 90°; this is checked using a square angle ruler. The specimen support is then moved vertically so that the specimen load blocks are equidistant between the upper and lower beams; this minimizes the error due to the horizontal movement of the transverse arms during testing. Before the transverse arms are attached, the attached springs are adjusted so that the arms hang freely in equilibrium at the same height as the specimen load blocks in order to negate the downward force due to the weight of the transverse arms during the test.

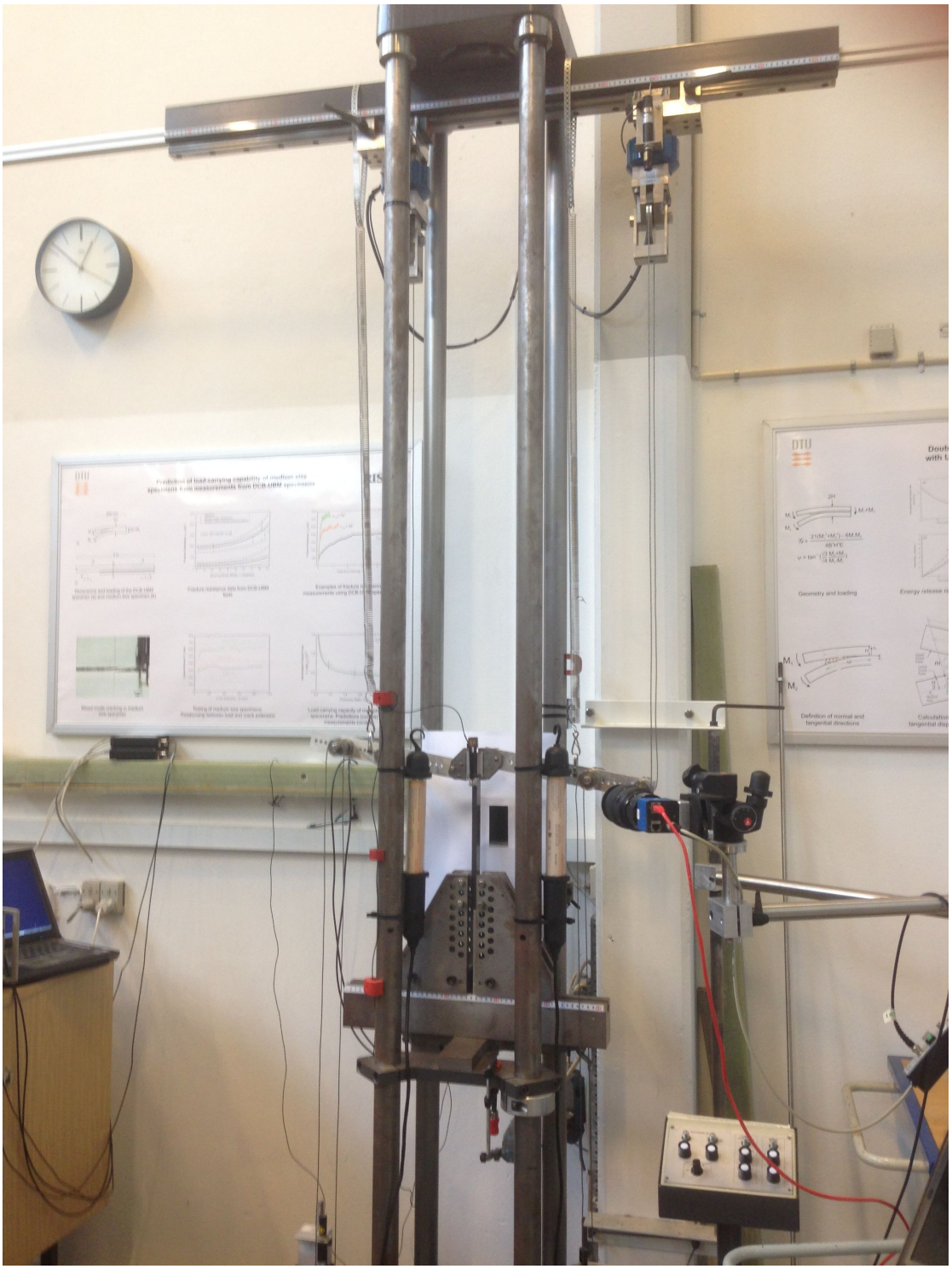

FIGURE 5.1: DCB-UBM test rig.

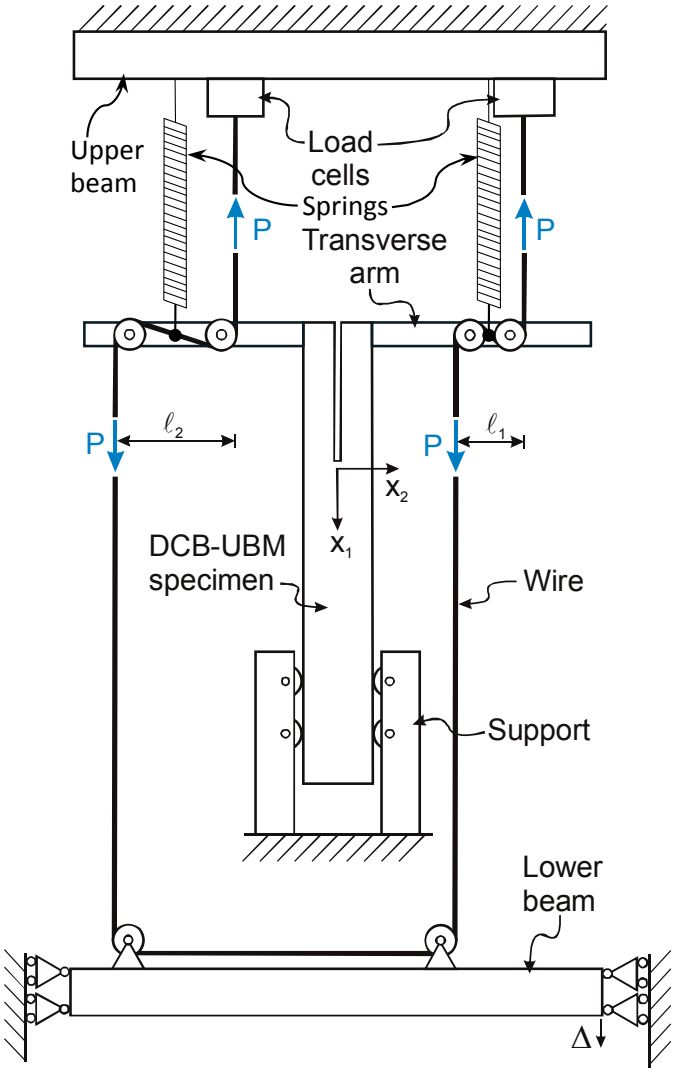

FIGURE 5.2: Schematic of DCB-UBM test rig [101].

When the transverse arms are attached, the top and bottom pulleys are then aligned with the transverse arm pulleys with the aid of a laser beam. At this point, it can be chosen in what direction the transverse arm will rotate; if an upwards rotation is required on a given arm, then the upper beam pulley is aligned with the outermost pulley of the transverse arm and the lower beam pulley with the innermost pulley of the transverse arm, and vice versa if a downward rotation is required. The wire loop is then placed around the transverse arm pulleys and pulled tight using the adjustable wire joiner which completes the loop. In the symmetric tests, the crack tip opening is also monitored. In these cases, an extensometer is attached to two pins, which are inserted into the centre of the beams at the crack tip during specimen preparation. The placing of the pins and extensometer are shown in fig. 5.3(a) and fig. 5.3(b) respectively. The extensometer openings are processed by a data acquisition system which synchronises the load cell readings and the the extensometer openings. During the test, a camera is

also mounted on the frame and focused at the crack tip. Images are taken with a 12 mega pixel camera at a rate of 1 image per second. The samples are sprayed with a speckled pattern using white water based spray paint to allow digital image correlation to be carried out after the test. Digital image correlation is intended for use here as a method of measuring the opening and shearing displacements at the crack tip, with a view to using these to deduce the mixed mode cohesive laws from the J integral method, as used by Sørensen and Jacobsen [102]. The data acquisition system is set up to trigger the camera so that the captured images can be synchronised with the measured load. The sample is illuminated with two LED lamps as shown in fig. 5.1. The results from the DIC analysis are presented in appendix E.

To start each test, the electric motor is ramped up to a constant speed, which results in the lower beam (fig. 5.2) being lowered at a constant speed of $\approx 2.5\ mm/min$. This increases the tension in the wire and results in pure moments being applied to the specimen. During the test, the load from both load cells is recorded and where applicable, the crack tip opening is recorded. The test is continued until the crack has reached the clamped area of the specimen, which ensures that at least 160 mm of crack growth is achieved in all cases. In some cases the test is stopped and unloaded following 20-30 mm of crack growth to allow the digital image correlation (DIC) camera to be moved from the initial crack tip to the new crack tip; the reasoning behind this was to see if changes in the traction separation could be measured between the initial crack tip and a fully developed damage zone, as observed numerically in chapter 3. When the crack reaches the roller supports, the lower beam is returned to its original position and the specimen is visually checked to ensure no permanent deformation has occurred.

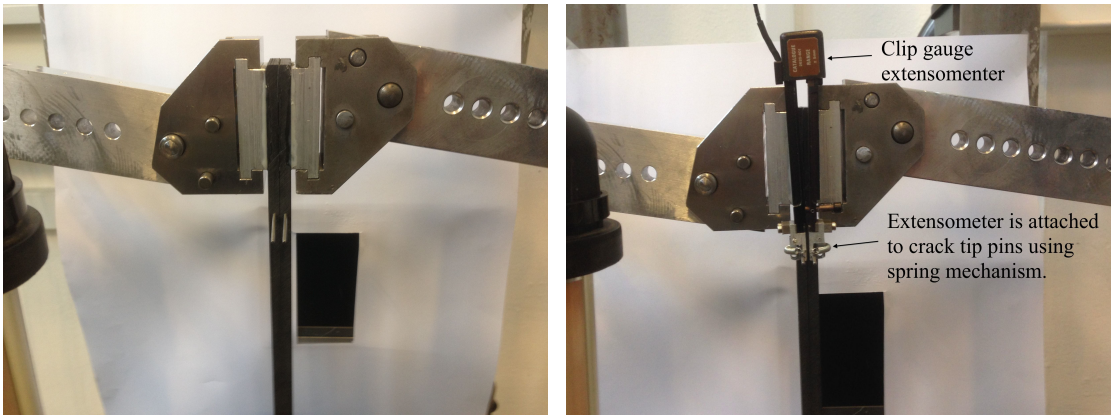

(a) Placement of pins at the crack tip.

(b) Placement of extensometer at the crack tip

FIGURE 5.3: Setup for monitoring the crack tip opening by mounting extensometer on pins, which are inserted into the beam centres at the crack tip.

5.2.3 Measuring Initiation Toughness, G_c

In order to obtain a value of the initiation toughness G_c, the value of load at crack initiation is required from each test. Crack initiation is measured from the PTFE insert. It was decided not to pre-crack the specimens before testing as there was no consistent way of pre-cracking the asymmetric specimens in mode I (due to disagreement between analytical partitioning theories as to what loading configuration produces mode I in asymmetric specimens) and it was believed that pre-cracking under mixed mode conditions would introduce varying levels of damage which would influence the re-initiation values. Therefore, as the aim of this test program is to try aand compare like with like between the symmetric and asymmetric tests, the initiation toughness G_c is measured from the insert in all cases. Also, as the PTFE insert is $< 12\mu m$ in thickness, it is deemed to be small enough to represent a physical crack. In all cases, fracture initiation is identified from a deviation in 'linearity' from a plot of the applied load vs. crosshead displacement (crosshead displacement is the displacment of the lower beam shown in fig. 5.2). An example plot of load vs. crosshead displacement is shown in fig. 5.4 for a mode I test. In all cases, the crosshead displacement is relative for each test as it is back calculated from the test time and the displacement rate, which is manually ramped up from zero. Therefore, shifts in the load vs. crosshead displacement curves along the x axis for different samples of the same batch are not indicative of a difference in the response of the samples. It is evident from fig. 5.4 that the increase in load is not directly proportional to crosshead displacement but instead takes a quadratic form. It is believed this non linear increase in load is caused by the increased tightening in the wire due to the rotation of the transverse arms towards the horizontal position, which acts to increase the length of the loop and hence further tightens the wire. In each case, the region of the curve that follows the quadratic pattern is identified and a quadratic function is fitted to this section. The maximum load up to the point of deviation from the quadratic curve is taken as the initiation load P_c. Deviation from the quadratic pattern is identified by checking for the following condition:

$$|P_{curve} - P_{test}| \geq .02P_{c\_av} \tag{5.4}$$

where P_{curve} is the quadratic fitted curve, P_{test} is the load from the test, and P_{c_av} is the average initiation load from all tests at that particular test loading and geometry. Therefore, when a deviation of 2% of the average initiation load from the fitted quadratic curve occurs, this is taken as the non-'linear' initiation point. The maximum load recorded up to this point is taken as the critical initiation load (P_c). This procedure for determining the fracture initiation point is referred to hereafter as the MAX/NL

approach. The value of 2% was chosen as it was found to be small enough to effectively detect non-'linearity', but not too small to be affected by noise in the load displacement curves. This critical load is then converted into an initiation toughness using eq. 5.2.

In the symmetric tests, an extensometer was also mounted on each specimen to monitor crack tip openings. The extensometer was mounted on two pins, which were placed at the crack tip during the specimen preparation stage (fig. 5.3). The pins, which have a diameter of $1mm$, were placed at the neutral axis of the beams so that there would be negligible effect on the stress distribution in the arms during testing and on the second moment of area of the beams. As with the digital image correlation, the measurement of the crack tip openings was intended as a method of deducing cohesive zone laws using the J integral approach, as in [82, 101, 102]. Results from both DIC and extensometer procedures are presented and discussed in appendix E. Another use for monitoring the crack tip openings is that they can be used as an alternative method of identifying fracture initiation, particularly in the mode I dominated tests. An example plot of load vs. extensometer opening is shown in fig. 5.5 for the same mode I test as is shown in fig. 5.4. In this case, the fracture initiation load is identified by taking the maximum load that occurs up to the point of a 10 μm extensometer opening. It was found that a 10 μm displacement was again small enough to detect fracture initiation but not small enough to be affected by slight misplacement of the extensometer pins, which may result in slight opening of the extensometer before fracture initiation. This procedure for identifying fracture initiation is referred to hereafter as the MAX/CTO(Crack tip open) approach. The initiation toughness, which is calculated using eq. 5.2, is compared to the results from the MAX/NL approach for each of the symmetric specimens. Unfortunately, the MAX/CTO approach could not be applied to the asymmetric specimens as the asymmetric samples were too thin to mount the extensometer pins without significantly affecting stress distribution in the beams. The use of smaller extensometer pins was not considered as they would be more likely to deform under the force of the extensometer and cause erroneous readings.

Also required in eq. 5.2 is the specimen heights and thickness, and substrate modulus E_{11}. The total thickness (h_t) is measured for each individual sample at three points using a micrometer and an average value is taken. The individual heights h_1 and h_2 are then obtained by multiplying this thickness by the beam height ratio being tested (i.e. the ratio of plies used above and below the crack starter film). The specimen width is also measured at three points along the sample using a vernier callipers and an average value is taken. The value of E_{11} required in eq. 5.2 is the flexural modulus as opposed to the direct tensile modulus, as these can differ slightly for composite materials due to the increased shear flexibility. The flexural modulus is calculated from the strain

measurements recorded during digital image correlation, and it is found to be 125 GPa; the calculation of the flexural modulus from DIC is outlined in appendix E.

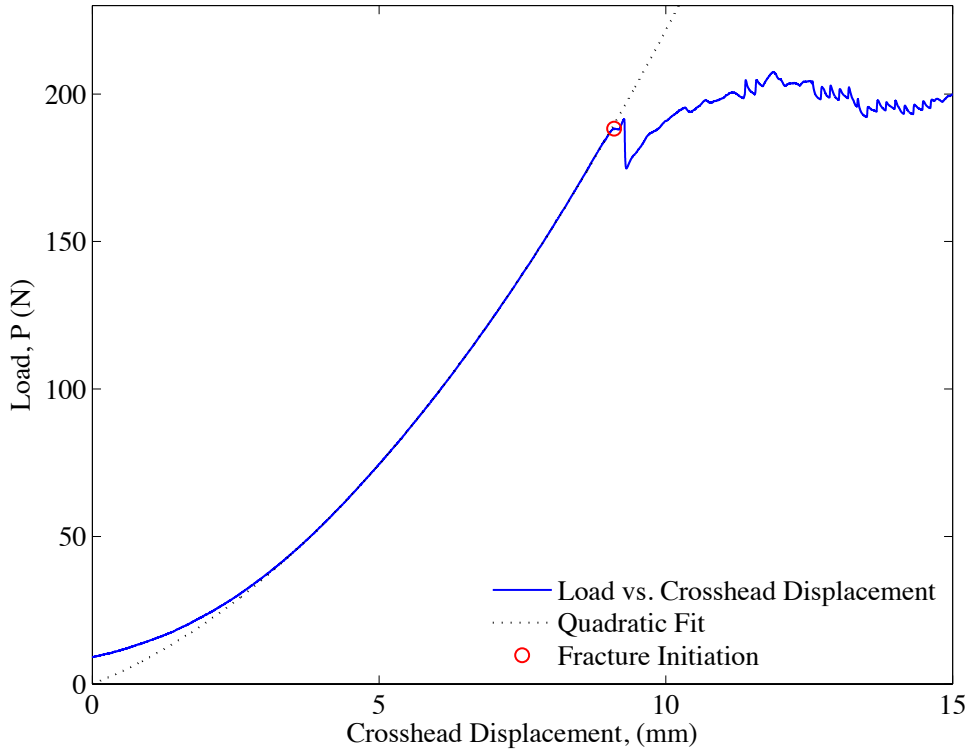

FIGURE 5.4: Example of load vs. crosshead displacement as measured in DCB-UBM mode I test.

5.3 Material and Specimen Preparation

5.3.1 Composite Material

The material used was a uni-directional AS4/8552 (carbon/epoxy) composite [103]. The high strength AS4 carbon fibres were shipped in 50 metre rolls with uncured 8552 epoxy resin already pre-impregnated in a combined prepreg tape. The nominal fibre volume of the prepreg tape is 57%. Hexply 8552 resin is a 180°C degree cure, high performance toughened epoxy resin. It is used in a wide variety of applications due to it's good impact resistance and damage tolerance. It also has excellent mechanical properties and performs well at elevated temperatures. All of these properties combine to make it ideal for use in primary aircraft structures [103]. The uncured material is stored in a freezer at $-18°$ C, where it has a shelf life of 12 months.

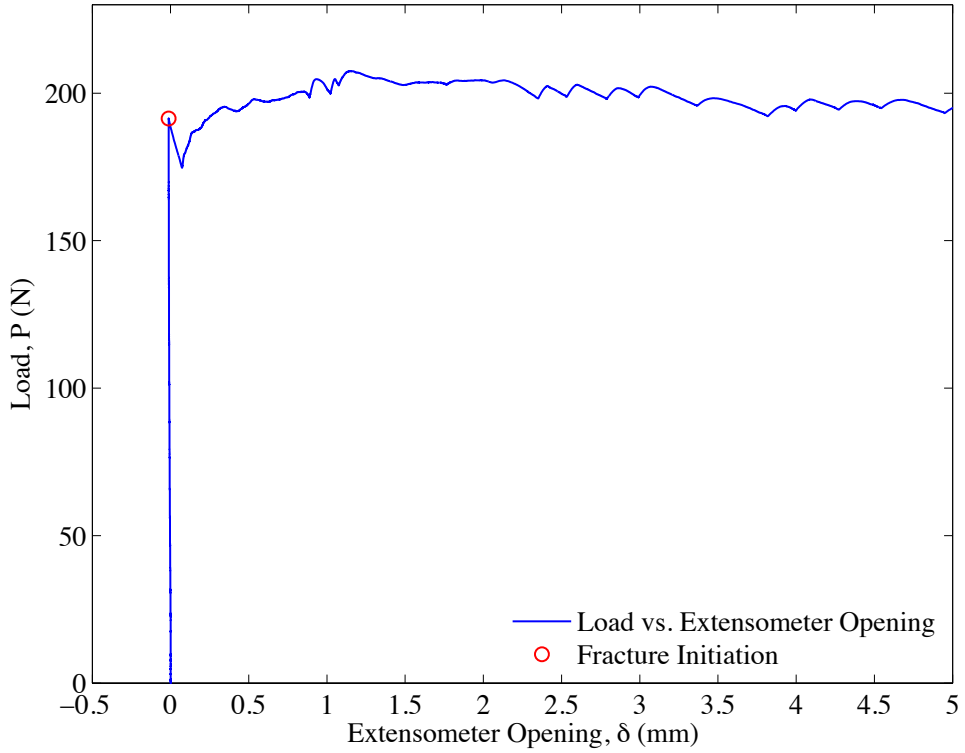

FIGURE 5.5: Example of load vs. crack tip opening as measured in the DCB-UBM mode I test.

5.3.2 Layup and Curing Procedure

To start the layup procedure, the UD tape is rolled out and cut into plies using a Stanley knife and square ruler. The required size of each ply is determined by the size and number of specimens required. The plies are then laid on top of each other by hand with the fibres aligning in the 0° direction. For the symmetric specimens, the total thickness in each case was $9.9mm$, with the precrack teflon film placed at the midplane. As each ply has a nominal cured thickness of .15 mm, this corresponded to a layup of $[0_{33}/0_{33}]$, where a PTFE crack starter film was placed after 33 plies. The crack starter film had a thickness of $\approx 12\ \mu m$, which is deemed to be sufficiently thin to represent a physical crack. The crack starter film was placed so that it would produce a pre-crack length of 60 mm when the samples were cut. The same layup procedure was carried out for the asymmetric specimens; however, different overall thicknesses and beam height ratios were required in these cases. The asymmetric beam height ratios tested are outlined in table 5.2 of the test program. These beam height ratios correspond to layup configurations of $[0_{22}/0_{44}]$ ($\gamma = 0.5$), $[0_{33}/0_{18}]$ ($\gamma = 1.833$), $[0_{33}/0_{11}]$ ($\gamma = 3$) and $[0_{33}/0_{7}]$ ($\gamma = 4.712$), where the crack starter film is again placed to produce a final pre-crack length of 60 mm in each case. As these samples are considerably thick and

contain many layers of individual plies, the layup is debulked for 30-45 mins after every 8-10 plies are added during layup to consolidate the plies and remove any air pockets. A sectioned view of the debulking procedure is illustrated in fig. 5.6. The composite layup is placed on a base plate and protected by PTFE release films on both sides. The PTFE release films allow the composite to be easily removed from the debulking unit and keeps the surfaces of the uncured composite clean. The composite is then covered by a breathing fabric, which allows the vacuum to reach then entire layup. The layup is then covered by a bagging film and sealed around all edges using a sealant tape. The base plate is then attached to a vacuum pump and the bagging film and sealant tape is checked for leaks. In the absence of any leaks, the vacuum pump is left on to debulk the composite for 30-45 mins.

Once the final debulking has taken place, the composite is ready for curing. In order to cure the composite correctly, both heat and pressure are required. The cure cycle is carried out in a converted press clave, which is illustrated in fig. 5.7. Further details on the conversion of the press clave can be found in Mohan [104]. The purpose of the press clave is to keep the aluminium base and top plates together so that they can sustain an internal pressure of 6-7 bar. Heat is applied through strip heaters, which are placed at the top and bottom of the hydraulic press. The strip heaters are placed in mild steel plates, which come into direct contact with the aluminium plates. A layer of insulation material is placed on the opposite side of the steel plates to ensure there is minimal heat loss to the press. The temperature is controlled using thermocouples, which are each connected to programmable temperature control units.

The final composite layup is again placed between two PTFE release films to allow for easy removal when cured. A layer of edge dam is placed around the edges of the composite to stop resin from leaking out during curing. Unlike in the debulking stage, a layer of release ply is placed on either side of the composite outside the PTFE release film. The release ply, which is a glass fibre cloth coated in PTFE, protects the composite and helps to provide a consistent surface finish on the top and bottom of the cured composite. A rubber caul pad is then placed over the release ply on the top surface; the rubber pad helps to evenly distribute the downward pressure on the laminate, which results in a more consistent laminate thickness throughout. These layers are finally topped off with a layer of breathing fabric followed by bagging film. The bagging film is then sealed with high temperature sealant tape, and this seal is checked, as before, by applying a vacuum and checking for leaks. This sealant tape is also used along the edges of the base plate and provides a sealant between the top and bottom aluminium plates.

Once the layup is ready and the bagging film is sealed, the top plate is placed on top of the base plate and the complete unit is inserted into the press clave. The hydraulic press is then lowered onto the top plate and a force of 30 ton pushes the top and bottom plates together; this effectively creates a sealed chamber inside the aluminium plates as the high temperature tape forms a sealant. Once the downwards force is applied from the press, a pressure of 6 bar is connected to the side of the top plate, creating a pressure chamber; this pressure is required to consolidate the composite during curing. The vacuum pump is then turned on before the cure cycle begins; this ensures no air inclusions form in the composite during cure. The cure cycle is then programmed into the temperature control units and the cycle is started. The cure cycle for this system is programmed as follows:

- heat up to 110° C over a period of 40 minutes.
- hold at 110° C for 60 minutes.
- increase to 180° C over a period of 30 minutes.
- hold at 180° for 120 minutes.
- cool at rate of $0.1 - 1°$ C per minute*.

*There is no cooling system on this press clave so the cooling rate cannot be controlled accurately. Instead, the heating system is switched off and allowed to cool naturally. Mohan [104] studied the rate of cooling from this system and found that it decreased exponentially as the temperature decreased, and found that the maximum rate of cooling observed was $0.8° \ C/min$. The maximum rate of cooling recommended in the material data sheet is $5° \ C/min$ [103], so it is well within this range.

The pressure is switched off when the temperature reduces to $60° \ C$, as recommended in the data sheet; this usually takes 3-4 hours from the time the heating system is switched off. The press clave and vacuum pump are then switched off and the system is left overnight to allow it to cool to a handling temperature. The cured panel is then removed from the press clave and is ready to be cut into test specimens.

5.3.3 Specimen Preparation

The specimens are cut to size from the composite panel using a diamond grinding disc. The final specimen dimensions are shown in fig. 5.8(a) for the symmetric specimen and in fig. 5.8(b) for the asymmetric specimens. In all cases, the specimens are 300 mm in

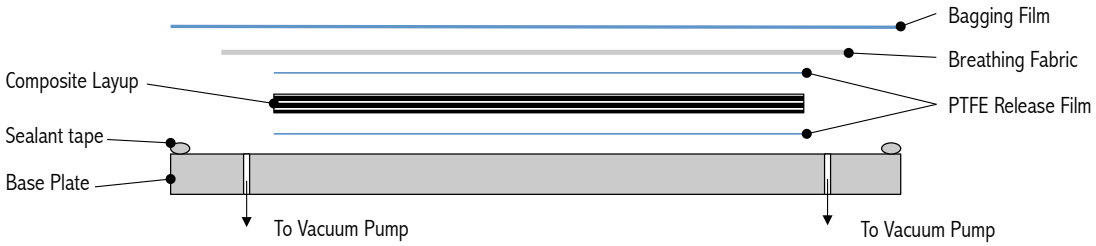

FIGURE 5.6: Illustration of the layup for composite debulking.

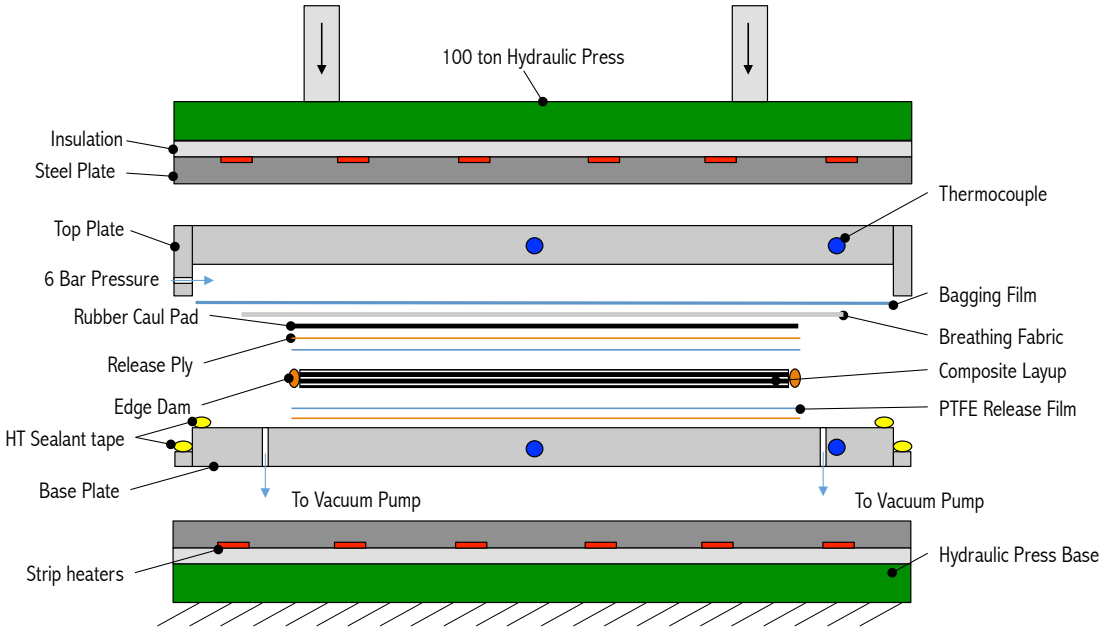

FIGURE 5.7: Illustration of the setup for composite curing in converted press clave.

length and 30 mm in width. The symmetric samples are all manufactured to the same specifications and differ only in how they are loaded; they each have a total height of 9.9 mm and the crack starter film is placed at the mid-plane. The specimen heights for the asymmetric specimens vary depending on the beam height ratio; the total beam height in given in table 5.2 for each γ ratio. The attachment and dimensions of the load blocks are also illustrated in fig. 5.8. The load blocks are attached on two sides of the symmetric specimens and only on one side for the asymmetric specimens (as $k = 0$). The load blocks, which are manufactured from aluminium, are machined to fit exactly into the transverse arms on the DCB-UBM test rig. They are attached using M5 countersunk screws with the aid of an epoxy adhesive. Pins of diameter $1mm$ are also inserted into the neutral axes of the top and bottom beams of the symmetric specimens, as shown in fig 5.8(a); these are inserted into $1mm$ holes, which are drilled to a depth of ≈ 10 mm. Finally, for samples where images are recorded for digital image correlation, the side of the sample is lightly sprayed with a white water based paint from an aerosol spray can;

this produces a very fine speckled pattern, which is required for accurate DIC.

The specific test program is outlined in the following section.

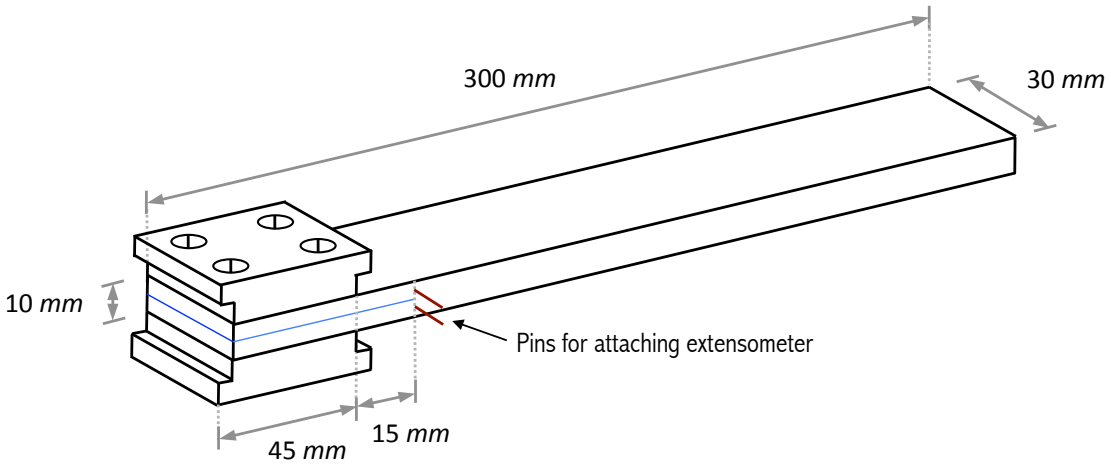

(a) Symmetric Specimens

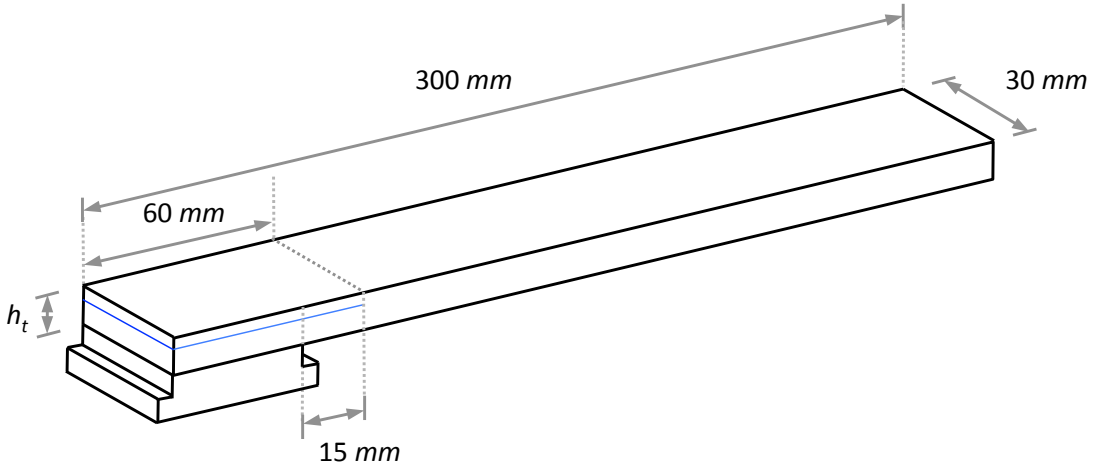

(b) Asymmetric Specimens

FIGURE 5.8: Dimensions for for test specimens.

5.4 Test Program

The test program is specifically split into two tasks. Task 1 involves measuring the failure locus of UD CFRP using symmetric specimens. Task 2 involves carrying out AFRMM tests on asymmetric specimens with varying γ ratios.

5.4.1 Task 1-Symmetric tests

Six tests are carried out on symmetric specimens using different moment ratios. The moment ratios are chosen to evenly cover the full range of mode mixities going from pure mode I to pure mode II. The distance between the pulleys on the transverse arms l_1, l_2 and the corresponding moment ratios are outlined in table 5.1 along with the resulting mode mixities. A moment ratio of $M_2/M_1 = 0.986$ is used instead of $M_2/M_1 = 1$ for the mode II test so that contact between the loaded beams will be avoided, which may lead to an increase in the recorded load due to friction.

l_1 (mm)	l_2(mm)	M_2/M_1	h_t (mm)	γ	G_{II}/G	No. of Repeats
86.5	-86.5	-1.000	9.9	1	0	4
409	-82.5	-0.202	9.9	1	0.2484	3
86.5	0	0.000	9.9	1	0.4286	4
289.5	86.5	0.299	9.9	1	0.7203	4
172.5	86.5	0.501	9.9	1	0.8716	4
139.5	137.5	0.986	9.9	1	1	4

TABLE 5.1: Task 1: Test program for measuring failure locus using symmetric specimens.

5.4.2 Task 2-Asymmetric tests

In the second task, asymmetric tests are carried out at a constant moment ratio ($k = 0$) by varying the γ ratio. The distances between the pulleys are outlined in table 5.2 along with the corresponding beam height ratios γ. The mode mixities at each of these γ ratios are outlined in table 5.3 for each of the analytical partitioning theories discussed in chapter 1.

l_1 (mm)	l_2(mm)	M_2/M_1	h_t (mm)	h_1(mm)	h_2 (mm)	γ	No. of Repeats
86.5	0	0	9.9	3.3	6.6	0.50	4
86.5	0	0	7.65	4.95	2.7	1.83	4
86.5	0	0	6.6	4.95	1.65	3.00	4
86.5	0	0	6.0	4.95	1.05	4.71	4

TABLE 5.2: Task 2: Test program for asymmetric specimens.

γ	M_2/M_1	G_{II}/G_W	G_{II}/G_{HS}	G_{II}/G_{D-NSF}	G_{II}/G_{WH}
0.50	0	0.0769	0.4030	0.2359	0.2308
1.83	0	0.8085	0.4646	0.6242	0.6080
3.00	0	0.9382	0.5003	0.7303	0.7297
4.71	0	0.9784	0.5324	0.7061	0.8149

TABLE 5.3: Task 2: Predicted mode partitions from Williams [20](W), Suo and Hutchinson [26](HS),Davidson et al. [27](D-NSF) and Wang and Harvey [28](WH) for γ ratios outlined in table 5.2.

5.5 Results and Discussion

5.5.1 Measurement of Failure Locus using Symmetric Specimens

The measured force is plotted as a function of crosshead displacement for each of the symmetric tests in fig. 5.9. Four samples are tested at each moment ratio, with the exception of $M_2/M_1 = -0.202$, where three samples were tested. In cases where the samples are unloaded shortly after initiation, only the initial load-displacement traces are shown for clarity. The quadratic functions and the fracture initiation points are also highlighted. The fracture initiation point is determined using the MAX/NL procedure, as described in section 5.2.3. The measured initiation force from this method, P_c, is outlined in table 5.4 for each sample. Also plotted in table 5.4 are the measured total beam heights ($h_t = h_1 + h_2$), beam widths (B), and the corresponding initiation toughness values (G_c) calculated using eq. 5.2. The mean initiation toughness values (G_{c_av}) for each configuration and standard deviations (SD) are also presented in table 5.4. The standard deviation is given by:

$$SD = \sqrt{\frac{\sum_{1}^{N}(G_c - G_{c\_av})^2}{N}} \tag{5.5}$$

where N is the number of tests for each configuration.

As an aside, standard fracture tests (DCB/FRMM/C-ELS) are also carried out on this composite system in accordance with the relevant standards [6–8] as a method of comparison with the DCB-UBM procedure. The test procedures are outlined in appendix D. The measured initiation values from these test methods from both the crack starter film and a precrack (in brackets) are outlined in table 5.4. There is very good agreement between the measured initiation toughness from the crack starter film in the DCB-UBM test and the standard fracture tests in both mode I and mixed mode ($G_{II}/G = 3/7$).

However, the average initiation toughness from the pre-crack in the C-ELS test is considerably higher than the initiation toughness measured in the corresponding mode II DCB-UBM test. This might be explained by looking at the corresponding force-displacement graphs from the DCB-UBM mode II test (fig. 5.9(f)) and the C-ELS test (D.4(a)). It is evident from fig. 5.9(f) that fracture in the DCB-UBM mode II test initiates from the crack starter film in a relatively stable manner in each case (no considerable drop in force at initiation); however, fracture initiates in a very unstable manner in the C-ELS test, as is evident from the sudden drop in load in fig. D.4(a). It is believed that the measured initiation toughness from the precrack in the C-ELS test is artificially high, and may have been due to the presence of a resin rich region at the crack tip in the three samples tested. By examining the R-curves for the DCB-UBM and C-ELS test in fig. 5.11(f) and D.4(b) respectively, it is evident that the propagation toughness measured in the C-ELS test is similar to that observed in the DCB-UBM test so there is no reason to believe that there was any inherent difference in the material tested in each case. It is also possible that slight differences in the applied moments in the DCB-UBM mode II test (k=0.986), which was set up as so to avoid friction between the arms, had the effect of reducing the likelihood of unstable fracture initiation. This is an area that warrants further investigation as it would be desirable to obtain stable fracture initiation with similar low levels of scatter in the standard ELS tests as seen in the DCB-UBM mode II tests.

The initiation toughness values from the pre-cracks in the DCB, FRMM and C-ELS tests are presented in brackets in table 5.4 alongside initiation toughness values obtained from the PTFE insert. The main aim of re-testing from a pre-cracked specimen is to examine possible discrepancies between testing from an insert and from a *natural* pre-crack. There is very good agreement between the initiation from the insert and initiation from the pre-crack in the mode I DCB test. The average initiation toughness from the pre-cracked tests is slightly lower than the average initiation toughness measured from the insert; however, this difference is within one standard deviation so is not statistically significant. This is an important result as it suggests that the crack starter film is sufficiently thin to represent a physical crack tip. The initiation toughness measured from the pre-crack in the FRMM test is slightly higher than the initiation toughness measured from the insert. This behaviour may be explained by considering the R-curve plotted in fig. D.3(b). It is clear that this increase in toughness between the insert and the pre-crack is following a general trend of increasing toughness as a function of increasing crack length. Therefore, the observed increase in toughness from the pre-crack compared to the insert can be attributed to a likely increase in damage zone size after $5mm$ of crack growth. Initiation from the mode II pre-crack occurs in a stable manner in each case

and so it is not surprising that the recorded toughness is much lower than the unstable initiation value obtained from the insert. Due to the stable nature of crack initiation in the pre-cracked test, it is believed that the measured initiation toughness from this method is more physical than the one obtained from the insert. The value obtained from the pre-crack is also much closer to the value obtained in the DCB-UBM mode II test. Overall, there is good general agreement between the standard fracture mechanics tests and the DCB-UBM tests, which verifies that the DCB-UBM testing from the PTFE insert is an accurate approach for estimating the true mixed mode failure locus.

The alternative method of identifying fracture initiation using crack tip openings in the DCB-UBM test is now examined and compared to the MAX/NL procedure. A plot of the measured force vs. extensometer opening for each DCB-UBM test case is given in fig. 5.10. In these cases, both the initial loading and reloading are plotted for each case where applicable. The initiation force is also outlined in these figures, where the initiation force is defined using the MAX/CTO procedure. The initiation loads and corresponding toughnesses for each test are presented in table 5.5 and compared to the values obtain from the MAX/NL initiation points. In all cases, the extensometer openings are plotted up to the point that the crack visibly reaches the support rollers during the test in fig 5.10. As the crack advance is proportional to the crack tip opening, plotting the toughness as a function of the crack tip opening gives a clear indication of the resistance (R) curve behaviour for each specimen. The measured forces are converted to toughnesses using eq. 5.2 and are plotted as a function of crack tip openings in fig. 5.11. In cases where there was a clear increase in the fracture resistance during the test (i.e. $G_{II}/G = 0.248, G_{II}/G = 0.4286$), this fracture was always accompanied by clearly visible fibre bridging. Images of the crack tip from the side of the specimen during testing are presented in fig. 5.12 for each loading configuration. Fibre bridging is clearly visible from these images in fig. 5.12(b) and 5.12(c), which correspond to $G_{II}/G = 0.248$ and $G_{II}/G = 0.4286$ respectively.

The initiation toughnesses from both the MAX/NL and the MAX/CTO method are shown in fig. 5.13 as a function of mode mixity. Firstly, it can be seen that there is very good agreement between both approaches across all mode mixities in general, with the exception of pure mode II loading. In the pure mode II test, the average initiation toughness is 750 J/m^2 from the MAX/NL initiation point compared to 807 J/m^2 from the MAX/CTO initiation point. This discrepancy is not surprising given that the extensometer does not open significantly in mode II throughout the test (≈ 0.25mm for entire test) and therefore it is very difficult to accurately pick up crack initiation using the MAX/CTO procedure when crack initiation does not occur in a sudden unstable manner. Other discrepancies between individual samples occur at $G_{II}/G = 0.721$ and

$G_{II}/G = 0.872$ also correspond to cases where fracture initiation does not occur in a sudden unstable manner under mode II dominated loading. This is evident from comparing the initiation points in fig. 5.9 and fig. 5.10. Despite these differences, the general agreement between both methods for identifying crack initiation gives confidence in the accuracy of both approaches. It is also noticeable that the standard deviations in measured toughness increases in mode II dominated loading; this is accompanied by more unstable fracture initiation compared to the mode I dominated tests, as is evident in fig. 5.9. This behaviour has been observed previously for composites [93, 105]

Overall, the initiation toughness is considerably dependent on the mode of loading and there is a 3-4 fold increase in the toughness between pure mode I and pure mode II. The pure mode I and mode II toughness values are in agreement with experimental results available in literature on the same composite; Bonhomme et al. [105] found the mode I initiation toughness to be $250 \pm 55\ J/m^2$, and the mode II initiation toughness to be $791 \pm\ 146.9 J/m^2$. The total toughness generally increases as the mode II component increases, with the exception of one case. Interestingly, when a small component of mode II is introduced, the overall toughness drops from $210 J/m^2$ at $G_{II}/G = 0$ to $159.4 J/m^2$ at $G_{II}/G = 0.248$. This behaviour is unusual in that it goes against the popular belief that the mode I fracture energy is always the smallest. This belief, however, has been originally founded on physical considerations of fracture in monolithic materials, where cracks have been shown to kink under mixed mode loading to stay locally in mode I [13]. The analysis for composites and adhesive joints is more complex than monolithic materials, as the crack now has a choice of material to propagate in, or whether to propagate along an interface. The reason that the initiation toughness is lower than pure mode I initiation toughness might be explained by considering an image of the crack tip from the side just after fracture initiation in fig. 5.14; in this case, $G_{II}/G = 0.2484$. It is evident from this image that the crack immediately kinks upwards slightly. This slight kinking is driven by the small amount of mode II loading, which kinks the crack to keep it locally in mode I in the resin rich region. It is believed that there may be two explanations why this causes a lower initiation toughness. Firstly, due to the mode of loading, the tensile stress field which develops at the crack tip will be concentrated at an upwards angle away from the resin rich zone; this means that the resin rich region, which occurs between the plies, will not be subjected to the same level of tensile stresses as under a pure mode I loading. This will result in lower energy being dissipated in this region due to plasticity and hence will result in a lower initiation toughness. Secondly, the toughness of the interface between the fibres and the resin may be slightly lower than the bulk toughness of the resin; therefore, by gently coaxing the crack towards this interface with a small amount of shear loading, a lower initiation toughness will be

observed. Dillard et al. [14] highlighted a number of cases where the measured fracture toughness under mixed mode loading (small mode II component) was less that the pure mode I toughness in adhesive joints; in all of these cases, kinking of the crack towards the adhesive substrate interface was observed.

The increase in toughness under higher mode II components in composite materials has been well documented in literature [16, 93, 106]. The fracture surfaces of AS4/8552 epoxy composite were studied by Bonhomme et al. [107] after being subjected to mode II fracture; the fracture surfaces were found to contain a hackled pattern. The hackled pattern, which is described by Johannesson et al. [108], is a series of angled cracks caused by local principal tensile stresses. In mode II loading of composites and adhesive joints, these hackled cracks tend to occur at angles of 45° to the global crack propagation direction [107, 109]. In fact, it is the formation of these hackles that make it very difficult to determine crack lengths in the standard mode II ELS test. This problem has lead to a modification of the test analysis by Blackman et al. [110] to allow for the effective crack lengths to be calculated from the specimen compliance. The increase in surface area can partly explain the increase in toughness observed in mode II loading; however, Mohan et al. [109] studied the crack paths in mode I and mode II loading of an adhesive and found the increase in path length in mode II loading could not fully account for the observed increase in fracture toughness. Mode II and mixed mode failure in composites is a complex process which involves the interaction of many different failure mechanisms, such as hackle formation, matrix plasticity, fibre matrix de-bonding, fibre breakage, fibre pull-out, void formation and coalescence, etc. It is therefore difficult to predict and explain the effect that different mixed mode loadings will have on the toughness of a system; and is the reason there is no sound predictive mixed mode failure criteria for fracture in composites. Numerous mixed mode failure criteria exist in the literature which attempt to capture the relationship between toughness and mode mixity; however, these are mainly empirical in nature. A number of these criteria are fitted to the current experimental data in the following section.

M_2/M_1	G_{II}/G	SAMPLE	(h_t) (mm)	B (mm)	P_c (N) - MAX/NL	$G_c(J/m^2)$	G_{c_av}	SD	G_c	SD
-1.000	0.000	A	9.74	29.99	162.0	181.4	210.1	27.6	233.2(220.2)	16.4(19.4)
-1.000	0.000	B	9.87	30	170.0	191.9				
-1.000	0.000	C	9.84	29.99	187.8	236.3				
-1.000	0.000	D	9.98	29.79	188.3	231.0				
-0.202	0.248	A	9.75	29.99	45.7	154.9	159.4	11.6		
-0.202	0.248	B	9.85	29.96	45.8	150.8				
-0.202	0.248	C	9.9	29.83	49.1	172.6				
0.000	0.429	A	9.94	30	320.2	291.7	296.1	11.7	280.3(313.9)	8.1(26.0)
0.000	0.429	B	9.52	30.02	300.0	290.8				
0.000	0.429	C	9.79	29.84	322.5	313.5				
0.000	0.429	D	9.86	30.03	314.6	288.3				
0.299	0.721	A	9.71	30.03	96.4	318.0	357.6	41.6		
0.299	0.721	B	9.82	29.93	100.2	334.3				
0.299	0.721	C	9.91	29.84	112.4	412.6				
0.299	0.721	D	9.91	29.86	105.9	365.5				
0.501	0.872	A	9.83	29.99	194.3	490.1	576.0	106.8		
0.501	0.872	B	9.82	29.93	198.8	517.5				
0.501	0.872	C	9.78	29.8	233.6	728.8				
0.501	0.872	D	10.37	29.96	226.5	567.4				
0.986	1.000	A	9.80	29.98	241.2	759.3	750.1	17.6	1044.4(654.7)	49.5(43.9)
0.986	1.000	B	10.23	30.02	258.8	767.2				
0.986	1.000	C	10.05	29.84	243.7	726.9				
0.986	1.000	D	9.87	29.86	240.8	746.9				

TABLE 5.4: Measured initiation force and toughness values for varying moment ratios applied to symmetric DCB specimens. Crack initiation is determined using the MAX/NL procedure. The values are compared to results obtained using standard fracture tests (in red) (details in appendix D - Nominal values indicate initiation toughness values measured from PTFE insert and values in brackets indicate initiation toughness values measured from a pre-crack).

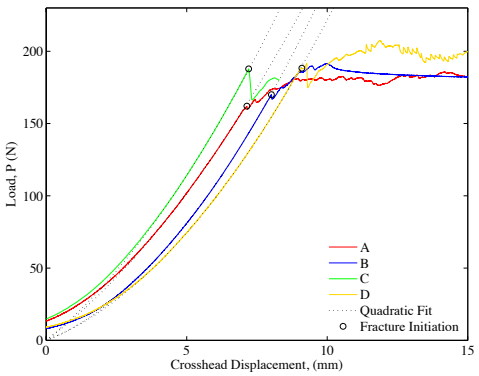

(a) $M_2/M_1 = -1$, $G_{II}/G = 0$

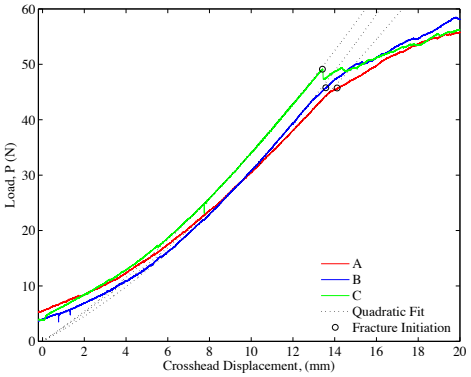

(b) $M_2/M_1 = -0.202$, $G_{II}/G = 0.2484$

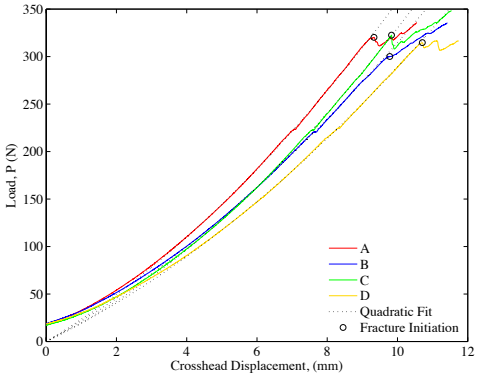

(c) $M_2/M_1 = 0$, $G_{II}/G = 0.4286$

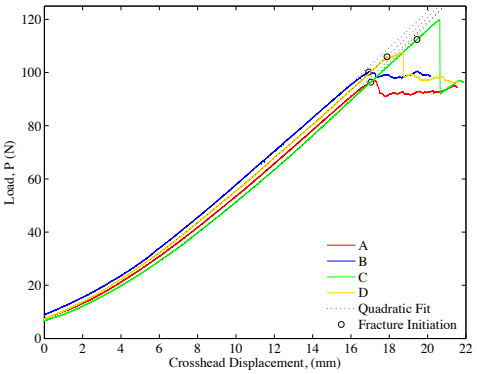

(d) $M_2/M_1 = 0.3$, $G_{II}/G = 0.72$

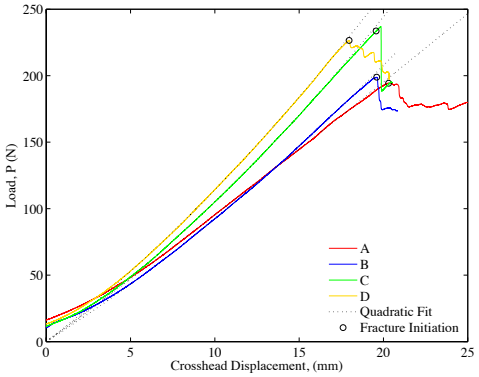

(e) $M_2/M_1 = 0.5$, $G_{II}/G = 0.87$

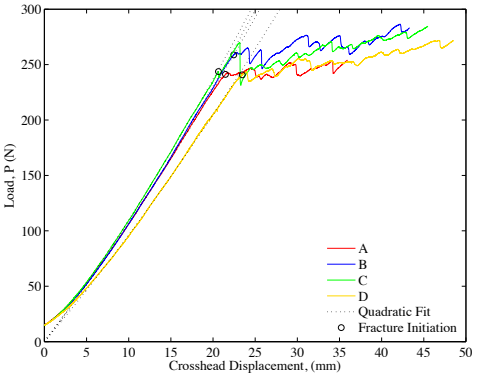

(f) $M_2/M_1 = 0.986$, $G_{II}/G = 1$

FIGURE 5.9: Load vs. crosshead displacement for symmetric DCB specimens loaded with uneven bending moments. Fracture initiation is determined from the MAX/NL procedure.

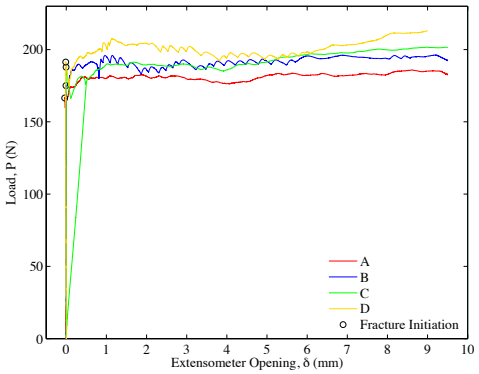

(a) $M_2/M_1 = -1$, $G_{II}/G = 0$

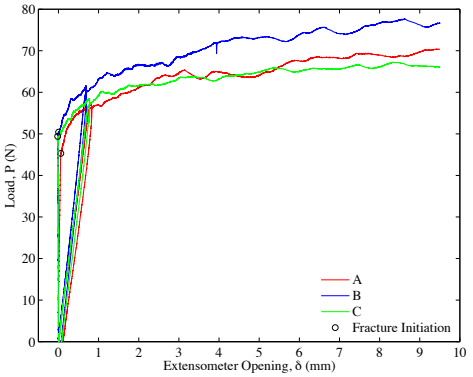

(b) $M_2/M_1 = -0.202$, $G_{II}/G = 0.2484$

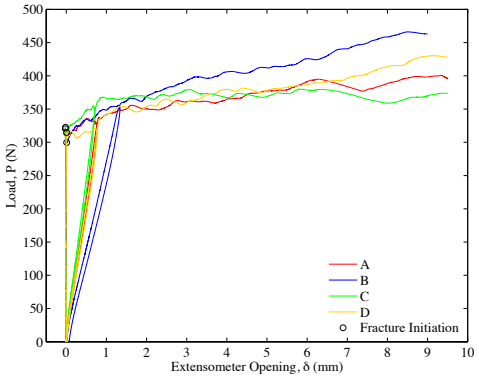

(c) $M_2/M_1 = 0$, $G_{II}/G = 0.4286$

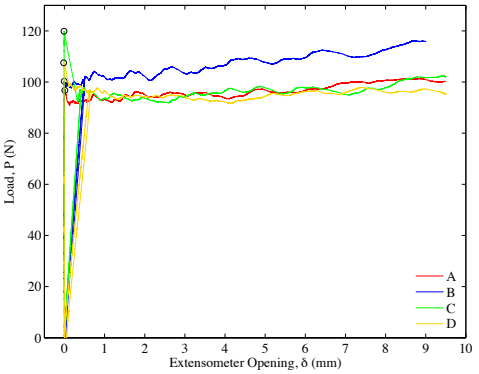

(d) $M_2/M_1 = 0.3$, $G_{II}/G = 0.72$

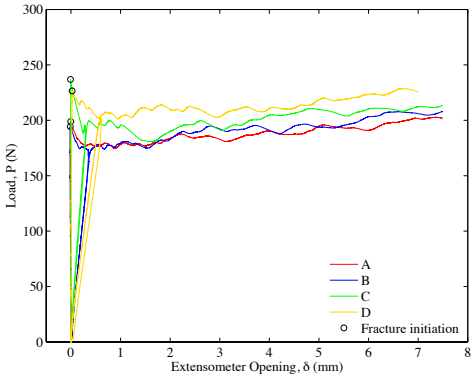

(e) $M_2/M_1 = 0.5$, $G_{II}/G = 0.87$

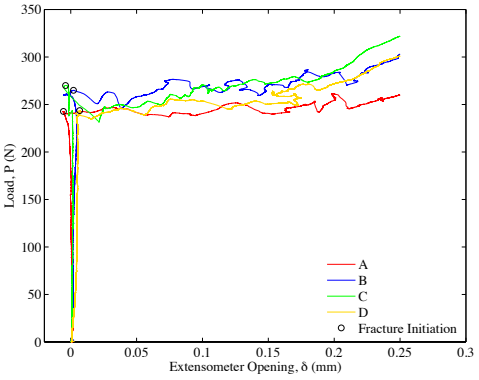

(f) $M_2/M_1 = 0.986$, $G_{II}/G = 1$

FIGURE 5.10: Load vs. crack tip opening displacement for symmetric DCB specimens loaded with uneven bending moments. Fracture initiation load is taken as the maximum load which occurs up to the point of 10 μm crack tip opening.

M_2/M_1	G_{II}/G	SAMPLE	P_c (N)	$G_c(J/m^2)$	G_{c_av}	SD	G_{c_av} (NL)	SD (NL)
-1.000	0.000	A	166.5	191.5	217.5	23.7	210.1	27.6
-1.000	0.000	B	175.1	203.5				
-1.000	0.000	C	187.8	236.3				
-1.000	0.000	D	191.4	238.7				
-0.202	0.248	A	45.3	152.0	169.9	16.0	159.4	11.6
-0.202	0.248	B	50.4	183.0				
-0.202	0.248	C	49.4	174.7				
0.000	0.429	A	320.2	291.7	295.9	11.8	296.1	11.7
0.000	0.429	B	299.7	290.2				
0.000	0.429	C	322.5	313.5				
0.000	0.429	D	314.6	288.3				
0.299	0.721	A	96.7	320.5	375.2	66.8	357.6	41.6
0.299	0.721	B	100.3	335.0				
0.299	0.721	C	119.8	468.8				
0.299	0.721	D	107.5	376.6				
0.501	0.872	A	194.3	490.1	580.7	116.9	576.0	106.8
0.501	0.872	B	198.8	515.9				
0.501	0.872	C	236.9	749.2				
0.501	0.872	D	226.5	567.4				
0.986	1.000	A	242.6	768.2	806.5	59.7	750.1	17.6
0.986	1.000	B	264.9	804.0				
0.986	1.000	C	269.9	891.7				
0.986	1.000	D	243.4	762.0				

TABLE 5.5: Measured initiation force and toughness values for varying moment ratios applied to symmetric DCB specimens. Crack initiation is determined from the MAX/CTO procedure. The average initiation toughness and standard deviations from this method are compared to the results obtained from the MAX/NL method(red) .

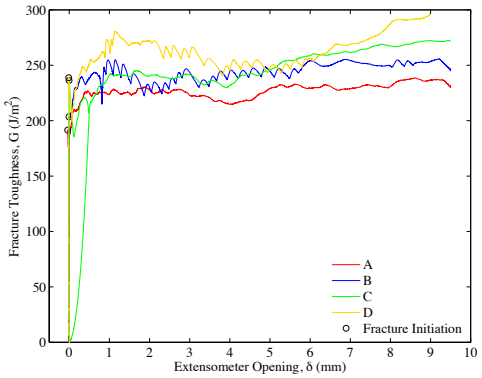

(a) $M_2/M_1 = -1$, $G_{II}/G = 0$

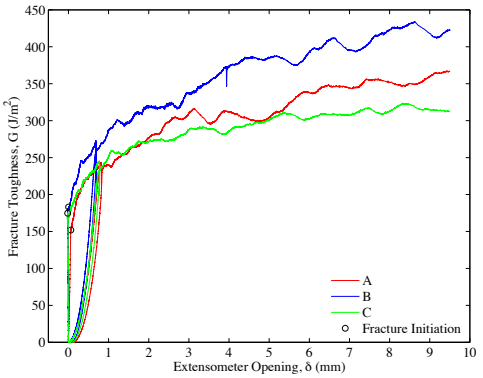

(b) $M_2/M_1 = -0.202$, $G_{II}/G = 0.2484$

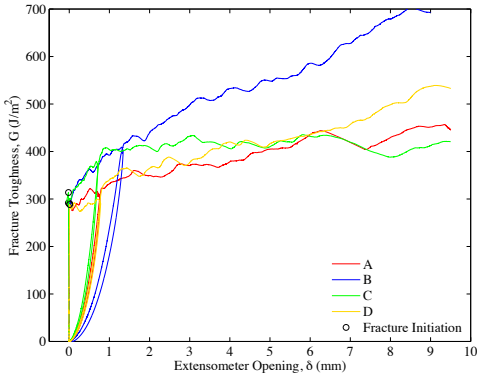

(c) $M_2/M_1 = 0$, $G_{II}/G = 0.4286$

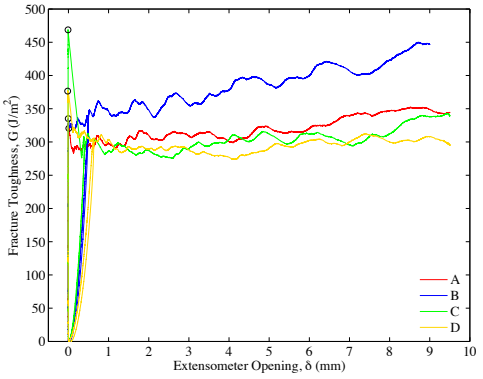

(d) $M_2/M_1 = 0.3$, $G_{II}/G = 0.72$

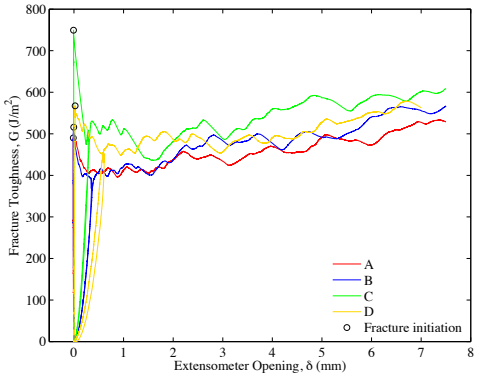

(e) $M_2/M_1 = 0.5$, $G_{II}/G = 0.87$

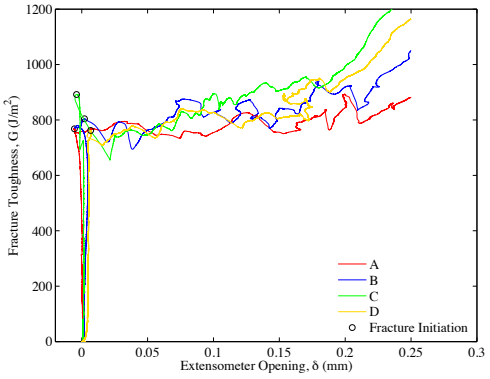

(f) $M_2/M_1 = 0.986$, $G_{II}/G = 1$

FIGURE 5.11: Fracture toughness as a function of crack tip opening displacement for symmetric DCB specimens loaded with uneven bending moments.

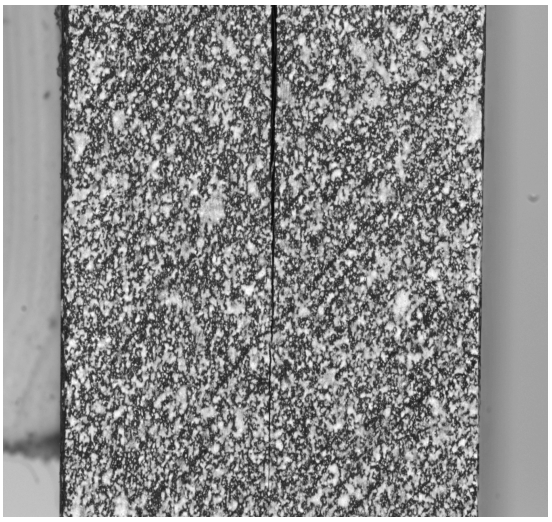

(a) $M_2/M_1 = -1$, $G_{II}/G = 0$

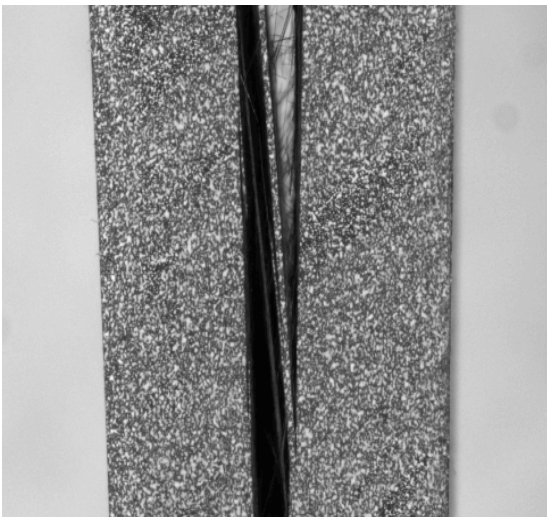

(b) $M_2/M_1 = -0.202$, $G_{II}/G = 0.2484$

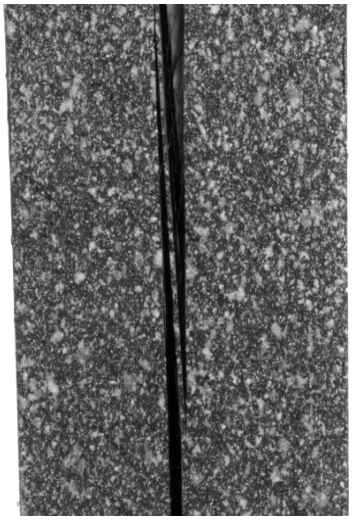

(c) $M_2/M_1 = 0$, $G_{II}/G = 0.4286$

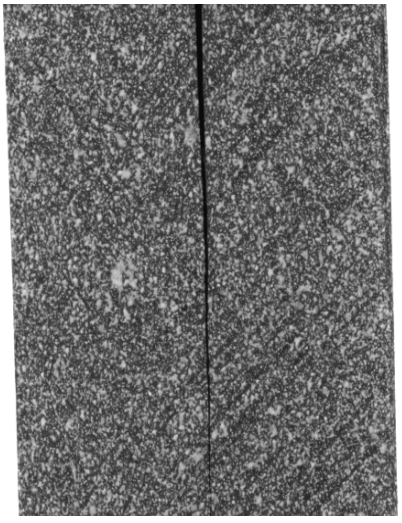

(d) $M_2/M_1 = 0.3$, $G_{II}/G = 0.72$

(e) $M_2/M_1 = 0.5$, $G_{II}/G = 0.87$

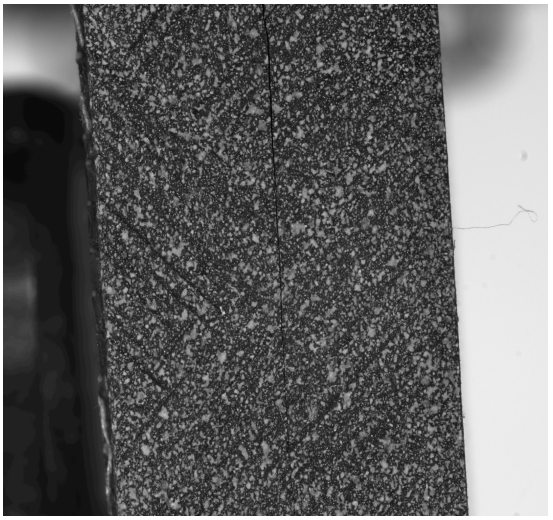

(f) $M_2/M_1 = 0.986$, $G_{II}/G = 1$

FIGURE 5.12: Pictures of symmetric samples during testing at varying moment ratios. Extensive fibre-bridging is evident in cases (b) and (c).

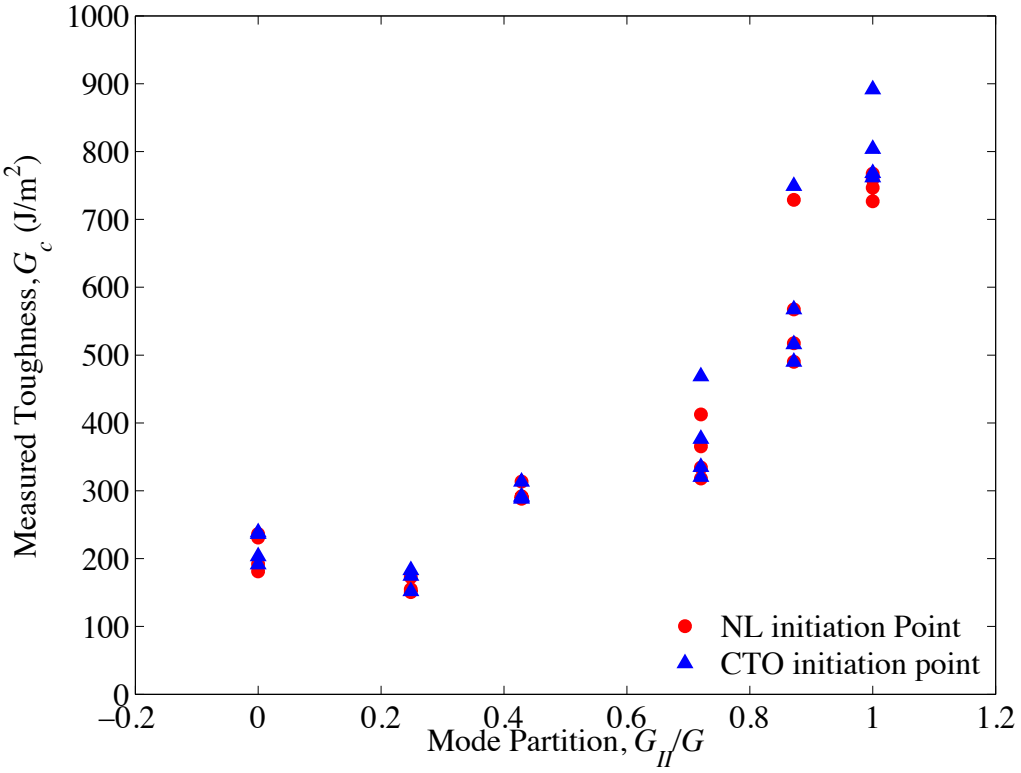

FIGURE 5.13: Plot of initiation fracture toughness as a function of mode mixity obtained from both non-'linear' (NL) and crack tip opening (CTO) initiation points.

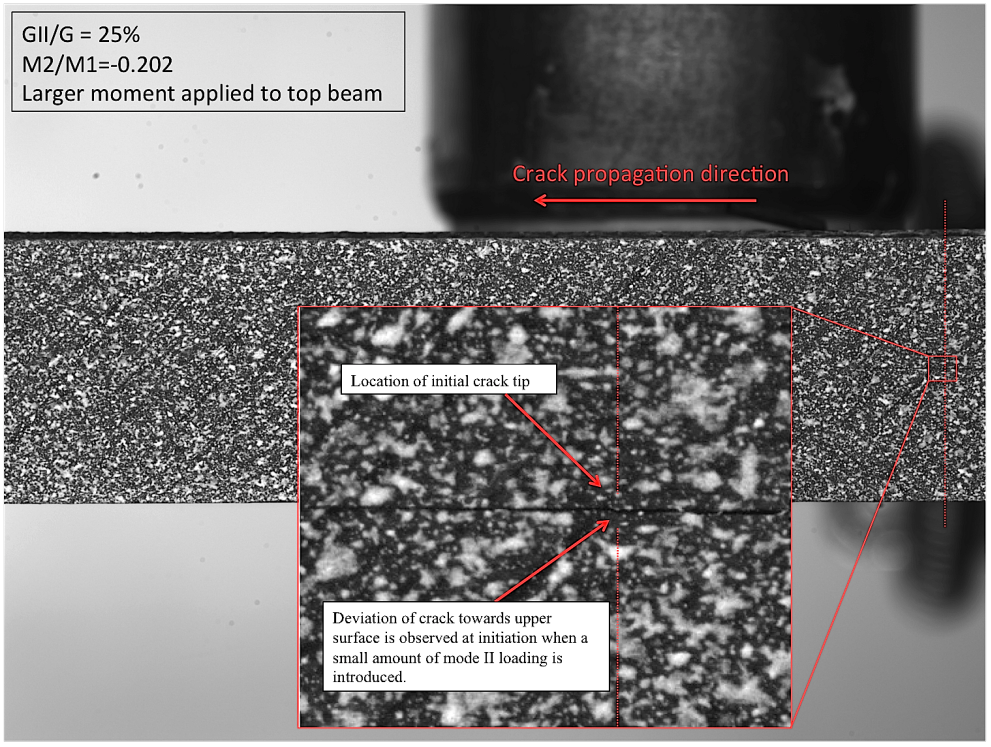

FIGURE 5.14: Image of crack path taken at $G_{II}/G = 0.2484$ just after crack initiation; it is evident that the crack deviates upwards, possibly towards the fibre matrix interface.

5.5.2 Mixed mode failure criterion

A number of mixed mode failure criteria exist in literature which attempt to describe the toughness as a function of mode mixity. Each of these criteria have a number of fitting parameters which can be obtained by carrying out a least squares fit to the experimental data. The failure criteria are fitted here to the experimental data presented in fig. 5.13. The data presented in fig. 5.13 contains intitiaion reaults from both the MAX/NL and MAX/CTO procedures; however, as the MAX/CTO method cannot be applied in the asymmetric tests due to the extensometer not being attached, only the MAX/NL initiation values are considered when fitting a failure locus; this is in the interest of keeping the methods consistent between the symmetric and asymmetric tests so that strong conclusions can be drawn. A number of mixed mode failure criteria are fitted in the following section.

The failure criteria considered in this section are the linear criterion [15], power law criterion [19], Benzeggagh-Kennane (BK) criterion [17], and the modified Benzeggagh-Kennane criterion [18]. These failure criteria are outlined in table 5.7 with the fitting parameters indicated. These parameters are found by minimising the least squares error between each failure criterion and the experimental data using Microsoft excel solver. The least squares error (LSE) is given by eq. 4.15. The results from fitting each of these failure criteria are given in table 5.8 and the resulting failure loci are plotted in fig. 5.15 along with the experimental data.

It is evident from fig. 5.15 that none of the failure criteria from literature accurately capture the shape of the experimentally measured mixed mode failure locus. The shape of the failure locus is unusual in that it shows a decrease in the initiation toughness G_c for a small amount of mode II loading (i.e. at $G_{II}/G = 0.2484$). This is not unprecedented, however; Dillard et al. [14] presents numerous examples where this is the case. Only the power law is capable of capturing this decrease in toughness for an increasing mode II component; however, it is unable to recover quickly enough to predict the correct mode mixity at $G_{II}/G = 0.4286$. The linear law does not perform well in predicting the failure locus for this composite system and produces the largest least squares error by a considerable margin. Both the BK law and the modified BK law produce a very similar failure locus with similar least square errors; these errors are in line with the errors produced by the power law fit. Overall, none of these failure criteria predict the measured failure locus with sufficient accuracy; therefore, in order to capture each measured point of the failure locus correctly, a piecewise linear function is fitted between the average initiation toughnesses at each mode mixity. The piecewise linear function is

given by eq. 5.6.

$$G_c = \Big(\frac{G^{i+1}_{c\_av} - G^i_{c\_av}}{G_{II}/G^{i+1} - G_{II}/G^i}\Big)(G_{II}/G - G_{II}/G^i) + G^i_{c\_av} \quad \text{for} \quad G_{II}/G^i \leq G_{II}/G \leq G_{II}/G^{i+1} \tag{5.6}$$

where the average initiation toughness $G^i_{c\_av}$ is given at each corresponding mode mixity G_{II}/G^i in table 5.6; these coefficients are taken directly as the average toughness values presented in table 5.4. The piecewise linear function effectively halves the least squares

i	G_{II}/G^i	$G^i_{c\_av}$
1	0	210.1
2	0.2484	159.4
3	0.4286	296.1
4	0.7203	357.6
5	0.8716	576.0
6	1	750.1

TABLE 5.6: Coefficients for the piecewise linear fit presented in fig. 5.15 and eq. 5.6.

error compared to the power law, BK and BK modified failure criteria (9.6% compared to 19.4%,17.9% and 18.27% respectively). Therefore, this piecewise linear function is used as the benchmark failure locus when analysing the performance of partitioning methods for asymmetric specimens.

Failure Critierion	Equation	Fitting Parameters
Linear [15]	$\frac{G_I}{G_{IC}} + \frac{G_{II}}{G_{IIC}} = 1$	None
Power Law [19]	$\left(\frac{G_I}{G_{IC}}\right)^{\alpha} + \left(\frac{G_{II}}{G_{IIC}}\right)^{\beta} = 1$	α, β
Benzeggagh-Kenane [17]	$G_c = G_{IC} + (G_{IIC} - G_{IC})\left(\frac{G_I}{G}\right)^m$	m
Modified BK [18]	$G_c = \frac{1}{\frac{G_I/G}{G_{IIC}+(G_{IIC}-G_{IC})\left(\frac{G_I}{G}\right)^{\chi}} + \frac{G_{II}/G}{G_{IC}+(G_{IIC}-G_{IC})\left(\frac{G_{II}}{G}\right)^{\eta}}}$	χ, η

TABLE 5.7: Mixed Mode Failure Criteria.

Failure Critierion	Fitted Parameters	Least Squares Error (LSE)
Linear [15]	-	35.7%
Power Law [19]	$\alpha = 3.2, \beta = 0.09$	19.4 %
Benzeggagh-Kenane [17]	m=3.67	17.9%
Modified BK [18]	$\chi = 0.007, \eta = 2.04$	18.27 %
Piecewise Linear	-	9.25%

TABLE 5.8: Results of fitting mixed mode failure criteria to experimental data.

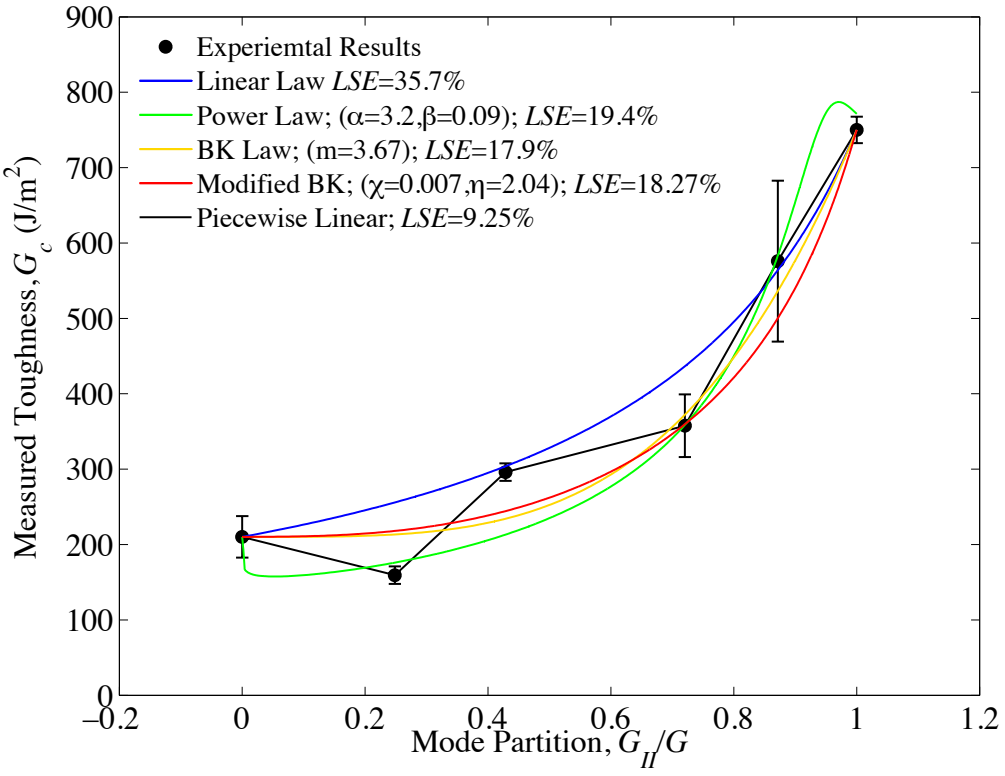

FIGURE 5.15: A comparison of linear, power law, BK, BK modified, and piecewise linear failure criteria fitted to mixed mode delamination experiments.

5.5.3 Asymmetric Fixed Ratio Mixed Mode Fracture Tests

The asymmetric geometries tested have been outlined previously in table 5.2; four beam height ratios are tested corresponding to $\gamma = 0.5, 1.833, 3, 4.712$. Four specimens are tested at each beam height ratio. The force vs. crosshead displacement plots for each of these tests are presented in fig. 5.16. Also presented in these plots are the quadratic fitting functions and fracture initiation points. The fracture initiation points are determined, as before, by taking the maximum load up to the point of a 2 % deviation in load from the fitted quadratic function (eq. 5.4). The critical initiation loads and corresponding initiation toughnesses are presented in table 5.9, along with the measured total specimen thickness ($h_t = h_1 + h_2$) and width (B) for each sample. The toughness is calculated as before by using eq. 5.2 for each case. The average initiation toughness G_{c_av} and standard deviation (SD) is also presented in table 5.9 for each beam height ratio.

The fracture toughness, G, is plotted as a function of crosshead displacement for each case in fig. 5.17. It is evident from this plot the fracture resistance of the specimens increases steadily after fracture initiation. A side-view of each test configuration during testing is presented in fig. 5.18. As with the symmetric specimens, this increase in fracture toughness is accompanied with notable fibre bridging, which is evident from fig. 5.18. Due to the mode of loading in each case, cracks are inclined to start in adjacent plies which promotes significant fibre bridging. These results from the asymmetric tests are discussed in the context of mode partitioning, which is presented in the following section.

5.5.4 Mode Partitioning of Asymmetric Tests

The mode partitioning solutions from each of the analytical partitioning theories (W[20], HS[26],D-NSF[27] and WH [28]) are presented in table 5.3 for each of the asymmetric beam height ratios tested. The SACA-L(Linear Softening) and SACA-D(Dugdale) partitioning solutions are also calculated for the current specimen material properties, geometries and loadings. As the toughness, G_c, is measured experimentally in each case, the remaining material properties required for SACA partitioning are the substrate elastic properties ($E_{11}, E_{22}, \nu_{12}, \nu_{23}, G_{12}$), cohesive strength ($t_C$), and cohesive shape parameter (M). The values used for each of the required properties are outlined in table 5.10. The Young's modulus in the fibre direction is calculated directly from strain measurements in the DIC analysis; this is outlined in section E.1.1. The Young's modulus in the transverse direction is taken from the material data sheet [103]. The Poisson's ratios

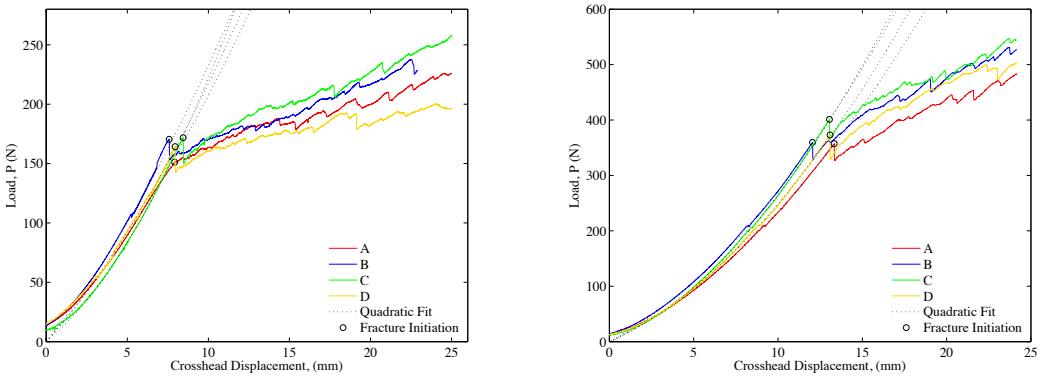

(a) $\gamma = 0.5$ (b) $\gamma = 1.833$

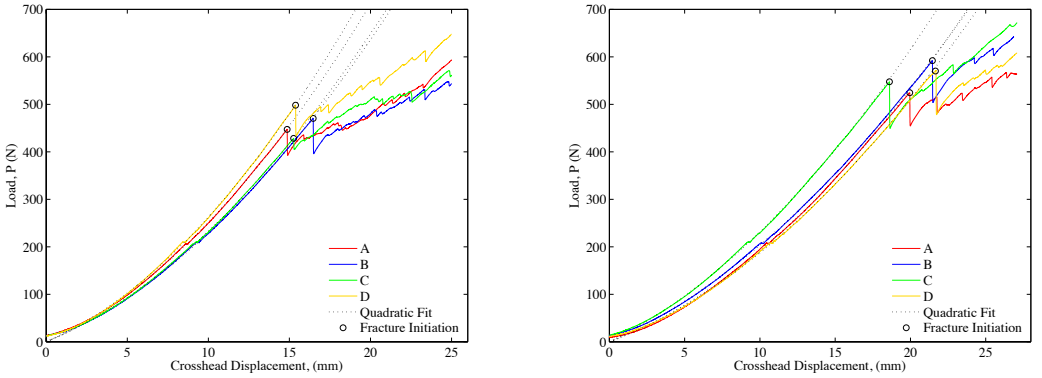

(c) $\gamma = 3$ (d) $\gamma = 4.712$

FIGURE 5.16: Load vs. crosshead displacement for asymmetric fixed ratio mixed mode (AFRMM) specimens.

and shear modulus are taken from literature for typical UD carbon epoxy composite [111, 112]. The cohesive strength is again taken as the interlaminar tensile strength, which is $60MPa$ for this material (Daniel Ng, Hexcel. Personal Communication). Finally, both the linear softening (L) and Dugdale (D) cohesive zone shape parameters are used as it is believed they will give an upper and lower bound to the SACA solution. A print out of the excel input and output for the SACA procedure is given in fig. 5.19(a) for SACA(L) and fig. 5.19(b) for SACA(D). The predicted mode partitions from each partitioning method are given together in table 5.11 and plotted in fig. 5.20 for each γ ratio tested.

It is evident from fig. 5.20 that the trend of the predicted SACA mode partitions for the current CFRP(AS4/8552) material is very similar to those presented in chapter 4 for the CFRP material (T300/6376) tested by Hashemi et al. [32]. Those SACA predicted mode partitions were presented in fig. 4.7. As before, the predicted mode partitions for mode I dominated fractures ($\gamma < 1$) are predicted to be very close to the local solution of

$\gamma(h_1/h_2)$	SAMPLE	(h_t) (mm)	B (mm)	P_c (N)	$G_c(J/m^2)$	G_{c_av}	SD
0.500	A	9.70	29.84	151.2	262.3	294.8	24.6
0.500	B	10.16	29.76	170.4	291.9		
0.500	C	9.88	29.86	171.8	320.3		
0.500	D	9.76	29.84	164.3	304.6		
1.833	A	7.43	29.78	357.2	339.2	350.6	14.6
1.833	B	7.48	29.79	359.6	336.8		
1.833	C	7.86	29.71	401.2	362.8		
1.833	D	7.48	29.70	373.0	363.7		
3.000	A	6.59	29.81	447.3	387.5	396.5	37.2
3.000	B	6.64	29.79	470.4	418.7		
3.000	C	6.63	29.82	428.3	348.1		
3.000	D	6.83	29.78	498.1	431.6		
4.714	A	5.96	29.80	524.5	410.3	469.3	79.2
4.714	B	5.74	29.81	592.1	585.9		
4.714	C	5.98	29.73	547.5	445.9		
4.714	D	6.20	29.69	570.1	435.1		

TABLE 5.9: Measured initiation force and toughness values for varying moment ratios applied to ssymmetric DCB specimens. Crack initiation is determined by taking the maximum force recorded up to the point of non-'linearity' according to eq. 5.4.

Suo and Hutchinson [26]; however, for mode II dominated fractures, the mode partition is predicted to deviate away from the local solution of Suo and Hutchinson [26] and tend towards the global solution of Williams [20]. The predicted solutions in this mode II dominated region lie half way between the local (HS) and global (W) solutions and lie very close to the predictions of Davidson et al. [27](D-NSF) and Wang and Harvey [28](WH). As before, the smaller damage zone lengths predicted by the Dugdale cohesive zone means that it always lies closer to the local solution compared to the linear softening cohesive zone solution.

Description	Property	Value	Source
Young's Modulus (Fibre Direction)	E_{11}	125 GPa	Section E.1.1
Young's Modulus (Transverse Direction)	E_{22}	10 GPa	Data Sheet[103]
In plane Poisson's ratio	ν_{12}	0.3	Kriz and Stinchcomb [111]
Out of plane Poisson's ratio	ν_{23}	0.38	Kriz and Stinchcomb [111]
Shear Modulus	G_{12}	4.6 Gpa	Zhou et al. [112]
Cohesive Strength	t_C	60 MPa	Daniel Ng, Hexcel. PC
Cohesive Shape Parameter	M	0.66(L)/0.33(D)	Chapter 4

TABLE 5.10: The material properties used in the SACA partitioning of UD AS4/8552 (carbon/epoxy) composite.

The predicted failure locus from each partitioning method is plotted individually in fig. 5.21 on top of the symmetrically measured failure locus. The predicted failure loci are plotted together in fig. 5.22 for direct comparison. Lines are drawn to connect both the upper and lower error bounds of each symmetric test in fig. 5.21; these upper and

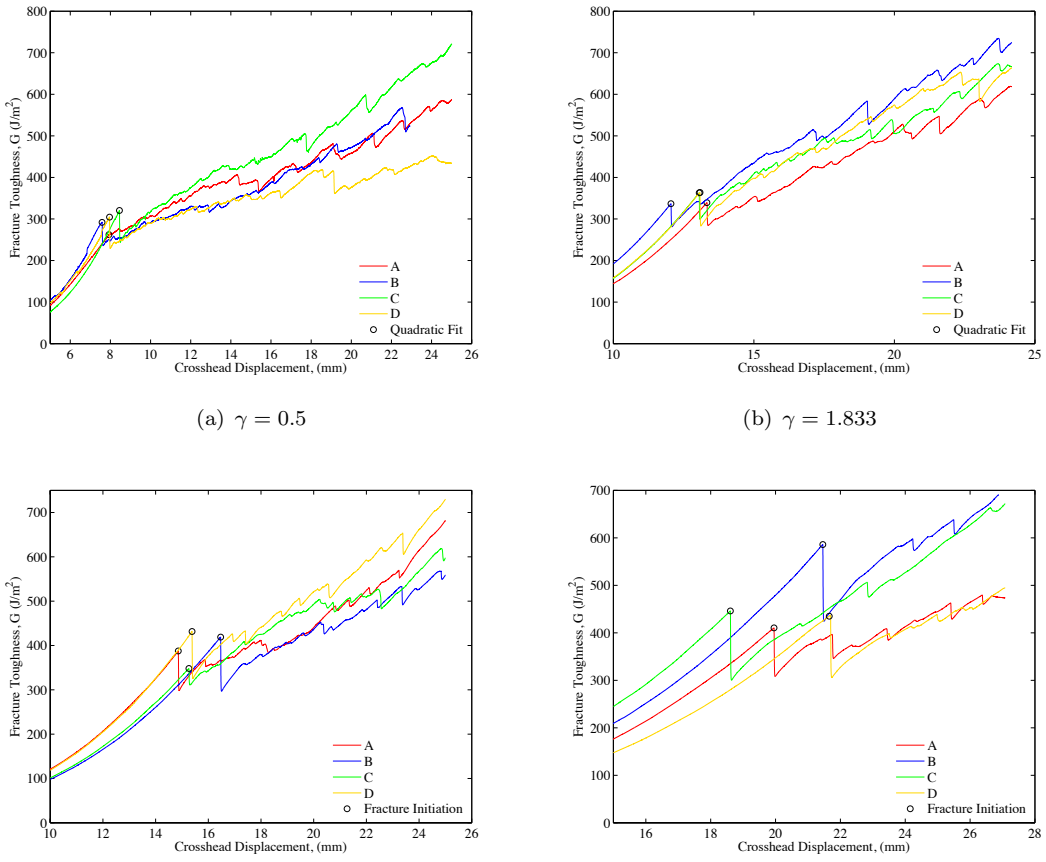

(a) $\gamma = 0.5$

(b) $\gamma = 1.833$

(c) $\gamma = 3$

(d) $\gamma = 4.712$

FIGURE 5.17: Fracture toughness vs. crosshead displacement for asymmetric fixed ratio mixed mode (AFRMM) specimens.

γ	M_2/M_1	G_{II}/G_W	G_{II}/G_{HS}	G_{II}/G_{D-NSF}	G_{II}/G_{WH}	$G_{II}/G_{SACA(L)}$	$G_{II}/G_{SACA(D)}$
0.50	0	0.0769	0.4030	0.2359	0.2308	0.3734	0.3955
1.83	0	0.8085	0.4646	0.6242	0.6080	0.5372	0.4933
3.00	0	0.9382	0.5003	0.7303	0.7297	0.6742	0.5843
4.71	0	0.9784	0.5324	0.7061	0.8149	0.8075	0.6904

TABLE 5.11: Task 2: Predicted mode partitions from Williams [20](W), Suo and Hutchinson [26](HS),Davidson et al. [27](D-NSF),Wang and Harvey [28](WH), SACA(L) and SACA(D) for γ ratios outlined in table 5.2.

lower bounds form a region that the asymmetric tests must overlap with if partitioned correctly. If the asymmetric tests overlap with this region when partitioned, then the partitioning theory is compatible with the experimental results; if they do not overlap with this region, then the partitioning theory is not compatible with the experimental results. To quantitatively compare the performance of each of the partitioning theories, the least squares error (LSE) between the predicted failure loci and the symmetrically measured failure locus is calculated using eq. 4.15 as before. The symmetrically measured failure locus is described by a piece-wise linear fit between the measured toughness

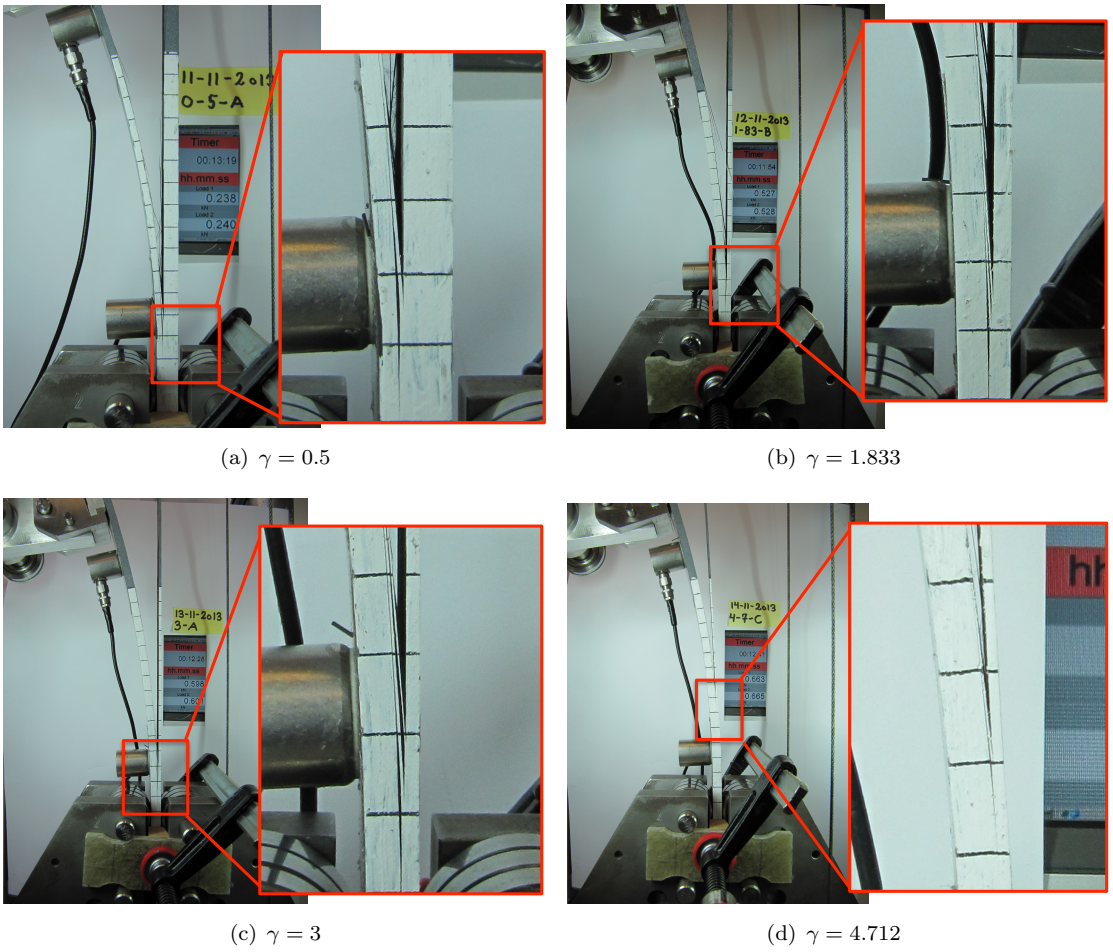

(a) $\gamma = 0.5$ (b) $\gamma = 1.833$

(c) $\gamma = 3$ (d) $\gamma = 4.712$

FIGURE 5.18: Images of the side of AFRMM test specimens during testing.

values at each tested mode ratio (eq. 5.6). The LSE values are presented in fig. 5.21 and table 5.12 for each method. In must be noted that in the assessment of each of the partitioning theories using this approach, it is assumed that the measured symmetric failure locus is unique and correct.

The predicted failure locus from the global(W) partitioning is shown in fig. 5.21(a); it is evident that this partitioning theory does not produce a failure locus that is compatible with the experimental results. The mode I dominated test ($\gamma < 1$) is shifted too far towards mode I, and conversely, the mode II dominated tests ($\gamma > 1$) are shifted too far towards mode II. The least square error between the asymmetric and symmetric failure locus is 50.33% for global(W) partitioning. The predicted failure locus from local(HS) partitioning is shown in 5.21(b); again, this partitioning theory produces a failure locus that is incompatible with the symmetrically measured failure locus. In this case, only one point is predicted to lie correctly on the true failure locus; this point corresponds to the mode I dominated test ($\gamma = 0.5$). The least squares error between the

UCD Mixed Mode Partition

Cohesive Shape: Linear Softenin

If experimental G_c data is inserted, this will be used in the calculation. If not, a failure locus must be specified with values of G_{Ic} and G_{IIc}.

Geometry and Loading			Substrate Elastic Properties (Plane Strai)					Cohesive Strength	Failure Locus (optional) Linear, m (BK Law) 1.5		Experiment (optional)	Results					
h_1 mm	h_2 mm	k	E_{11} GPa	E_{22} GPa	G_{12} GPa	ν_{12}	ν_{23}	σ MPa	G_{Ic} J/m²	G_{IIc} J/m²	G_c J/m²	G_{Ic}/G	l_{ch} mm	f	G_{Ic}/G (W) f = 0	G_{Ic}/G (HS) f = 1	No. of Loops i
3.3	6.6	0	125	10	4.6	0.3	0.38	60			294.76	0.3734	2.3523	0.9093	0.0769	0.4030	6
4.95	2.7	0	125	10	4.6	0.3	0.38	60			350.613	0.5372	3.7688	0.7888	0.8085	0.4646	6
4.95	1.65	0	125	10	4.6	0.3	0.38	60			396.48	0.6742	4.4899	0.6028	0.9382	0.5003	6
4.95	1.05	0	125	10	4.6	0.3	0.38	60			469.29	0.8075	5.3458	0.3832	0.9784	0.5324	6

(a) SACA partitioning of UD CFRP using linear softening cohesive zone shape parameter (L) (M=0.66).

UCD Mixed Mode Partition

Cohesive Shape: Dugdale

If experimental G_c data is inserted, this will be used in the calculation. If not, a failure locus must be specified with values of G_{Ic} and G_{IIc}.

Geometry and Loading			Substrate Elastic Properties (Plane Strai)					Cohesive Strength	Failure Locus (optional) Linear, m (BK Law) 1.5		Experiment (optional)	Results					
h_1 mm	h_2 mm	k	E_{11} GPa	E_{22} GPa	G_{12} GPa	ν_{12}	ν_{23}	σ MPa	G_{Ic} J/m²	G_{IIc} J/m²	G_c J/m²	G_{Ic}/G	l_{ch} mm	f	G_{Ic}/G (W) f = 0	G_{Ic}/G (HS) f = 1	No. of Loops i
3.3	6.6	0	125	10	4.6	0.3	0.38	60			294.76	0.3955	1.2228	0.9772	0.0769	0.4030	5
4.95	2.7	0	125	10	4.6	0.3	0.38	60			350.613	0.4933	1.8240	0.9164	0.8085	0.4646	6
4.95	1.65	0	125	10	4.6	0.3	0.38	60			396.48	0.5843	2.1111	0.8080	0.9382	0.5003	6
4.95	1.05	0	125	10	4.6	0.3	0.38	60			469.29	0.6904	2.4965	0.6457	0.9784	0.5324	6

(b) SACA partitioning of UD CFRP using Dugdale cohesive shape parameter (D) (M=0.33).

FIGURE 5.19: Input and output from SACA excel macro using both linear softening (L) and Dugdale (D) cohesive zone shape parameters.

asymmetric and symmetric failure locus predicted by the local partitioning is 20.73%. Both the partitioning theories of Davidson et al. [27] and Wang and Harvey [28] predict very similar failure loci from the asymmetric tests; these are plotted in fig. 5.21(c) and 5.21(d) respectively. In the mode II dominated region, both partitioning theories predict a failure locus that is in very good agreement with the true failure locus; however, in the mode I dominated test, the predicted partitions by both theories are not compatible with the experimentally measured failure locus. The least squares errors between the predicted failure locus and the true failure locus are 25.87% and 22.85% for D-NSF and WH partitioning respectively. The predicted failure loci from SACA(L) and SACA(D) partitioning are shown in fig. 5.21(e) and fig. 5.21(f) respectively. The predicted failure locus from SACA(L) partitioning is in very good agreement with the experimentally measured failure locus across all beam height ratios. The least squares error for the SACA(L) partitioning is 10.37%. The predicted failure locus from SACA(D) partitioning does not produce as good a fit to the symmetric failure locus as SACA(L) partitioning; however, the error margins from both the symmetric and asymmetric failure loci just about overlap, and so the results are still compatible. The least squares error for the SACA(L) partitioning is 16.76%.

Only the SACA partitioning approach succeeds in predicting the true measured failure locus for this test program. This serves as experimental evidence that a damage based approach must be used in order to obtain accurate mode partitioning solutions. Experimentally, the correct mixed mode partition has been confirmed to lie between the local (HS) and global (W) partitioning solutions, and to lie closer to the local(HS) partitioning in mode I dominated fracture; only SACA predicts this behaviour, which had been

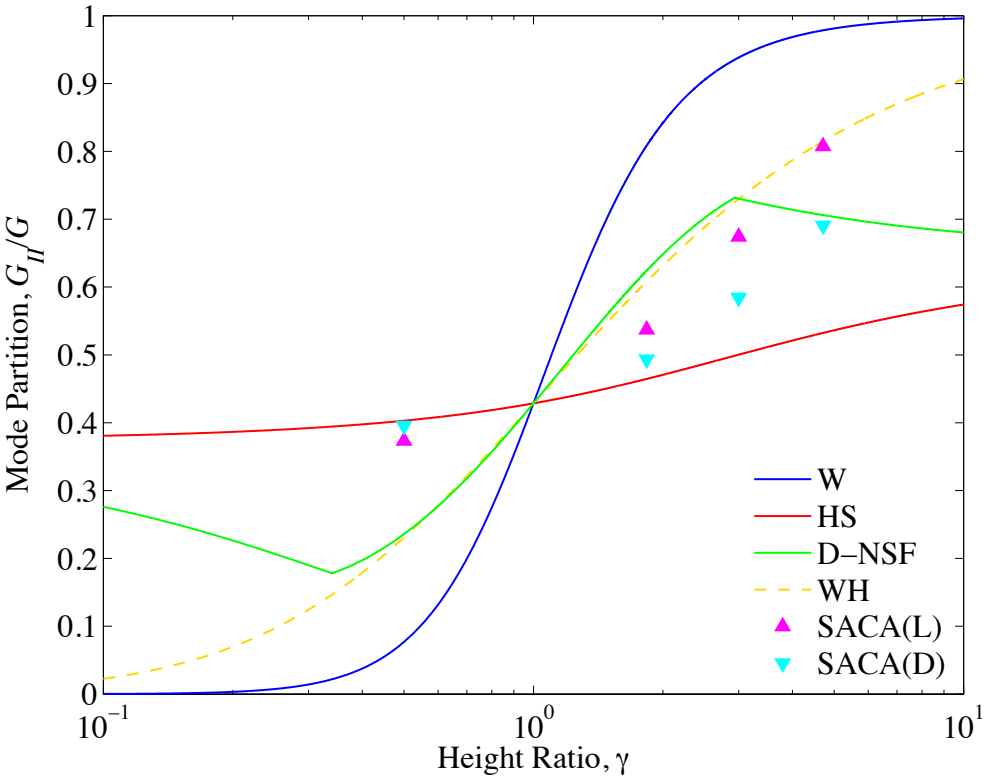

FIGURE 5.20: SACA partitioning (L-Linear softening, D-Dugdale) of asymmetric tests.

observed numerically in chapter 3. In the analysis of results from Hashemi et al. [32] in the previous chapter, no concrete conclusions could be made about the validity of each of the partitioning theories, as each of W, D-NSF, WH and SACA partitioning produced plausible failure loci; only HS partitioning seemed to produce an un-physical failure locus. This shortfall is addressed in the current test program by explicitly measuring the mixed mode failure locus using symmetric specimens. The in-ability of each of the analytical partitioning theories to correctly predict the correct failure locus is further evidence that a new damage dependent partitioning theory is required. The ability of the SACA approach to correctly predict the symmetrically measured failure locus, for both the current experiments and those presented in Ducept et al. [33], confirms that the numerically observed relationship between damage zone length and mode mixity holds true and can be used to obtain accurate mixed mode partitions in real life experiments.

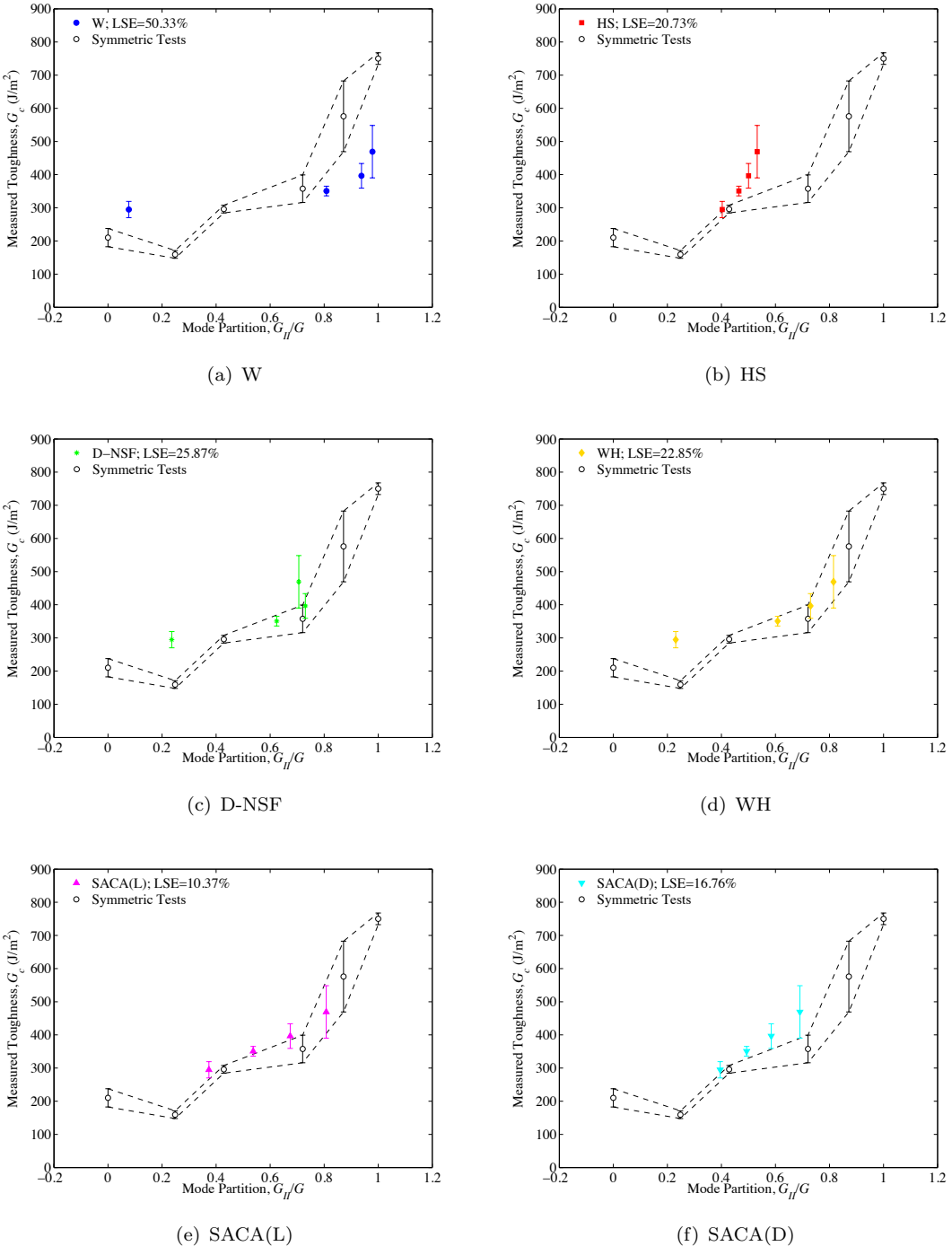

(a) W (b) HS

(c) D-NSF (d) WH

(e) SACA(L) (f) SACA(D)

FIGURE 5.21: Predicted failure loci based on various partitioning techniques compared to true failure failure, which is measured using symmetric specimens.

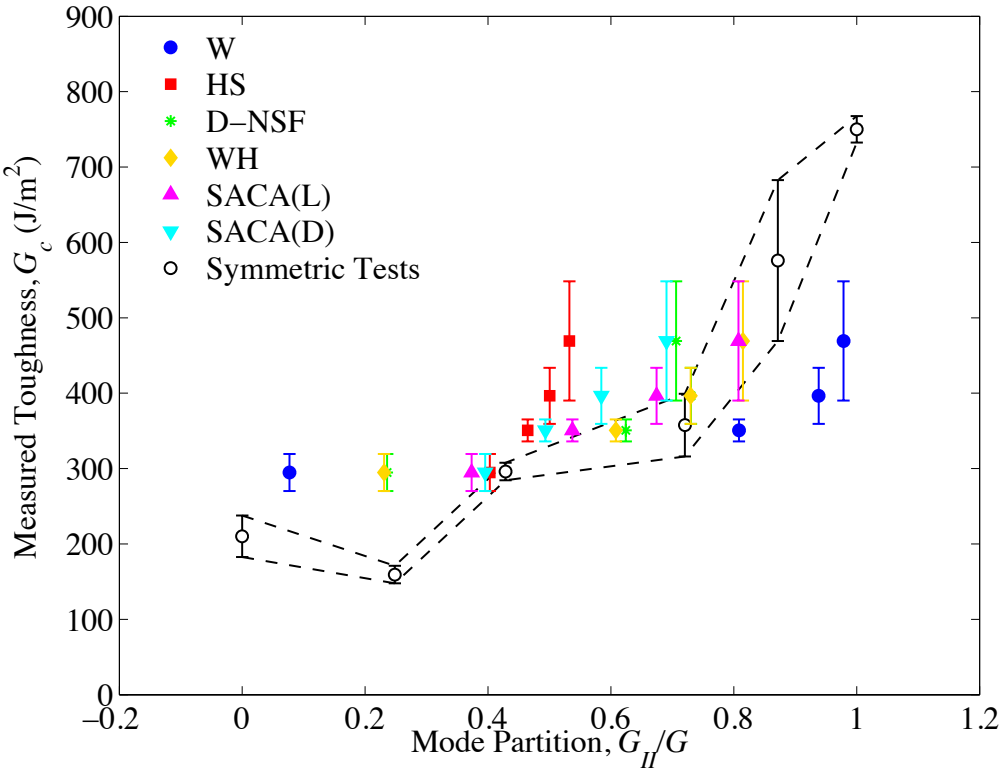

FIGURE 5.22: Predicted failure loci resulting from various partitioning of the Asymmetric tests.

Partitioning Method	Least Squares Error (LSE)
W	50.33%
HS	20.73%
D-NSF	25.87%
WH	22.85%
SACA(L)	10.37%
SACA(D)	16.76%

TABLE 5.12: Least square errors associated with each partitioning technique.

5.6 Chapter Conclusions

This chapter outlines an experimental study in which the mixed mode failure locus of AS4/8552 (carbon/epoxy) is measured using symmetric specimens, and then various partitioning theories are assessed in their ability to produce this failure locus when applied to partition fracture energies obtained in asymmetric tests on the same material. The first part of this chapter deals with the measurement of the mixed mode failure locus using symmetric specimens. A DCB-UBM (double cantilever beam loaded with uneven bending moments) test rig is used to obtain this. The moment ratio is varied to obtain different mode mixities in order to cover the full failure locus ranging from pure mode I to pure mode II; six different moment ratios are tested corresponding to $G_{II}/G = 0; 0.248; 0.4286; 0.72; 0.8716; 1$. The fracture initiation is measured in each case using two procedures; by taking the maximum load up to a deviation from 'linearity' in the load displacement curve (MAX/NL), and by taking the maximum load up to a 10 μm crack tip opening (MAX/CTO). The fracture initiation values from both of these methods are found to be in very good agreement for each mode ratio, with the exception of pure mode II, where the initiation values were slightly higher for the MAX/CTO method. This discrepancy could be attributed to the fact that the extensometer does not open significantly due to mode I fracture initiation, and hence the fracture initiation may not have been captured correctly. However, the general agreement between the measured fracture initiation values from both methods indicates that fracture initiation is picked up in a consistent manner. The measured failure locus was verified at three points corresponding to mode I, mixed mode ($G_{II}/G = 3/7$) and mode II using standard DCB, FRMM, and C-ELS tests respectively. It was found that there was, in general, very good agreement between the measured toughness values from the DCB-UBM and the standard tests, which backs up the assumption that the true mixed mode failure locus can be accurately obtained using the DCB-UBM test method.

The measured failure locus shows a general increase in toughness as the mode II component is increased; however, there is an exception to this trend when a small amount of mode II loading is introduced ($G_{II}/G = 0.248$). In this case, the measured initiation toughness is seen to drop from the pure mode I value of 210 J/m^2 to 159 J/m^2 at $G_{II}/G = 0.248$. It was discussed that this drop in toughness may be attributed to either:

- A reduction in the stress concentration in the resin rich region due to the principal tensile stresses being concentrated away from this region; this would lead to a reduced level of plasticity, and hence toughness, upon fracture initiation.

- A lower interface toughness between the matrix and the fibres. It is observed from an image that the crack initially kinks towards the fibre matrix interface at crack initiation. It is possible that fracture initiated here first due to the way the stress field is angled at this mixed mode loading.

This observed drop in toughness at a low mode II component has been reported previously by Dillard et al. [14] for fractures in adhesive joints. However, this behaviour in composites requires further investigation. A number of mixed mode failure criteria from the literature are fitted to the experimental data; the failure criteria tested are the linear failure law [15], power law [19], Benzeggagh-Kenane law [17], and modified Benzeggagh-Kenane law [18]. Out of each of these theories, only the power law can pick up the initial drop in toughness for increasing mode II component; however, it is unable to accurately predict the measured toughness at $G_{II}/G = 0.43$. Therefore, none of the mixed mode failure criteria found in literature could accurately describe the measured data for this material. For the purpose of comparing the asymmetric tests, a piece-wise linear failure locus is therefore assumed.

In the second part of this chapter, asymmetric fracture tests are carried out on the DCB-UBM test rig. In each case, the applied moment ratio is zero. Four different beam height ratios ($\gamma = h_1/h_2$) are tested, corresponding to $\gamma = 0.5; 1.833; 3; 4.712$. The fracture initiation point in these tests are determined only using the MAX/NL procedure, as no extensometer was attached to the samples in this case. After crack initiation in each case, it is found that the measured toughness increases as a function of crack length. On inspection of the side of the sample during testing, it is evident that a secondary interlaminar crack always forms in the loaded beam, adjacent to the main interlaminar crack. This secondary crack eventually become the main crack, creating significant fibre bridging in the process. This behaviour is observed in the symmetric specimens at $G_{II}/G = 0.248$ and $G_{II}/G = 0.43$, where significant increasing R curve behaviour is also observed.

The measured initiation fracture toughness is partitioned according to the analytical partitioning theories; these are Williams [20](W), Suo and Hutchinson [26](HS), Davidson et al. [27](D-NSF), Wang and Harvey [28] (WH), and the newly developed SACA partitioning. Both the linear softening (L) and Dugdale (D) cohesive zone shapes are used in SACA partitioning. It is found that only SACA(L) and SACA(D) partitioning of the asymmetric tests produce a failure locus that is compatible with the symmetrically measured failure locus. SACA(L) performs the best, however, which suggests that the correct cohesive law is given by a linear softening shape. Both the D-NSF and WH partitioning produce consistent results in the mode II dominated cases; however,

they do not predict the correct mode partition for the mode I dominated case, which is predicted to be close to the local solution of Suo and Hutchinson [26]. The local partitioning only predicts this point correctly, as the correct mode partition evidently moves away from the local solution towards the global solution in the mode II dominated cases, as is predicted by the numerics. The global solution of Williams [20] does not perform well in predicting the correct failure locus either; in the mode I dominated case, it predicts it is almost pure mode I (92%), whereas the measured toughness is close to the local solution, which is only 60% mode I; in the mode II dominated cases, the global solution also predicts that they are too close to mode II, where the correct solution evidently falls in between the prediction of the local and global solution. The ability of the SACA partitioning to accurately predict the mode partitioning based on the substrate and cohesive zone properties is further evidence that the mode partition is indeed dependent on damage in reality, and the numerical simulations can accurately capture this dependence.

Chapter 6

Conclusions and Future Work

6.1 Introduction

This chapter outlines a summary of the main conclusions and contributions arising from the thesis, and outlines some recommendations for future work in the area.

6.2 Summary and Conclusions

The first chapter of this thesis presents an overview of mixed mode fracture in laminated composite materials. Current analytical theories for decomposing energy release rates in beam like geometries are reviewed, along with their applications to experimental data in the literature. The main theories discussed are the local solution of Suo and Hutchinson [26], the global solution of Williams [20], the non-singular field solution developed by Davidson et al. [27] and the Euler beam theory solution of Wang and Harvey [28]. It is shown that there is considerable disagreement between each of these theories when a crack is located off-centre between beams. Various experimental studies were carried out in the literature to assess the performance of each of these theories [27, 32, 33, 35]; however, the conflicting results from each of these studies suggest that there is no one-size-fits-all procedure available for obtaining accurate partitions.

The second chapter of this thesis examines various methods of obtaining numerical partitions in beam like geometries. In particular, the virtual crack closure technique (VCCT), interaction domain integral (IDI) and mode decomposed J (MDJ) integral are all examined. The mixed mode partitioning of the asymmetric fixed ratio mixed mode (AFRMM) test is investigated as a function of beam height ratio and compared to the

analytical solutions of Williams [20], Suo and Hutchinson [26], Wang and Harvey [28] and Davidson et al. [27]. Elastic properties are used in all cases and no crack propagation or damage is modelled. Overall, it is found that each of the partitioning techniques (VCCT, IDI, MDJ) predict the correct ERR to a high degree of accuracy ($< .06\%$ error). Each numerical partitioning technique also predicts the same mixed mode partition up to the third significant digit. Most interestingly, this predicted partition is very close to the analytical prediction of Suo and Hutchinson [26], and it is evident that the other analytical solutions of Williams [20], Wang and Harvey [28] and Davidson et al. [27](D-NSF) should not be used to predict mode partitions in ideally elastic beam-like geometries. It is no surprise that the local solution of Suo and Hutchinson [26] performs so well in predicting the elastic mixed mode partitions as the assumptions made in the analytical analysis are matched in the numerical simulations. This main assumption is the presence of singular stress fields at the crack tip, which is allowed to develop in the numerical simulations in the absence of any damage law or cohesive zone.

In the third chapter of this thesis, damage is introduced into the models using a cohesive zone model. Fracture is modelled by inserting cohesive elements along the expected fracture plane. Upon loading, the cohesive elements initiate and a fracture process zone develops and propagates. Initially, a number of partitioning techniques were tested for accuracy and/or appropriateness against the benchmark of the FRMM test. Partitioning using the crack tip element (CTE) was found to produce a different partition than the known analytical partition. This was attributed to the fact that all of the elements in a developing damage region undergo a different loading history, and while globally the mode partition is correct, there is no requirement that locally this has to be the case. Integration along the cohesive surfaces ($J_{\Gamma_{coh}}$) was initially found to give an incorrect mixed mode partition during damage development, but this could be explained by the fact that it does not account for all of the applied energy. At the point of crack initiation, it was found to give the analytical mode partition. The mode decomposed J integral ($J_{\Gamma_{ext}}$) predicted the correct partition for all stages of loading in the FRMM test and was deemed to be the most robust method of partitioning.

In the second part of this chapter, the mode partition is studied as a function of varying cohesive properties in both AFRMM and ADCB test geometries. The mode partitions are obtained by integrating along the cohesive surfaces when the simulation reaches steady state. Two different cohesive zone formulations are used in the study; a coupled linear softening cohesive zone formulation, which is readily available in Abaqus [42], and an uncoupled Dugdale (constant traction) formulation developed by Yang et al. [67]. Due to thermodynamic inconsistencies in the coupled cohesive zone, it is required to keep the pure mode strengths, and toughnesses, equal under mixed mode loading

conditions. The uncoupled cohesive zone does not suffer from such problems, and a number of cases are tested where $G_{IC} \neq G_{IIC}$. A number of conclusions are drawn from this study:

- When the fracture process zone is small, the local partitioning solution is also recovered from the cohesive zone solution. This is in agreement with results presented in Parmigiani and Thouless [40].
- As the cohesive zone size grows, the partition deviates away from the local solution, and in all cases moves towards the global solution, which seems to form the upper bound.
- The cohesive zone properties are chosen to represent values which would typically be expected in composites and adhesive joints, and it is found that in most cases the numerical partition lies between the local and global solutions, suggesting limited applicability of both the local and global approaches in their current form.

Based on these numerical findings, it is proposed that the cohesive length relative to the size of the K dominant region is the controlling factor in determining the mode mixity between local and global solutions. A mixed mode parameter, f, is introduced which uniquely describes how global $f = 0$ or local $f = 1$ a particular solution is. When the normalised cohesive length for all cases are plotted against this mixed mode parameter, a unique dependency is observed which is independent of test geometry (AFRMM or ADCB), cohesive properties, cohesive zone type (coupled linear softening or uncoupled Dugdale), and whether $G_{IC} < G_{IIC}$ or $G_{IC} > G_{IIC}$.

In chapter 4 of this thesis, a semi-analytical cohesive analysis (SACA) is proposed for calculating mixed mode partitions based on this observed unique dependency. An exponential function of the form $f = ae^{bl_{nd}+ce^{dl_{nd}}}$ is found to accurately describe the observed unique dependency, and the various parameters are found by obtaining a least squares fit to the data. The SACA approach utilises analytical estimations of cohesive zone length [96] to determine the mode mixity from the unique dependency curve. Equations are proposed for calculating cohesive zone lengths in asymmetric geometries under general mixed mode conditions; these are found to give reasonable estimates when a shape factor, M, of 0.66 is used for the linear softening cohesive zone, and a shape factor of 0.33 is used for the Dugdale cohesive zone. The required parameters in the SACA analysis are; substrate elastic properties; beam geometry and loading; cohesive strength and shape factor M. A value of G_c is also required for the analysis; this can be obtained directly from experiments, or in the absence of this data, can be estimated directly from an assumed failure locus. The method is found to work well in predicting mixed mode

partitions when compared directly to numerically measured values in a verification test case using the coupled linear softening cohesive zone. The proposed unique dependency curve is also found to hold true for this verification test case.

In the final part of this chapter, the proposed SACA method is used to re-partition AFRMM and ADCB/AMMB test data from previously contrasting reports in the literature [32, 33]. Both linear softening and Dugdale cohesive zone shape factors are used as they give an upper and lower bound to the trapezoidal law. It is found that the SACA partitioning (Linear softening and Dugdale) could be used to explain the results from both cases, based on the estimated cohesive length scale parameter. Two main conclusions can be drawn from this:

- The cohesive zone approach captures the experimentally observed shift from the local towards the global partitioning as the level of damage increases.
- The proposed semi-analytical cohesive analysis proves an efficient and accurate method for predicting mixed mode partitions.

Chapter 5 of this thesis outlines an experimental study in which the mixed mode failure locus of AS4/8552 (carbon/epoxy) is measured using symmetric specimens, and then various partitioning theories are assessed in their ability to produce this failure locus when applied to partition fracture energies obtained in asymmetric tests on the same material. The measured initiation fracture toughness is partitioned according to the analytical partitioning theories; these are Williams [20](W), Suo and Hutchinson [26](HS), Davidson et al. [27](D-NSF), Wang and Harvey [28] (WH), and the newly developed SACA partitioning. Both the linear softening (L) and Dugdale cohesive zone shapes are used in SACA partitioning. It is found that only SACA(L) and SACA(D) partitioning of the asymmetric tests produce a failure locus that is compatible with the symmetrically measured failure locus. SACA(L) performs the best, however, which suggests that the correct cohesive law is given by a linear softening shape. Both the D-NSF and WH partitioning produce consistent results in the mode II dominated cases; however, they do not predict the correct mode partition for the mode I dominated case, which is predicted to be close to the local solution of Suo and Hutchinson [26]. This is the only case that local partitioning accurately predicts, as the correct mode partition evidently moves away from the local solution towards the global solution in the mode II dominated cases. The global solution of Williams [20] does not perform well in predicting the correct failure locus either; in the mode I dominated case, it predicts it is almost pure mode I (92%), whereas the measured toughness is close to the local solution, which is only 60% mode I; in the mode II dominated cases, the global solution also predicts that

they are too close to mode II, where the correct solution evidently falls in between the local and global solution. The ability of the SACA partitioning to accurately predict the mode partitioning based on the substrate and cohesive zone properties is further evidence that the mode partition is indeed dependent on damage in reality, and the numerical simulations can accurately capture this dependence.

6.3 Future Recommendations

This sections outlines a number of areas where there is considerable scope for future work.

6.3.1 Accurate measurement of cohesive zone laws

It was attempted to directly measure the cohesive zone laws during fracture testing using both DIC and with an extensometer placed at the crack tip. However, sufficient accuracy was not obtained and there was no consistency achieved between the DIC and extensometer measurements in the mode I case. It is believed that there is scope to carry out these experiments in-situ on a smaller scale under the microscope, so that the fracture processes can be monitored in much more detail. DIC can then be used to extract much more accurate crack tip opening and shearing displacements, which could be obtained very close to the crack tip. Along with obtaining accurate cohesive zone laws, the particular failure mechanisms under the various modes of loading could be studied in much greater detail as they develop under the microscope; this information could lead to the development of a physically based predictive failure criteria.

6.3.2 Micro-mechanical modelling of mixed mode fracture process zones

Currently, there is no predictive mixed mode failure criteria for failure in laminated composite materials. This is partly down to the fact that often these failures occur as a mixture of many different failure mechanisms, and it is not straightforward to predict the contributions of each. Alongside experimental observations, it is believed that micro-mechanical models of the composite structure at the micro scale could be used to identify the various damage mechanisms which occur under different loadings, and therefore predict the toughness at a given global mode of loading. These models could be used to attain a deeper understanding as to what happens at the micro level that contributes to the changes in fracture toughness observed in experimental tests under different loadings.

6.3.3 Measurement of physical damage zone size

The damage zone size has been shown to be a critical parameter in determining the mode mixity in the current work. An important area of future work would be to try to directly measure the damage zone size in fracture samples to see if there is a direct correlation between the damage zone lengths measured in experiments and those predicted by numerical simulations. Possible techniques for estimating damage zone size could include X-ray CT scanning, scanning electron microscopy(SEM) and fractography.

6.3.4 Uniqueness of mixed mode failure locus.

Finally, it is assumed throughout this work that the mixed mode failure locus is unique. i.e. a single mode partition corresponds only to a single toughness value. This idea is deeply rooted in linear elastic fracture mechanics, where the crack behaves in an elastic manner and therefore exhibits path independence. However, more work needs to be carried out on actual fracture process zones to see if the final toughness is dependent on the loading path, or only on the final applied mode ratio, as assumed currently. This could also be investigated using the micro mechanical models in conjunction with in-situ experiments.

Appendix A

Limitations of Cohesive Zones derived from General Potential Functions

An example potential function is given below in eq. A.1

$$\frac{G}{G_{IIC}} = \frac{(\delta^*/\delta_0 + \xi)^n - \xi^n}{(1+\xi)^n - \xi^n}\left(\frac{\pi/2 + \theta}{\pi}\right); \quad \text{for} \quad 0 \geq \delta^*/\delta_0 \leq 1 \tag{A.1}$$

where G is the ERR, G_{IIC} is the critical mode II ERR, δ_0 is the critical displacement, which is set to 2 mm, δ^* is the current effective displacement given by:

$$\delta^* = \sqrt{\delta_N^2 + \delta_S^2} \tag{A.2}$$

where δ_N and δ_S are the normal and shear displacements in the cohesive zone. ξ and n are shape factors and are set to 0.1 and 0.2 respectively. θ adds a dependence on the ratio of displacements and is given by:

$$\theta = \tan^{-1}\frac{\delta_S}{\delta_N} \tag{A.3}$$

The potential function of eq. A.1 is adapted from Sørensen and Kirkegaard [82] but with the last term in brackets added to give the function a dependence on the mode of

loading. Three different test loadings are carried out corresponding to:

$$\begin{aligned} A &: \theta = \pi/4 \quad \text{(Constant displacement ratio)} \\ B &: \theta = (\frac{\pi}{2}) - (\frac{d^*}{d_0})(\frac{\pi}{4}) \quad \text{(Initially pure mode II)} \\ C &: \theta = (\frac{d^*}{d_0})(\frac{\pi}{4}) \quad \text{(Initially pure mode I)} \end{aligned} \tag{A.4}$$

In case A, the displacement ratio remains constant throughout the loading; in case B, the loading starts out in pure mode II and mode I loading is gradually introduced; in case C, the loading starts out in pure mode I and mode II loading is gradually introduced. In all cases the final displacement ratio is equal with $\delta_S/\delta_N = 1$. The potential function of eq. A.1 is plotted in fig. A.1 showing the three different loading paths A, B and C. Using the chain rule, the normal and shear tractions (t_N, t_S) are obtained by partially differentiating the potential function as follows:

$$\begin{aligned} t_N(\theta, \delta^*) &= \frac{\partial G}{\partial \delta_N} = \cos\theta \frac{\partial G}{\partial \delta^*} - \frac{\sin\theta}{\delta^*}\frac{\partial G}{\partial \theta} \\ t_S(\theta, \delta^*) &= \frac{\partial G}{\partial \delta_S} = \sin\theta \frac{\partial G}{\partial \delta^*} + \frac{\cos\theta}{\delta^*}\frac{\partial G}{\partial \theta} \end{aligned} \tag{A.5}$$

When expanded, the normal and shear tractions are given by:

$$t_N(\theta, \delta^*) = \cos\theta \frac{G_{IIC} n}{\delta_0} \Big(\frac{\pi/2 + \theta}{\pi}\Big) \frac{(\delta^*/\delta_0 + \xi)^{n-1}}{(1+\xi)^n - \xi^n} - \frac{\sin\theta}{\delta^*}\frac{G_{IIC}}{\pi}\frac{(\delta^*/\delta_0 + \xi)^n - \xi^n}{(1+\xi)^n - \xi^n} \tag{A.6}$$

$$t_S(\theta, \delta^*) = \sin\theta \frac{G_{IIC} n}{\delta_0} \Big(\frac{\pi/2 + \theta}{\pi}\Big) \frac{(\delta^*/\delta_0 + \xi)^{n-1}}{(1+\xi)^n - \xi^n} + \frac{\cos\theta}{\delta^*}\frac{G_{IIC}}{\pi}\frac{(\delta^*/\delta_0 + \xi)^n - \xi^n}{(1+\xi)^n - \xi^n} \tag{A.7}$$

These normal and shear traction functions are plotted graphically in fig. A.2(a) and fig. A.3(a) respectively, and the individual traction-displacement curves for loadings A, B and C for both normal and shear openings are shown in fig. A.2(b) and fig. A.3(b) respectively as a function of the respective opening and shear displacements. Integration of these normal traction-normal opening and shear traction-shear opening curves up to the critical displacement yields the mode I and mode II ERR for the given loading cycle. i.e.

$$\begin{aligned} G_I &= \int_0^{\delta_0} t_N(\theta, \delta^*) d\delta_N; \quad \theta = A, B, C \\ G_{II} &= \int_0^{\delta_0} t_S(\theta, \delta^*) d\delta_S; \quad \theta = A, B, C \end{aligned} \tag{A.8}$$

To calculate these integrals, δ^* is incremented from 0 to δ_0 in steps of .01 mm and at each step, δ^* is decomposed into δ_N, δ_T using the definition of θ given in eq. A.4. This gives a value of t_N and t_S corresponding to the respective displacements δ_N,δ_S for each

loading case (i.e. Curves in fig. A.2(a) and fig. A.3(a)). The integration of these curves is performed numerically using the trapezoidal rule; this is carried out in Matlab and the results are presented in table A.1.

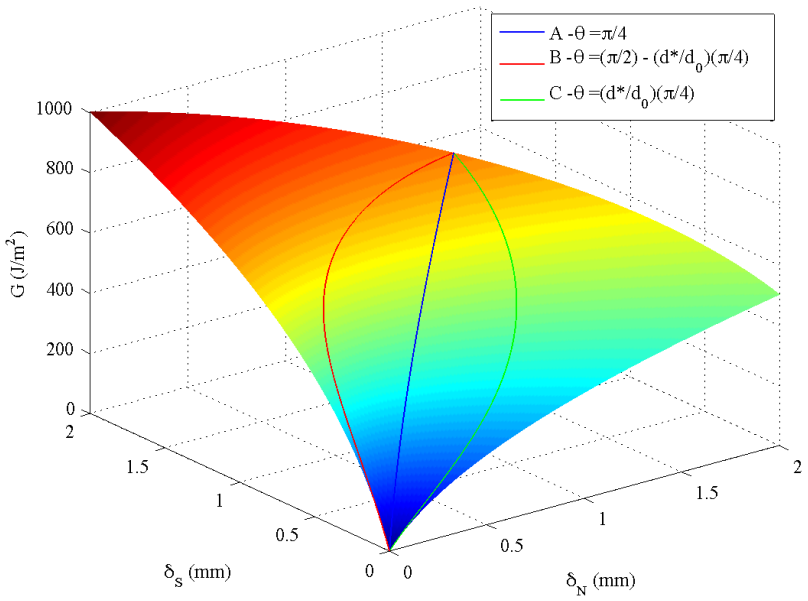

FIGURE A.1: Potential surface given by eq. A.1

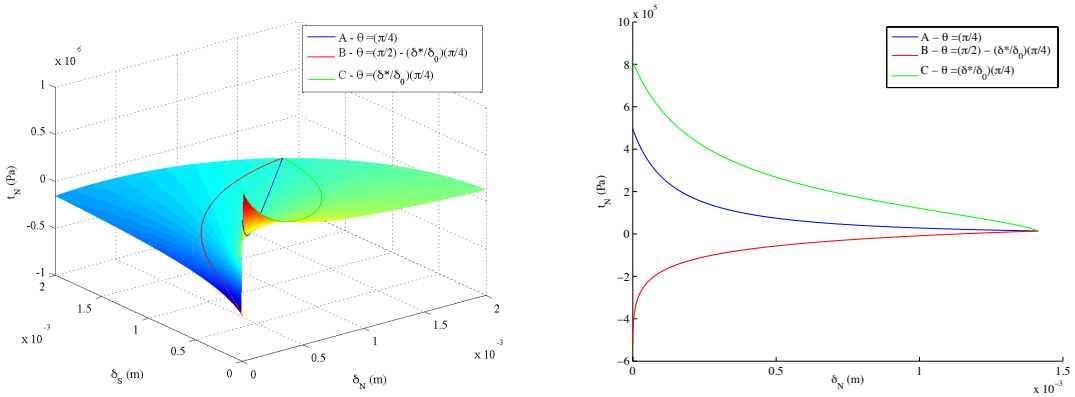

(a) Normal traction function given by eq. A.6

(b) Normal traction vs. normal displacement

FIGURE A.2: Normal traction

It is clear from the results in table A.1 that the total ERR G is equal in all cases, as is required by the potential function for loading cases that end up at the same displacement ratio at final failure. However, the energies dissipated in mode I and mode II vary significantly depending on the path taken to arrive at the final displacement. This example confirms eq. 3.1 and therefore this potential cohesive zone is not consistent

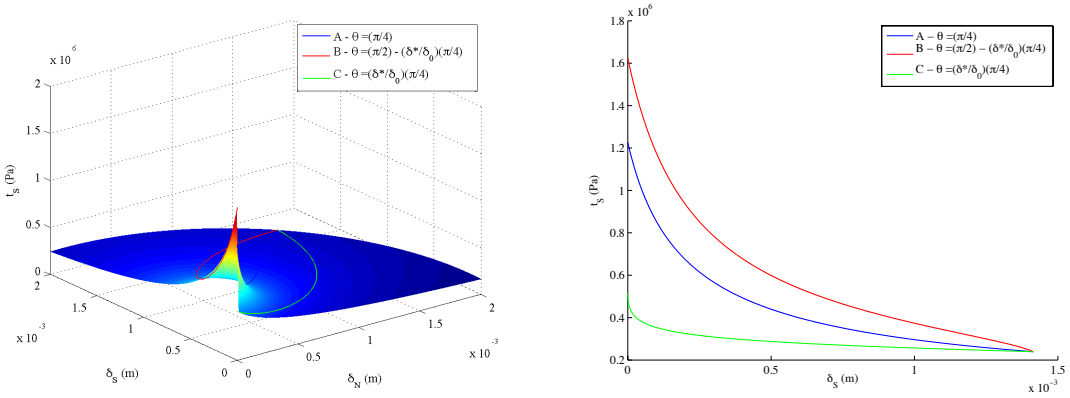

(a) Shear traction function given by eq. A.7

(b) Shear traction vs. shear displacement

FIGURE A.3: Shear traction

Loading	G_I (J/m^2)	G_{II} (J/m^2)	G (J/m^2)	G_{II}/G
A	123.9	626.0	750.0	0.8347
B	-78.6	828.6	750.0	1.1048
C	348.3	401.7	750.0	0.5356

TABLE A.1: Mode I ERR G_I, mode II ERR G_{II}, total ERR G and mode partition G_{II}/G from the potential function outlined by eq. A.1 for the various loadings outlined in eq. A.4

with the definition of the failure locus defined in chapter 1. Also, loading B exhibits another downside of the general potential function in that a negative energy contribution is predicted by the normal traction-displacement curve (fig. A.2).

Appendix B

Limitations of Coupled Linear-Softening Cohesive Zone

B.0.5 Introduction

It has been highlighted in chapter 3 that the current abaqus CZM suffers from inaccurate energy dissipation when the pure mode I toughness (G_{IC}) and the pure mode II toughness (G_{IIC}) are set to different values. There is also inaccuracy when the cohesive strengths (t_{NC}, t_{SC}) and the initial penalty stiffnesses (k_{yy}, k_{xx}) are unequal. The cohesive zone model is illustrated graphically in fig. 3.1. The individual effects of each of these properties are investigated in this section. These issues have also been highlighted in previous publications [86, 87, 94]. Turon et al. [87] proposed a modification to this cohesive zone formulation but this requires the normal and shear cohesive strengths to be set at a certain ratio to ensure correct energy dissipation under changing mode mixity [91, 94].

B.0.6 Case Setup

The AFRMM model is utilised in this analysis with $\gamma = 1$. Again, this case is of particular interest because the mode partition is known to be exact. The model setup is shown in fig. 3.11(a). As before, a quadratic initiation criterion (eq. 3.2) and linear failure locus (eq. 3.7) are used. The cohesive and substrate properties used in the current case studies are outlined in table B.1

In case A, the strengths, toughnesses and penalty stiffnesses are set to be equal and simulations with three beam stiffnesses are carried out. In case B, the mode II toughness

Case	G_{IC} (J/m^2)	G_{IIC} (J/m^2)	t_{NC} (MPa)	t_{SC} (MPa)	k_{yy} (Pa/m)	k_{xx} (Pa/m)	Beam Stiffness (GPa)
A1/A2/A3	200	200	45	45	1.00E+15	1.00E+15	50/500/1000
B1/B2/B3	200	400	45	45	1.00E+15	1.00E+15	50/500/1000
C1/C2/C3	200	200	30	60	1.00E+15	1.00E+15	50/500/1000
D3	200	200	60	30	1.00E+15	1.00E+15	1000
E3	200	200	45	45	1.00E+13	1.00E+17	1000

TABLE B.1: Cohesive Zone properties used for the investigation of energy dissipation.

is set greater than the mode I toughness, with all remaining properties remaining equal. In case C, the shear cohesive strength is set higher than the normal cohesive strength, with all other properties remaining equal. In case D, the normal cohesive strength is set higher than the shear cohesive strength, with all other properties remaining equal. In case E, the shear penalty stiffness is set higher than the normal penalty stiffness, with all other properties remaining equal. For cases A, B and C, three cases are carried out to examine the effect of substrate stiffness on the result, with cases $1, 2$ and 3 corresponding to beam stiffnesses of $50\ GPa$, $500\ GPa$ and $1000\ GPa$ respectively. A larger substrate stiffness results in a larger cohesive zone length so it is believed that this will increase the local variation of mode mixity in a cohesive element from initiation to failure, and hence increase the error.

B.0.7 Results and Discussion

For each of the cases outlined in table B.1, the mode decomposed J integral (eq. 3.11) is applied to the cohesive surfaces once steady state crack propagation is reached. This yields values for G_I and G_{II}, which are plotted against each other for each case in fig. B.1. For cases A, B and C, the beam stiffness is varied to examine the effect of increasing the size of the damage zone. The larger data points indicate larger beam stiffness.

For case A ($G_{IC} = G_{IIC}, t_{NC} = t_{SC}, k_{xx} = k_{yy}$), all of the data points lie along the specified failure locus. Therefore, the correct amount of energy is dissipated by the CZM. Also the increase in beam stiffness, and hence the extent of damage, has no effect on the accuracy of the energy dissipated. For case B ($G_{IC} < G_{IIC}, t_{NC} = t_{SC}, k_{xx} = k_{yy}$), there is more energy dissipated than is specified for that given mixed mode ratio. The error increases as the size of the damage region increases. This is an interesting point as it gives a major clue as to why such inaccuracy exists in this CZM. It is seen in chapter 3 that under the current AFRMM mixed mode loading ($k = 0$), the cohesive zone tends to initiate in pure mode II when the damage region is fully developed. When the cohesive zone initiates, it uses its current mode mix to estimate displacement at failure (δ_f fig. 3.1) based on the required energy dissipation. The displacement at failure is needed in order to be able to soften the tractions linearly with increasing

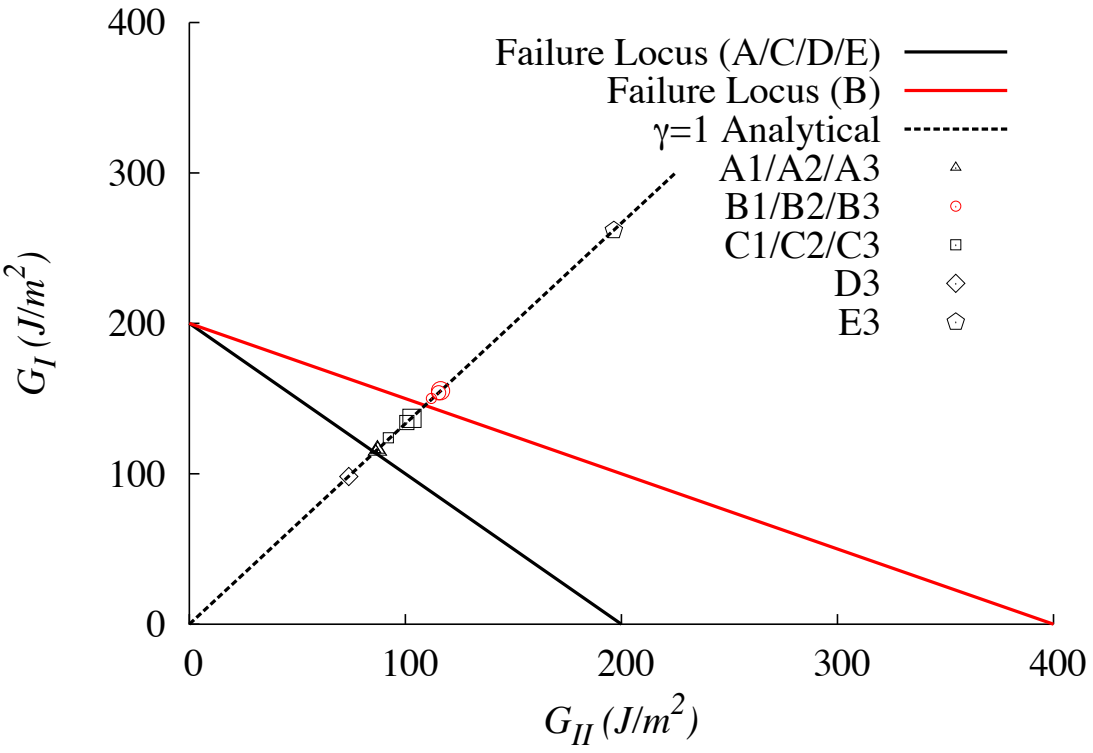

FIGURE B.1: Plot of CZM energy dissipation

effective displacement. However when the mode mix changes, the current CZM re-estimates δ_f based on the updated mode mix and does not consider the energy already dissipated by the cohesive element (i.e. it assumes it has always been operating at the current mode mix). This can lead to an incorrect amount of energy being dissipated. A similar pattern is seen in case C ($G_{IC} = G_{IIC}, t_{NC} < t_{SC}, k_{xx} = k_{yy}$) where the shear cohesive strength, t_{SC}, is set higher than the normal cohesive traction, t_{NC}. In this case, initiation occurs at a higher traction in mode II and as the mode mix starts to change, δ_f will increase in order to dissipate the correct energy at the current mode mix. However it does not realise it has already dissipated a larger amount of energy at a higher traction and so more energy is again dissipated than is specified. The opposite effect is seen in case D ($G_{IC} = G_{IIC}, t_{NC} > t_{SC}, k_{xx} = k_{yy}$) where the shear cohesive strength, t_{SC}, is set lower than the normal cohesive strength, t_{NC}. In this case the critical displacement, δ_f , will start to decrease as the mode mix changes. This will result in less energy being dissipated than is specified. Figure B.2 plots the effective traction separation curves for each of the cases discussed. The most worrying case by far is case E ($G_{IC} = G_{IIC}, t_{NC} = t_{SC}, k_{xx} > k_{yy}$) in which the initial stiffnesses of the cohesive zone are set to be different. It is now required to discuss the governing equations to explain the poor accuracy in energy dissipation and erratic traction separation behaviour

seen in case E.

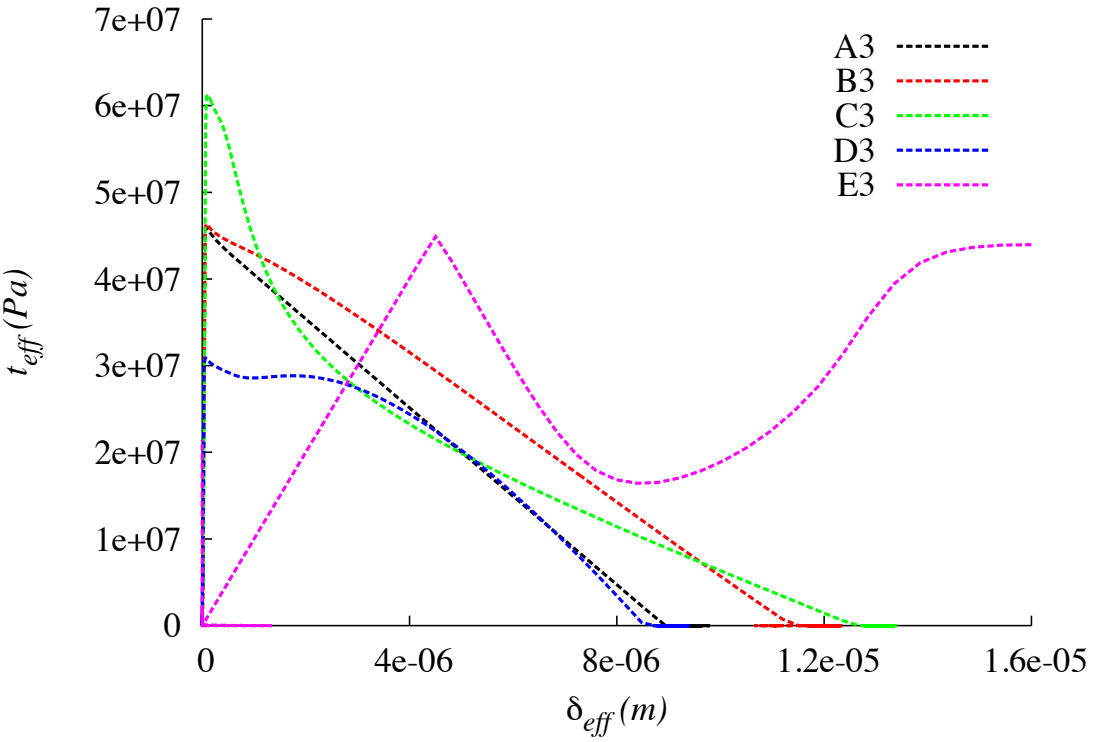

FIGURE B.2: Effective traction separation curves.

After the initiation traction of the cohesive element has been reached, the effective traction ($t_{eff} = \sqrt{t_N^2 + t_S^2}$) is softened linearly with increasing effective displacement ($\delta_{eff} = \sqrt{\delta_N^2 + \delta_S^2}$), according to equation 3.6, where the damage variable D is incremented linearly with increasing effective displacement, starting at zero at damage initiation and reaching a value of one at the critical displacement, δ_f according to eq. 3.5. By substituting expressions for the un-damaged tractions ($\bar{t}_N, \bar{t}_S$) given by the pre-damage stiffness matrix in eq. 3.4 (i.e. $\bar{t}_N = k_{yy}\delta_N$; $\bar{t}_S = k_{xx}\delta_S$) directly into eq. 3.6, the effective traction, t_{eff} can be rewritten as a function of the effective displacement δ_{eff} as follows:

$$t_{eff} = (1 - D)\sqrt{\frac{(xk_{yy})^2 + (k_{xx})^2}{1 + x^2}}\delta_{eff} \tag{B.1}$$

where $x = \delta_N/\delta_S$. It is clear from eq. B.2 that there will only be a linear relationship between the effective traction and effective displacement if the ratio of normal to shear displacement in the cohesive element remains constant from initiation to failure. It has been observed that this is not the case for large damage regions as the mode mix changes considerably from initiation to failure. Equation B.2 coupled with a changing ratio of δ_N/δ_S can therefore explain the erratic behaviour of the traction separation curve and hence the large error in energy dissipation observed in case E3. It should be noted that

if $k_{xx} = k_{yy} = K$, eq. B.2 reduced to:

$$t_{eff} = (1 - D)K\delta_{eff} \tag{B.2}$$

and hence there is no issue with a changing mode mix (assuming there is no change in the predicted δ_f as seen in cases B-D). As the penalty stiffnesses are only only a numerical artefact, it is not a problem to set them to be equal. However, it is very important to be aware of the possible errors which may be created of they are set differently in the current formulation; something which is not mentioned in the abaqus documentation [42].

B.0.8 Conclusion

Issues with the current cohesive zone model have been highlighted in this section. It has been shown that the model suffers from incorrect energy dissipation when the parameters of toughness, strength and stiffness are not chosen to be equal in the mode I and mode II directions. It has also been shown that the changing mode mix leads to incorrect energy dissipation in this cohesive zone element. Abaqus documentation [42] only mentions the assumption of a constant mode mix and it does not warn against the use of these elements under conditions of a changing mode mix. It is clear that though the current cohesive zone model allows the mode mix ratio to change, it does not correctly account for it in its overall energy estimation.

Appendix C

Excel Macro: Semi-Analytical Cohesive Analysis

```
Sub Partition()
     j = 11
    m = Cells(7, 11)
    Do While Cells(j, 1).Value <> "" 'Loop through All Cells
    f = 0.5       'Initial guess for f
    'Read in Values
    'Geometry
    h1 = Cells(j, 1).Value / 1000
    h2 = Cells(j, 2).Value / 1000
    g = h2 / h1
    hc = WorksheetFunction.Min(h1, h2) 'Smallest Characteristic
  Length
    bc = WorksheetFunction.Max(h1, h2)
    k = Cells(j, 3).Value
    h = (h1 + Abs(k) * h2) / (1 + (bc / hc) * Abs(k))
    'Substrate elastic properties
    E11 = Cells(j, 4).Value * 1000000000#
    E22 = Cells(j, 5).Value * 1000000000#
    E33 = E22
    G12 = Cells(j, 6).Value * 1000000000#
    v12 = Cells(j, 7).Value
    v21 = v12 * (E22 / E11)
    v23 = Cells(j, 8).Value
    'Cohesive Properties
    S = Cells(j, 9).Value * 1000000#
    GIC = Cells(j, 10).Value
```

```
  GIIC = Cells(j, 11).Value
  Gc = Cells(j, 12).Value
  v31 = v12 * (E33 / E11)
  v21 = v12 * (E22 / E11)
  v13 = v12
  v32 = v23
  'Calculate plane strain elastic properties
  E11o = E11 / (1 - v13 * v31)
  E22o = E22 / (1 - v23 * v32)
  v21o = (v21 + v23 * v31) / (1 - v23 * v32)
 'Determine whether plane stress or plane strain option is
chosen
  'Plane Stress Option
  If Cells(7, 4).Value = 1 Then
  b11 = 1 / E11
  b22 = 1 / E22
  b21 = -v21 / E22
  b66 = 1 / G12
  'Plane Strain Option
  ElseIf Cells(7, 4).Value = 2 Then
  b11 = 1 / E11o
  b22 = 1 / E22o
  b21 = -v21o / E22o
  b66 = 1 / G12
  End If
  'Calculate effective mode I and mode II elastic constants
  EI = 1 / ((Sqr(b11 * b22 / 2)) * Sqr(Sqr(b22 / b11) + (2 *
b21 + b66) / (2 * b11)))
  EII = E11 / (1 - v13 * v31)
  'Calcuation of Mode Mix
  For i = 1 To 1000
  GIGw = GIGwn(f, g, k) 'Calculate GI/G from global analytical
solution (Williams)
  GIGhs = GIGhsn(f, g, k) 'Calculate GI/G from local
analytical solution (Hutchinson & Suo)
  GIG(i) = (1 - f) * GIGw + (f) * GIGhs 'Calculate mode mix
based on the value of the normalised mode mixity.
      If i >= 1 Then 'Enter only if at least one loop hs
occurred previosly
       If (Abs(GIG(i) - GIG(i - 1))) <= 1e-05 Then 'Check if
the solution is converged
      Cells(j, 18).Value = i 'Print number of loops if
convergence is reached
```

```
        Exit For
        End If
    End If
    If i = 1000 Then 'Check if too many iterations have occurred
     Cells(j, 18).Value = "Not Converged"
     Exit For
    End If
    If Cells(j, 12).Value = "" Then 'Check if Gc value has been
entered
    'If no Gc value is enetered, calculate GI and GII according
to Failure Locus
    'If linear failure locus is chosen
    If Cells(6, 10).Value = 1 Then
    If GIG(i) < 1 Then
    GIICg = 1 / ((GIG(i) / ((1 - GIG(i)) * (GIC))) + (1 / GIIC))
    GICg = GIC * (1 - (GIICg / GIIC))
    Else
    GICg = 1 / (((1 - GIG(i)) / ((GIG(i)) * (GIIC))) + (1 / GIC))
    GIICg = GIIC * (1 - (GICg / GIC))
    End If
    'If BK failure locus is chosen
    ElseIf Cells(6, 10).Value = 2 Then
    Gbk = GIC + (GIIC - GIC) * ((1 - GIG(i)) ^ m)
    GICg = GIG(i) * Gbk
    GIICg = Gbk - GICg
    End If
    Else
    GICg = GIG(i) * Gc
    GIICg = (1 - GIG(i)) * Gc
    End If
    'Calculate Cohesive Zone lengths
    lchI = (((EI * (GICg)) / (S ^ 2)) ^ (1 / 4)) * (h ^ (3 / 4))
'Calculate mode I cohesive zone length
    lchII = Sqr((EII * (GIICg) / (S ^ 2)) * h) 'Calculate mode
II cohesive zone length
    If Cells(3, 9).Value = 1 Then 'Check if linear softening or
Dugdale cohesive zone shape is chosen
    lcz = 0.66 * WorksheetFunction.Max(lchI, lchII) 'For linear
softening cohesive zone shape
    ElseIf Cells(3, 9).Value = 2 Then
    lcz = (1 / 3) * WorksheetFunction.Max(lchI, lchII) 'For
Dugdale cohesive zone shape
    End If
```

```
    lnd = lcz / hc 'Calculate the normalised cohesive zone length
    f = 0.9585 * Exp(-0.2326 * lnd) + 0.0985 * Exp(-0.018 * lnd)
  'Calculate normalised mode mixity based on unique curve
    If f >= 1# Then
    f = 1# 'If f>1, return f=1. This means singular zone is so
  small that local solution is correct
    End If
    Next i 'Repeat step
    'Print values when the loop is exited
    Cells(j, 13).Value = 1 - GIG(i) 'Print estimated mode mix
  GII/G
    Cells(j, 14).Value = lcz * 1000 'Print estimated cohesive
  zone length
    Cells(j, 15).Value = f 'Print normalised mode mix
    Cells(j, 16).Value = 1 - GIGw 'Print analytical mode mix
  (Global)
    Cells(j, 17).Value = 1 - GIGhs 'Print analytical mode mix
  (Local)
    j = j + 1
    Loop
End Sub
Function GIGwn(f, g, k) 'Function to calculate global mode mix
  (Williams)
X3 = (1 + g) ^ 3 - 1
X4 = (((1 + g) / g) ^ 3 - 1)
lam1w = g ^ 3
lam2w = 1
GIw = (X3 + (lam2w ^ 2) * X4 + 2 * lam2w) * ((lam1w / (lam1w +
  lam2w)) ^ 2) * (1 - k / lam1w) ^ 2
GIIw = (X3 + (lam1w ^ 2) * X4 - 2 * lam1w) * ((lam2w / (lam1w +
  lam2w)) ^ 2) * (1 + k / lam2w) ^ 2
GIGwn = GIw / (GIw + GIIw)
End Function
Function GIGhsn(f, g, k) 'Function to calculate local mode mix
  (Hutchinson Suo)
X3 = (1 + g) ^ 3 - 1
X4 = (((1 + g) / g) ^ 3 - 1)
If g >= 1 Then
P = 0.75 * (1 - 0.2 * ((g - 1) / g))
lam1hs = (g ^ 2) * (3 + 3 * g + g ^ 2) / (Sqr(3 * P) * ((1 + g)
  ^ 2) + g)
lam2hs = (g ^ 2) * P * (3 + 3 * g + g ^ 2) / (Sqr(3 * P) * ((1 +
  g) ^ 2) - P * g)
```

```
Else
P = 0.75 * (1 - 0.2 * (1 - g))
lam1hs = (g ^ 2) * P * (3 + 3 * g + g ^ 2) / (Sqr(3 * P) * ((1 +
  g) ^ 2) - P * g)
lam2hs = (g ^ 2) * (3 + 3 * g + g ^ 2) / (Sqr(3 * P) * ((1 + g)
  ^ 2) + g)
End If
GIhs = (X3 + (lam2hs ^ 2) * X4 + 2 * lam2hs) * ((lam1hs /
  (lam1hs + lam2hs)) ^ 2) * (1 - k / lam1hs) ^ 2
GIIhs = (X3 + (lam1hs ^ 2) * X4 - 2 * lam1hs) * ((lam2hs /
  (lam1hs + lam2hs)) ^ 2) * (1 + k / lam2hs) ^ 2
GIGhsn = GIhs / (GIhs + GIIhs)
End Function
```

Appendix D

Standard fracture mechanics test methods

D.0.9 Introduction

In this appendix, the results of standard fracture mechanics tests carried out on UD AS4/8552 composite (same material used in chapter 5) are presented. The main aim of this study is to verify, at three modes of loading ($G_{II}/G = 0, 3/7, 1$), that the toughness values measured using the DCB-UBM test rig are correct. The standard tests carried out are the DCB, FRMM and the calibrated ELS (C-ELS). DCB, FRMM and C-ELS produce equivalent modes of loading to the DCB-UBM when k=-1, k=0 and k=1 respectively. Good agreement between the measured toughness values from these methods which produce same mode of loading is therefore expected. In this study, specimens are tested both from the crack starter film (as in chapter 5) and from a $\approx 5mm$ precrack; this may allow possible artefacts of initiating from a crack starter film to be identified.

D.0.10 Specimen Preparation

Composite plates were manufactured in UCD following the exact procedure outlined in chapter 5. The mode I specimens were manufactured to be 3.0 mm in total thickness $[0_{10}/0_{10}]$, 20mm wide, 150 mm long and with an initial crack length of 50 mm; the mode II and mixed mode specimens were each manufactured to be 3.9 mm in total thickness $[0_{13}/0_{13}]$, 25 mm wide, 190 mm long and with an initial crack length of 55 mm. A PTFE crack starter film with a thickness of $\approx 12\ \mu m$ was inserted at the mid-plane during layup to create the initial crack starter defect in each case. Aluminium load blocks were attached to the end of the specimens using rubber toughened cyanoacrylate

adhesive; prior to bonding of the load blocks, the composite surfaces were roughened using light grit blasting and then cleaned with methanol. Water based correction fluid was painted onto the sides of the specimens and then marked at intervals to facilitate tracking of crack growth using a travelling microscope during testing.

D.0.11 Test Procedures

DCB, FRMM, and C-ELS fracture tests were carried out according to ISO 15024:2001 [7], Blackman et al. [6] and ISO 15114:2014 [8] respectively. Each test configuration can be seen in figure D.1. A screw driven Tinus-Olsen 50k tensile test machine was used for all tests. After crack propagation of $\approx 5mm$ in DCB and FRMM tests, the samples are unloaded and re-tested from a more physical crack. Due to unstable initiation in the C-ELS test, the crack rapidly propagated $\approx 30mm$ in each case before being arrested; these samples were unloaded fully at this point and re-tested. A 1 kN load cell and a displacement rate of 1 mm/min was used for DCB, FRMM and ELS tests. During each test, the load-displacement trace was recorded and the corresponding crack lengths were monitored using a travelling microscope and recorded at approximately 5 mm intervals. Five specimens were tested in the DCB test, and three for each the FRMM and C-ELS tests. The fracture toughness for DCB, FRMM and C-ELS were calculated using eqs. (D.1) to (D.3) respectively. In each case, the initiation values were obtained using the $MAX/C_{0-5\%}$ point, as defined in [7].

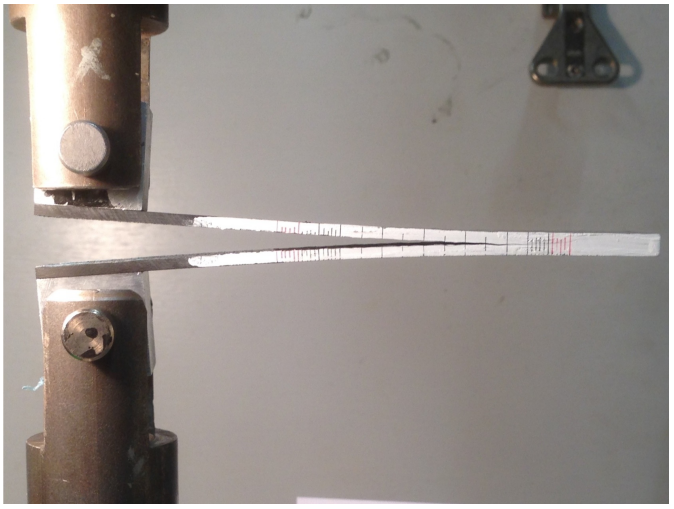

(a) DCB

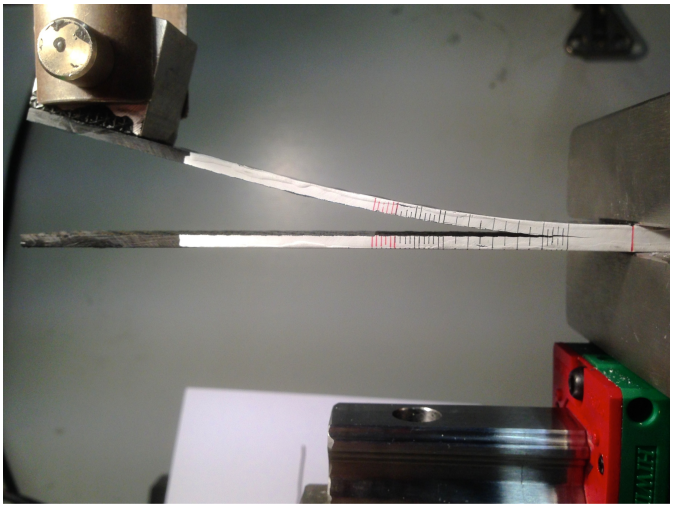

(b) FRMM

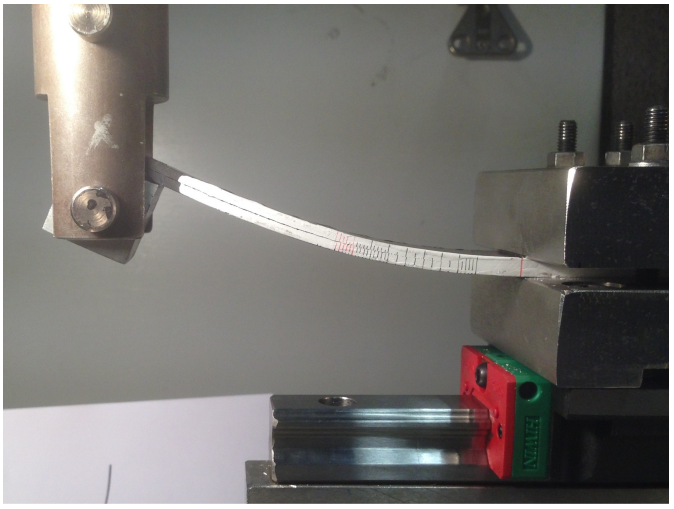

(c) C-ELS

FIGURE D.1: Standard Fracture Test Methods.

$$\underline{\text{DCB}} \Longrightarrow G_{IC} = \frac{3P\delta}{2B(a+|\Delta_I|)}.\frac{F}{N} \tag{D.1}$$

$$\underline{\text{FRMM}} \Longrightarrow G = G_I + G_{II} \tag{D.2a}$$

$$G_I = \frac{3P^2(a+\Delta_I)^2}{B^2Eh^3}.\frac{F}{N} \tag{D.2b}$$

$$G_{II} = \frac{9P^2(a+\Delta_{II})^2)^2}{4B^2Eh^3}.\frac{F}{N} \tag{D.2c}$$

$$\underline{\text{C-ELS}} \Longrightarrow G_{IIC} = \frac{9P^2(a_e)^2}{4B^2Eh^3}.\frac{F}{N} \tag{D.3}$$

where P is the load, δ is the crosshead displacement, B is the specimen width, h is the substrate thickness, E is the substrate flexural or tensile modulus, a is the crack length, and a_e is an effective crack length. F,N,Δ_I and Δ_{II} are correction factors for large displacement, load block effects and root rotation of the crack tip respectively; expressions for estimating these can be found in the corresponding test standards [7],[6] and [8]

D.0.12 Results

The results from the DCB test are presented in fig. D.2 and table D.1; the results from the FRMM test are presented in fig. D.3 and table D.2 and the results from the C-ELS test are presented in fig. D.4 and table D.3.

Mode I test	G_c (J/m^2)	SD
DCB (insert)	233.2	16.4
DCB (pre-crack)	220.2	19.4
DCB-UBM (k=-1) (insert)	210.1	27.6

TABLE D.1: Average initiation toughness values (G_c) and standard deviation (SD) for mode I DCB tests from PTFE insert and from pre-crack compared with initiation values obtained in the DCB-UBM mode I test (Chapter 5).

Mixed mode test	G_c (J/m^2)	SD
FRMM (insert)	280.3	8.1
FRMM (pre-crack)	313.9	26.0
DCB-UBM (k=0) (insert)	296.1	11.7

TABLE D.2: Average initiation toughness values (G_c) and standard deviation (SD) for FRMM tests from PTFE insert and from pre-crack compared with initiation values obtained in the DCB-UBM (k=0) test (Chapter 5).

Mode II test	G_c (J/m^2)	SD
C-ELS (insert)	1044.4	49.5
C-ELS (pre-crack)	654.7	43.9
DCB-UBM (k=1) (insert)	750.1	17.6

TABLE D.3: Average initiation toughness values (G_c) and standard deviation (SD) for C-ELS tests from PTFE insert and from pre-crack compared with initiation values obtained in the DCB-UBM (k=1) test (Chapter 5).

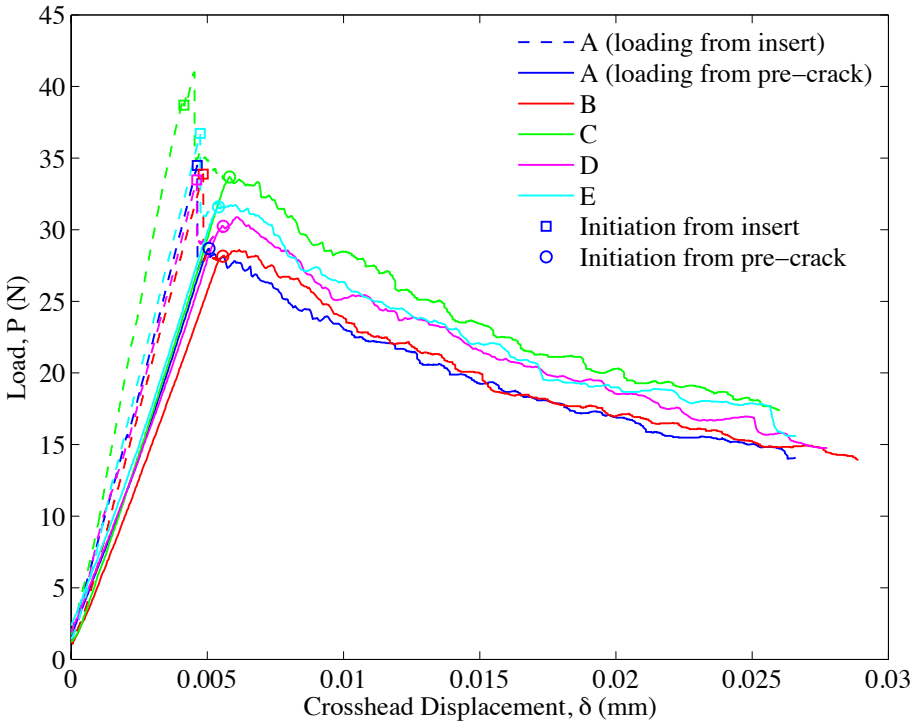

(a) Force vs. crosshead displacement

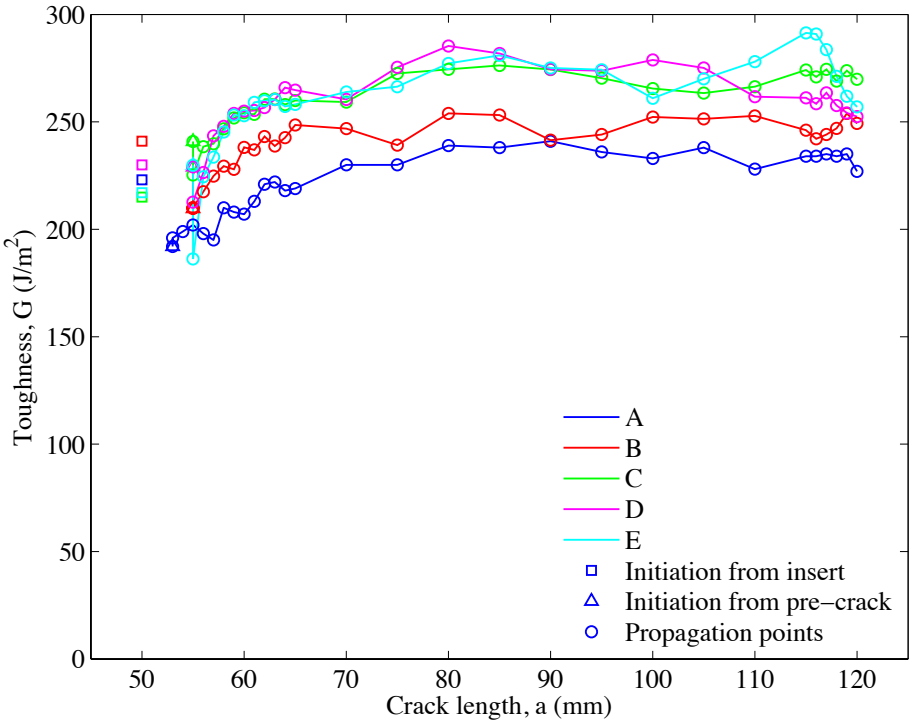

(b) Toughness vs. crack length

FIGURE D.2: Mode I DCB test

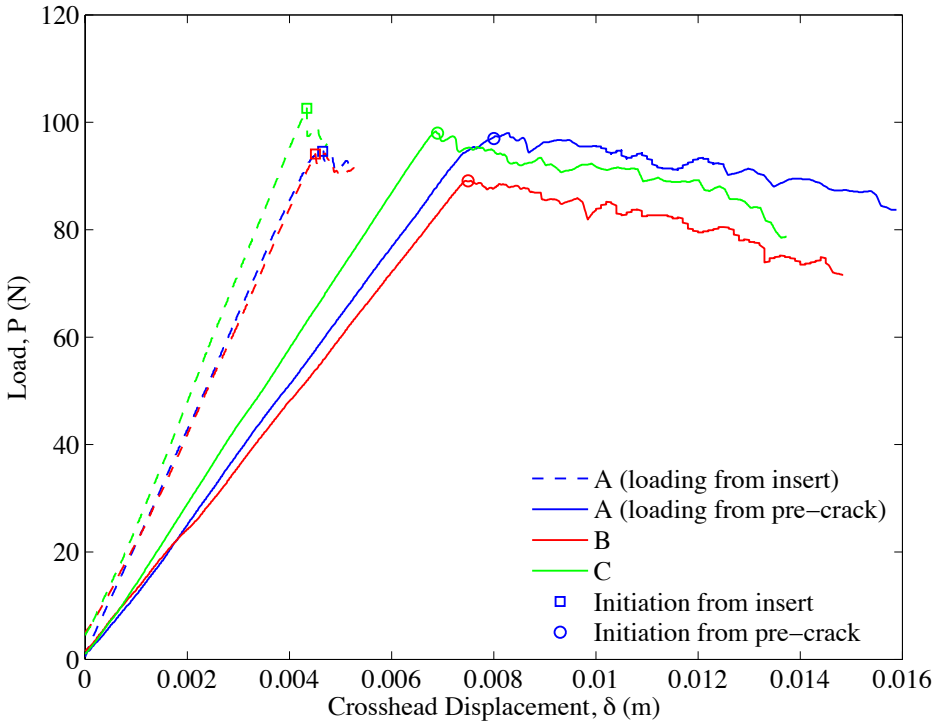

(a) Force vs. crosshead displacement

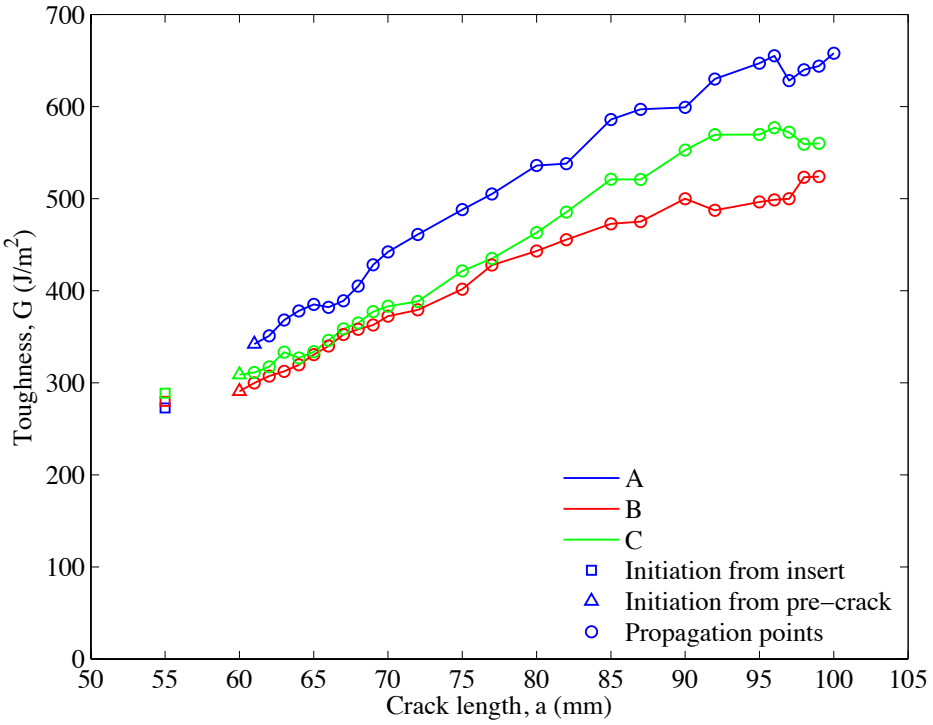

(b) Toughness vs. crack length

FIGURE D.3: Mixed Mode FRMM test

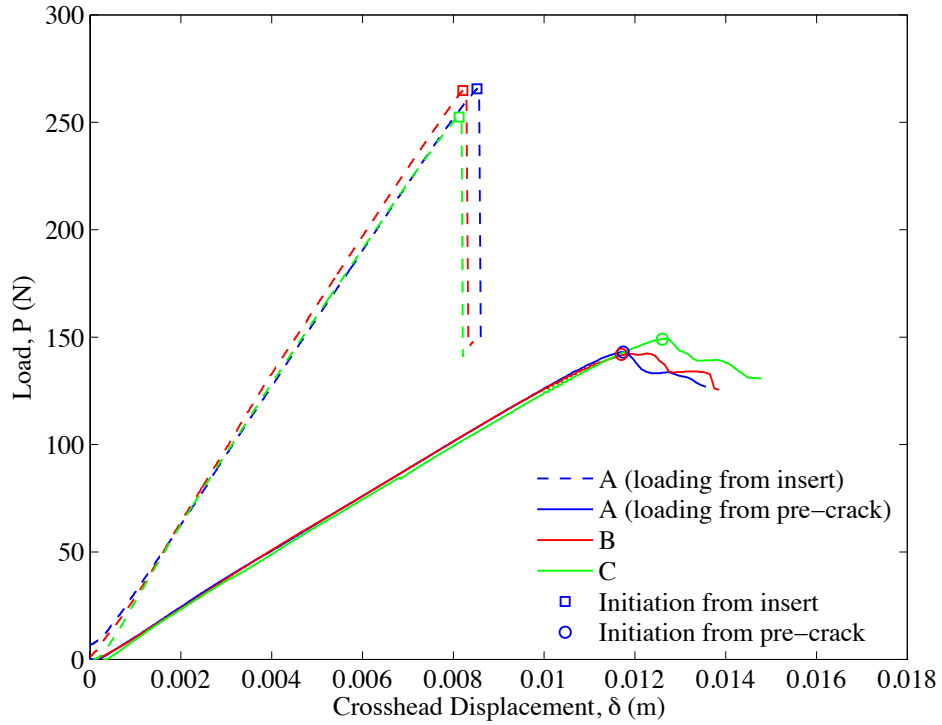

(a) Force vs. crosshead displacement

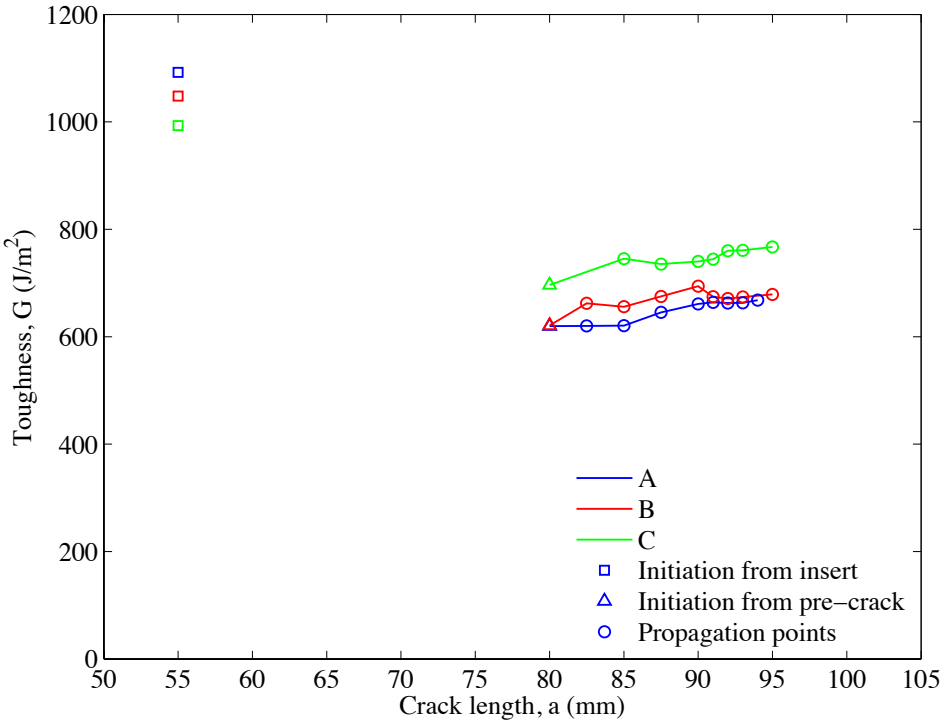

(b) Toughness vs. crack length

FIGURE D.4: Mode II C-ELS test

Appendix E

Measurement of Cohesive Laws using DIC

E.1 Measurement of Cohesive Laws

It was intended to measure the mixed mode cohesive laws by monitoring the applied energy release rate G, where G is equated to the J integral as calculated by eq. 5.2, as a function of the crack tip opening δ_N and shearing δ_S displacements. If it is assumed that the cohesive laws are path independent and all go through the same loading history, the respective cohesive law in opening and shear can then be obtained by differentiating the applied ERR vs. crack tip opening curves. i.e.:

$$\begin{aligned} t_N(\theta, \delta^*) &= \frac{\partial G}{\partial \delta_N} \\ t_S(\theta, \delta^*) &= \frac{\partial G}{\partial \delta_S} \end{aligned} \tag{E.1}$$

This method has been used to successfully obtain cohesive laws of adhesive joints and composites [76, 99, 101]. Sørensen and Jacobsen [101] used an extensometer and two LVDT's (linear variable displacement transducer) to monitor the crack tip opening and shearing displacement respectively; in the test cases carried out here, the samples were not thick enough to mount LVDT's, so shearing displacements could not be determined in this way. However, in the pure mode I case where no shear displacements occur, the extensometer opening can be used alone to determine the mode I cohesive zone law. An explanation of the mounting procedure for the extensometer is given in section 5.3.3. A plot of the results from the extensometer opening vs. applied ERR, G, is given for each mode I symmetric test case in fig. 5.11(a).

Svensson et al. [99] used digital image correlation(DIC) to quantify both the crack tip openings and shearing displacements. The openings for one mode I test are also measured virtually here using digital image correlation (DIC). DIC is a full field method where images are captured of a particular pattern on a specimen throughout testing. The specimen can be subdivided in to square facets (or elements) that can be tracked based on the recognised pattern. As the specimen is deformed, the movement of the facets can be continually related back to the original state, which allows the deformation gradient, and hence strain, to be calculated for each facet. An example of the pattern sprayed onto a tested specimen is shown in fig. E.1. The optimum facet size for this particular pattern was found to be 30 pixels by 30 pixels, which corresponded to a size of $370\mu m \times 370\mu m$. If a smaller facet size is chosen, there will not be sufficient contrast within each facet to make it uniquely recognisable, and hence the images during the test can not be correlated; if a larger facet size is chosen, the resolution of the facets will not be high enough to accurately pick up strain gradients. An image of the facet mesh for the current configuration is shown in fig. E.2. The digital image correlation is carried out using ARAMIS software. The opening is tracked virtually by monitoring the displacement between the two symmetric points on the beams as shown in fig. E.3; the two symmetric points are chosen to be directly in line with the extensometer pins, which were placed in the neutral axis of each of the beams at the crack tip on opposite side of the specimen (fig 5.3(a)). As the camera images are triggered from the data acquisition unit, the crack tip openings can be correlated with the applied load, as seen on the left of fig. E.3.

The measured openings vs. applied loads are plotted for the physical extensometer and the DIC measurements in fig. E.4 for sample A (mode I). Along with the measurement from two points in line with the physical extensometer (DIC (Crack tip)), a number of other DIC measurements are shown in this plot; firstly, the sensitivity of placement of the virtual extensometer is tested by monitoring the displacement a distance of 1.2 mm behind (DIC +1.2 mm) and ahead (DIC -1.2 mm) of the crack tip; secondly, the sensitivity to the distance between measuring points is tested by monitoring the displacements of two points that were only 2.5 mm apart (DIC (Crack Tip, 2.5 mm apart)), as opposed to the original placement of points at the centre of the beams, which are 5 mm apart. This final test serves as a check to see if there is any considerable strain in the transverse direction which may lead to overestimated crack tip opening measurements.

It is evident from fig. E.4 that there is considerable disagreement between the physical extensometer measurement and the DIC measurements of crack tip openings. The physical extensometer records negative opening displacements up to crack initiation, whereas the DIC measurements indicate a gradual opening up to $\approx 18\mu m$ before crack

initiation. The negative openings recorded by the physical extensometer suggests that it was placed inaccurately ahead of the crack tip, where compressive normal stresses are known to develop (figs. E.3,3.12); this was checked visually after testing and the extensometer pins appeared to be placed directly in line with the crack tip to a high degree of accuracy. The placement of the virtual DIC extensometer deliberately ahead of and behind the crack tip by a distance of $1.2mm$ is seen to influence the recorded opening vs. load displacement curves; however, the effect of pin placement seen here is not sensitive enough to explain the discrepancy between the physical and DIC crack tip opening measurements. Also, it is seen that there is negligible effect of carrying out the DIC measurement at two closer points, which confirms the assumption that there is negligible transverse strains and that the recorded openings are primarily down to crack tip openings. One possible explanation for the discrepancy is that there was an uneven load applied to both sides through the transverse arms; however, there was no visible twisting of the specimens observed throughout testing which would support this argument. If it is assumed for a moment that the DIC openings are accurate, the resulting cohesive law can be measured by differentiating the applied ERR G vs. crack tip opening according to eq. E.1. To facilitate accurate differentiation, an idealised function is fitted to the curve, and is illustrated in fig. E.5(a). The idealised curve was found to fit a quadratic opening pattern, and the function is given by:

$$G(\delta_N) = \begin{cases} 3.231 \times 10^1 1\delta_N^2 + 4.279 \times 10^6 \delta_N + 8.160, & \text{if } 0 \leq \delta_N \leq 1.786 \times 10^{-5} m \\ 187.7 J/m^2, & \text{if } \delta_N \geq 1.786 \times 10^{-5} m \end{cases} \tag{E.2}$$

Differentiation of this function leads to the mode I cohesive law, which is described by the equation below and plotted graphically in fig. E.5(b)

$$t(\delta_N) = \begin{cases} 6.462 \times 10^1 1\delta_N + 4.279 \times 10^6, & \text{if } 0 \leq \delta_N \leq 1.786 \times 10^{-5} m \\ 0, & \text{if } \delta_N \geq 1.786 \times 10^{-5} m \end{cases} \tag{E.3}$$

The cohesive law shown in fig. E.5(b) is unusual in that it predicts that the cohesive stress rises steadily as a function of opening displacement; the highest predicted cohesive strength is also very low and is only one quarter of the transverse tensile strength for this material. While there may be some physical arguments for an increasing cohesive strength, it does not seem physical that the cohesive strength should only be a fraction of the transverse tensile strength. This unusually low cohesive strength suggest that the crack tip opening displacements are over-estimated. Given the discrepancy between the physical extensometer and DIC measurements, it was not clear if either of these methods

were accurate enough for the measurement of cohesive laws. Unfortunately, there was not time to further investigate the reasons for these discrepancies, and so it was decided not to rely on either method for obtaining physical cohesive zone laws. Though Sørensen [76] and Sørensen and Jacobsen [101] used this method for cohesive law measurement in adhesive joints and GFRP laminates respectively, the critical opening displacements in these cases were the order of mm, as opposed to μm in the current CFRP tests. It is believed that if accurate crack tip opening and shearing displacements are to be achieved in CFRP, then micro-mechanical tests would need to be carried out under the microscope, and high resolution images then analysed with DIC.

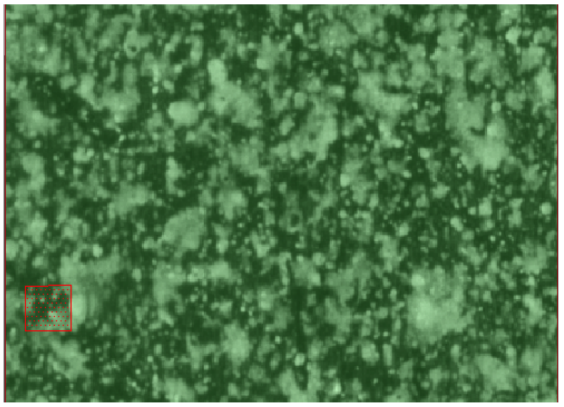

FIGURE E.1: DIC pattern obtained with water based spray paint. Facet is shown as red square, and corresponds to 30 pixels x 30 pixels ($370\mu m \times 370\mu m$)

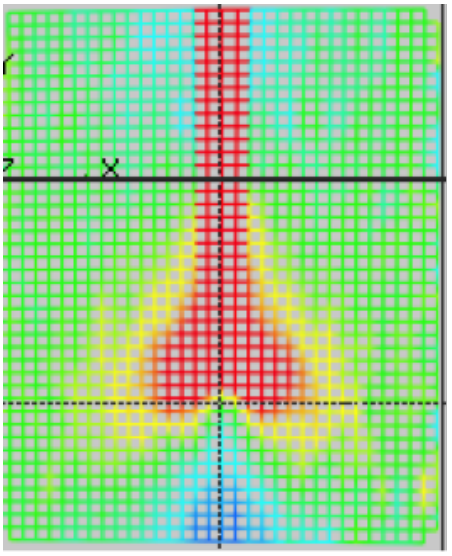

FIGURE E.2: Facet mesh based on $370\mu m \times 370\mu m$ facet size for mode I test. Image corresponds to mode I test shown in fig. E.3.

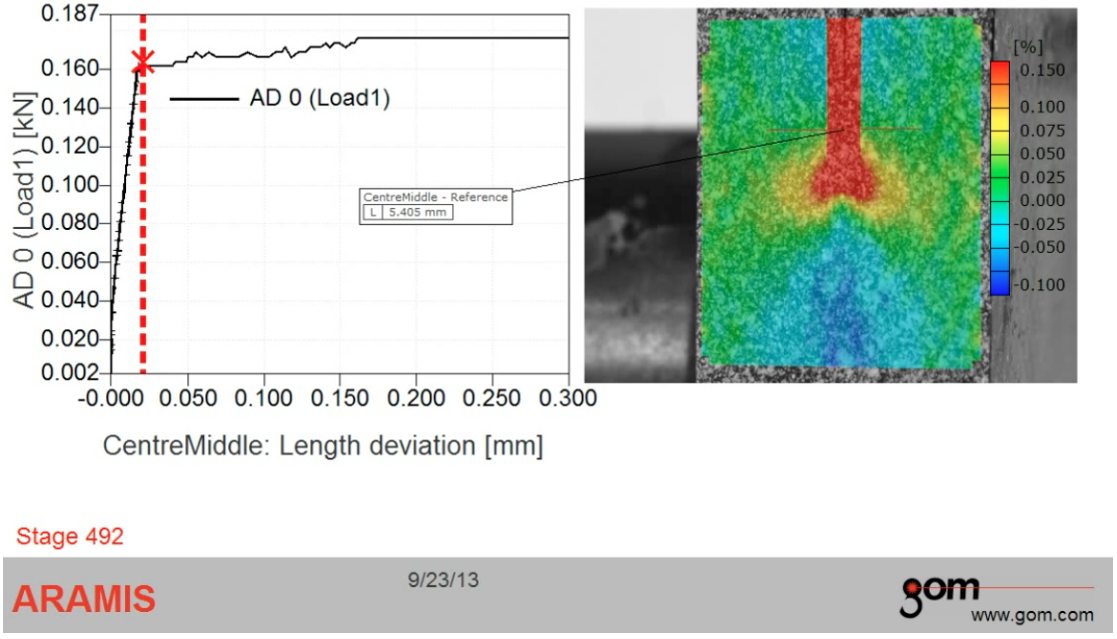

FIGURE E.3: Applied load vs. crack tip opening measured using DIC measurement is shown in the left image; corresponding strain distribution in the transverse xx direction, as calculated from DIC, is shown in the right image. Image orientation and loading is equivalent to fig .5.12(a).

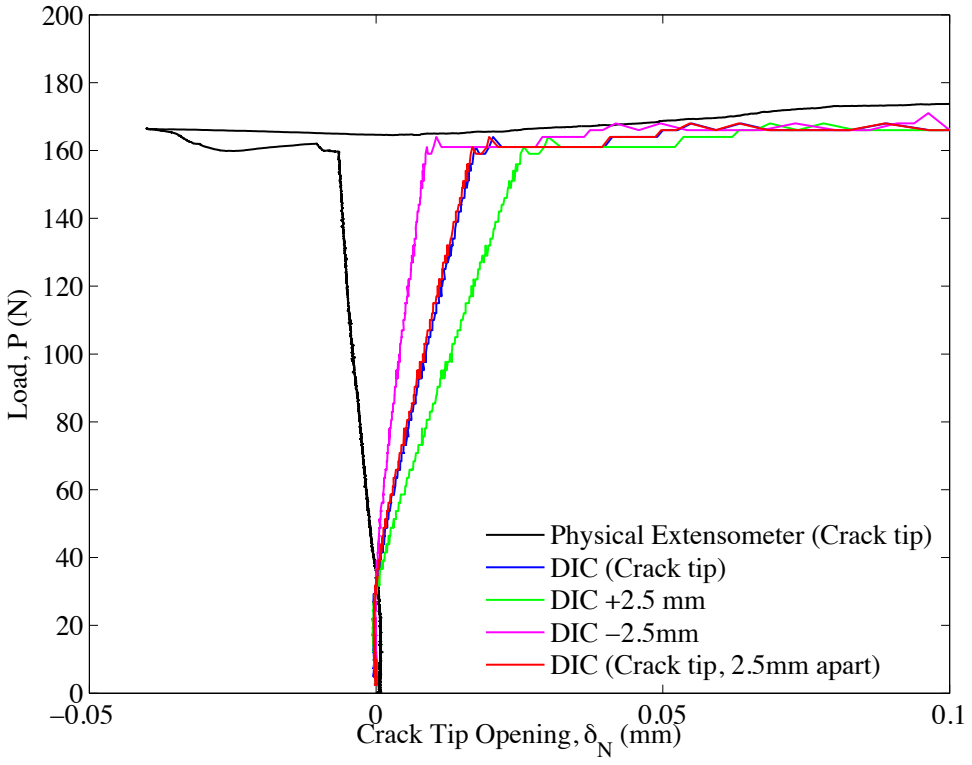

FIGURE E.4: Applied load vs. crack tip opening measured using physical extensometer and DIC.

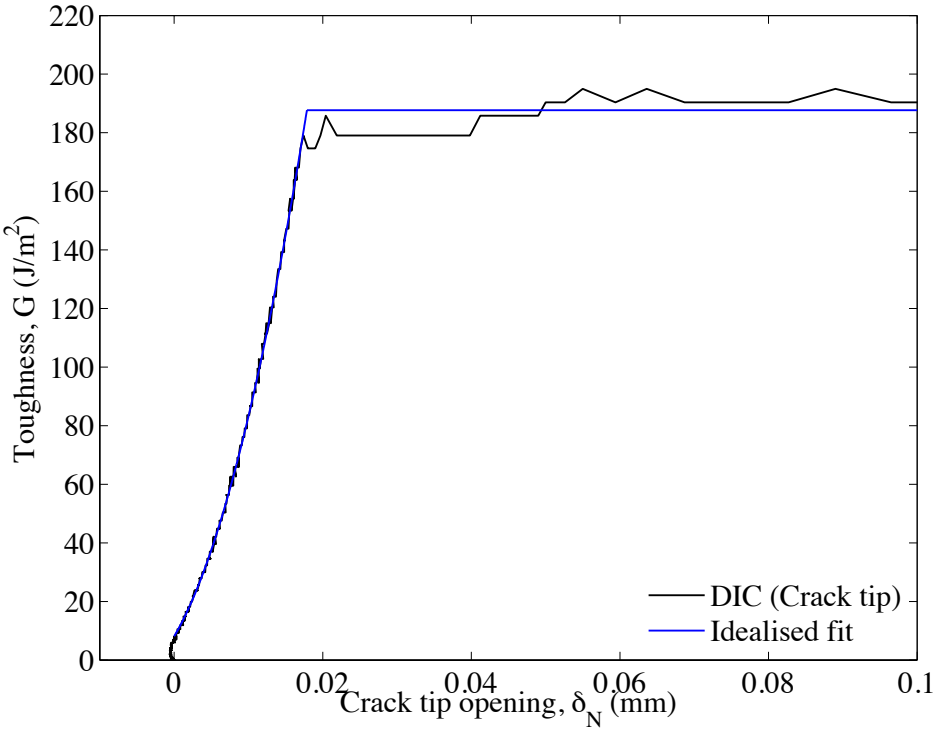

(a) Crack tip opening measured using DIC.

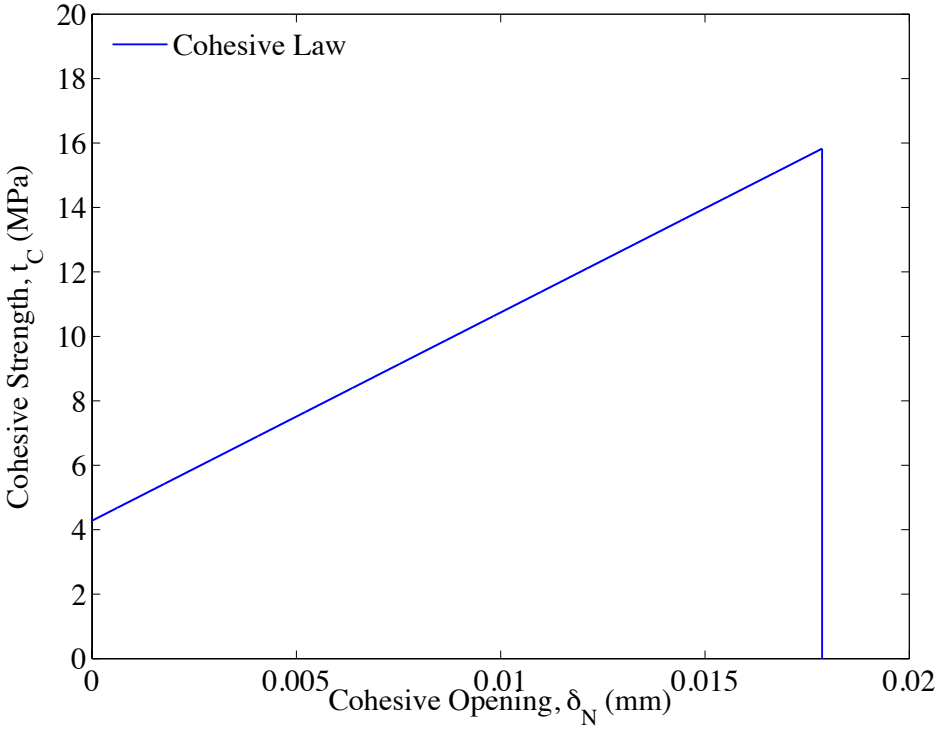

(b) Mode I cohesive zone law obtained by differentiation of toughness vs. opening curve shown in fig. E.5(a).

FIGURE E.5: Direct measurement of mode I cohesive zone law.

E.1.1 Calculation of bending flexural modulus

Although DIC was not ultimately used to obtain the cohesive laws, accurate readings of the specimen strain field were obtained. As pure moments were applied to the beams, the stress distribution in the beams could be accurately approximated by:

$$\sigma = \frac{My}{I} \tag{E.4}$$

where σ is the bending stress in the beam, M is the applied moment, y is the distance from the neutral axis to the point the stress is being estimated, and I is the second moment of area of the beam, given by:

$$I = \frac{Bh^3}{12} \tag{E.5}$$

where B is the beam thickness, and h is the beam height. As the stress and strain are then known at a material point, the bending modulus, E, can be calculated from the well known 1D Hookes law:

$$E = \frac{\sigma}{\epsilon} \tag{E.6}$$

The measured strain distribution in the bending direction (yy) during steady state crack propagation in the mode I test (sample A) is shown in fig. E.6. The measured strain as a function of the position is shown in the left of the figure, where the path starts at the left edge of the left beam and finishes at the right edge of the left beam. It is evident from both plots of strain, that the strain distribution is constant along the beam, and it is linear, as expected due to the pure moment applied. In order to estimate the flexural modulus (E), the approximated stress at the outermost edge is divided by the measured strain at the outermost edge according to eq. E.6.

The average applied moment throughout steady state propagation (from 0.5 mm to 9.5 mm in fig. 5.11(a)) was 15.65 N/m, which corresponds to an outer stress of $-125.2MPa$ using eq. E.4. The average outer strain recorded throughout propagation was -0.1%, as seen in fig. E.6; the estimated modulus is then given by:

$$E = \frac{\sigma}{\epsilon} = \frac{125.2MPa}{.0001} = 125.2GPa \tag{E.7}$$

As expected, this modulus is slightly lower than the tensile modulus (141 GPa) quoted in the material data sheet [103].

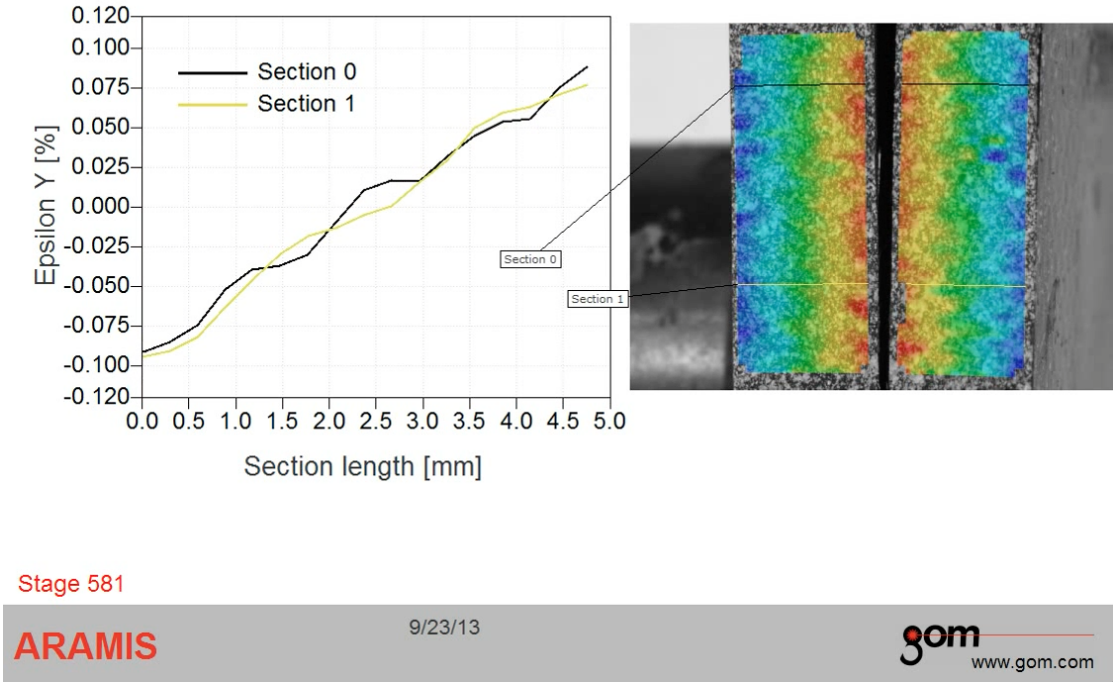

FIGURE E.6: Strain distribution from DIC measurements in mode I test during steady state fracture.

Appendix F

Publications arising from this Thesis

Journal Papers

- **M. Conroy**, A.J Kinloch, J.G. Williams and A. Ivankovic, Mixed Mode Partitioning of Beam Like Geometries: A Damage Dependent Solution. *Engineering Fracture Mechanics*, July 2015, *In Press*

Pending Journal Papers

- **M. Conroy**, B.F. Sørensen and A. Ivankovic, Combined Numerical and Experimental Investigation of Mode Mixity in Beam Like Geometries. *In Preparation*
- **M. Conroy** and A. Ivankovic, An investigation into the performance of widely used cohesive zone formulations when subjected to variable mixed mode loading. *In Preparation*

Conference Proceedings

- **M. Conroy** and A. Ivankovic, Mode Mixity in Beam Like Geometries: A Semi-Analytical Cohesive Analysis. *Proceedings of the 38th annual meeting of the Adhesion Society, Savannah, GA, February 20-25, 2015*
- **M. Conroy**, B.F. Sørensen and A. Ivankovic, Combined Numerical and Experimental Investigation of Mode Mixity in Beam Like Geometries. *Proceedings of the 37th annual meeting of the Adhesion Society, San Diego, CA, February 23-26, 2014*

- **M. Conroy** and A. Ivankovic, Mixed Mode Partitioning of Cohesive Zones. *Proceedings of the 12th International Adhesion Conference, York, UK, Sept 4-6, 2013*
- **M. Conroy**, A. Ivankovic, A. Karac and J.G. Williams, Mode Mixity in Beam Like Geometries: Global Partitioning with Cohesive Zones. *Proceedings of the 36th annual meeting of the Adhesion Society, Daytona Beach, FL, March 3-6, 2013*
- B. Blackman, **M. Conroy**, A. Ivankovic, A. Karac, A.J. Kinloch and J.G. Williams, Mode Mixity in Beam Like Geometries: Linear Elastic Cases and Local Partitioning. *15th European Conference on Composite Materials, Venice, Italy, June 24-28, 2012*

Conference and Seminar Presentations

- Mixed Mode Partitioning of Beam Like Geometries: A Damage Dependent Solution.
  - *Joint symposium of Irish Mechanics Society and Irish Society for Scientific and Engineering Computation: Advances in Mechanics, Galway, Ireland, December 8-9, 2014*
  - *7th International Conference on Fracture of Polymers, Composites and Adhesives, Les Diablerets, Switzerland, September 14-18, 2014*
- Combined Numerical/Experimental Investigation of Mode Mixity in Beam Like Geometries.
  - *Irish Polymers and Materials Conference, Dublin, Ireland, April 30, 2014*
  - *Joint symposium of Irish Mechanics Society and Irish Society for Scientific and Engineering Computation: Advances in Mechanics, Dublin, Ireland, December 5, 2013*
- Mixed Mode Partitioning of Cohesive Zones.
  - *12th International Adhesion Conference, York, UK, September 6, 2013*
- Mode Mixity in Beam Like Geometries: Global Partitioning with Cohesive Zones.
  - *17th International Conference on Composite Structures, Porto, Portugal, June 19, 2013*
  - *36th annual meeting of the Adhesion Society, Daytona Beach, FL, March 4, 2013*
- Aspects of Mixed-Mode Adhesive Failure.

  - *The Irish Adhesion, Surface Coating and Composites Conference, Dublin, Ireland, May 23, 2013*

- Mixed Views on Measuring Toughness.

  - *Sir Bernard Crossland Symposium, Dublin, Ireland, April 11, 2013*
  - *BOC Postgraduate Symposium, Dublin, Ireland, February 25, 2013*

- Mode Mixity in Beam Like Geometries: Linear Elastic Cases and Local Partitioning.

  - *15th European Conference on Composite Materials, Venice, Italy, June 27, 2012*

- Why are adhesives tough (to work with)?

  - *The Irish Adhesion, Surface Coating and Composites Conference: Challenges in Transport, Energy and Sustainability, Limerick, Ireland, April, 2012*

Awards

- **International Scholarship Award, Lord Edward Fitzgerald Memorial Fund**, 2013.
- **BOC Postgraduate Symposium Award**, University College Dublin, 2013.
- **Peebles Award for Graduate Student Research in Adhesion Science**, The Adhesion Society, 2013.

References

[1] K.B. Katnam, L.F.M. Da Silva, and T.M. Young. Bonded repair of composite aircraft structures: A review of scientific challenges and opportunities. *Progress in Aerospace Sciences*, 61(0):26–42, August 2013.

[2] R.M. Jones. *Mechanics Of Composite Materials*. Materials Science and Engineering Series. Taylor & Francis, 1998. ISBN 9781560327127.

[3] D. Quan and A. Ivankovic. Effect of coreshell rubber (CSR) nano-particles on mechanical properties and fracture toughness of an epoxy polymer. *Polymer*, 66: 16–28, June 2015.

[4] J.E. Gordon. *The New Science of Strong Materials: Or Why You Don't Fall Through the Floor*. Penguin Books Limited, 1991. ISBN 9780141927701.

[5] Aviation Saftey: Status of FAAs Actions to Oversee the Safety of Composite Airplanes. US Government Accountability of Office report: GAO-11-849. September 2011.

[6] B.R.K. Blackman, A.J. Brunner, and P. Davies. Delamination fracture of continuous fibre composites: Mixed-mode fracture. In D.R. Moore, A. Pavan, and J.G. Williams, editors, *Fracture Mechanics Testing Methods for Polymers, Adhesives and Composites*, pages 225 – 270. Elsevier Science, Amsterdam, 2001.

[7] ISO 15024:2001. Fibre-reinforced plastic composites Determination of mode I interlaminar fracture toughness, G_{IC}, for unidirectionally reinforced materials, 2001.

[8] ISO 15114:2014. Fibre-reinforced plastic composites Determination of the mode II fracture resistance for unidirectionally reinforced materials using the calibrated end-loaded split (C-ELS) test and an effective crack length approach, 2014.

[9] ASTM Standard D 5528-13. Standard Test Method for Mixed Mode I Interlaminar Fracture Toughness of Unidirectional Fiber-Reinforced Polymer Matrix Composites, 2013.

[10] ASTM Standard D 6671/6671M -13e1. Standard Test Method for Mixed Mode I Mode II Interlaminar Fracture Toughness of Unidirectional Fiber-Reinforced Polymer Matrix Composites, 2013.

[11] B.F. Sørensen. Cohesive laws for assessment of materials failure: Theory,experimental methods and application. Doctor of Technices thesis.

[12] T.L. Anderson. *Fracture Mechanics: Fundamentals and Applications, Third Edition*. Taylor & Francis, 2005. ISBN 9780849316562.

[13] B. Cotterell and J.R. Rice. Slightly curved or kinked cracks. *International Journal of Fracture*, 16(2):155–169, 1980.

[14] D.A. Dillard, H.K. Singh, D.J. Pohlit, and J.M. Starbuck. Observations of Decreased Fracture Toughness for Mixed Mode Fracture Testing of Adhesively Bonded Joints. *Journal of Adhesion Science and Technology*, 23(10-11):1515–1530, January 2009.

[15] J.R. Reeder. An evaluation of mixed-mode delamination failure criteria, NASA technical memorandum 104210. Langley Research Center, Hampton, VA, 1992.

[16] M. Charalambides, A.J. Kinloch, Y. Wang, and J.G. Williams. On the analysis of mixed-mode failure. *International Journal of Fracture*, 54(3):269–291, 1992.

[17] M.L. Benzeggagh and M. Kenane. Measurement of mixed-mode delamination fracture toughness of unidirectional glass/epoxy composites with mixed-mode bending apparatus. *Composites Science and Technology*, 56(4):439 – 449, 1996.

[18] Q.V. Bui. A modified benzeggagh-kenane fracture criterion for mixed-mode delamination. *Journal of Composite Materials*, 45(4):389–413, 2011.

[19] B. Spencer and J.T. Barnby. The effects of notch and fibre angles on crack propagation in fibre-reinforced polymers. *Journal of Materials Science*, 11(1):83–88, 1976.

[20] J.G. Williams. On the calculation of energy release rates for cracked laminates. *International Journal of Fracture*, 36(2):101–119, 1988.

[21] J.R. Reeder and J.R. Crews Jr. Mixed Mode Bending Method for Delamination Testing. *AIAA Journal*, 28(7):1270–1276, 1990.

[22] J.R. Reeder and J.R. Crews Jr. Nonlinear analysis and redesign of the mixed-mode bending delamination test, NASA technical memorandum TM102777. Langley Research Center, Hampton, VA, 1992.

[23] J.R. Reeder. Refinements to the Mixed-Mode Bending Test for Delamination Toughness. *Journal of Composites Technology and Reserach*, 25(4):1270–1276, 2003.

[24] G. Fernlund and J.K. Spelt. Mixed-mode fracture characterization of adhesive joints. *Composites Science and Technology*, 50(4):441–449, January 1994.

[25] B.F. Sørensen, K. Jørgensen, T.K. Jacobsen, and R.C. Østergaard. DCB-specimen loaded with uneven bending moments. *International Journal of Fracture*, 141(1-2): 163–176, September 2006.

[26] Z. Suo and J.W. Hutchinson. Interface crack between two elastic layers. *International Journal of Fracture*, 43(1):1–18, 1990.

[27] B.D. Davidson, P.L. Fariello, R.C. Hudson, and V. Sundararaman. Accuracy Assessment of the Singular-Field Based Mode-Mix Decomposition Procedure for the Prediction of Delamination. *Composite materials: Testing and Design, ASTM STP 1242, S.J. Hooper, Ed., American Society for Testing and Materials*, 13: 109–128, 1997.

[28] S. Wang and C.M. Harvey. Mixed mode partition theories for one dimensional fracture. *Engineering Fracture Mechanics*, 79:329–352, January 2012.

[29] D. Bruno and F. Greco. Mixed mode delamination in plates: a refined approach. *International Journal of Solids and Structures*, 38(5051):9149–9177, 2001.

[30] S. Bennati, M. Colleluori, D. Corigliano, and P.S. Valvo. An enhanced beam-theory model of the asymmetric double cantilever beam (ADCB) test for composite laminates. *Composites Science and Technology*, 69(11-12):1735–1745, September 2009.

[31] Q. Luo and L. Tong. Analytic formulas of energy release rates for delamination using a global local method. *International Journal of Solids and Structures*, 49 (23-24):3335–3344, November 2012.

[32] S. Hashemi, A.J. Kinloch, and J.G. Williams. Mixed-mode fracture in fiber-polymer composite laminates. *Composite Materials: Fatigue and Fracture ASTM STP 1110, T.K O'Brien, Ed., American Society for Testing and Materials, Philadelphia*, 3:143–168, 1991.

[33] F. Ducept, D. Gamby, and P. Davies. A mixed-mode failure criterion derived from tests on symmetric and asymmetric specimens. *Composites Science and Technology*, 59(4):609–619, March 1999.

[34] B. Davidson, R. Bialaszewski, and S. Sainath. A non-classical, energy release rate based approach for predicting delamination growth in graphite reinforced laminated polymeric composites. *Composites Science and Technology*, 66(10):1479–1496, August 2006.

[35] C.M. Harvey and S. Wang. Experimental assessment of mixed-mode partition theories. *Composite Structures*, 94(6):2057–2067, May 2012.

[36] B.R.K. Blackman, M. Conroy, A. Ivankovic, A. Karac, A.J. Kinloch, and J.G. Williams. Mode-Mixity in Beam-Like Geometries : Linear Elastic Cases and Local Partitioning. In *15th European Conference on Composite Materials. June 24-28*, Venice, Italy, 2012.

[37] R.A. Schapery and B.D. Davidson. Prediction of Energy Release Rate for Mixed-Mode Delamination Using Classical Plate Theory. *Applied Mechanics Reviews*, 43 (5S):S281–S287, May 1990.

[38] B.D. Davidson, H. Hu, and R.A. Schapery. An Analytical Crack-Tip Element for Layered Elastic Structures. *Journal of Applied Mechanics*, 62(2):294–305, June 1995.

[39] T.L. Becker, J.M. McNaney, R.M. Cannon, and R.O. Ritchie. Limitations on the use of the mixed-mode delaminating beam test specimen: Effects of the size of the region of K-dominance. *Mechanics of Materials*, 25(4):291–308, May 1997.

[40] J.P. Parmigiani and M.D. Thouless. The effects of cohesive strength and toughness on mixed-mode delamination of beam-like geometries. *Engineering Fracture Mechanics*, 74(17):2675–2699, November 2007.

[41] R.B. Sills and M.D. Thouless. The effect of cohesive-law parameters on mixed-mode fracture. *Engineering Fracture Mechanics*, 109(0):353–368, 2013.

[42] ABAQUS. Version 6.11 documentation. *Dassault Systemes Simulia Corp. Providence, RI, USA.*, 2011.

[43] E.F. Rybicki and M.F. Kanninen. A finite element calculation of stress intensity factors by a modified crack closure integral. *Engineering Fracture Mechanics*, 9 (4):931–938, January 1977.

[44] J.F. Yau, S.S. Wang, and H.T. Corten. A Mixed-Mode Crack Analysis of Isotropic Solids Using Conservation Laws of Elasticity. *Journal of Applied Mechanics*, 47 (2):335–341, June 1980.

[45] H. Ishikawa, H. Kitagawa, and H. Okamura. J integral of a mixed mode crack and its application. In K J MILLERR.F. SMITH, editor, *Mechanical Behaviour of Materials*, pages 447–455. Pergamon, 1980. ISBN 978-1-4832-8414-9.

[46] Z. Suo. Delamination Specimens for Orthotropic Materials. *Journal of Applied Mechanics*, 57(3):627–634, September 1990.

[47] Z. Suo, G. Bao, B. Fan, and T.C. Wang. Orthotropy rescaling and implications for fracture in composites. *International Journal of Solids and Structures*, 28(2): 235 – 248, 1991.

[48] W.K. Wilson. Plane Strain Crack Toughness Testing of High Strength Metallic Materials. *ASTM STP 410, American Society for Testing and Materials, Philadelphia*, pages 75–76, 1966.

[49] C.E. Inglis. Stresses in a plate due to the presence of cracks and sharp corners. *Proceedings of the Institute of Naval Architects*, 55:219 – 230, 1913.

[50] G.R. Irwin. Fracture. In S Flügge, editor, *Elasticity and Plasticity*, volume 3 of *Handbuch der Physik*, pages 551–590. Springer Berlin Heidelberg, 1958. ISBN 978-3-642-45889-7.

[51] T.S. Ramamurthy, T. Krishnamurthy, K.B. Narayana, K. Vijayakumar, and B. Dattaguru. Modified crack closure integral method with quarter point elements. *Mechanics Research Communications*, 13(4):179–186, July 1986.

[52] I.S. Raju. Calculation of strain-energy release rates with higher order and singular finite elements. *Engineering Fracture Mechanics*, 28(3):251–274, 1987.

[53] J.A. Nairn. Generalized crack closure analysis for elements with arbitrarily-placed side nodes and consistent nodal forces. *International Journal of Fracture*, 171(1): 11–22, September 2011.

[54] R. Krueger. Virtual crack closure technique: History, approach, and applications. *Applied Mechanics Reviews*, 57(2):109–143, April 2004.

[55] J.R. Rice. A Path Independent Integral and the Approximate Analysis of Strain Concentration by Notches and Cracks. *Journal of Applied Mechanics*, 35(2):379–386, June 1968.

[56] C.F. Shih and R.J. Asaro. Elastic-Plastic Analysis of Cracks on Bimaterial Interfaces: Part ISmall Scale Yielding. *Journal of Applied Mechanics*, 55(2):299–316, June 1988.

[57] D.M. Barnett and R.J. Asaro. The fracture mechanics of slit-like cracks in anisotropic elastic media. *Journal of the Mechanics and Physics of Solids*, 20 (6):353–366, December 1972.

[58] C.F. Shih, B. Moran, and T. Nakamura. Energy release rate along a three-dimensional crack front in a thermally stressed body. *International Journal of Fracture*, 30(2):79–102, 1986.

[59] J.A. Nairn. Phase 1 report. *ESIS TC4 Mixed Mode Round Robin*, 2011.

[60] H.M. Westergaard. Bearing pressures and cracks. *Journal of Applied Mechanics*, 6:A49–59, 1939.

[61] D.S. Dugdale. Yielding of steel sheets containing slits. *Journal of the Mechanics and Physics of Solids*, 8(2):100–104, May 1960.

[62] G.I. Barenblatt. The Mathematical Theory of Equilibrium Cracks in Brittle Fracture. *Advances in Applied Mechanics*, Volume 7:55–129, 1962.

[63] G. Bao, S. Ho, Z. Suo, and B. Fan. The role of material orthotropy in fracture specimens for composites. *International Journal of Solids and Structures*, 29(9): 1105 – 1116, 1992.

[64] G.C. Sih, P.C. Paris, and G.R. Irwin. On cracks in rectilinearly anisotropic bodies. *International Journal of Fracture Mechanics*, 1(3):189–203, 1965.

[65] V. Cooper, A. Ivankovic, A. Karac, D. McAuliffe, and N. Murphy. Effects of bond gap thickness on the fracture of nano-toughened epoxy adhesive joints. *Polymer*, 53(24):5540–5553, 2012.

[66] P.P. Camanho, C.G. Dávila, and M.F. De Moura. Numerical simulation of mixed-mode progressive delamination in composite materials. *Journal of Composite Materials*, 37(16):1415–1438, 2003. cited By 282.

[67] Q.D. Yang, M.D. Thouless, and S.M. Ward. Numerical simulations of adhesively-bonded beams failing with extensive plastic deformation. *Journal of the Mechanics and Physics of Solids*, 47(6):1337–1353, 1999.

[68] A. Hillerborg, M. Modéer, and P.E. Petersson. Analysis of crack formation and crack growth in concrete by means of fracture mechanics and finite elements. *Cement and Concrete Research*, 6(6):773–781, November 1976.

[69] Q.D. Yang and M.D. Thouless. Mixed-mode fracture analyses of plastically-deforming adhesive joints. *International Journal of Fracture*, 110(2):175–187, 2001.

[70] A. Ivankovic, K.C. Pandya, and J.G. Williams. Crack growth predictions in polyethylene using measured tractionseparation curves. *Engineering Fracture Mechanics*, 71(4-6):657–668, March 2004.

[71] N. Murphy and A. Ivankovic. The prediction of dynamic fracture evolution in PMMA using a cohesive zone model. *Engineering Fracture Mechanics*, 72(6):861–875, April 2005.

[72] B.R.K. Blackman, H. Hadavinia, A.J. Kinloch, and J.G. Williams. The use of a cohesive zone model to study the fracture of fibre composites and adhesively-bonded joints. *International Journal of Fracture*, 119(1):25–46, 2003.

[73] D. Carolan, A. Ivanković, and N. Murphy. A combined experimentalnumerical investigation of fracture of polycrystalline cubic boron nitride. *Engineering Fracture Mechanics*, 99:101–117, February 2013.

[74] Q.D. Yang, B.N. Cox, R.K. Nalla, and R.O. Ritchie. Fracture length scales in human cortical bone: The necessity of nonlinear fracture models. *Biomaterials*, 27(9):2095–2113, 2006.

[75] A. Tabaković, A. Karač, A. Ivanković, A. Gibney, C. McNally, and M.D. Gilchrist. Modelling the quasi-static behaviour of bituminous material using a cohesive zone model. *Engineering Fracture Mechanics*, 77(13):2403–2418, September 2010.

[76] B.F. Sørensen. Cohesive law and notch sensitivity of adhesive joints. *Acta Materialia*, 50(5):1053–1061, March 2002.

[77] Y. Sun, N. Pugno, B. Gong, and Q. Ding. A simplified hardening cohesive zone model for bondline thickness dependence on adhesive joints. *International Journal of Fracture*, pages 1–8, 2015.

[78] A. Needleman. A Continuum Model for Void Nucleation by Inclusion Debonding. *Journal of Applied Mechanics*, 54(3):525–531, September 1987.

[79] X.P. Xu and A. Needleman. Numerical simulations of fast crack growth in brittle solids. *Journal of the Mechanics and Physics of Solids*, 42(9):1397–1434, September 1994.

[80] V. Tvergaard and J.W. Hutchinson. The influence of plasticity on mixed mode interface toughness. *Journal of the Mechanics and Physics of Solids*, 41(6):1119–1135, June 1993.

[81] G.T. Camacho and M. Ortiz. Computational modelling of impact damage in brittle materials. *International Journal of Solids and Structures*, 33(20-22):2899–2938, August 1996.

[82] B.F. Sørensen and P. Kirkegaard. Determination of mixed mode cohesive laws. *Engineering Fracture Mechanics*, 73(17):2642–2661, November 2006.

[83] K. Park, G.H. Paulino, and J.R. Roesler. A unified potential-based cohesive model of mixed-mode fracture. *Journal of the Mechanics and Physics of Solids*, 57(6): 891–908, June 2009.

[84] J.P. McGarry, É. Ó Máirtín, G. Parry, and G.E. Beltz. Potential-based and non-potential-based cohesive zone formulations under mixed-mode separation and over-closure. Part I: Theoretical analysis. *Journal of the Mechanics and Physics of Solids*, 63:336–362, February 2014.

[85] É. Ó Máirtín, G. Parry, G.E. Beltz, and J.P. McGarry. Potential-based and non-potential-based cohesive zone formulations under mixed-mode separation and over-closure. Part II: Finite element applications. *Journal of the Mechanics and Physics of Solids*, 63:363–385, February 2014.

[86] S. Goutianos and B.F. Sørensen. Path dependence of truss-like mixed mode cohesive laws. *Engineering Fracture Mechanics*, 91:117–132, September 2012.

[87] A. Turon, P.P. Camanho, J. Costa, and C.G. Dávila. A damage model for the simulation of delamination in advanced composites under variable-mode loading. *Mechanics of Materials*, 38(11):1072–1089, November 2006.

[88] G. Alfano and M.A. Crisfield. Finite element interface models for the delamination analysis of laminated composites: mechanical and computational issues. *International Journal for Numerical Methods in Engineering*, 50(7):1701–1736, March 2001.

[89] P.P. Camanho and F.L. Matthews. Delamination Onset Prediction in Mechanically Fastened Joints in Composite Laminates. *Journal of Composite Materials*, 33(10): 906–927, May 1999.

[90] J.C. Brewer and P.A. Lagace. Quadratic Stress Criterion for Initiation of Delamination. *Journal of Composite Materials*, 22(12):1141–1155, December 1988.

[91] A. Turon, P.P. Camanho, J. Costa, and J. Renart. Accurate simulation of delamination growth under mixed-mode loading using cohesive elements: Definition of interlaminar strengths and elastic stiffness. *Composite Structures*, 92(8):1857–1864, July 2010.

[92] J.C.J. Schellekens and R. De Borst. On the numerical integration of interface elements. *International Journal for Numerical Methods in Engineering*, 36(1): 43–66, January 1993.

[93] M. Mathews and S. Swanson. Characterization of the interlaminar fracture toughness of a laminated carbon/epoxy composite. *Composites Science and Technology*, 67(7-8):1489–1498, June 2007.

[94] C. Sarrado, A. Turon, J. Renart, and I. Urresti. Assessment of energy dissipation during mixed-mode delamination growth using cohesive zone models. *Composites Part A: Applied Science and Manufacturing*, 43(11):2128–2136, November 2012.

[95] A. Turon, C.G. Dávila, P.P. Camanho, and J. Costa. An engineering solution for mesh size effects in the simulation of delamination using cohesive zone models. *Engineering Fracture Mechanics*, 74(10):1665 – 1682, 2007.

[96] Q. Yang and B. Cox. Cohesive models for damage evolution in laminated composites. *International Journal of Fracture*, 133(2):107–137, 2005.

[97] P.W. Harper and S.R. Hallett. Cohesive zone length in numerical simulations of composite delamination. *Engineering Fracture Mechanics*, 75(16):4774–4792, November 2008.

[98] J. Planas and M. Elices. Nonlinear fracture of cohesive materials. *International Journal of Fracture*, 51(2):139–157, 1991.

[99] D. Svensson, K.S. Alfredsson, A. Biel, and U. Stigh. Measurement of cohesive laws for interlaminar failure of CFRP. *Composites Science and Technology*, 100 (0):53–62, August 2014.

[100] UK Ciba Geigey Composites, Duxford. Fibredux 6376C/T-300 material data sheet.

[101] B.F. Sørensen and T.K. Jacobsen. Characterizing delamination of fibre composites by mixed mode cohesive laws. *Composites Science and Technology*, 69(3-4):445–456, March 2009.

[102] B.F. Sørensen and T.K. Jacobsen. Determination of cohesive laws by the J integral approach. *Engineering Fracture Mechanics*, 70(14):1841–1858, September 2003.

[103] Hexcel 8552/as4 material data sheet. `http://www.hexcel.com/Resources/DataSheets/Prepreg-Data-Sheets/8552_eu.pdf`. Accessed: 25-08-2015.

[104] J. Mohan. *An Investigation of Composite-to-Composite Bonding*. PhD thesis, University College Dublin, 2010.

[105] J. Bonhomme, J. Viña, A. Argüelles, I. Viña, and V. Mollón. Influence of the Matrix Toughness in Carbon-Epoxy Composites Subjected to Delamination under Modes I, II, and Mixed I/II. *Mechanics of Advanced Materials and Structures*, 20 (8):679–686, June 2012.

[106] A.J. Kinloch, Y. Wang, J.G. Williams, and P. Yayla. The mixed-mode delamination of fibre composite materials. *Composites Science and Technology*, 47(3): 225–237, January 1993.

[107] J. Bonhomme, A. Argüelles, J. Viña, and I. Viña. Fractography and failure mechanisms in static mode I and mode II delamination testing of unidirectional carbon reinforced composites. *Polymer Testing*, 28(6):612–617, September 2009.

[108] T. Johannesson, P. Sjöblom, and R. Seldén. The detailed structure of delamination fracture surfaces in graphite/epoxy laminates. *Journal of Materials Science*, 19 (4):1171–1177, 1984.

[109] J. Mohan, A. Ivanković, and N. Murphy. Mixed-mode fracture toughness of co-cured and secondary bonded composite joints. *Engineering Fracture Mechanics*, 134:148–167, January 2015.

[110] B.R.K. Blackman, A.J. Brunner, and J.G. Williams. Mode II fracture testing of composites: a new look at an old problem. *Engineering Fracture Mechanics*, 73: 2443–2455, 2006.

[111] R.D. Kriz and W.W. Stinchcomb. Elastic moduli of transversely isotropic graphite fibers and their composites. *Experimental Mechanics*, 19(2):41–49, 1979.

[112] G. Zhou, E.R. Green, and C. Morrison. In-plane and interlaminar shear properties of carbon/epoxy laminates. *Composites Science and Technology*, 55(2):187–193, January 1995.